CORRELATING GEOMETRY, HAEMODYNAMICS AND INTIMAL HYPERPLASIA IN RADIOCEPHALIC ARTERIOVENOUS FISTULAE

Thesis submitted in accordance with the requirements of the University of Liverpool for the degree of Doctor in Philosophy by

Sharmila Sivanesan, *BSc, ARCS, MSc.*

December, 1996

CONTENTS

ABSTRACT

A significant number of late failures of arteriovenous fistulae for haemodialysis access are related to the progression of intimal hyperplasia. Although, the aetiology of this process is still unknown, the geometry of the fistula and haemodynamics have been implicated as large factors in this process. A two part study was, therefore, devised to identify sites of stenosis in patients with fistulae and relate the findings to haemodynamic parameters, such wall shear stress and turbulence, measured in an *in vitro* environment.

The clinical study using duplex and colour-flow ultrasonography to assess end vein-to-side artery fistulae isolated these stenotic lesions to three specific sites: at the anastomosis (Type 1), on the inner wall of the curved region of the cephalic vein (Type 2) and just proximal to this curved segment where the vein straightens out (Type 3).

To investigate the haemodynamics, a series of transparent fistula models with differing geometries was constructed. Each model was installed in a flow loop system circulating a blood analogue fluid of aqueous glycerol and salt. Flow patterns were obtained by planar illumination of micro-particles suspended in the fluid. Flow visualization studies, along with quantitative measurements, using laser Doppler anemometry, were performed over a range of flow conditions corresponding to those recorded in patients.

A large vortex was seen on the floor of the anastomosis, at the union of proximal and distal arterial flow. Large oscillating wall shear stresses were measured in the region of this vortex and at the fluctuating flow reattachment point. This region corresponded to Type 1 stenosis. Turbulence was the dominant feature in the vein, with high Reynolds shear stresses measured near the anastomosis. Wall shear stresses on the inner wall of the vein (site of Type 2 stenosis) were generally much

lower than on the outer wall. Also, wall shear stresses in the curve of the vein were bidirectional. The site of Type 3 stenosis coincided with a region of low shear.

There were differences in the axial and radial distribution of turbulence. The peak absolute turbulence and peak Reynolds shear stress near the anastomosis appeared to increase with decreasing anastomotic angle. There was no clear trend with vein-to-artery diameter ratio.

There was a correlation between stenotic sites found *in vivo* and flow features characterized in the models. High levels of wall shear stress have been shown to be injurious to the endothelium and blood elements in contact with it. The Reynolds shear stresses at the anastomosis were found to be in the range associated with haemolysis and platelet lysis. A coagulation cascade may be initiated causing intimal cell proliferation. In low shear regions, lipid transport across the wall into the blood may be inhibited.

The study has identified anastomotic configurations that are associated with reduced flow disturbances. Modifying access surgery accordingly may lead to improved long-term patency.

ACKNOWLEDGMENTS

My principal debt of gratitude is to Dr. Thien How for supervising this project, proffering much helpful advice, imparting his great wisdom and devoting much of his time. I would also like to thank Mr. Ali Bakran for overseeing the clinician content of this research project and for putting the laboratory work into a clinically-relevant context.

Credit also goes to Mr. James Blackhurst whose technical assistance and advice has been invaluable throughout my model-making and laboratory experiments. I hope I haven't been too much trouble - I know he hides whenever he hears my footsteps on the stairs leading to the workshop. And to my great mentor and buddy, Dr. Adam Shortland, whose jokes have kept me laughing and without whose technical knowledge I definitely wouldn't have got this far. I would also like to thank Trevor Carpenter, Andrew Rattray, Stephan Gaupp and Dr. Richard Black for all their help with the model-making and the LDA experiments and data analysis.

There are many others who have helped me with this project - including Ann Evans and Diane Donnelly, in the ultrasound scan room, the nurses and ward clerks of 9A, the clinicians of the Renal Transplant Unit, Nicky and the Theatre receptionists. Also, I would like to thank Mr. Malcolm Brown, Consultant Renal Transplant Surgeon, for his cooperation and assistance in collecting some of the clinical data, and for his approachability.

I am also very grateful to the many friends I have made during my three years in Liverpool who have brightened my days and made those periods of stress and frustration bearable, especially, Debra, Shona, Jo, Shirley, Nick, Patrick, Figen, Gowry and Nisreen. Also, thank you, Adam and Amita for putting me up when I was a homeless miserable wretch.

Most importantly, I would like to thank my little beebie, Ged, without whom

I would never have got through this PhD in one piece. Thank you for being there for me and putting up with all my moanings and groanings and for coming to my rescue many many times. And thank you for stealing the Genetics Department dark-room key so that I could print my photos.

Finally, I would like to give a special thanks to my parents for their continuing support and encouragement - although I seldom say it, I do appreciate all they have done for me. My father has been a great inspiration to me over the years; I wish he had lived at least a couple of months longer to see me finally finish.

CHAPTER 1

INTRODUCTION

INTRODUCTION

The lifetime of an arteriovenous fistula for haemodialysis access can be anywhere between months and tens of years, in a few cases. Stenosis and subsequent thrombosis cause a significant number of late failures (after 3 months). Stenosis occurs through the development of intimal hyperplasia in a fibroproliferative response to endothelial dysfunction. The localized development of these stenotic lesions would seem to implicate the geometry of the fistula and haemodynamics in the aetiology of this process. Both high shear and low shear influence the permeability of the endothelium to plasma constituents and platelet-derived factors. Low shear allows the accumulation of platelet aggregates, mitogens and chemoattractants, and high shear may damage blood elements.

Some of the causes of flow disturbances are largely unavoidable or cannot be corrected. Some, though, could be eliminated at the stage of fistula construction if there were more information available on the effects of shear stress, anastomotic length and angle, anastomotic configuration, vessel diameters and flow distributions on patency. The minimization of flow disturbances which occur in fistulae first requires the identification of locations predisposed to the formation of stenotic lesions and an full characterization of the contributory processes. With further knowledge, the surgical technique could then be tailored to provide the optimum configuration for long-term patency in each individual patient. This might reduce the need for secondary, or multiple, access procedures, save valuable resources and shield the patient and their families from even more disappointment and distress.

To assess the contribution of haemodynamics to fistula failure, a two-part project was devised to monitor primary access fistulae in patients, identifying stenoses, and to model flow through fistulae in the laboratory. As end-to-side fistulae

were created in the majority of the patients admitted to the Royal Liverpool University Hospital for vascular access procedures for haemodialysis, this project has been confined to an analysis of end vein-to-side artery fistulae.

Chapter 2 provides a review and general background to arteriovenous fistulae for haemodialysis access and their performance. The main cause of late fistula failures, intimal hyperplasia, is reviewed in Chapter 3, in relation to haemodynamics. The clinical study, the procedure for making intraoperative measurements, the protocol for postoperative follow-up with ultrasonography and the instruments used are discussed in Chapter 4. The range of parameters derived from the clinical study were used to design fistula models and establish the pulsatile flow conditions and parameters subsequently used in the *in vitro* study. The analysis of the clinical data for this purpose is given in Chapter 5.

Chapter 6 describes the protocol for producing models suitable for use in flow visualization studies and laser Doppler anemometry experiments. The idealized models were designed using a CAD/CAM software package using data defined mathematically, based on the surgical technique. Six models with differing geometries (varying anastomotic angle and vein-to-artery diameter ratio) were constructed from transparent silicone rubber using a lost-wax technique.

The flow visualization experiments are discussed in Chapter 7. This Chapter contains details of the experimental set-up, the seeded flow solution, the protocol for conducting the experiments, photographs of the flow patterns and an analysis of the results. The main objectives of this set of experiments were to characterize the overall flow features in arteriovenous fistulae and, through the qualitative analysis, to limit the number of experiments and measurement positions necessary in the quantitative experiments.

Quantitative measurements in the six fistula models were carried out using a 2-component laser Doppler anemometer. The flow conditions and parameters

employed in these experiments were defined by the results of the flow visualization study. The analysis of the velocity data centred on levels of absolute turbulence and turbulence intensity, Reynolds shear stress and wall shear stress at specific points. The materials, methods and results of the laser Doppler anemometry study are discussed in Chapter 8.

Chapter 9 provides the results of the long-term patient follow-up. The sites of stenosis in individual patients and patient medical history are presented in this chapter. The general conclusions drawn from the clinical study are also given.

The final chapter, Chapter 10, deals with the relationship between the clinical findings and the haemodynamic parameters measured in the *in vitro* models. The significant parameters are compared with respect to varying anastomotic angle and diameter ratio.

CHAPTER 2

REVIEW OF HAEMODIALYSIS AND VASCULAR ACCESS

REVIEW OF HAEMODIALYSIS AND VASCULAR ACCESS

2.1 THE HISTORY OF HAEMODIALYSIS

In December 1993, almost twenty thousand people in the United Kingdom were suffering from end-stage renal failure, and four thousand of those were new cases diagnosed during that year (figures from the EDTA Registry Centre).

Up until the first half of this century, the prognosis for patients with end-stage renal disease was usually fatal. At best, a physician would be able to prolong life for a few months by rigid dietary protein restriction, but the progressive and agonizing course towards death by uraemia was inevitable. The accumulation of urea and other nitrogenous waste compounds in the blood, normally excreted by the kidneys, affects almost every organ in the body. Thus, the clinical symptoms of uraemia are manifold.

The first glimmer of hope for patients with end-stage renal failure issued in 1861 with the invention of "dialysis" by Thomas Graham. This procedure was subsequently applied by others to create the first "artificial kidney" (1913). The principle involved passing a stream of arterial blood through the dialyser on one side of a semi-permeable membrane. A solution of similar electrolytic composition circulates on the other side. Water and waste products from the patient's blood filter through the membrane whose pores are too small to allow the passage of blood cells and proteins. The purified blood is then returned to the patient's body via a peripheral vein. Modifications to the original apparatus over the next three decades produced a system capable of successfully dialysing a human being (Willem Johan Kolff, 1945).

The dialyser was used exclusively in the treatment of patients with acute reversible types of renal failure, and then only in exceptional cases: many regarded

the procedure with scepticism; many thought it experimental, laborious, expensive and dangerous. With the invention of the "twin coil kidney" in 1955, interest in the treatment of acute renal failure heightened. There still remained a huge barrier to multiple dialyses in that the number of treatments that could be administered to each patient was limited by multiple arterial and venous cutdowns: originally, a peripheral artery and vein were individually cannulated for haemodialysis, and these vessels were sacrificed on completion of each dialysis. This problem was overcome by creating an external arteriovenous (AV) shunt (Quinton, Dillard and Scribner, 1960) by connecting the arterial and venous cannulae (both bent into a 180° turn beneath the skin) with a polytetrafluoroethylene (Teflon) bypass tube using a stainless steel arm plate. This technique ensured long-term patency of the cannulated vessels when the dialyser was not connected. The "Quinton-Scribner shunt" and its subsequent modifications paved the way for chronic maintenance haemodialysis (Scribner *et al.*, 1960) in the hospital and the home. The external AV shunt using silicone rubber (Silastic) cannulae with Teflon vessel tips is still the predominant method of achieving vascular access in patients suffering from acute renal failure.

The Silastic cannula AV shunt was far from trouble-free. Complications included thrombosis, infection, haemorrhage, displacement of the cannulae and erosion of the skin overlying the shunt (Brown *et al.*, 1962; Haimov, Singer and Schupak, 1971). The average survival of the AV shunt ranged between two months and a maximum of 24 months (Editorial, *N. Engl. J. Med.*, 1966; Haimov, Singer and Schupak, 1971; Haimov, 1975). Numerous shunt revisions left patients feeling demoralized and consumed time and money.

The next major advance in the history of haemodialysis occurred in 1966: Brescia *et al.* (1966) described the use of a subcutaneous arteriovenous fistula in chronic maintenance haemodialysis. In the original Brescia-Cimino fistula, the radial artery and adjacent cephalic vein were anastomosed, side-to-side, at wrist-level.

Haemodialysis is effected by selecting two sites for venipuncture following venous engorgement using a tourniquet. Blood is withdrawn from the distal (upstream) needle and returned from the dialyser through the proximal (downstream) needle. The fistula provides the high flow rate needed for dialysis, as well as supplying enough flow between the two needles during dialysis to prevent thrombosis (desirable flow rates for haemodialysis are at least 350ml/min). As the fistula matures, the cephalic vein becomes more prominent and dilated and its walls become thicker. These phenomena facilitate successful percutaneous venipuncture.

Once successfully established, the lifetime of the AV fistula is considerably longer than that of the external shunt. The superficial veins are used in the creation of fistulae because they are accessible for needling. Patients can be taught to insert the needles themselves (Shaldon, 1969), therefore easing the burden on medical personnel and hospital resources. These advantages make subcutaneous arteriovenous fistulae the method of choice for achieving vascular access for chronic haemodialysis today.

2.2 TECHNIQUES FOR SUBCUTANEOUS CHRONIC ACCESS

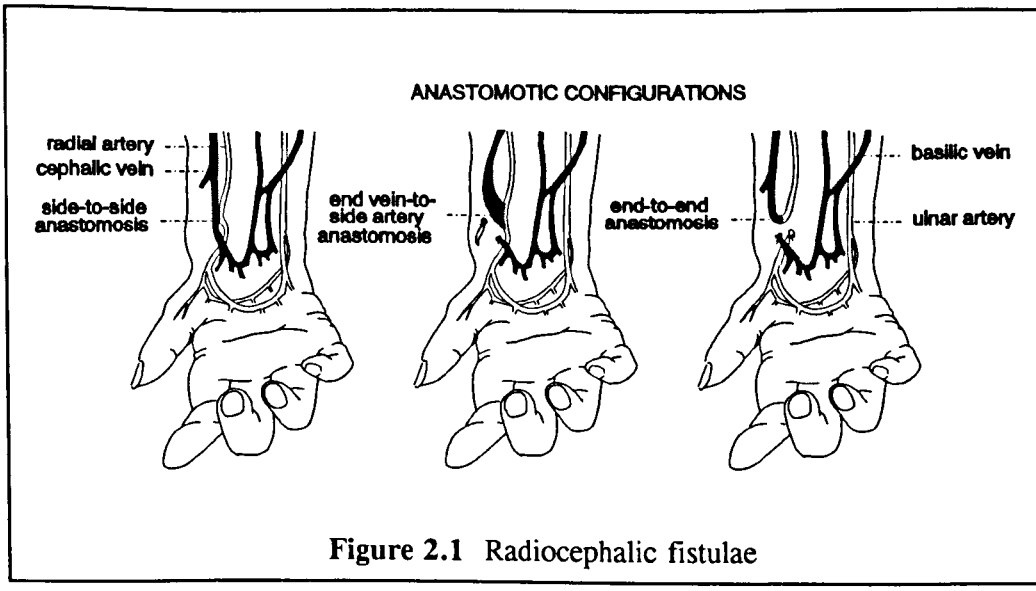

Figure 2.1 Radiocephalic fistulae

Although the original Brescia-Cimino AV fistula was based on a side-to-side technique, the end vein-to-side artery, end artery-to-side vein and end-to-end anastomosis can also be performed (Figure 2.1). The choice of anastomotic configuration is partly dependent on the personal preference of the surgeon but is sometimes dictated by the anatomical position (and availability) of the radial artery and cephalic vein since the side-to-side fistula is technically only possible when the artery and the vein are close together and approximately parallel. Each anastomotic technique has its advantages and disadvantages, but the end vein-to-side artery anastomosis has been favoured because of ease of construction, while still allowing the surgeon full control over the size of the anastomosis. Fistula longevity does depend, to some extent, on the experience and competency of the surgeon and surgical staff.

Apart from the wrist, other sites (see Figure 2.2) widely used for the creation of AV fistula are the antecubital space (site 3), the upper arm (site 4) and the "anatomical snuffbox" (site 1). The ulnar artery and basilic vein can also be used if the radial artery and cephalic vein are not suitable. The most distal site available should be used to spare vessels and allow for future revisions. In patients

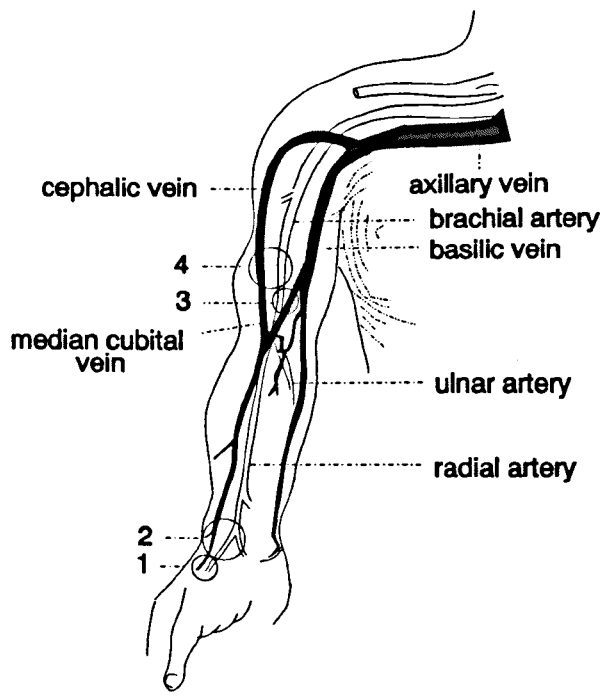

Figure 2.2 The most widely used sites for the creation of AV fistulae are circled.

whose upper extremity sites have been exhausted, the saphenous vein may be used *in situ* as a loop fistula in the thigh.

In patients with small calibre veins or recurrent fistula complications, saphenous vein grafts (May *et al.*, 1969), bovine heterografts (Chinitz *et al.*, 1972) or grafts made from synthetic prosthetic materials (Beemer and Hayes, 1973; Flores *et al.*, 1973; Baker, Johnson and Goldfarb, 1976) may be used to construct AV fistulae in the forearm. As a necessary course of action, these techniques are useful but none has proved to be as successful as a well created classical Brescia-Cimino AV fistula.

2.3 PATENCY AND COMPLICATIONS

A high frequency "thrill" should be immediately palpable over the fistula. This is a valuable prognostic sign as the absence of a thrill, and a bounding pulse, denotes insufficient flow. This could be a result of outflow obstruction caused by twisting, sharp angulation or thrombosis of the vein. The initial failure rate (within the first 3 months) for AV fistulae can be as high as 25% (Haimov, 1975). Thrombosis is the most common cause of fistula failure. This can be due to any combination of technical errors at operation, hypotension, external pressure on the fistula, small sized vessels (often a problem in women), proximal obstructions, atherosclerotic arteries (common in the elderly and diabetic patients), vessel spasm, dehydration immediately following construction or during dialysis or poor general condition at time of surgery (Haimov, 1975; Klauber *et al.*, 1971). If careful attention is exercised during the operation, many of the factors that predispose to thrombosis formation may be combatted. A patent AV fistula does not automatically lead to sufficient distension to be utilized for repeated haemodialysis. This failure may be related to excessive subcutaneous fat or impaired flow. Major surgery unrelated to renal failure has also been implicated as a contributory factor to early

fistula failure (Haimov *et al.*, 1975). This could be due to pressure on the fistula arm, dehydration or hypotension during surgery. The hypercoagulable state which follows any major procedure will predispose to fistula failure. The immediate failure rate (within the first 48 hours) may be in the range of 11% (Bitker, Rottembourg and Mehama, 1984).

Stenosis, and subsequent thrombosis, causes a large percentage of late fistula failures, through the development of fibrous intimal hyperplasia near or at the anastomosis itself. Clinical studies show patency rates at 6 months to one year to be between 60-80% (Wedgwood, Wiggins and Guillou,1984; Reilly, Wood and Bell, 1982; Kinnaert *et al.*, 1971; Wong *et al.*, 1996). Lower patency rates may reflect the greater incidence of thrombotic complications in elderly or diabetic patients with arteriosclerotic disease.

Very few direct comparative studies have been performed to assess the optimum fistula configuration in humans. Varying conditions in the retrospective clinical investigations makes a comparison of the results difficult. Lidman and Thomsen (1986) concluded, in an animal study, that end-to-side anastomoses had a higher patency rate than end-to-end anastomoses. The higher patency for end-to-side anastomoses is surprising in the light of the conclusions reached by Sottiurai *et al.* in 1988 (see Section 3.4), but this may be indicative of a difference in the biogenesis of intimal-hyperplasia between artery-artery anastomoses (in the study by Sottiurai *et al.*) and arteriovenous anastomoses. In humans, long-term patency rates with end vein-to-side artery and side-to-side AV fistulae have been found to be comparable (Wedgwood, Wiggins and Guillou, 1984).

Aneurysm formation can frequently occur at the anastomotic site and along areas of the vein where repeated venipunctures are made due to localized weakening of the vein wall. In many cases, the overlying skin may become thin and erode with danger of aneurysm rupture, or the aneurysm can thrombose or become septic. Most

Brescia-Cimino fistulae with thrombosed aneurysms cannot be repaired and an alternative site has to be sought. Aneurysms also form when fistulae are constructed proximal to a venous obstruction or in a vein which has a high resistance (Haimov *et al.*, 1975). Repeated needling at the same site does not allow regular distension of the venous tract, and can cause aneurysmal dilatation of the vein and subsequent thrombotic complications. Vein distortion and angulation predisposes the vein to aneurysmal dilatation (Kinnaert *et al.*, 1971).

Ischaemic complications in the hand or forearm distal to a fistula do occasionally arise (more commonly in diabetic patients). The low flow state through the peripheral vascular bed may be due to the incidence of the arterial steal syndrome and distal venous hypertension (Bussell, Abbott and Lim, 1971) caused largely by excessive fistula flow (Vanderwerf, Williams and Koep, 1983). With the fistula open, cardiac output is increased. This increase may not be enough to allow for fistula blood flow - the difference (approximately 20% of total fistula flow (Wedgwood, Wiggins and Guillou, 1984)) is "stolen" from the peripheral vascular bed. This steal phenomenon develops when the flow through the fistula becomes equal to about 30% of control cardiac output (Frank *et al.*, 1955; Owens and Bower, 1980). Problems arise when the resistance of the fistula is so low that the arterial pressure in the hand falls resulting in poor perfusion of the hand and fingers. The problem can be solved by ligating the distal radial artery so that the hand is supplied by the ulnar artery via the palmar arches. This may decrease fistula flow by around 15%, but increases peripheral flow by 50-70% (Owens and Bower, 1980). In the chronic fistula, ligation of the distal artery may improve peripheral perfusion but primary ligation of the distal artery, as in the end-to-end and side vein-to-end artery anastomoses, prevents the full development of the collaterals, possibly leading to distal ischaemia, and primary failure rates have been reported to be as high as 55% (Abbott *et al.*, 1973). The incidence of steal is much lower at the more distal sites

for vascular access, the wrist and the anatomical snuffbox (Bonalumi *et al.*, 1982). If the proximal artery is narrowed or obstructed, the distal artery may still function to provide a satisfactory fistula (Anderson *et al.*, 1977a). Occlusion of the proximal artery, though, decreases fistula flow and flow in the peripheral vascular bed, but this is less pronounced in chronic fistulae due to collateral flow (Owens and Bower, 1980). The end vein-to-side artery configuration, results in a greatest proximal vein flow of all the anastomotic configurations and maintains normal peripheral vascular flow. This anastomosis also has the advantage of preserving the continuity of the artery. Any ischaemic symptoms tend to improve within several weeks of the angioaccess procedure.

Fistula flows in excess of about 20% of total cardiac output can cause cardiac failure (Owens and Bower, 1980). This is most likely due to a clash between increased heart rate, stroke volume and oxygen consumption by the heart in response to the AV fistula, on the one hand, and decreased coronary perfusion, on the other. The patients that develop this complication are characterized by pre-existing cardiac disease, including congestive heart failure, prolonged hypertension or coronary arterial disease (Anderson *et al.*, 1976). Fistula flow at the wrist is relatively low compared to normal cardiac output and so, high output cardiac failure is more commonly associated with AV fistulae created from the brachial or femoral arteries (Anderson *et al.*, 1977b).

2.4 THE FISTULA AS A PHYSICAL CIRCUIT

As flowing blood seeks the path of least resistance, the fistula is effectively a short-circuit between the high pressure arterial system and the low pressure venous system (see Figure 2.3). It acts as a very low resistance, high compliance system. A thrill is normally palpable in the region of the fistula (and a loud, continuous, machine-like murmur on auscultation) due to turbulence caused by the non-anatomic,

non-physiologic flow state.

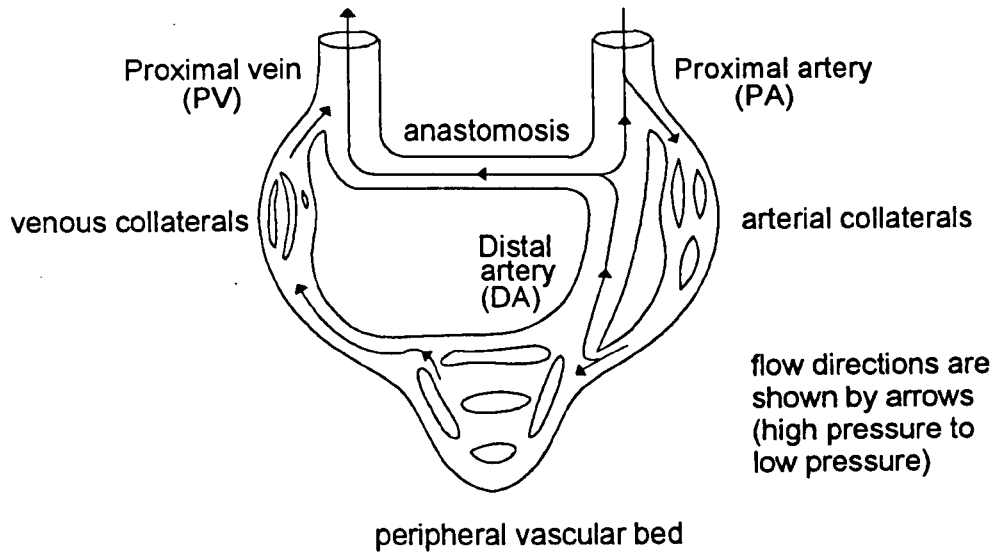

Figure 2.3 Flow in the various sections of the fistula

Opening the fistula reduces peripheral resistance and dramatically increases flow through the proximal artery. This results in a temporary drop in proximal arterial pressure (Owens and Bower, 1980). Any lowering of blood pressure causes sodium and water retention as a compensatory measure to increase the total volume of circulating fluid. The increase in blood volume through the fistula is also partly supplied by blood flowing through the non-fistulous circuit. To accommodate this increased volume of blood flowing through the fistula, without increasing the wall shear stress excessively, there must be a widening of the fistulous circuit. The volume of blood flowing through the fistula will increase until the resistance provided by the limited distensibility of the vessel walls and the resistance offered by the fistula opening, equals the resistance to flow in the non-fistulous circuit, and the two systems reach equilibrium (Holman, 1923).

The blood flowing through the fistula is determined by the sum of the flow

resistance of the arterial system between the left ventricle and the anastomosis, the flow resistance of the anastomosis itself and the flow resistance of the venous system between the anastomosis and the right atrium, and the relevant pressure gradients. As a general rule, the direction of blood flow in all the arterial limbs of the fistula will be towards the anastomosis (high pressure to low pressure), and in the venous limbs, away from the anastomosis. Thus, flow in the distal artery is generally retrograde with blood flowing into the fistula from the ulnar artery via the palmar arches. The arterial collaterals, stimulated by the pressure differential across the collateral bed, also enlarge as the fistula matures and so an otherwise reduced peripheral perfusion is augmented by greater collateral inflow (Owens and Bower, 1980; Gordon, 1996). Distal arterial pressure becomes progressively raised by collateral flow. Where pressure is greatest, flow becomes bidirectional. Distal to this point, the pressure gradient between the distal artery and the peripheral vascular bed is normal and flow is antegrade.

The inflow of arterial blood into the veins is accompanied by a considerable increase in the local venous pressure as the veins become distended: the pressure in the cephalic vein increases from just above zero to between 30 and 80 mmHg, depending on the relative resistances of the artery and vein. Proximal venous pressure does not rise more owing to the very low resistance and the capacity of the veins to dilate. The pressure gradient between the proximal vein and the right heart rises so that the flow of blood into the venous bed is equal to the amount of venous return. Thus, blood flow within the vein increases by at least ten times (normal range of flows: 150 to 600ml/min). When the amount of blood leaving the veins per unit time to enter the right heart matches that entering the venous system through the fistula, a new equilibrium is reached.

This anatomical circuit may not always be regarded as a closed system, as multiple venous branching may cause impaired flow: flow, towards the hand, into

a venous branch may deprive the main proximal cephalic limb of flow. Even in the absence of thrombosis, the proximal cephalic vein may fail to develop adequately (Wong *et al.*, 1996). Branches may be ligated and the problem resolved effectively.

Normal flow in the radial artery exhibits high resistance characteristics with a triphasic velocity waveform (i.e. reverse flow during early-mid diastole). Once the artery is anastomosed to the vein, however, this profile changes to a monophasic high diastolic flow pattern indicative of low resistance flow. The velocity waveform in the proximal vein shows an arterial pulsation pattern with overlying turbulence. The distal artery flow waveform may show continued antegrade flow, wholly retrograde flow, or oscillating flow. Outflow obstructions more proximal to the fistula, including prolonged spasm, kinking and rotation of the vein, diminish flow. Stenoses in the proximal venous limb can be further indicated by a flow waveform with a relatively large systolic peak more distally. A triphasic velocity waveform in the proximal artery is another sign.

To maintain a normal blood pressure while total peripheral resistance has decreased, the greater volume of blood leaving the arterial system through the fistula via the proximal artery limb must be offset by an increase in cardiac output. To increase cardiac output without raising blood pressure, the heart must work with greater force to output a larger stroke volume. The physiologic response to this increased work is dilatation, hypertrophy of the cardiac musculature, and maybe, resultant cardiac failure. In the struggle for cardiovascular reflexes to keep blood pressure to a standard level, tachycardia can also be a clinical manifestation of an AV fistula (Johnson and Blythe, 1970).

CHAPTER 3

INTIMAL HYPERPLASIA AND HAEMODYNAMICS

3.1 MORPHOLOGICAL CHANGES IN THE FISTULA

As arteries and veins develop out of a common capillary plexus in the embryonic peripheral vascular bed, vessels which have served as arteries may eventually become veins, and vice versa. This forms the physiologic and pathologic basis for creating an arteriovenous fistula (Sabin, 1917).

Physical forces related to pressure and flow direct influence cell biosynthesis and modulate structural adaptations to haemodynamic changes. Over the first few months' maturation period, there is lengthening and dilatation of the vessels as a result of altered normal stresses and shear stresses. The proximal vein develops a subintimal increase in smooth muscle, fibrous tissue, collagen and elastin (Fuchs, Mitchener and Hagen, 1978). Cyclic stretching of smooth muscle cells has been shown, in tissue culture experiments, to stimulate the synthesis of certain connective tissue components (Leung, Glagov and Mathews, 1976). Thus, the proximal vein becomes more prominent and thick-walled, making venipuncture easier. There are a number of factors (Owens and Bower, 1980) that may induce vessel dilatation: (i) increased lumen diameter to maintain a constant wall shear rate as the flow rate through the vessel increases; (ii) an increase in distensibility caused by the effect of turbulence on vascular elastic fibres (Halsted, 1918; Holman, 1954; Robicsek *et al.*, 1958); (iii) intramural degenerative changes through lack of nutritional supply, or due to mechanical damage (Stebhens, 1974). Vessel elongation is due to a longitudinal stretching force caused by an axial drop in pressure and the increased vessel diameter, and velocity and flow of blood (Ingebrigtsen, Fönstelien and Solberg, 1970; Owens and Bower, 1980). Initial dilatation of the efferent vein at the AV anastomosis progresses for around 6-8 weeks and then tails off or halts (Ehrenfeld, Grausz and Wylie, 1972).

The normal vein consists of a thin *endothelial* layer covering the fenestrated basement membrane and scattered *intimal* cells. The *media* consists of two layers of smooth muscle cells (the cells in the inner layer oriented longitudinally and in the outer layer, circumferentially) interlaced with collagen and elastic fibres. Venous endothelial cells are similar to arterial cells, but in addition, have a large number of plasmalemmal vesicles open at the cell surface and microvilli on the luminal face of the endothelium. These differences would inevitably influence transendothelial transport of plasma molecules and atherogenesis. Metabolic activity seems to be greater in veins than arteries. Hence, in atherogenic conditions, the uptake of serum lipids may be faster in venous tissue than arterial. The changes observed in the vein, thought to constitute intimal thickening in an adaptive response to altered haemodynamic environment, were initially called "arterialization".

Vein grafting in arterial bypasses can give an insight into the adaptation of venous tissue to the arterial environment (Fuchs, Mitchener and Hagen, 1978; Dilley, McGeachie and Prendergast, 1988). Soon after grafting, the intima shows evidence of endothelial sloughing. Leucocyte adherence and fibrin can be found on the exposed sub-endothelial surface. The presence of non-occlusive intimal thrombi can often be detected, and early occlusive thrombosis even occurs in some cases. The endothelium regenerates within about six weeks. During this period, the media becomes more fibrous. Many sources have reported that intimal hyperplasia develops within two to four weeks after grafting. Over a period of a few months, the intima undergoes a similar inflammatory fibroproliferative response to that observed in arteries (see Section 3.3). In some regions, atherosclerotic plaques may eventually develop. At the anastomosis, adventitial scarring of the transected end of the vein may produce stenosis. Fibrotic stenosis may also originate from intraoperative clamping of the vein graft or constriction from sutures, or fibrosis of venous valve cusps. The process of regeneration of cells and the matrix from surviving tissues

occurs from the onset, depending on the severity of injury. Despite these changes, intimal hyperplasia is limited in a large number of cases, and the graft remains patent.

Studies conducted by Zwolak, Adams and Clowes (1987) also provide definite evidence of injury. They transplanted the jugular vein into the carotid artery of rabbits and found that the endothelial layer in the region of the anastomosis was sloughed early after implantation. The endothelial layer however, was fully restored after two weeks, and intimal thickening regressed.

Animal studies can provide valuable evidence for the role of haemodynamics in fistula maturation and failure. Stehbens (1974) based his studies on a side-to-side arteriovenous anastomosis in young sheep. As a control, the artery and vein were incised and repaired but not anastomosed. Histologically, the anastomosed artery retained its basic form but it was considerably wider than the control and thin-walled shallow aneurysmal pouches in the proximal segment were found in some sheep. Non-atherosclerotic intimal thickening was also more noticeable in the anastomosed artery. The anastomosed vein was longer and wider than the control vein and exhibited a large aneurysmal and tortuous dilatation. Intimal-medial hyperplasia was also evident; tears up to 1.5 cm in length were seen on the intimal surface and multiple ruptures of the internal elastic lamina were observed, indicative of mechanical weakness or fragility. The wall of the dilated vein was irregularly thickened. The intima was two or three times thicker than the media and no longer separated from it by the internal elastic lamina. Stehbens related the observed changes in the vein to complications associated with atherosclerosis, including poststenotic dilatation and structural fatigue induced by haemodynamic disturbances. In a case study on two patients with severe atherosclerosis interfering with the functioning of the AV fistulae, Stehbens and Karmody (1975) found that the development of intimal hyperplasia and venous atherosclerosis was histologically

similar to that found previously in the experimental fistulae in sheep. It was concluded that the risk of late complications may dependent on the geometry of the anastomosis and on the local haemodynamics at the site of the fistula.

3.2 THE ROLE OF HAEMODYNAMICS IN ATHEROGENESIS

Haemodynamics plays a major role in atherogenesis, but this role has not yet been properly defined. The evidence for the involvement of haemodynamic forces in the formation of an atheromatous plaque centres on the focal nature of the lesions and their predilection for regions of arterial branching and curvature. The present view is that flow disturbances, which almost certainly occur in these areas, would account for this. In 1966, Fox and Hugh proposed a theory of localization of atheroma based on "boundary layer separation". This process creates static zones separated from the mainstream, where flow separation occurs under the action of a positive pressure gradient: the layer of blood lining the vessel wall, the boundary layer, has a low momentum because of frictional forces exerted by the wall and so may be rapidly brought to rest by the adverse pressure gradient; flow reversal occurs beyond this stagnation point and vortices are produced near the wall. If the positive pressure gradient is not large enough, the boundary layer will not separate, but the velocity profile across the lumen will be distorted. Pulsatile flow in the vessels would cause oscillation of the stagnation point, and growth and decay of the separated flow region during each cycle. Positive pressure gradients and flow separation regions can occur in diverging channels, at bends and at junctions (see Figure 3.1).

The principles of boundary layer separation apply equally well to the AV fistula. Careful analysis of vessel geometries and flows should therefore enable us to pinpoint locations for the eventual formation of atherosclerotic lesions. Flow separation regions at the anastomosis are possible sites for the development of intimal hyperplasia. The orientation of endothelial cells is normally both parallel and oblique

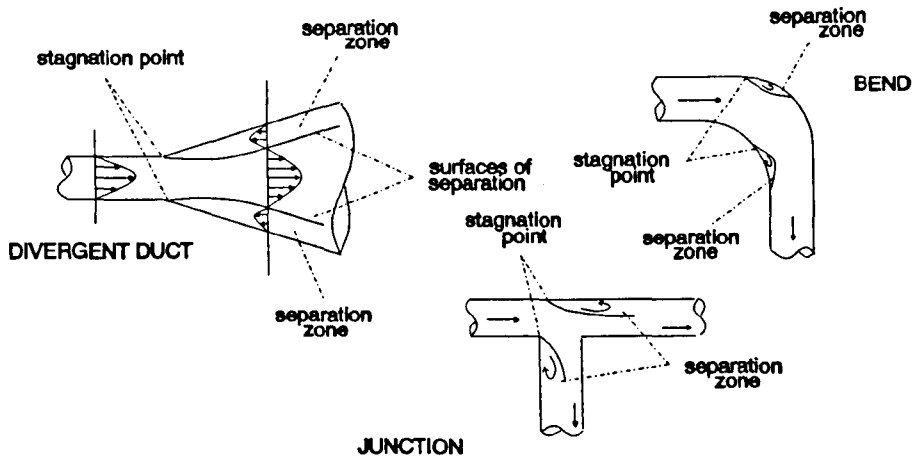

Figure 3.1 Examples of boundary layer separation

to the direction of blood flow. Reversal of flow at the points of flow separation and reattachment can lift the overlap between one endothelial cell and the next, allowing blood-borne substances to enter the subendothelial space through the disrupted gap junction (Sottiurai *et al.*, 1988). The stagnant or slowly moving fluid in areas of flow separation may permit the accumulation of platelet aggregates, leading to thrombosis (Leonard, 1972) and intimal-medial hyperplasia. This may be because platelets require incubation with an activator to release mitogens maximally on adhesion. Therefore maximum release of platelet factors occurs in separated, recirculation zones (Nerem and Cornhill, 1980). Also, mitogens and chemoattractants within low shear regions have an increased residence time and, hence, have a greater potential to induce monocyte recruitment and smooth muscle cell proliferation.

The branch-to-trunk area ratio, the degree of vessel tapering, the division of flow in the branches, blood pulsatility, vessel compliance and geometry are all parameters that influence the stability of flow. Many of these undergo changes in various disease states and complicate the flow characteristics further. The Reynolds number (*Re*) is used to characterize the transition from laminar to turbulent or

disturbed flow. It relates the effects of vessel diameter (D) and blood density (ρ), viscosity (μ), and velocity (V) in one dimensionless parameter (see Equation 1). In steady flow through a straight tube, the Reynolds number at which this transition occurs is approximately 2200. The other parameter governing flow is the dimensionless Womersley parameter(α), where R is the radius of the vessel, ω is the angular frequency of the cardiac cycle ($\omega = 2\pi f$ where f is heart rate in Hz) and ν is the kinematic viscosity of blood ($\nu = \mu/\rho$). When α is large, the oscillatory boundary layer on the vessel wall is thin and the velocity profile across the central region is effectively flat. When α is small, the velocity distribution across the lumen can be assumed to be parabolic at every instant of the cardiac cycle.

$$Re = \frac{\rho VD}{\mu} \quad \text{—— (1)}$$

$$\alpha = R(\omega/\nu)^{\frac{1}{2}} \quad \text{—— (2)}$$

Branch-to-trunk area ratios (in symmetrical branched tubes) less than 1 (Walburn, Blick and Stein, 1979) and acute angles of branching (Krovetz, 1965) tend to reduce flow disturbances at branches (i.e. raise the critical Reynolds number). Arterial tapering (Walburn and Stein, 1981) and vessel distensibility (Stein, Walburn and Blick, 1980) also minimize disturbances. There is also a relationship between branch-to-trunk ratio and flow separation: it has been suggested that flow separation occurs when the branch-to-trunk area ratio exceeds 1.2 (Walburn, Blick and Stein, 1979) and that the extent of the separation region increases as the branch-to-trunk area ratio increases above this value: when flow accelerates in a branch, the velocity profile near the wall tends to promote stability.

When blood flows through a vessel, its wall is subjected to the radial and tangential wall stress components of intraluminal pressure, and the haemodynamic wall shear stress, due to the frictional force exerted by a viscous fluid moving along a solid surface. The shear stress at the wall is the product of blood viscosity (μ) and the shear rate (du/dx) at the wall (the velocity gradient at the wall).

In turbulent flow, random velocity fluctuations superimposed on the mean flow are present. Near the wall, a laminar sub-layer, dominated by viscous effects, separates the wall from the turbulent core. Reynolds stresses quantify shear stresses in the turbulent boundary layer.

$$shear\ stress = \mu\left(\frac{du}{dx}\right) \quad \text{—— (3)}$$

To account for the greater energy loss due to turbulence, an increase in viscosity ("eddy viscosity") is introduced. The resulting "apparent" stresses are termed as Reynolds shear stresses. Although the Reynolds stresses are added to the laminar shear stresses, the viscous terms are negligible by comparison away from the wall. The Reynolds shear stress τ_{uv}, acting in the y-direction, is the product of blood density (ρ) and the time-averaged instantaneous velocity fluctuations about the mean (u' and v') in the x- and y- directions.

$$\tau_{uv}(t) = -\rho\overline{u'(t)v'(t)} \quad \text{—— (4)}$$

It has been postulated that high shear stress may also affect the arterial wall and contribute to atherogenesis. Fry (1968) has shown that endothelial cells can be eroded by acute shear stresses above a certain value (35-40N/m^2), while shear stress below the threshold may lead to increased permeability of the endothelial layer. These critical shear stresses depend on the flow regime and shear stress exposure times. Pulsatility and other longer period blood flow variations (e.g. respiration, Traube-Hering-Mayer and Burton waves) introduce oscillating shear stresses at the vessel wall. High temporal and spatial wall shear stress gradients have also been associated with the development of intimal hyperplasia.

High Reynolds shear stresses, inherent in turbulent flow, deform erythrocytes and, at high enough levels, can lead to fragmentation. Alongside erythrocyte damage, the red cells release their cellular contents including factors that produce irreversible platelet aggregation. Platelets themselves show enhanced adhesiveness with increasing wall shear stress (Brown *et al.*, 1975). This observation may tie in with

the fact that, at high shear rates, von Willebrand factor and fibronectin have been found to promote platelet adhesion to the subendothelium (Mustard *et al.*, 1987). Beyond a certain level of shear, platelet functionality becomes diminished, and platelet distortion and fragmentation occur - at critical values approximately thirty times less than for erythrocytes (Brown *et al.*, 1975). In regions of low shear, like flow separation zones, the transport of accumulated lipids across the arterial wall into the blood is inhibited (Caro, Fitzgerald and Schroter, 1971), and lipid particles become trapped in a mesh of platelets and fibrin.

Also associated with flow at an anastomosis is the secondary helical motion induced by the curvature of the flow boundary at the anastomosis. Secondary flows are caused by transverse pressure gradients that arise during a change in flow direction, and are superimposed onto the main streamwise motion along the vessel axis. The increased kinematic energy of the main stream during systole could create low pressure regions at an anastomosis and cause secondary swirl flow (Shu, Noon and Hwang, 1987).

3.3 THE PROGRESSION OF INTIMAL HYPERPLASIA

Intimal hyperplasia causes a large percentage of late fistula failures through stenosis of the vessel lumen. The intima becomes thickened by the proliferation of intimal smooth muscle cells and by the migration and proliferation of smooth muscle cells derived from the underlying media (Ross, Glomset and Harker, 1977). Lipid deposition follows and the connective tissue content is increased. The aetiology of the intimal changes observed is still not fully understood.

Intimal hyperplasia is believed to be a principal step in the development of atherosclerosis. One hypothesis is that the formation of atheromatous plaque is an inflammatory-fibroproliferative response to earlier endothelial damage. Potential sources of injury may be mechanical, chemical (e.g. chronic hyperlipaemia, uraemia)

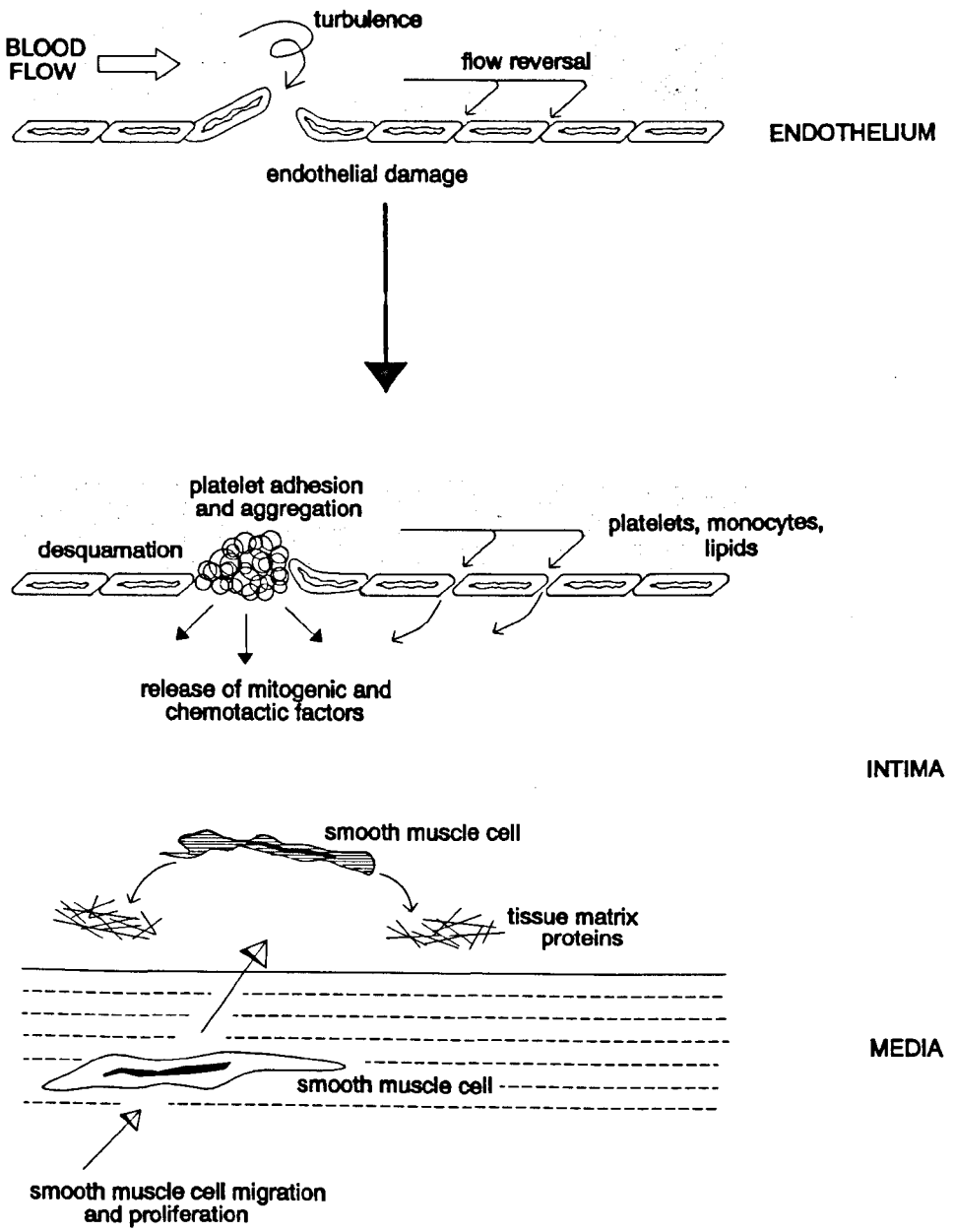

Figure 3.2 The progression of intimal hyperplasia

or immunological (Wheeler *et al.*, 1989). Mechanical injury may be the result of increased shear stress applied to the endothelial cells by haemodynamic forces at particular sites. Low shear stress can equally be destructive to the endothelium (see

Section 3.2). Injury leads to an alteration in endothelial cell-cell attachment or endothelial cell-matrix attachment, possibly allowing haemodynamic forces to cause focal desquamation of the endothelial cells (see Figure 3.2) from the vascular wall (Ross, Glomset and Harker, 1977).

Under normal circumstances, the endothelium is thromboresistant and does not promote platelet adherence (Stary *et al.*, 1992). This is partly due to the thrombomodulin content of the endothelial cell membrane and antithrombin III, an inhibitor found in blood plasma, which readily binds to the endothelium. Both inactivate thrombin and blood coagulation factors (Mustard *et al.*, 1987). Furthermore, endothelial cells can metabolise platelet aggregating agents (adenosine diphosphate, serotonin, angiotensin and prostaglandin), and synthesize and secrete agents which prevent platelet aggregation (prostacyclin and plasminogen activator). Normal arterial endothelium does not support the adherence of large numbers of monocytes, neutrophils and lymphocytes.

However, the inflammatory and immune response of endothelial cells is to express leucocyte-specific adhesive glycoproteins and chemotactic proteins, as well as growth factors (stimulators of cell proliferation) and scavenger receptors. The arterial endothelium is permeable to all plasma proteins. Transendothelial transport takes place via plasmalemmal vesicles in the endothelial cells, by transcytosis, and through endothelial intercellular clefts. The rates of transport of lipoproteins and other macromolecules across the endothelium and their final concentration in the intima depends on factors such as the plasma concentrations, the size and charge of the molecules, and the rates of degradation and efflux (Stary *et al.*, 1992).

Loss of endothelium leaves the sub-endothelial connective tissue exposed and within seconds leucocytes and platelets gather and adhere at the site of vascular injury. Over a brief period this is followed by further platelet aggregation, thrombin generation and the formation of a platelet-fibrin mural thrombus. Platelet aggregation

is induced by fibrillar collagen (in the presence of von Willebrand factor), adenosine diphosphate (ADP) released by platelets, epinephrine and serotonin. Platelet adhesion and platelet-platelet cohesion requires immobilized von Willebrand factor (vWF) (found in the pool of plasma on the surface of the damaged endothelium), fibronectin (present in the subendothelium, plasma and platelet alpha granules), possibly, thrombospondin (deposited on the subendothelial surface and in very low concentrations in plasma) and certain receptors for adhesive glycoproteins in the platelet membrane (Mustard *et al.*, 1987; Coller, 1987). The activated platelets secrete a mitogenic (induces DNA synthesis and cell division) and chemotactic factor into the underlying vascular wall. The platelet-derived factors and plasma constituents, such as monocytes, lymphocytes, lipoproteins and hormones, infiltrate the vessel wall, and cause focal intimal proliferation of smooth muscle cells. When attached to collagen, the smooth muscle cells are able to migrate from the media to the intima in a chemotactic response to platelet-derived growth factor (PDGF).

PDGF also attracts and activates connective tissue fibroblasts for the proliferative response needed to repair the injury (Grotendorst *et al.*, 1981). The smooth muscle cells are stimulated to synthesize various connective tissue matrix proteins (including collagen, elastin and proteoglycans). In addition, PDGF increases the uptake of low density lipoprotein. Thus, intracellular and extracellular lipid deposition also occurs. PDGF expression is coupled with the expression of PDGF receptor genes, forming an auto-amplification loop.

Activated endothelial cells, monocytes/macrophages, smooth muscle cells, platelets, plasma and T-lymphocytes also express other growth factors and cytokines (peptides that regulate immune function) which may stimulate smooth muscle cell migration, proliferation, and altered metabolism, either directly or by inducing secondary gene expression of PDGF (see Table 3.1).

Table 3.1 Growth factors, cytokines and leukotrienes potentially important in atherogenesis

SUBSTANCE		CELLULAR SOURCES
Platelet-derived growth factor $^{SMC\rightarrow,SMC+}$	PDGF	EC, M, P, SMC
Basic fibroblast growth factor $^{EC+,SMC+}$	bFGF	EC, M, SMC
Interleukin-1 $^{EC-,SMC+}$	IL-1	EC, M, P, SMC, T
Interferon-γ $^{SMC\pm}$	IFN-γ	M, T
Vascular endothelial growth factor $^{EC+,M\rightarrow}$	VEGF	M, SMC
Transforming growth factor-α $^{EC+}$	TGF-α	M, (P)
Transforming growth factor-β $^{EC-,M\rightarrow,SMC\rightarrow,SMC\pm}$	TGF-β	EC, M, P, SMC, T
Platelet-derived endothelial cell growth factor $^{EC+}$	PD-ECGF	P
Insulin-like growth factor-1 $^{SMC\rightarrow,SMC+}$	IGF-1	EC, M, P, SMC
Epidermal growth factor $^{SMC+}$	EGF	(M), P
Heparin-binding EGF-like growth factor $^{SMC\rightarrow,SMC+}$	HB-EGF	EC, M, SMC
Tumour necrosis factor-α $^{EC-,SMC+}$	TNF-α	EC, M, SMC, T
Monocyte chemotactic protein-1 $^{M\rightarrow}$	MCP-1	EC
Colony-stimulating factors $^{M\rightarrow,M+}$	CSFs	EC, M, SMC, T
Oxidised low-density lipoprotein $^{M\rightarrow,SMC\rightarrow}$	ox-LDL	EC, M
Leukotriene B_4 $^{SMC\rightarrow}$	LTB_4	N
Thrombin $^{SMC+}$		Pl

Key to cellular sources: EC, endothelial cell; M, monocyte/macrophage; N, neutrophil; P, platelet; Pl, blood plasma; SMC, smooth muscle cell; T, T-lymphocyte.

Key to other symbols: $^{\rightarrow}$, chemoattractant; $^{+}$, mitogen; $^{-}$, inhibitor of proliferation; $\pm$ growth agonist and antagonist, depending on conditions.

Thrombospondin, a glycoprotein component of the extracellular matrix, also promotes smooth muscle cell proliferation. Along with osteonectin and tenascin, these three matrix-associated glycoproteins facilitate cell rounding and partial detachment from the substratum, allowing cell migration, growth and repair.

Regression of the thickness of the healing intima is largely due to spontaneous regression and re-endothelialization from adjacent areas spared injury. Once the endothelial layer is re-established, smooth muscle cell proliferation and connective tissue synthesis ceases. Regeneration of the endothelial barrier may allow the lesion to regress to leave a slightly thickened intima, but repeated or chronic cycles of injury may inhibit endothelial replication and may cause progressive intimal smooth muscle proliferation (Ross, Glomset and Harker, 1977).

Endothelial cell dysfunction, more often than direct denuding injury, may be the principal step in the response-to-injury hypothesis. Animal studies have highlighted that the initiating event in atherogenesis is the adhesion of monocytes to an intact endothelial surface (Davies and Woolf, 1993) in areas characterised by increased endothelial permeability to plasma proteins. The later accumulation of foam cells in the intima is said to precipitate focal endothelial cell loss, as lipid-laden foam cells try to wind their way back into the bloodstream by pushing apart the endothelial cells. This leads to the formation of platelet mural thrombi at these sites, and release of growth factors to act alongside those released by activated macrophages and smooth muscle cells. Lesion-prone sites are structurally and functionally different to non-lesion-prone sites. The glycocalyx coat (consisting of free polysaccharides and glycosaminoglycans and glyco- side chains emanating from the plasma membrane) of the endothelial surface at lesion-prone sites is reduced in thickness, and both spontaneous monocyte recruitment and endothelial cell turnover is greater (Schwartz *et al.*, 1991).

The smooth muscle cells (Ross, 1993; Raines and Ross, 1993) normally found

in the intima and media are termed as "contractile". However, smooth muscle cells observed in lesions (termed "synthetic") are different. These synthetic cells are capable of expressing genes and receptors for a number of growth factors and cytokines, and can synthesize extracellular matrix. Vasoactive agents derived from activated cells alter the equilibrium levels leading to a reversible modulation of smooth muscle cell phenotype.

It is evident that lipid metabolism plays an important role in atherogenesis. Fatty streaks within the intima are generally seen to be the precursors to atherosclerotic plaques (Ross, 1986). These are largely composed of lipid-rich macrophages (derived from invading monocytes) and T-lymphocytes, and so may represent an inflammatory response to lipid deposition. The streaks expand by the continuing influx of monocytes into the vessel wall, which become macrophages, and by the gradual accumulation of smooth muscle cells migrating from the media. Thus, intermediate lesions of atherosclerosis consist of alternating layers of lipid-laden macrophages and lipid-rich smooth muscle cells. The smooth muscle cells and macrophages attempt to remove the foreign substance by phagocytosis (engulfment and digestion of foreign bodies). Unable to hydrolyse engulfed lipid, these cells become loaded with cholesterol and cholesteryl ester, and are converted into the foam cells commonly seen within atherosclerotic lesions. Smooth muscle cells may also remove deposited lipoproteins by expression of lipoprotein receptors. In later stages, most of the foam cells die, generating fatty streaks (Esterbauer, Wäg and Puhl, 1993).

In 1984, it was shown that endothelial cells, smooth muscle cells and monocyte/macrophages all generate the reactive oxygen species or free radicals necessary to oxidize low density lipoprotein (Steinbrecher *et al.*, 1984). It has been suggested that oxidative modification of low density lipoprotein (LDL), the major cholesterol-carrying lipoprotein, renders it more atherogenic (Parthasarathy,

Steinberg and Witztum, 1992). Oxidized LDL (ox-LDL) is relentlessly taken up by macrophages. It stimulates endothelial cells to release monocyte-chemotactic factors and growth factors for monocytes, as well as endothelial-leucocyte adhesion proteins. It also inhibits monocyte migration and so constrains these cells to the intima. The products of ox-LDL decomposition can be cytotoxic to cells, and this may contribute to atherosclerotic progression. Glycation (non-enzymatic binding of glucose to protein molecules) of LDL (gly-LDL) is also believed to increase its atherogenicity (Lyons, 1993), including increasing its potential to covalently bond to vascular matrix proteins. Glycation may also generate free radicals potentially leading to glycoxidation. The products of glycoxidation can be especially atherogenic. If the matrix proteins are themselves glycated or glycoxidized, adherence of LDL will be even greater and adherence of gly-ox-LDL even greater still. Collagen glycoxidation may cause vascular rigidity, and create abnormal shear stresses that may injure the endothelium. Other lipoproteins, such as lipoprotein(a), are also subject to oxidation and other types of modification, and may contribute to the atherogenic process (Schwartz, Valente and Sprague, 1993).

Advanced atherosclerotic lesions become fibrous plaques, gradually increasing in size. The luminal surface is a dense cap of collagen-rich connective tissue with embedded smooth muscle cells, covering a core of extracellular lipid and necrotic debris. Surrounding the lipid core are the lipid-filled foam cells and T-lymphocytes characteristic of intermediate lesions. As more and more collagen is produced, the fibrous cap may project into the vessel lumen and obstruct flow. The obstruction may not be immediately noticeable as the media is constantly remodelled during the formation of the intimal lesion, increasing the external diameter of the atherosclerotic vessel. In the final stage of atherosclerosis, fissuring, cracking or ulceration of the plaque may be seen. Haemorrhaging from the lumen or from vessels within the plaque occurs. The direct exposure of blood to the subendothelium causes intraplaque

thrombosis, which expands and distorts it. This may lead to intraluminal thrombosis over the site of plaque disruption, depending on the extent of plaque injury. As the lesions enlarge and encroach on the lumen, the restored endothelial cells would potentially be at greater risk from further injury due to the region of altered blood flow. Eventually, this process may lead to lipid accumulation, calcification, thrombosis and occlusion of the vessel, and possibly to more life-threatening clinical sequelae (see Figure 3.3).

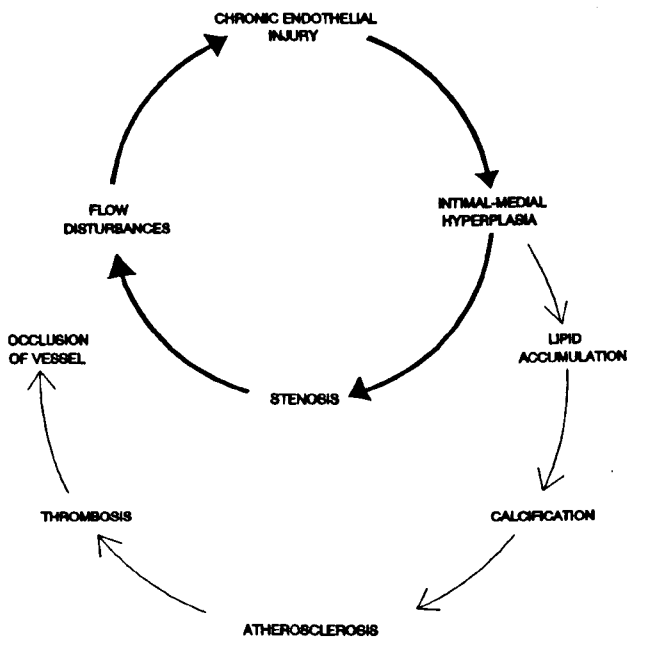

Figure 3.3 Vicious circle leading to fistula failure

3.4 VASCULAR REMODELLING TO ALTERED HAEMODYNAMICS

Adaptive intimal thickening has a similar composition to normal intima except for proportional increases in the thickness of the two layers of the intima. Adaptive intimal thickening may be thought of as an attempt by the tissue to maintain normal conditions of flow, wall normal stresses and wall shear stress by inducing functional changes to strengthen the intimal layers and restore wall shear and tensile stress to

within the normal range (Glagov and Zarins, 1989). In regions with adaptive intimal thickening, the formation of advanced atherosclerotic lesions may be greater than in other locations, although this is not solely confined to these sites.

Although Sottiurai *et al.* (1988, 1989) researched primarily into intimal hyperplasia in prosthetic grafts, their work does give us some insight into its effects in the endogenous fistula. They suggested that "...intimal hyperplasia is an active, viable biologic entity that undergoes constant remodelling, perhaps dictated by the haemodynamics of blood flow...". The authors discovered histologically a structure of specific cell orientation and transformation within various regions of the intimal hyperplasia. This might point to a functional specificity of cell types, and supports a theory of adaptive response to local haemodynamics. The end-to-side distal anastomosis does not naturally occur in the human vascular system (except patent ductus arteriosus). Sottiurai *et al.* (1988, 1989) also showed that intimal hyperplasia is reversible within two months in the end-to-end anastomosis (canine artery-artery autogenous interposition grafts) but progresses indefinitely at the distal end-to-side anastomosis (canine autogenous artery-artery bypass). In the end-to-side anastomosis regions of low shear stress are consistently found at the heel and toe of the anastomosis, while at the floor of the recipient artery a zone of high shear stress gradient exists. These are specific regions where intimal hyperplasia is found to occur (see Figure 3.4). There were differences in the cellular and extracellular components at the heel and the toe, but the same morphologic structure was evident in both, resembling the

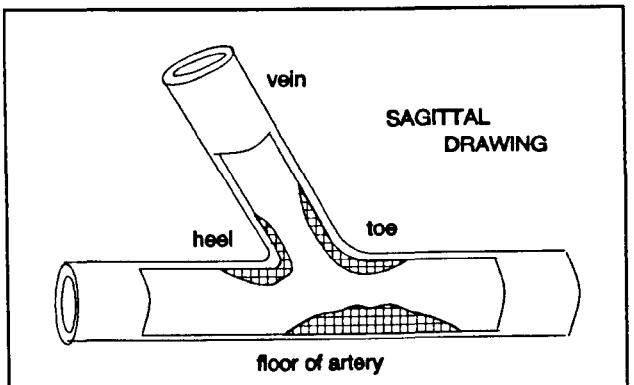

Figure 3.4 Distal anastomosis depicting intimal hyperplasia (shaded regions).

media of an artery. Even in the case of arteriovenous grafts, Sottiurai *et al.* stated that the geometry of the distal end-to-side anastomosis is the initiating factor in intimal hyperplasia - although compliance mismatch between the artery and the graft enhances the thickening process. This theory is also supported by the studies of Abbott *et al.* (1987). As the compliance of a vein graft is similar to the native artery, compliance mismatch may not be a factor in the development of intimal hyperplasia at an arteriovenous anastomosis.

The transformation into atheromatous lesions most probably depends on the influence of atherogenic stimuli. For example, hypercholesterolaemia could trigger the transition of regions with adaptive intimal thickening to atherosclerotic lesions: cholesterol exchange by the plasma membranes of endothelial cells chronically bathed in abnormally high levels of LDL could occur. This could lead to increased membrane viscosity which might decrease the malleability of the endothelial cells, particularly at sites of flow disturbances, allowing the infiltration of blood-borne substances. Endothelial cells may separate, providing the opportunity for platelets to interact with the exposed connective tissue. Thus, in this scenario, growth factors may initially be released from any or all of the following sources: endothelium, monocytes/macrophages and platelets. This same pathway, or minor variants, may be applicable in patients with a higher risk of developing atherosclerosis, such as diabetics, hypertensives and cigarette smokers (Ross, 1986). These potential sources of arterial injury are chronic, and so lesion regression is highly unlikely unless the injurious agents are removed. Stehbens (1992) does not agree with Ross and others that hyperlipaemia, hormone dysfunction and increased shear stress in hypertension can be potential sources of endothelial injury. These may be atherogenic stimuli, but haemodynamics, he has concluded from reviewing a wide range of experimental evidence, is the predominant factor governing the development of atherosclerosis - not injury and thrombosis.

CHAPTER 4

INTRAOPERATIVE AND POSTOPERATIVE METHODS

4.1 INTRODUCTION

Radiocephalic fistulae were studied in patients requiring primary access procedures for haemodialysis at the Royal Liverpool University Hospital. The initial part of the project consisted of a retrospective study of fistula geometry and flow distribution in each limb of the fistula. Flow measurements were taken intraoperatively and then the development of each fistula was monitored regularly for a period of up to 2 years. The clinical data obtained was used to model the fistula situation *in vitro*. The second part of the clinical study was concerned with the development and location of stenoses. The intention was to relate the clinical observation to flow structures characterized by laboratory studies, to determine whether geometrical parameters are associated with fistula failure.

4.2 PROCEDURE FOR MAKING INTRAOPERATIVE MEASUREMENTS

The surgical procedure for constructing an AV fistula is given overleaf and shown pictorially in Figure 4.1. The length of the arteriotomy was measured using stainless steel callipers (1mm resolution) placed within the arterial incision (these data gave an indication of the clinical spread although absolute values were unreliable due to spasm and stretching of the arterial tissue). Once the anastomosis had been completed and flow through the fistula had settled, measurements were taken of the length of the anastomosis and its angle, both in the plane of the anastomosis. Angle measurement was carried out by bending a wire to the shape of the proximal artery/proximal vein junction. This angle was then estimated with a protractor.

Fistula flow was measured using a transit-time ultrasonic flowmeter with a 4mm Perivascular Flowprobe (see Figure 4.2). The flowprobe was applied to the vessel so that the region under study lay within the acoustic window formed by the

SURGICAL TECHNIQUE FOR CONSTRUCTING AN AV FISTULA AT THE WRIST
(END VEIN-TO-SIDE ARTERY ANASTOMOSIS)

1. Surgery is generally performed under local anaesthesia

2. The distal cephalic vein (of the non-dominant arm) is outlined with methylene blue

3. Iodine solution is brushed over the patient's arm as an antiseptic

4. A 3cm longitudinal/transverse incision is made at the wrist, over the radial artery and cephalic vein

5. The fascia and subfascial layers are gently dissected exposing the vein and the artery for an adequate distance

6. The vein is mobilized first, all branches for a distance of about 3cm are ligated and interrupted (Figure 4.1 (a))

7. Heparinised saline is used locally throughout the procedure for irrigation to prevent thrombosis formation

8. The vein is ligated distally and transected

9. To enlarge the venotomy, the transected end of the cephalic vein is spatulated (Figure 4.1 (b))

10. An umbilical catheter is inserted into the vein and it is flushed intermittently during the procedure with heparinised saline to dilate it and ensure patency

11. The radial artery is then mobilized for a similar distance with small atraumatic clamps

12. A longitudinal incision, about 10mm in length, is made in the artery or, if the artery is firm or calcified, a small ellipse is removed

13. The end-to-side anastomosis is then performed with continuous suture (7/0 Prolene) with the naked eye or under two times magnification

14. The occlusive vessel loops, encircling tapes and clamps are removed and a thrill should be immediately palpable at the site of the fistula

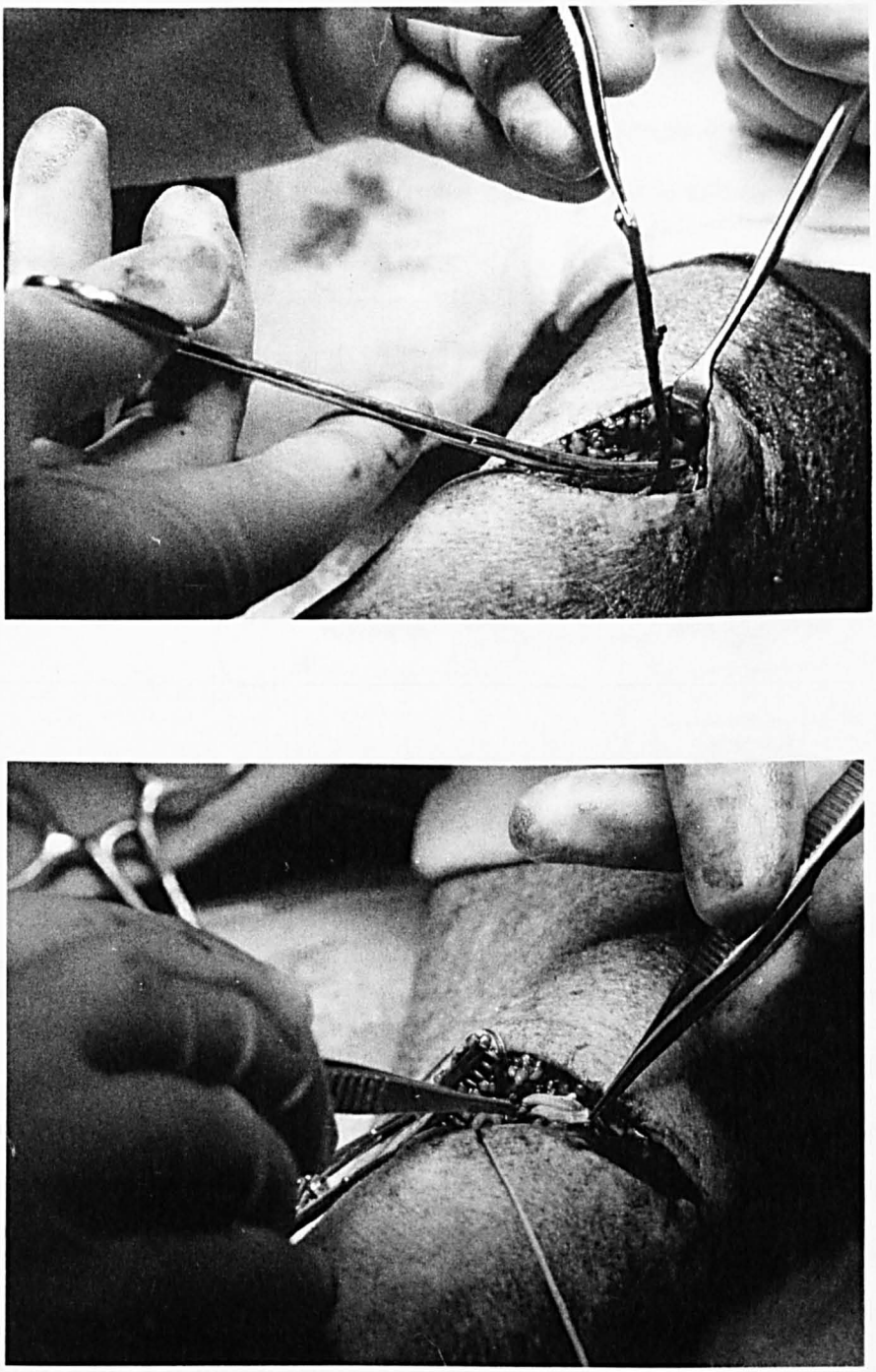

Figure 4.1 Constructing an end-to-side fistula at the wrist: transecting the vein (above) and spatulating the end (below)

probe's transducer body and the attached reflector bracket. The probe has a sliding cover. The space between the vessel and the probe was completely filled with an acoustically matched couplant. Care was taken to ensure that there were no sutures or air bubbles in the acoustic window and that flow through the vessel was not restricted in any way. A calibration procedure, taking less than one minute, was first performed (see Section 4.5).

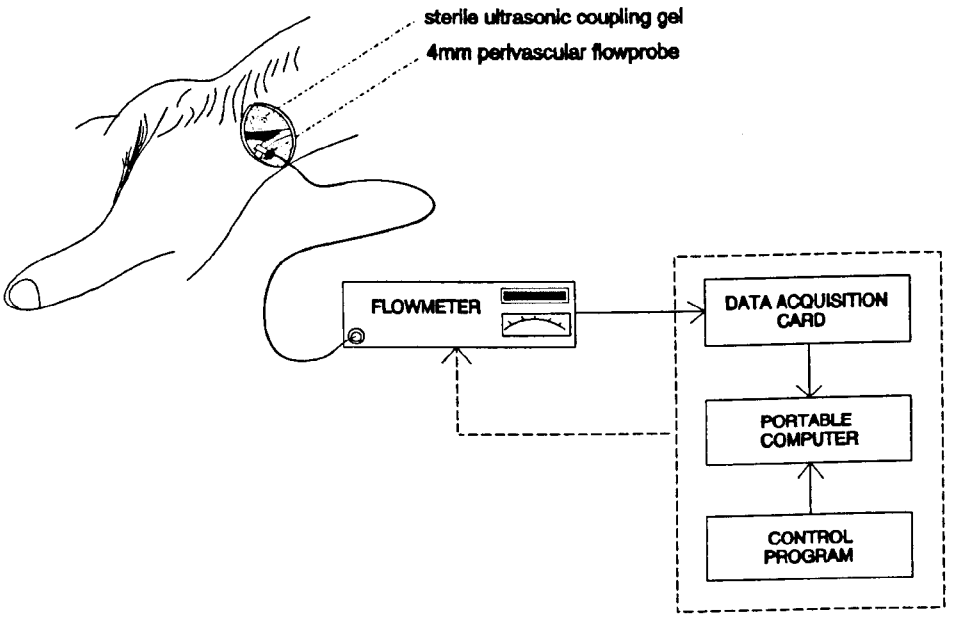

Figure 4.2 Schematic showing collection of flow data

Flow through the proximal vein, proximal and distal artery, and distal vein (depending on the anastomotic configuration), in sequence, was measured. The probe was placed as far from the anastomosis (where flow would be less disturbed) as the incision at the wrist allowed. Vessel handling and manipulation was minimized to reduce vessel spasm. The probe was either held in position by the surgeon or secured around the vessel and left without further manipulation, depending on which method provided the greatest flow. Flow can be affected by the tissues of the wound tending to dislodge the probe, causing vessel kinking. Measurements were taken once the

mean flow displayed on the flowmeter had stabilized. More than one set from each site may have been taken, if vessel spasm appeared to relax and the mean flow displayed on the flowmeter significantly increased.

Determination of simultaneous flow in all limbs would, of course, have been ideal, but because of the size of the probe, the limited area to manoeuvre in and the single channel flowmeter available, this was not possible.

4.3 STERILIZATION OF MEASUREMENT DEVICES USED INTRAOPERATIVELY

The callipers and wire used for angle measurement were first washed and disinfected, before being sterilized in a dry oven at 180° for 30 minutes. Autoclave tape was used to seal the edges of the sterilization pack. The appearance of dark stripes on the tape indicates completion of the sterilization process.

The callipers and wire were also sterilized by autoclaving at 121°C for 15 minutes. They were placed in special sterilizing pouches with an indicator strip that changes colour when steam sterilization has been performed properly.

The perivascular flowprobe, on the other hand, cannot withstand sterilization at high temperatures. It can, however, be sterilized at lower temperatures using ethylene oxide (EO) gas. The probe body and cable were thoroughly washed with a bactericide, using a soft-bristled brush to remove any remnants of ultrasonic coupling gel and biological matter. The dried probe was double-packed in standard seal/peel paper/polyethylene film packets (Steri-pouch 10x5x30, DRG Medical Packaging Supplies). This pack contains a chemical indicator strip which will change colour from blue to yellow when exposed to a given concentration of ethylene oxide. The EO sterilizer used was the Anprolene AN72 Sterilizer (Andersen Products). Each ethylene oxide ampule is sealed in a plastic bag of known gas permeability. The bag releases the gas given off by the ampule at a controlled rate during the sterilization

cycle. After a period of 12 hours in a fume cupboard, the lid of the sterilizer was partially removed. The sterilizer and contents were aired in the fume cupboard for at least 24 hours to ensure complete removal of all ethylene oxide residuals.

4.4 TRANSONIC HT107 TRANSIT-TIME FLOWMETER

The Transonic HT107 Blood Flowmeter (Transonic Systems Inc., New York, USA) with perivascular flowprobe is designed specifically for human intraoperative use. Measurements have minimal impact on the patient because neither vessel constriction nor mechanical contact is necessary to assess flow through the probe.

The Transonic flowprobe contains two ultrasonic transducers positioned on one side of the vessel under study and an acoustic reflector bracket situated midway between the two transducers on the opposite side of the vessel. One transducer is electrically excited to emit an ultrasonic wave which intersects the vessel under study, bounces off the acoustic reflector, again intersects the vessel and is received by the other transducer where it is converted into electrical impulses. The flowmeter records these as a measure of the time taken for the ultrasonic beam rays to travel from one transducer to the other. The two transducers alternate a sequence of transmit and receive, so that blood flowing in the vessel is intersected in both the upstream and downstream directions. During the upstream cycle, the ultrasonic wave travels against the blood flow and the total transit-time is increased by an amount dependent on the axial flow. During the downstream cycle, the acoustic wave travels with the flow and the total transit-time is decreased by the same axial flow-dependent amount. Therefore, the difference in transit-time between the upstream and downstream signals is a measure of volume flow. The full transit-time of the ultrasonic beam is the sum of the two vector components of the intersected flow. These vector components vary with the alignment of the vessel/probe axes but their sum always represents the axial component of the flow. The measured flow is also

largely independent of the velocity profile, random velocity fluctuations or haematocrit.

A H4S (65° angle of illumination) perivascular flowprobe was used to monitor fistula flow, designed for application on vessels of 2.5 - 4mm diameter. According to the manufacturer's specifications, this probe provides a resolution of 0.8ml/min, a maximum range of 2000ml/min and a maximum error of $\pm 15\%$. Zero flow readings may differ in different media; the maximum unadjusted zero flow error of the probe was 6ml/min. Because of the difficulty in carrying out *in situ* calibration, the manufacturer's *in vitro* calibration procedure was followed.

An acoustically matched ultrasound gel (Aquasonic 100 Sterile Ultrasound Transmission gel, Parker Laboratories Inc.) was used as an acoustic couplant. This was water soluble, and so could be easily removed from the measurement site.

4.5 FLOW DATA COLLECTION AND PROCESSING

The flowmeter provides an analogue voltage output corresponding to volume flow as a fraction of the scale factor for the probe connected. It provides a 1V ± 0.01V reading at the full scale flow of 400ml/min for the 4mm flowprobe and a range of ± 5V corresponding to a range of blood flow of 2000ml/min.

The pulsatile flow signal was interfaced to a 286 portable computer via a 12 bit A/D converter board (DT2814, Data Translation Inc.). To calibrate the A/D converter, the computer is first instructed to sample a calibrate-zero signal-factor signal, and then a calibrate-scale-factor signal. Using an appropriate scaling factor, the sampled data were stored as true flow values. The input voltage signal was sampled at 300Hz for 25 seconds for each set of flow data. Flow probe calibration was carried out prior to positioning *in situ*, with the flowprobe immersed the coupling gel.

The flow data were imported into a digital signal processing package,

DADiSP2 for display and analysis of the flow waveforms.

4.6 PATIENT DATA/MEDICAL HISTORY

The main factors predisposing to thrombosis are low flow rates (resulting from hypovolaemia or hypotension), increased coagulability of the blood, and changes in the vessel wall. Uraemic patients in end-stage renal failure tend to have a low haematocrit (the percentage of packed cells to serum) and hence, a low blood viscosity. Thus, higher preoperative whole blood viscosity values in patients could increase the likelihood of fistula failure (Dormandy and Edelman, 1973). A higher preoperative blood platelet count could also be a predicator for subsequent thrombotic problems (Bouhoutsos *et al.*, 1974; Reilly *et al.*, 1983). Lower blood viscosity and platelet count values, though, may only improve the clinical manifestations of the underlying stenotic process by reducing platelet-surface interactions at the sites of turbulence, without affecting the process itself.

Patients with polycystic kidney disease have a higher haematocrit and, subsequently, a higher blood viscosity. Nephrotic syndrome is associated with coagulation disorders, and possible thrombosis, due to functional deficiencies of the blood contact Factors IX and XII, and an increase in Factor VIII, fibrinogen and platelets. Polycythaemia vera, a disorder involving hyperplasia of all bone marrow elements, is a hyperviscosity syndrome, resulting in impaired blood flow. It is characterised by an increase in red blood cell mass (erythrocytosis) and haemoglobin concentration. Platelet counts are usually increased, and in both treated and untreated patients, giant-sized platelets are a characteristic finding; this would also predispose to thrombosis. Polycythaemia can also be caused by smoking and stress, but the polycythaemic values are reversible. Hyperviscosity is also associated with multiple myeloma, a malignant disease of the bone marrow. Platelets counts are also high in myleofibrosis and chronic leukaemia. Hyperfibrinogenaemia is another blood

disorder that might increase the likelihood of occlusion, as occlusive thrombi have been found to be rich in fibrin (Davies and Woolf, 1993; Goldwasser *et al.*, 1994). Also patients with systemic lupus erythematosus and collagen diseases may be more susceptible to thrombotic episodes (White, 1996).

Evidence of atherosclerotic disease can be derived from its complications, such as angina pectoris, myocardial infarction, arrhythmias, stroke and peripheral arterial disease. In considering long-term patency of the fistula, the risk factors for atherosclerosis should also be taken into account. These include hypertension, diets rich in cholesterol and saturated and short-chain fatty acids, cigarette smoking, diabetes mellitus, and obesity. Hyperlipaemia is a common clinical presentation in uraemic patients, and so probably already contributes to accelerated atherosclerosis in these patients. Serum lipoprotein(a) has also been implicated as an independent risk factor in vascular access occlusion (Glodwasser *et al.*,1994). It has the ability to inhibit fibrinolysis and the generation of TGF-ß. Serum Lp(a) levels have been found to be significantly higher in patients with end-stage renal failure.

It was necessary to identify cases where non-haemodynamic factors could have been primarily responsible for fistula failure. Therefore, details from the patient's medical records were noted if they could possibly influence the outcome: a case study of each patient was compiled (see Section 9.2) containing information on whether the patient suffered from diabetes mellitus, congestive heart failure, had indications of ischaemic heart disease or peripheral arterial disease, had undergone previous surgical procedures (that might have involved an intravenous infusion etc.) or had any rheological factors that might affect long-term patency.

4.7 USE OF DUPLEX AND COLOUR-FLOW ULTRASONOGRAPHY FOR SCANNING AV FISTULAE

B-mode imaging can effectively provide anatomical information on the

positions of the arterial and venous vessel walls from hyperechogenic signals at the blood/soft tissue interface. Normal fistulae have walls with smooth contours. Thrombus can be identified as weak echogenic material protruding into the anechogenic vessel lumen and stenosis as a circumscribed constriction of the vessel lumen. Real-time B-mode imaging may not give a complete, or wholly accurate, picture of what is going on within the fistula circuit. Some of the limitations of B-mode imaging, however, can be overcome by combining pulsed Doppler analysis with B-mode imaging in the Duplex scanner. Doppler ultrasound relates flow velocity (υ) to the change in frequency (f_d) that results from scattering of the ultrasound beam from a red blood cell travelling at an angle Θ to the beam (see Equation 5; c is the speed of sound in soft tissue and f_t is the frequency of the transmitted ultrasound). B-mode imaging may be used to detect and localise the vessels of interest and pinpoint irregularities in vessel walls. This facilitates accurate positioning of the pulsed Doppler sample volume to obtain velocity profiles and flow information at specific distances from the transducer. Also, B-mode imaging enables the measurement of the angle of insonation. Stenotic regions are characterised by turbulent high-velocity systolic flows and low diastolic flows. Colour Doppler imaging shows blood flow within vessels, including disturbances caused by stenotic lesions and regions of turbulence or low velocity. In a normal vessel, the colour Doppler signal completely fills the lumen. At regions of stenosis there is a corresponding constriction of the colour-Doppler flow stream. Stenoses may be associated with aneurysmal dilatation downstream. These aneurysms are identified as circumscribed regions of dilatation of the vessel lumen with distinct borders filled with low velocity colour-Doppler signals. As mild stenoses may easily be missed with any one ultrasonic method, it is preferable to employ a combination of B-mode imaging and colour Doppler imaging to identify stenotic lesions.

$$f_d = \frac{2\upsilon f_t}{c}\cos\theta \quad \text{——} \quad (5)$$

Volumetric blood flow can be estimated from the product of the luminal cross-sectional area and the time-averaged intensity-weighted mean Doppler frequency over an integral number of cardiac cycles. The sample volume is aligned with longitudinal axis of the vessel. As it encompasses the whole cross-section of the vessel, the velocity waveform obtained will include the high velocities associated with centre-line blood flow, as well as the slower moving blood cells near the vessel wall. One source of error, though, in this calculation will be from non-uniform insonation of the blood vessel by the ultrasonic beam (Evans, 1985) due to difficulty in imaging the plane of the anastomosis. Also, the vessel radius varies throughout the cardiac cycle and, hence, there is the difficulty of accurately assessing a mean cross-sectional area of the vessel. Therefore, for volumetric blood flow measurement, the root-mean-square error can be of the order of 15-30%.

The performance of colour Doppler sonography in evaluating fistulae for haemodialysis generally compares well with angiography (Middleton *et al.*, 1989; Nonnast-Daniel *et al.*, 1992) although duplex scanning is more operator-dependent. However, stenoses in AV fistulae are especially difficult to detect with ultrasonic methods as, firstly, it is difficult to image in the plane of the anastomosis and, secondly, vessels may be variable anatomically. Thus, measurements of diameter and luminal area reduction by direct visualisation, which depend on comparing "normal" to stenosed segments, may yield misleading results - especially in the case of AV fistulae where there is, typically, non-uniform dilatation of the efferent vein. Significant discrepancies are also observed when correlating linear and area parameters - more so with mild stenoses (Alexandrov *et al.*, 1993), due to the asymmetrical nature of intimal hyperplasia, or in superficial vessels, where pressure applied by the ultrasonic probe could distort the luminal cross-section. Tordoir *et al.* (1990) showed that the maximal systolic frequency in the Doppler spectrum could be used to detect significant stenoses (50-99% diameter reduction) in the vein.

4.8 PROTOCOL FOR POSTOPERATIVE SCANNING OF AV FISTULAE

Postoperative evaluation of the fistulae was carried out using an ultrasound colour-flow scanner (Acuson Computed Sonography 128XP/5) with linear-array transducer (L7384 probe) incorporating a 5MHz pulsed Doppler system and a 7MHz B-mode imager.

IMAGING TECHNIQUE	USE
B-mode imaging (7.0 MHz linear array)	• Localise and detect fistula vessels • Examine fistula geometry • Measure luminal cross-sectional area in the transverse image plane • Identify and assess stenoses along the proximal vein and at the anastomosis • Identify major venous branches near the wrist
Pulsed-wave Doppler ultrasound spectral display (5.0 MHz)	• Approximate blood flow through the proximal and distal artery and downstream of the anastomosis where flow through the vein is undisturbed • Identify and assess stenoses by comparing the peak sytolic velocity
Colour-flow Doppler ultrasound imaging (7.0 MHz)	• Identify flow disturbances and stenotic regions • Provide a hard copy of flow patterns in the region of the anastomosis and of stenoses

All patients were investigated in the supine position and prior to dialysis. The 2-D imaging, Doppler and colour Doppler imaging parameters were all standard for each scan. Care was taken to ensure that the probe was adequately cushioned on ultrasonic coupling gel so as not to compress the superficial vessel.

Fistulae were scanned longitudinally and in transverse section. The radial

artery was examined proximal and distal to the anastomosis. Also the efferent vein was examined, from the anastomosis upwards to the elbow (and distal of the anastomosis, in the side-to-side fistula). The presence of venous branches near the anastomosis was noted. (See Appendix A for the anatomy of the upper extremity.)

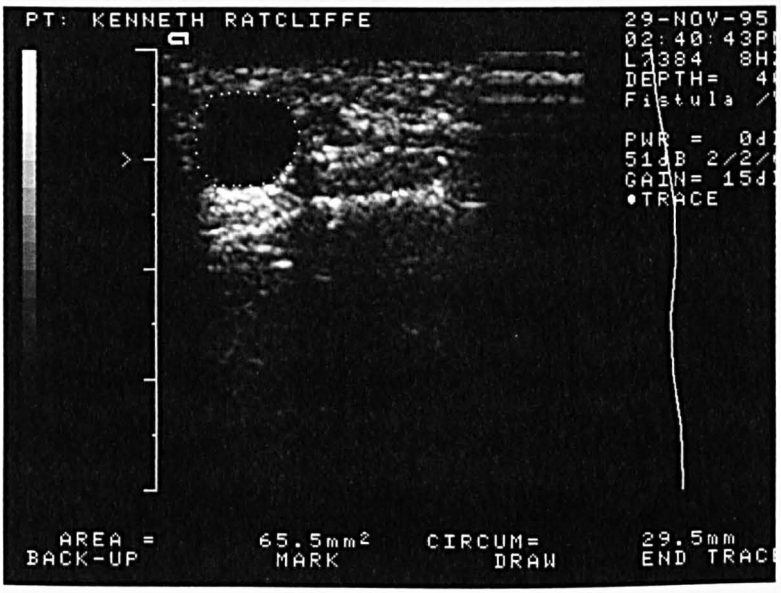

Figure 4.3 The TRACE function

Cross-sectional area measurements were made on each of the vessels (including venous branches) by tracing the luminal outline (see Figure 4.3) under maximum resolution. Velocity measurements were also made in each vessel: the vessel was scanned longitudinally, the Doppler gate was increased to encompass the whole vessel lumen and the time-averaged velocity over a number of integral cardiac cycles, and from these, the average flow was obtained (see Figure 4.4). Area and velocity measurements were made at the same place along the vessel to avoid errors in flow calculation due to vessel non-uniformities. The above measurements were made in regions of undisturbed flow, identified with colour Doppler. It was noted whether flow in the distal segments of the fistula was antegrade, alternating forward

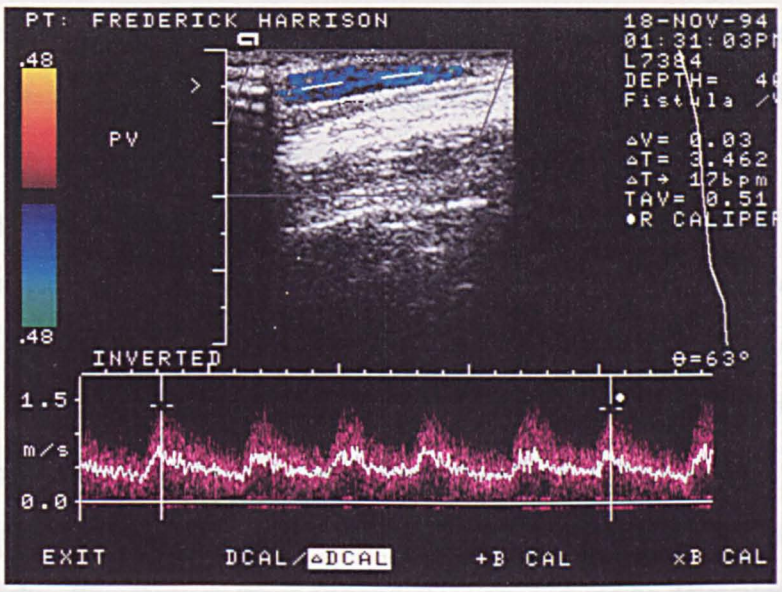

Figure 4.4 Calculating the time-averaged velocity

and retrograde or permanently retrograde. Proper alignment of the incident angle to flow marker with the vessel was ensured. Aliasing and cross-talk were minimised.

When stenoses were present in any of the vessels, their position with respect to the anastomosis was noted, as well as the residual diameter and lumen cross-sectional area. In regions of probable stenosis, a small Doppler gate was gradually moved along the vessel and large variations in the maximum peak systolic velocity were noted.

Hardcopies of the anastomosis and other regions of interest were made to enable comparison with future scans. After the initial postoperative scan, scans concentrated on the maturation of the vein and the presence of stenoses at or near the anastomosis or along the vein.

4.9 DISCUSSION

Intraoperative and postoperative surveillance of fistulae can be efffective in

highlighting possible problems at an early stage. However, a thorough preoperative assessment of the patient and evaluation of the major vessels of the upper extremity are imperative for optimizing fistula patency and providing easy access to long segments of vein in an individual patient.

Preoperatively, patency (and the quality of the collateral supply via the ulnar and interosseous arteries and palmar arch) can be simply assessed with the Allen Test (compress both the radial or ulnar arteries at the wrist, watch the colour drain out of the hand and come back as one or other of the vessels is released). This is both useful as a precursor for possible ischaemic complications of the hand and as fistula flow is critically limited by the calibre of the radial artery. Using duplex ultrasonography, flow through the radial and ulnar arteries can be determined. Veins are more difficult to effectively visualize with duplex ultrasonography. However, Wong *et al.* improved visualisation of the cephalic vein by employing a pulse generated run-off system (Oak Medical Ltd.) first used to determine calf vessel patency (Beard *et al.*, 1988). Arteriography and venography can also help to determine patency. Soft tissue x-rays of the upper extremity can be of use to show significant arterial calcifications especially in older or diabetic patients. In obese patients, the vein may be deeply embedded in adipose tissue, and hence, difficult to cannulate even though the fistula may mature satisfactorily. Careful attention to the veins is necessary in patients who have had subclavian catheters, intravenous lines cannulation or invasive monitoring lines.

Good planning and patient assessment can reduce the incidence of complications and minimise the necessity for multiple procedures or revisions. Poor planning, technical errors during access surgery, patient unsuitability and inadequate postoperative surveillance are limiting factors in fistula outcome. Once these issues have been addressed, it may be easier to determine the role of haemodynamics in fistula failure.

CHAPTER 5

ANALYSIS OF CLINICAL DATA

5.1 INTRODUCTION

Radiocephalic fistulae were studied in patients requiring primary access procedures for haemodialysis between May 1994 and August 1995. Flow measurements were made intraoperatively and 1 day postoperatively on these patients in order to define the parameters required for haemodynamic modelling (see Chapter 4). In 22 cases, the development of the fistula was monitored at regular intervals for periods up to 24 months. Some patients who either live a substantial distance away from the hospital or who have moved out of the area, have been lost to follow-up. For various reasons, the patient data sets may not all be complete.

A total of 35 patients were studied during this time period (see Figure 5.1).

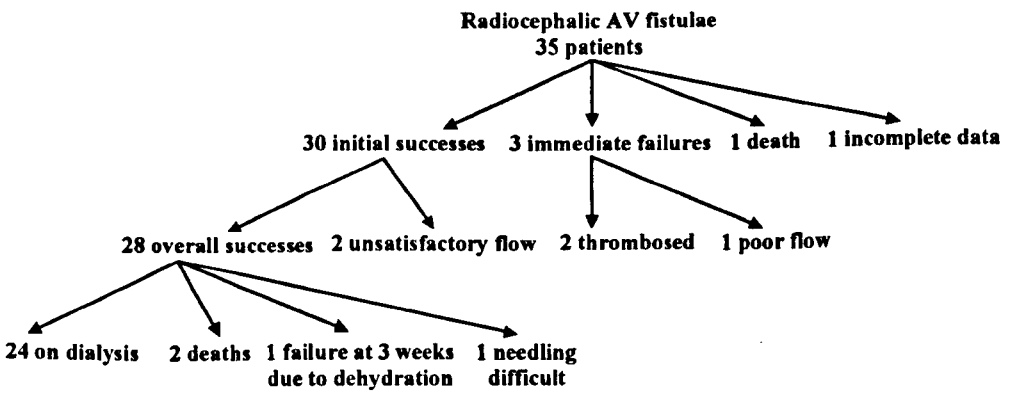

Figure 5.1 Outcome of the 35 fistulae studied

Intraoperative and postoperative data on flow and diameter ratio have not been included from 5 of these patients: 3 immediate (within 24 hours of surgery) failures (patent fistulae over which the characteristic high frequency thrill was not palpable, denoting insufficient flow, or fistulae which thrombosed soon after surgery), 1 death (at 2 weeks postoperatively) and 1 patient with insufficient intra- and postoperative

flow data. The other 30 patients (25 men and 5 women) ranged in age from 23 to 83 years (mean, 62 years) at the time of fistula construction. All but 2 fistulae matured satisfactorily (in 2 cases, after ligation of major cephalic branches) according to duplex parameters. Four of the 28 satisfactory fistulae were not subsequently used for dialysis: dehydration and diarrhoea caused one fistula to fail after 3 weeks, 2 patients died within 3 months of access surgery and in one patient, adipose tissue hindered palpation of the vein for needling. In the remaining 2 cases, the vessels did dilate to some extent but fistula flow was still insufficient after 3 months.

5.2 GEOMETRICAL CLASSIFICATION OF THE FISTULAE

The diameters of the radial artery and the cephalic vein vary widely from patient to patient. In order to determine the geometrical parameters for the construction of fistula models, data were obtained from clinical measurements. Patients were not assessed preoperatively in the present study. In a study previously conducted at the Royal Liverpool University Hospital by Wong *et al.* (1996) vessel diameters measurements were made using an ultrasound colour-flow scanner and pulse generated run-off system for visualising the vein (Figure 5.2). The lines drawn in Figure 5.2 denote the four specific ratios of vein-to-artery diameter that represent the wide range observed *in vivo*. The mean vein to artery diameter ratio in these patients was approximately 1.25.

Since the diameters of the radial artery and cephalic vein increase with time after access surgery, it was important to chart postoperative dimensional changes in patients. Figures 5.3 and 5.4 show the data obtained at one day and three months after access surgery. Although the patient data sets on the two graphs were different, the spread of the both the graphs was similar. Vein and artery diameters were also plotted at 3 months after access surgery (see Figure 5.4). Although data on all the patients included in Figure 5.3 were not available, a shift in the mean vein to artery

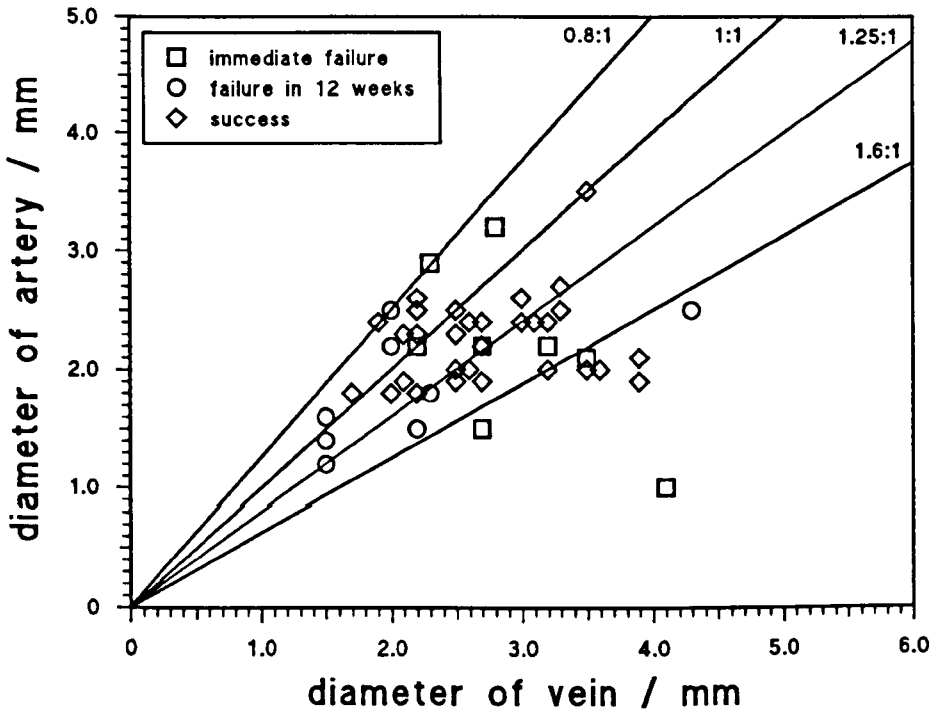

Figure 5.2 Preoperative diameters of the radial artery and cephalic vein at the wrist and fistula outcome (N=46). Data from Wong et al. (1994). Lines denote vein to artery diameter ratios

diameter ratio to approximately 1.6 was observed in these 12 good fistulae. All three figures show that four vein-to-artery diameter ratios 0.8, 1.25, 1.6 and 2.0 (with an anastomotic angle of 30°) adequately represent the ratios seen *in vivo*.

A statistical comparison of the data contained in both Figure 5.3 and Figure 5.4 was carried out using the paired-sample *t*-test (see Table 5.1). The observed *t* (1.209) exceeds the value obtained for 11 degrees of freedom and 30% probability (1.088). Hence, in over 70% of cases, the vein-to-artery diameter ratio is greater at 3 months than at 1 day ($P<0.3$).

The intraoperative angle measurements taken on the patients in Section 3.1 are shown in Table 5.2. Also shown in Table 5.2 are the distributions of the anastomotic length and length of the arteriotomy, measured intraoperatively.

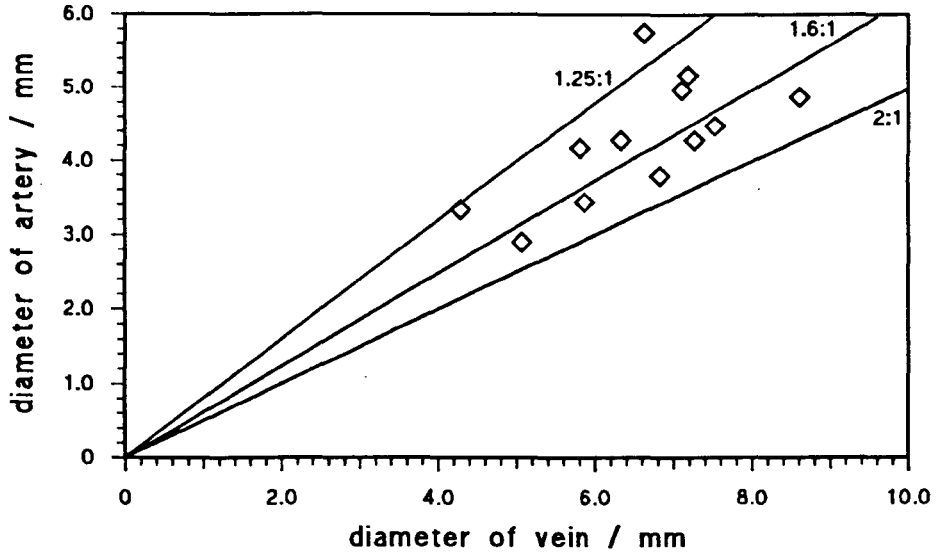

Figure 5.4 Radial artery and cephalic vein diameters in fistulae, measured 3 months postoperatively (N=12)

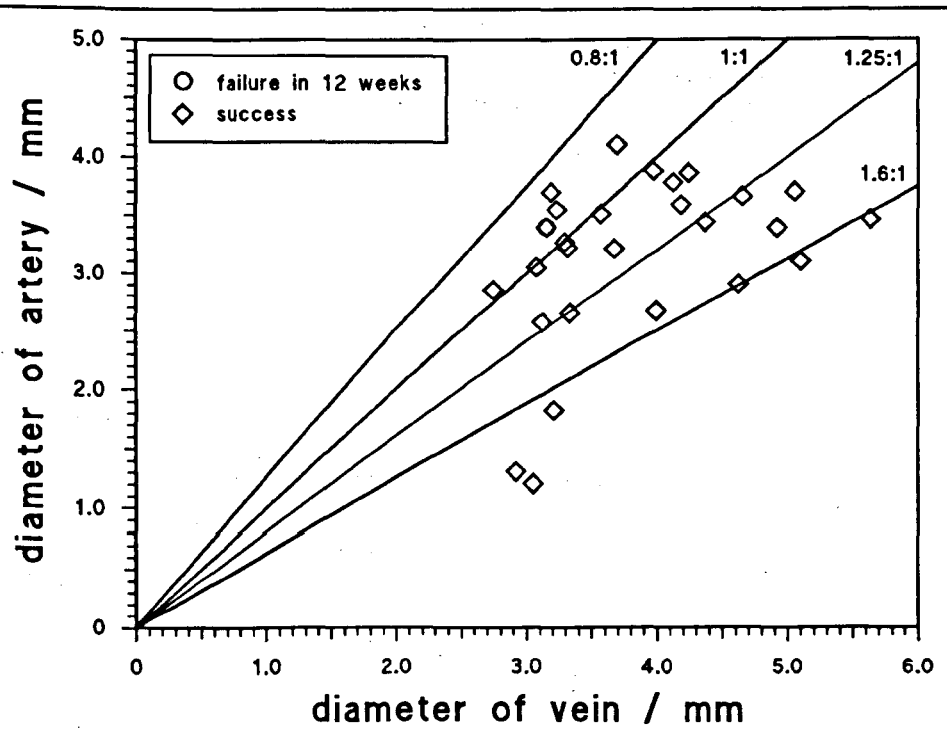

Figure 5.3 Radial artery and cephalic vein diameters in fistulae, measured 1 day postoperatively (N=28)

Table 5.1 Vein-to-artery diameter ratio in 12 patients at 1 day and 3 months

Patient No.	Vein-to-artery diameter ratio		$z=y-x$
	at 1 day (x)	at 3 months (y)	
3	1.365	1.426	0.061
5	1.645	1.762	0.117
6	2.542	1.281	-1.261
9	1.028	1.477	0.449
12	1.630	1.388	-0.242
14	1.257	1.745	0.488
17	1.164	1.149	-0.015
18	1.270	1.386	0.116
21	1.098	1.679	0.581
22	1.017	1.795	0.778
24	1.143	1.703	0.560
25	1.006	1.696	0.690

Table 5.2 Intraoperative measurements in 35 patients

Statistics:	Anastomotic Angle	Length of the arteriotomy	Anastomotic length
No. of patients	32	23	22
Mean ± S.D.	47 ± 15°	8 ± 2mm	8 ± 2mm
Median	42.5°	7.5mm	8mm
Range	25 - 80°	5 - 11.5mm	5.5 - 11mm

The results in Table 5.2 indicate that anastomotic angles of 30°, 50° and 70° with a vein-to-artery diameter ratio of 1.6 (the mean at 3 months after access surgery) would cover the range of anastomotic angles obtained in this series.

5.3 FLOW DIVISION IN THE FISTULA LIMBS

The flow distribution through the fistula was determined from intraoperative and 1 day postoperative flow data. Of the 30 fistulae that were satisfactory after the access surgery, 23 (77%) showed evidence of retrograde flow (towards the fistula) in the distal artery and 7 (23%) of antegrade flow (towards the hand) in the distal artery (Table 5.3). In Figure 5.5 the 30 patients have been divided into Group I, those with retrograde flow in the distal artery, and Group II, those with antegrade flow in the distal artery. Certain statistical parameters have been calculated for each group, such as the mean and standard deviation. The results show that, for fistulae in Group I, outflow in the proximal vein is supplied by 74 ± 15% proximal arterial flow and 26 ± 15% distal arterial flow (a ratio of approximately 3:1). The range in flow division varies from 1:1 to 19:1 proximal to distal arterial inflow. In the group with antegrade distal arterial flow, 79 ± 13% of the proximal arterial inflow flows out into the vein and the remaining 21 ± 13% flows into the distal artery.

Table 5.3 Direction of distal arterial flow in all patients studied

Patient group:	No. of patients		
	Retrograde flow in distal artery	Antegrade flow in distal artery	Total
Good fistulae	23	7	30
Immediate failures	1	2	3
Others†	1	1	2

†1 death and 1 incomplete data

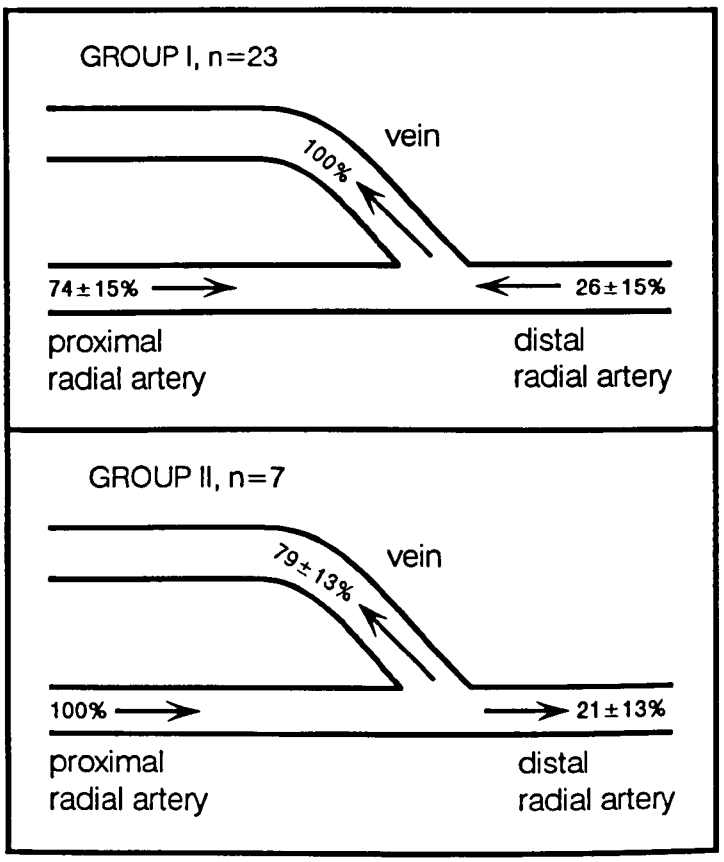

Figure 5.5 Initial flow distributions in the 30 fistulae. Group I is the group with retrograde flow in the distal artery, while in Group II, flow is antegrade.

As errors associated with flow determination using the Duplex ultrasound scanner can be as high as 15-30% (Evans, 1985), it was, therefore, necessary to verify that inflow was similar to the outflow in the fistula. In most cases a good agreement was obtained (mean discrepancy 20%). Vessel spasm during surgery may affect the magnitude of flow through the fistula. Consequently, if a large discrepancy was seen between the ratios of flows in the segments of the fistula obtained intraoperatively to that obtained the next day, the postoperative calculations were deemed more accurate, and those figures are reported here. In the majority of cases,

the two ratios were very similar (mean discrepancy 9%).

The results suggest that 5 different flow divisions would be sufficient to model the whole clinical range seen in our 30 patients: for the retrograde distal arterial flow experiments, flow division ratios of 100%, 75%, 50% and 0% proximal arterial inflow into the vein; for the antegrade distal arterial flow experiments, a single flow condition of the vein supplied by 75% of the flow in the proximal artery.

5.4 PARAMETERS CHARACTERIZING THE PULSATILE WAVEFORM

The dimensionless flow parameters, namely Reynolds number and Womersley's α parameter, were determined for each patient included in the study. The results are summarized in Tables 5.4 and 5.5 for data obtained from 1 day and 3 month postoperative duplex ultrasound measurements in the vein.

Table 5.4 Dimensionless parameters defining pulsatile flow at 1 day postoperatively

Statistics:	Velocity in vein	Re	α
No. of patients	27	27	27
Mean $\pm$ S.D.	62 $\pm$ 27 cm/s	650 $\pm$ 260	3.0 $\pm$ 0.6
Median	58 cm/s	640	2.9
Range	17 - 131 cm/s	150 - 1300	2.0 - 4.0

Table 5.5 Dimensionless parameters defining pulsatile flow in 3 month-old fistulae

Statistics:	Velocity in vein	Re	α
No. of patients	16	16	16
Mean $\pm$ S.D.	44 $\pm$ 15 cm/s	770 $\pm$ 260	4.7 $\pm$ 0.9
Median	43 cm/s	730	4.7
Range	22 - 77 cm/s	470 - 1300	2.9 - 6.6

Upon comparing the Re and α values in new and mature fistulae, 4 different flow conditions were chosen to represent both states: Re=300, α=3; Re=600, α=3; Re=600, α=4.7; Re=1000, α=4.7. In the case of the antegrade distal arterial flow experiments, the last flow condition was omitted.

There appeared to be a random spread in the scattergraph of peak to peak flow against mean flow (see Figure 5.6) in the vein. Therefore, the mean pulsatility index, PI, (peak-to-peak to mean flow) of 0.44 $\pm$ 0.17 ($\pm$ 1 S.D.) was used in the *in vitro* experiments. The pulsatility index is difficult to measure accurately in the course of postoperative Doppler ultrasound assessment due to the turbulent flow regime. Visual comparisons of successive velocity traces in each of the patients followed-up showed no evidence of any trend in the pulsatility index with time.

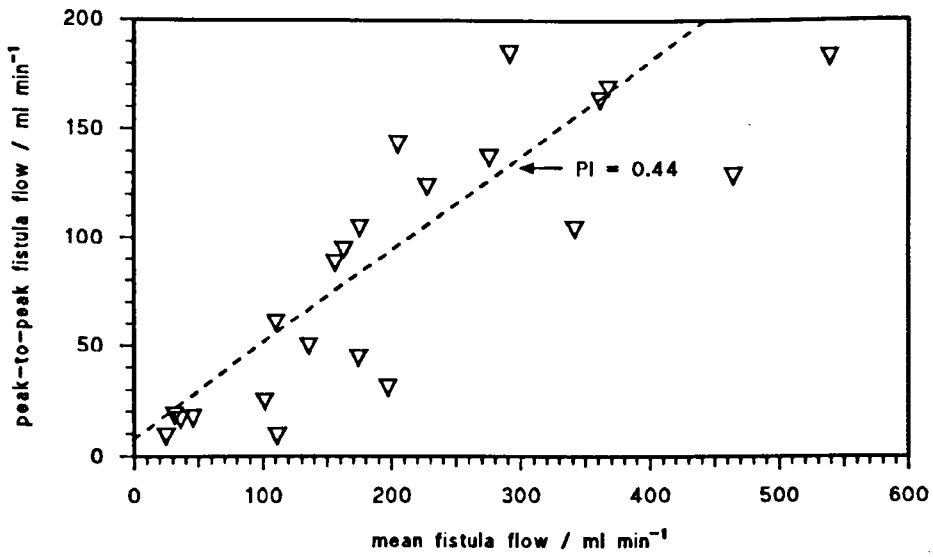

Figure 5.6 Pulsatility Index (PI) for intraoperative flow in the vein (N=22)

5.5 THE FISTULA FLOW WAVEFORM

In order to reliably simulate physiological flow in the *in vitro* study, it was necessary to reproduce a typical *in vivo* waveform. Therefore, intraoperative flow waveforms from all patients were studied. A data segment where the waveform was

relatively stable was chosen from these as a representative sample of venous flow. Thirty-four cycles collected during the 25-second sampling period were extracted individually from the sample and averaged. A typical averaged waveform is shown in Figure 5.7, containing 204 data points.

This waveform was translated into a displacement file to be accessed by the computer program controlling the pulsatile pump used in the *in vitro* experiments. The flow waveform was shifted along the time axis, so that the first data point was positive (to ensure that the displacement data would be positive), and was then integrated. The displacement waveform was suitably scaled for the gain of the pump and again shifted so that the first point was at zero. These data were imported into MATLAB to perform the cubic spline data interpolation for the displacement signal to the pulsatile pump. Two displacement signals were required: one with a period of 1.6 seconds (α=3) and another with a period of 1.0 seconds (α=4.7). The two signals contained 160 and 100 points, respectively. (Figure 5.8 shows the second of these traces.)

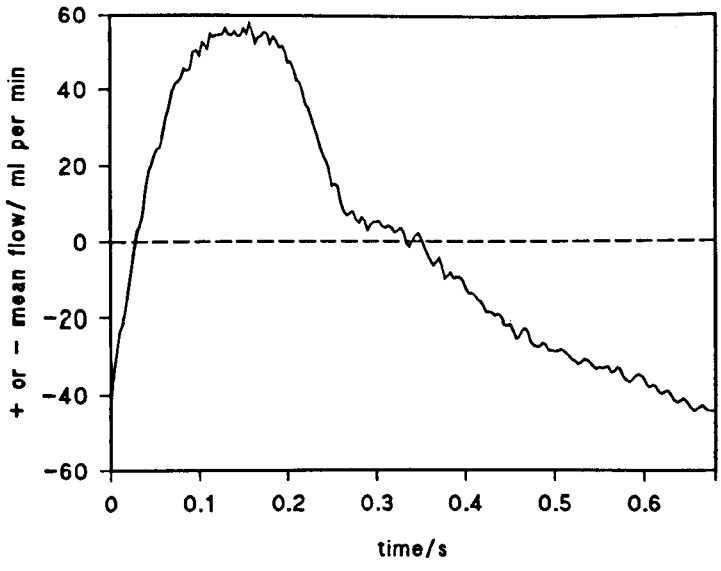

Figure 5.7 Intraoperative pulse profile used in the pulsatile flow studies

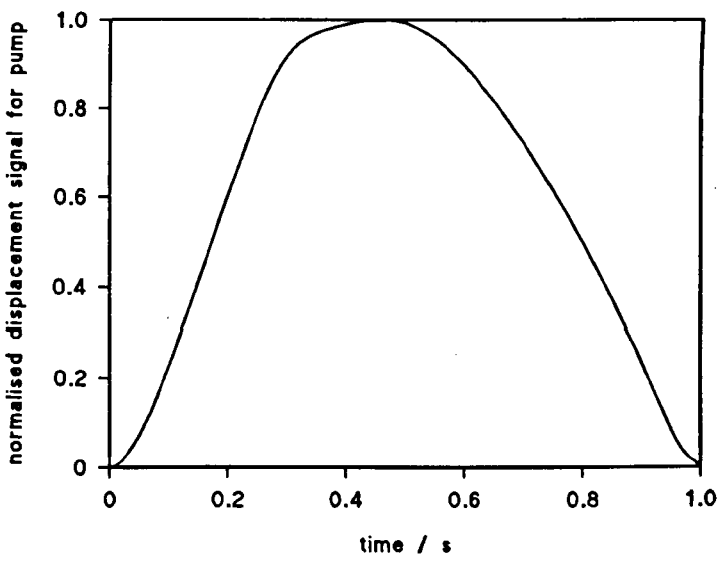

Figure 5.8 Normalized displacement signal for pulsatile pump (α=4.7)

5.6 SUMMARY

After careful analysis of all the available clinical data, matrices of the different flow conditions needed to cover the clinical range were devised for the *in vitro* experimental protocol (see Tables 5.6 and 5.7). Six models with differing anastomotic angle and vein to artery diameter ratio were selected (Table 5.8).

Table 5.6 Conditions for *in vitro* studies on fistulae with retrograde distal arterial flow (PA = proximal artery and DA = distal artery)

	Re=300	Re=600		Re=900
Flow division into vein:	α=3.0	α=3.0	α=4.7	α=4.7
100% PA, 0% DA flow	*	*	*	*
75% PA, 25% DA flow	*	*	*	*
50% PA, 50% DA flow	*	*	*	*
0% PA, 100% DA flow	*	*	*	*

Table 5.7 Conditions for *in vitro* studies on fistulae with antegrade distal arterial flow (PV = vein and DA = distal artery)

	Re=300	Re=600	
Proximal artery flow division	α=3.0	α=3.0	α=4.7
75% PV, 25% DA flow	*	*	*

α=3 and α=4.7 corresponded to a cycle length of 1.6 and 1.0 seconds, respectively. A peak-to-peak to mean flow (pulsatility index) of 0.44 was chosen for all pulsatile flow experiments.

Table 5.8 The geometrical configuration of the 6 fistula models

Anastomotic angle	Vein to artery diameter ratio
30°	0.8
30°	1.25
30°	1.6
30°	2.0
50°	1.6
70°	1.6

CHAPTER 6

IN VITRO MODELLING METHODOLOGY

6.1 MODELLING USING COMPUTER-AIDED DESIGN AND MANUFACTURE

Generic geometrical models of fistulae, based on the surgical procedure and duplex scans of fistulae, were constructed. The artery diameter in each model was fixed at 4.5mm. The vein diameters were, therefore, 3.6mm, 5.6mm, 7.0mm and 9.0mm, for models with vein-to-artery diameter ratios of 0.8, 1.25, 1.6 and 2.0, respectively.

The models are kinematically similar to the clinical case, as their geometric shapes of the vessels are similar. The models will also be dynamically similar if the Reynolds number for the two systems are the same. Since the flow is pulsatile, it was also necessary to ensure that Womersley's α parameter was the same.

Modelling using a computer-aided design and manufacture (CAD-CAM) package (DUCT 5.1, Delcam Inter., Birmingham) allowed models to be easily altered, smoothed, curved, intersected and filleted. By producing models this way, dimensions and tangents to the surface could be accurately specified (especially useful when making quantitative measurements - Chapter 8).

In mathematically modelling the floor of the artery, it was assumed that $a = \frac{diameter\ of\ vein}{2\sin(anastomotic\ \angle)}$ $b = \frac{diameter\ of\ vein}{2}$ transecting the vein at a specific angle produced an elliptical end with a major axis of length 2a and a minor axis of length 2b (see right for equation of an ellipse). When the vein is sutured around the edges of the arteriotomy, it was assumed that the elliptical shape is maintained so that the artery bulges out in the anastomotic region to accommodate the vein. Another important assumption at this stage was that the artery circumference was a circular arc in

$$\frac{x^2}{a^2} + \frac{y^2}{b^2} = 1$$

section. The radius and centre of each section were calculated at 0.5mm intervals (i.e. x-axis increments of 0.5mm) along the length of the anastomosis. Appendix B contains the more detailed calculations for each of the models. The shape of the anastomosis was specified by 3 circular sections: one at the centre of the anastomosis ($x=0$) and by the sections where the floor of the anastomosis reached a maximum, symmetrically on either side. The artery was smoothed between these sections and the normal circular lumen at $x=\pm 10$mm from the centre of the anastomosis. The vein was originally designed to be a cylinder. This was rotated at the appropriate anastomotic angle to intersect the artery. Two sections near its end were rotated until they were parallel to and separated by a distance of 25mm from the proximal artery. The second section in the vein was then shifted along its axis as necessary, to make the transition a gradual one. The vein was then filleted at the intersection with a constant fillet radius (0.8mm), in order to produce a smooth blend.

Models designed in DUCT were manufactured in epoxy resin using stereolithography. As this process is quite time-consuming and expensive, the models were limited to a length of 100mm models and extensions were then added to each of the limbs. To facilitate the connection of the models to the flow-rig, the ends of the artery and smaller veins were tapered up to 6mm.

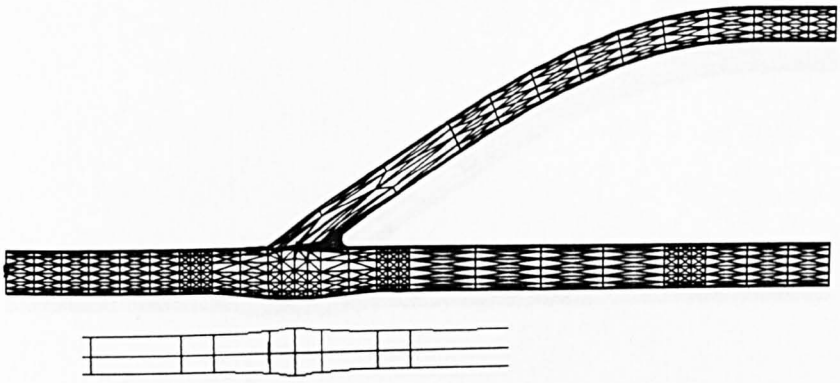

Figure 6.1(a) DUCT plot of AV fistula model diameter ratio 0.8 and anastomotic angle 30°

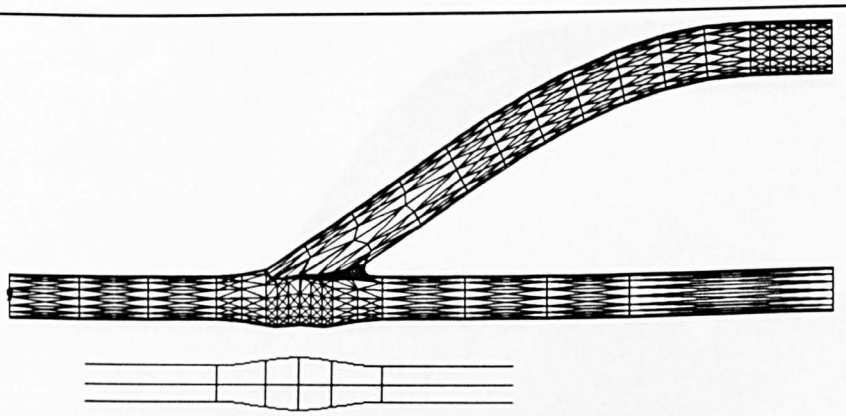

Figure 6.1(b) DUCT plot of AV fistula model diameter ratio 1.25 and anastomotic angle 30°

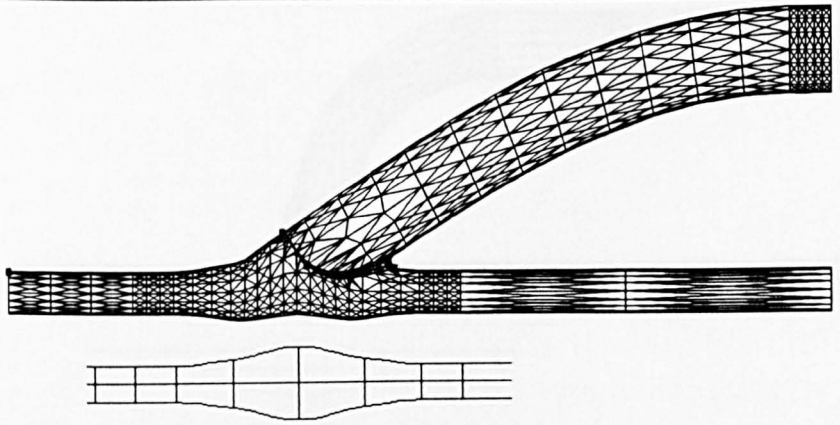

Figure 6.1(c) DUCT plot of AV fistula model diameter ratio 2.0 and anastomotic angle 30°

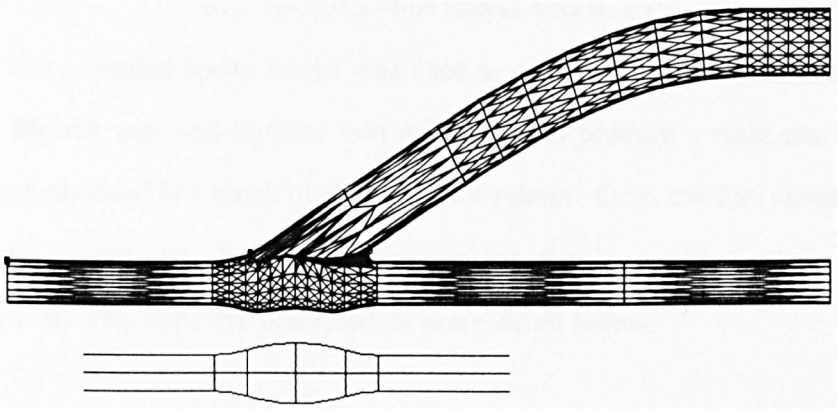

Figure 6.1(d) DUCT plot of AV fistula model diameter ratio 1.6 and anastomotic angle 30°

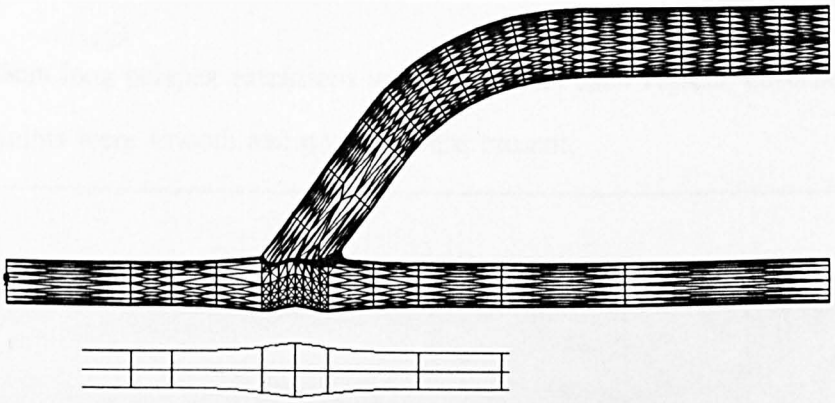

Figure 6.1(e) DUCT plot of AV fistula model diameter ratio 1.6 and anastomotic angle 50°

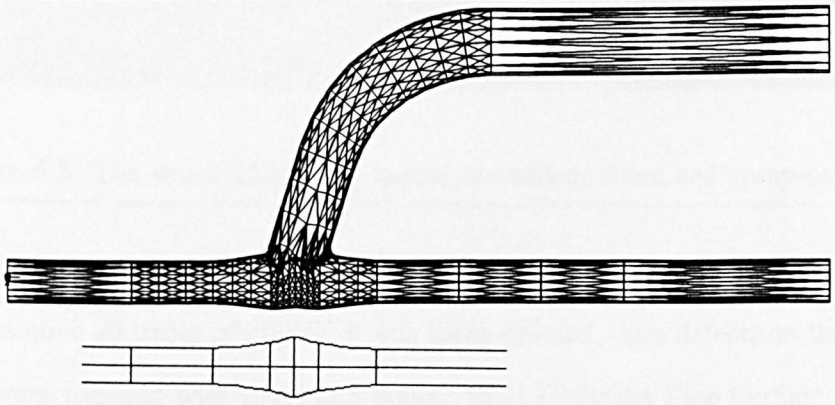

Figure 6.1(f) DUCT plot of AV fistula model diameter ratio 1.6 and anastomotic angle 70°

6.2 MODEL-MAKING PROCESS

The extended epoxy model was used to create a split female silicone rubber mould. Molten wax was injected into this mould to produce a male cast. The wax cast was embedded in a block of clear silicone rubber. Once this had cured fully, the wax was melted out, leaving the transparent fistula model used in the flow experiments. The steps are described in more detail below:

1. The epoxy model, as produced by laser stereolithography, was smoothed with fine grade silicon carbide paper.

2. 8cm long perspex extensions were fixed onto each vessels, ensuring that the joints were smooth and no gaps were present.

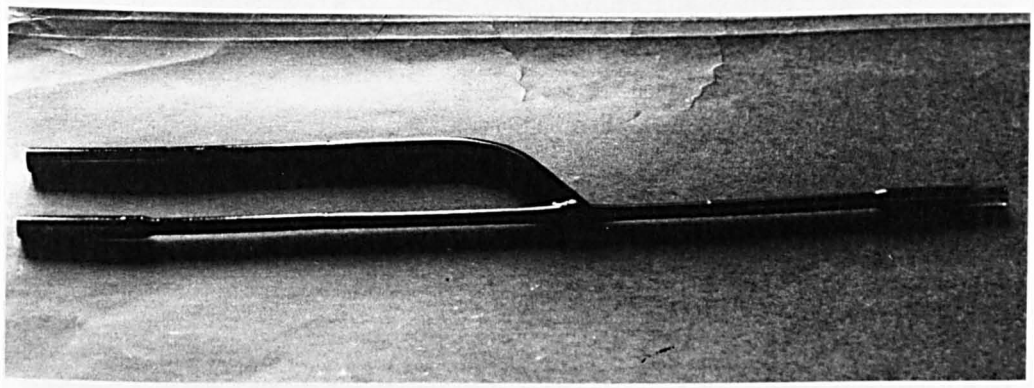

Figure 6.2 The stereolithography model, extended, filled and spray-painted

3. The model was cleaned with detergent and water, followed by isopropanol to remove all traces of grease. It was spray-painted. Any defects on the surface were repaired with fine grain plaster filler (Polyfilla Fine Surface, Polycell Products Ltd., Welwyn Garden City). The smoothed model was re-sprayed (see Figure 6.2).

4. A perspex box was constructed to hold the model. One long side of the box was temporarily secured in place with a silicone rubber adhesive sealant (Silcoset 151, Ambersil Ltd., Bridgwater). The inside surfaces were greased with petroleum jelly. The model was then mounted, level, in the box.

5. Approximately 650ml of red silicone mould rubber (RTV-31, Alec Tiranti Ltd., Reading) was thoroughly mixed with 0.25% by weight of catalyst, and was then degassed for 15 minutes in a vacuum of 950mbar. Greased locating pins were placed around the model. The silicone rubber was slowly poured into the box until the level of silicone rubber reached exactly half-way (see Figure 6.3).

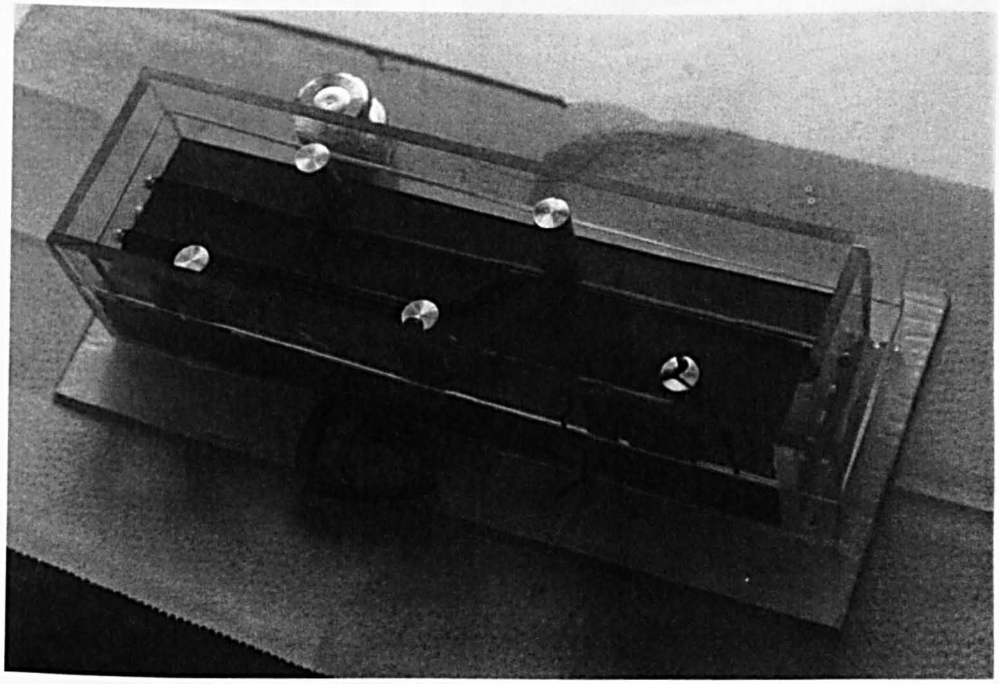

Figure 6.3 Pouring the first half of the silicone rubber mould

6. After 2 days' curing at room temperature, the exposed surface of the silicone rubber was lightly greased and the second half of the mould was poured. This

was left to cure at 40° for approximately 2 days.

7. The mould was removed, the two halves were separated and the epoxy model was removed. The inside surfaces of the mould were cleaned with acetone. A metal frame was made by double-bending tinned copper or steel wire to provide support for a wax cast of the model. The halves of the mould were refitted, encasing the metal frame. Wooden blocks and elastic bands ensured that the halves were bound tightly together. A 6mm straight polypropylene tubing connector was wedged into the distal artery opening. A length of rubber tubing was attached to the other end.

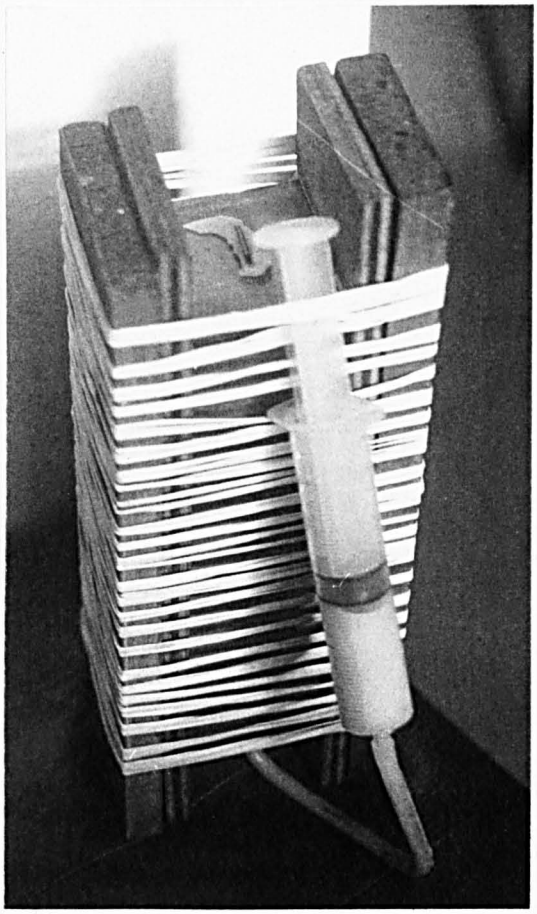

Figure 6.4 Producing the wax cast

8. The mould was stood upright in a convection oven heated to 105°C, along with a 50ml polypropylene syringe and wax (Type 1710, Speciality Waxes Ltd., Kingston, Surrey) in a metal container for 2-3 hours. The syringe was filled with the molten wax, attached to the rubber tubing.

9. The wax was slowly injected into the mould. Once wax was seen to overflow from both vessels, the inlet tubing was clamped. The mould was removed from the oven and left to cool overnight (Figure 6.4). The halves of the rubber mould were carefully separated (Figure 6.5) and the wax cast removed.

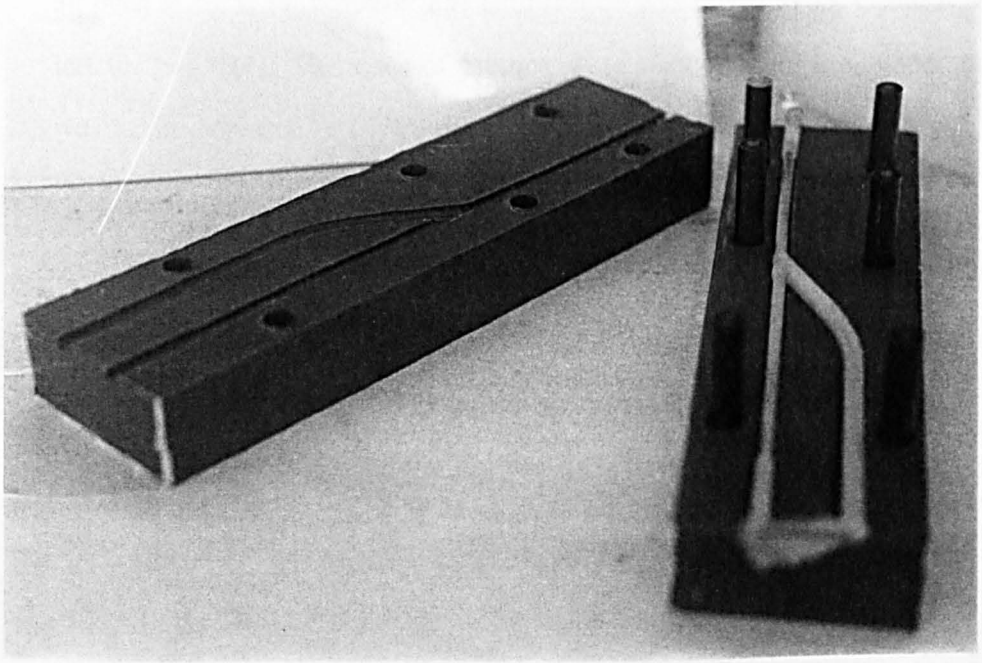

Figure 6.5 Removing the wax cast from the female mould

10. The wax cast was cleaned with acetone. Any holes in the wax were filled with fine grain plaster. The cast was then sprayed with an even coat of paint.

11. Another perspex box was created to hold the wax cast. Holes were made for metal connectors. The longer sides were polished using a proprietary car paint restorer (T-cut). These were then thoroughly washed with detergent and water. They were temporarily held in place with silicone rubber sealant. The wax cast was supported while the metal connectors were eased in place.

12. Approximately 350ml of clear silicone elastomer (Sylgard 184, Dow Corning, Houndslow) mixed with 10% (by weight) curing agent was de-gassed in a vacuum of 950mbar for 1-2 hours. This was slowly poured into the perspex box and then degassed again for 20 minutes. The clear silicone rubber was cured at room temperature for a day (see Figure 6.6). It was then placed in an oven at 40°C for 6 hours. The temperature was raised to 55°C and it was left for two days. The sides of the box were removed and the temperature was again increased to 65°C, overnight.

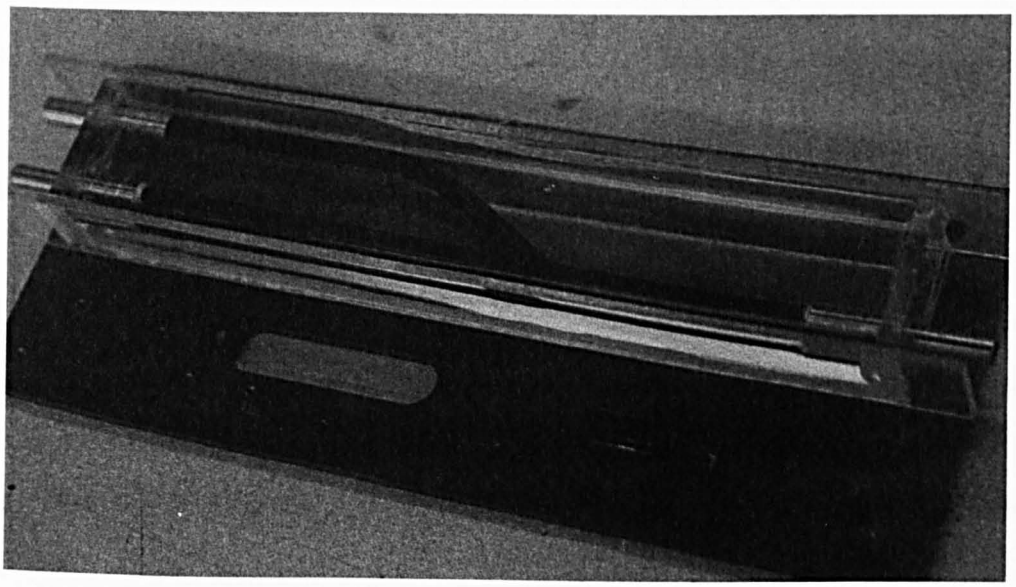

Figure 6.6 Pouring the clear silicone rubber model

13. A metal support was secured to the base of the perspex box, the sides were loosely reattached to the box and the whole box was clamped upright in an oven at 95°C for 1½ hours, until the wax had melted out. The model was flushed through with boiling water for several minutes. Detergent, boiling water, acetone, pipette brushes and long cotton buds were used to remove paint coating the insides of the transparent silicone rubber model. The final model (see Figure 6.7) was then dried in the oven for several days.

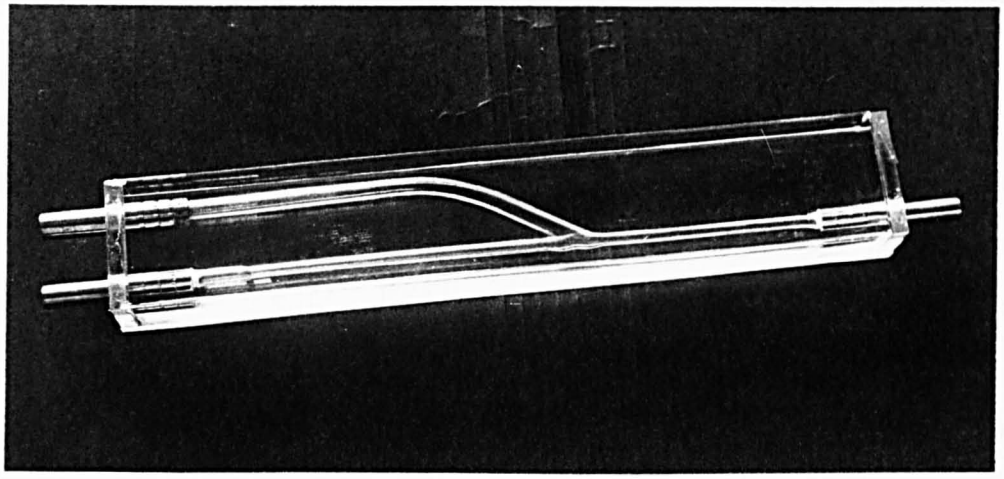

Figure 6.7 The final transparent fistula model

ALTERNATIVE METHOD

A similar technique to that described above was initially used to produce a thin-walled polyurethane model of the fistula. However, this method was difficult to reproduce and the models were frequently discoloured. Another disadvantage was that polyurethanes have a higher refractive index than silicone elastomers, and hence, refractive index matching for laser Doppler anemometer experiments proved difficult.

Two polyurethane grafts were sutured together by a renal surgeon to geometrically resemble a cephalic vein to radial artery end-to-side 30° anastomosis. Acrylic resin (Acrulite, Rubert & Co. Ltd., Cheadle, Cheshire) was injected under pressure into the graft model. Once the resin had set, the graft material was then stripped off to reveal an internal cast of the fistula, with artery and vein diameters of 4.5mm and 7mm. A highly polished perspex replica was produced by hand from rods of the same diameter as that of the acrylic artery and vein, and a small block which was fashioned to form the anastomosis. The perspex model was used to create a split female silicone rubber mould and wax cast (steps 4-9 above). The wax cast

was dipped (15 full coats) and sprayed (to reinforce the wall thickness near the heel of the anastomosis) with 8% polyurethane solution (Tecoflex, Thermedics Inc., Woburn) in dimethylacetamide (DMAC). Between each coat/spraying the wax model was mounted by its metal frame in a rotational jig set in an oven maintained at a temperature of 46°C to allow successive coats to dry. After the final coat had dried thoroughly, the wax cast was melted away in an oven at 95°C and hexane solution was used to remove any remaining traces of wax.

Flow visualization results using this model are displayed in Figures 7.5, 7.6, 7.10, 7.11, 7.12 and 7.13. These figures are comparable to those obtained using the equivalent silicone rubber model.

6.3 SUMMARY

Computer models of fistulae were created, based on surgical procedure and duplex scans of fistulae. From these, a series of transparent silicone rubber models were constructed with differing vein-to-artery diameter ratios and anastomotic angles. The models were designed in a CAD/CAM package (DUCT 5.1) and manufactured in epoxy resin using stereolithography. The epoxy model was used to create a split female silicone rubber mould. Molten wax was injected into this mould to produce a male cast. The wax cast was embedded in a block of clear silicone rubber. The wax was melted out, leaving the transparent fistula models.

CHAPTER 7

FLOW VISUALIZATION IN MODELS OF END VEIN-TO-SIDE ARTERY FISTULAE

FLOW VISUALIZATION IN MODELS OF END VEIN-TO-SIDE ARTERY FISTULAE

7.1 INTRODUCTION

Postoperative follow-up of AV fistulae using duplex ultrasonography can provide information on fistula maturation, measure fistula flow rates and highlight regions of disturbed flow (see Figure 7.1). However, because of the temporal and spatial limitations of current Duplex scanners, very little can be learnt about the nature of these flow disturbances. Hence, the need for *in vitro* modelling, for a clearer interpretation of flow structures in fistulae and their contribution to the development of stenoses. In this chapter, flow visualization studies carried out in AV fistula models under different flow conditions are described.

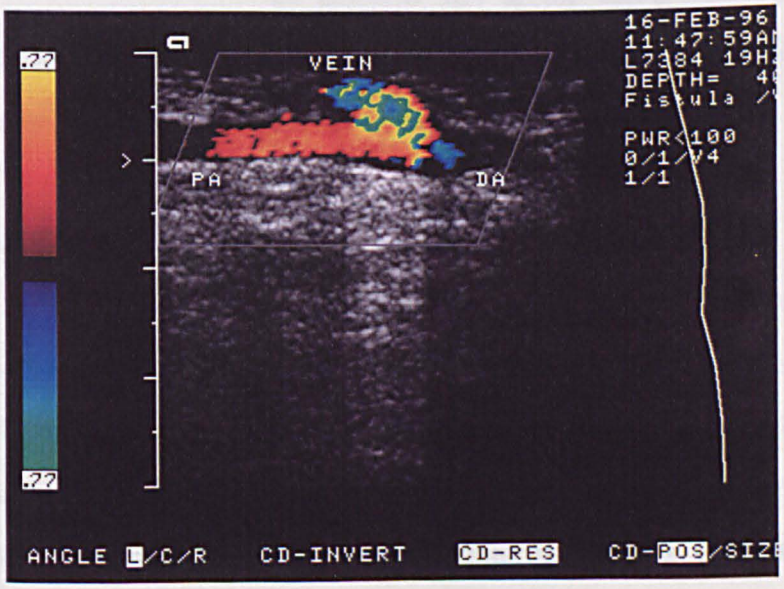

Figure 7.1 Colour-Doppler image of the anastomosis

7.2 MATERIALS AND METHODS

7.2.1 The blood analogue solution

Each of the transparent silicone rubber models described in Chapter 4 was installed in a flow loop system (Figure 7.2) circulating a blood analogue of 40% (w/w) glycerol and 7% (w/w) sodium chloride in distilled water. Light-scattering beads (Rilsan Blue, Elf AtoChem. U.K. Ltd.) of between 75-150μm in diameter were suspended in the analogue fluid as tracer particles (0.2%, w/w). Along with the flow particles, a surfactant (sodium dodecyl sulphate, BDH) was also added (0.01%, w/w). The blood analogue fluid matched the viscous properties of blood at high shear and provided a transparent medium for flow visualization.

The density (ρ) and viscosity (μ) of the analogue solution were 1160Kg/m^3 and 3.6 x 10^{-3} Pa s, respectively, giving a kinematic viscosity of 3.1 x 10^{-6} m^2/s. These values, along with the diameter (D) of the model vein were used to equate the flow patterns observed with a particular Reynolds number (Re) in the *in vivo* vein, by measuring the mass flow rate Q_m (see equation).

$$Re = \frac{\rho V D}{\mu} = \frac{4Q_m}{\pi \mu D}$$

7.2.2 The flow rig

A peristaltic pump was employed to take fluid from the main reservoir to the header tank supplying both the proximal and distal artery via a Y-section inlet section. Flow through the vein was returned to the reservoir through a smaller cylindrical header tank. By adjusting the pressure differential between the two header tanks or the valve immediately following the larger header tank, the mean flow rate could be altered. The case of antegrade flow through the distal artery was also modelled and the experimental set-up for this was very similar to the retrograde case; a Y-section inlet was not needed here, and flow from the distal artery was fed back into the main reservoir via a second cylindrical header tank (see Figure 7.3). Two

6mm diameter in-line flowprobes attached to a transit time flowmeter (Transonic HT107, Transonic Systems Inc., N.Y., USA) were also plumbed into the flow loop, at the venous exit and at the entrance of the distal artery. A computer-controlled servo pump provided the pulsatile flow component. The pump system also recorded an ensemble averaged (over 32 cycles) flow waveform measured in the vein. The flow distribution was determined by the resistance of the flow system which could be varied by adjusting the inlet valve and the outlet clamps. The mass flow rate through the vein was measured by weighing the fluid collected over a period of 60s.

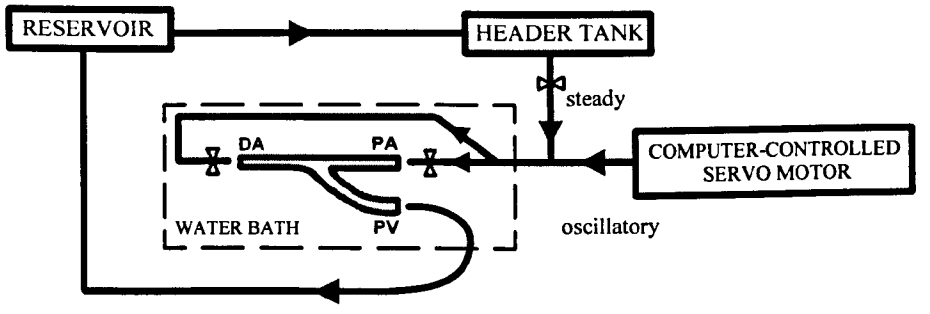

Figure 7.2 Experimental set-up for flow visualization (retrograde flow in distal artery)

7.2.3 Flow conditions

Steady and pulsatile flow experiments were performed over a range of Reynolds numbers simulating those recorded in patients. The effects of varying the ratio of proximal to distal arterial inflow into the vein were also investigated. (Refer to section 5.6 for the specific flow conditions modelled.)

7.2.4 Flow visualization and image recording

Flow patterns were obtained by planar illumination of the model using a

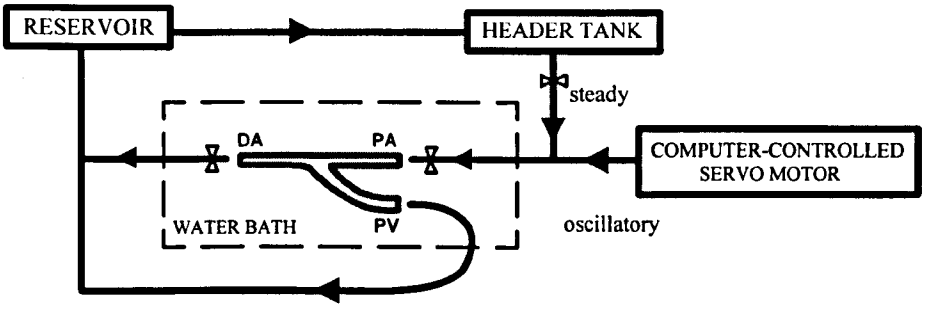

Figure 7.3 Experimental set-up for flow visualization (antegrade flow in distal artery)

16mW HeNe laser (wavelength = 632.8nm) with a cylindrical lens and a plano-convex lens. They were photographed with a 35mm camera (Nikon F-301) and 35-80mm macro lens on Kodak T-max P3200 film and also recorded on S-VHS video tape using a CCD camera (Hitachi KP-M1E/K modified by KRP Power Source, U.K.) and framegrabber (IP8 2M-C, Matrox U.K. Ltd) (Shortland *et al.*, 1996). For the photography, a shutter speed of 1/8 second was used for Re = 100, 1/15 second for Re = 300, 1/30 second for Re = 600 and 1/60 second for Re = 900. The displacement signal from the pump was used to trigger the 35mm camera shutter at specific times in the cycle. The computer controlling the framegrabber synchronized the start of video capture with the pulsatile cycle by sending a TTL pulse to the computer controlling the pump. Video capture was controlled by a digital/input output board (DAS-16, MetraByte, U.K.). The video camera images were recorded in normal mode (images integrated for 40ms).

Three planes of view were studied: one parallel to the symmetry plane of the anastomosis (z=0 plane); the other two, orthogonal to the symmetry plane but parallel to the axes of the artery (y=0 plane) and vein (v=0 plane), respectively.

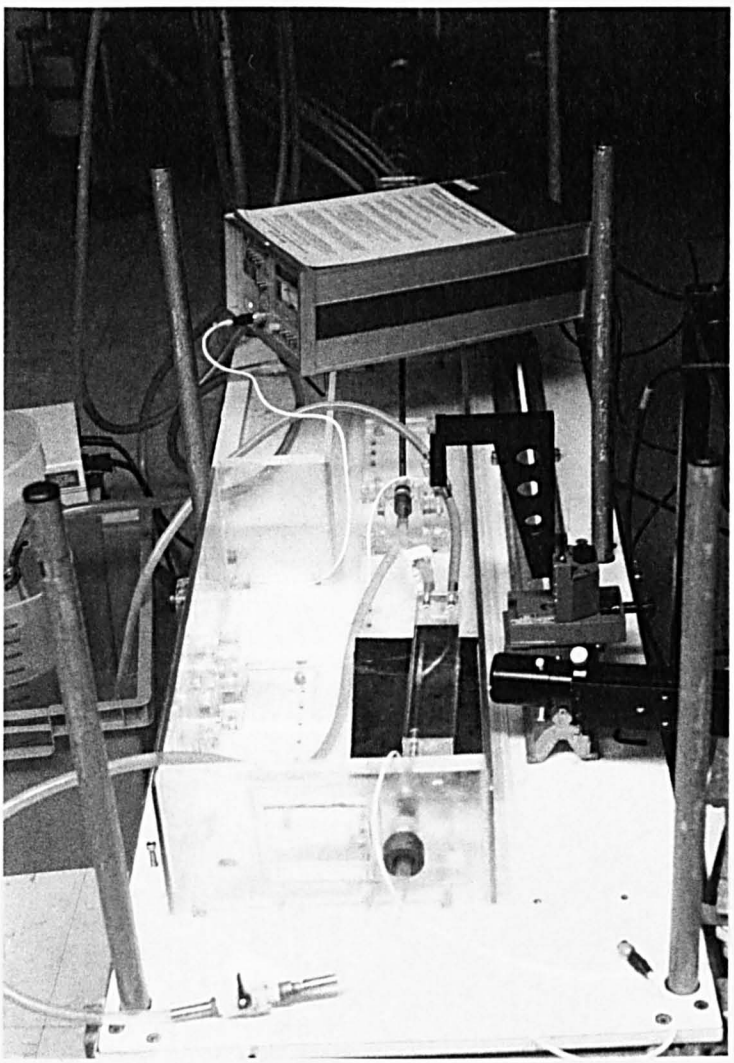

Figure 7.4 Photograph of the flow visualization set-up

7.3 RESULTS

7.3.1 The effects of varying Re in steady flow

Figures 7.5 and 7.6 show the transition from laminar flow (Re=100) with its ordered pathlines, to turbulent flow (Re=600) where flow at the anastomosis and in the vein (PV) is disturbed (Re=600 is the mean Reynolds number observed in

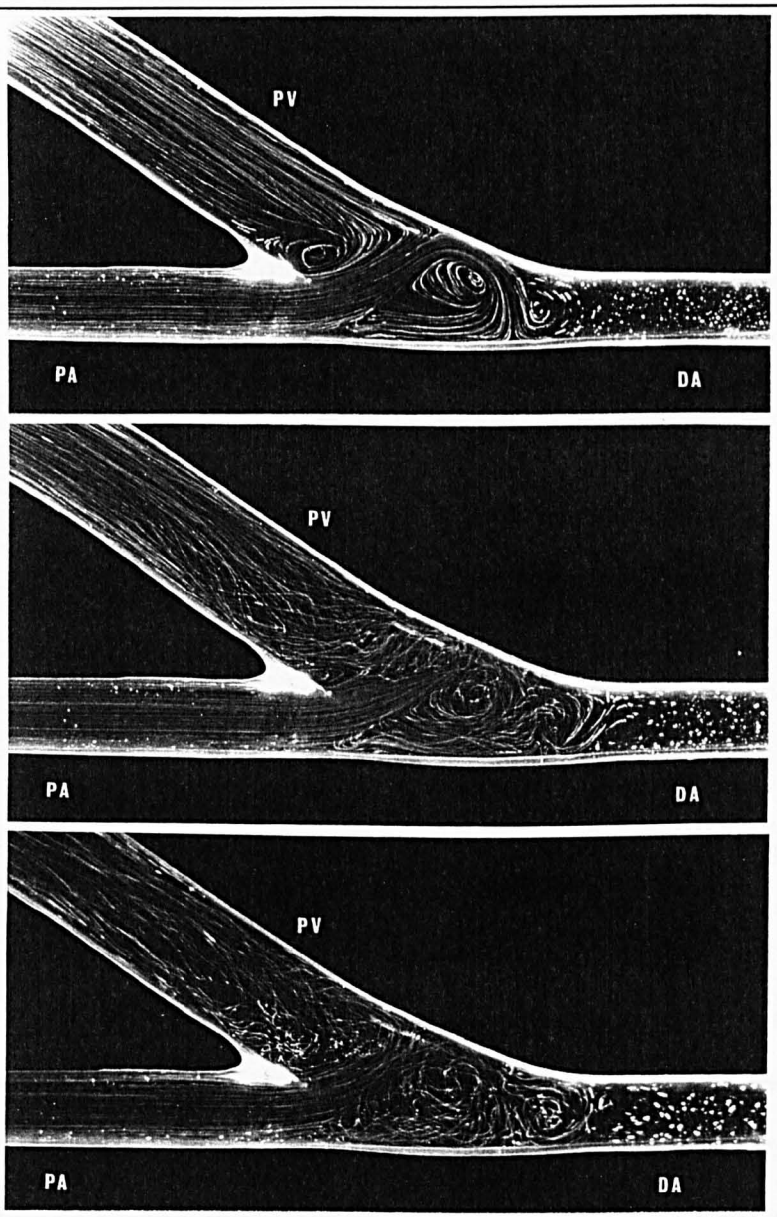

Figure 7.5 Flow patterns in steady flow (top, Re=100; middle, Re=300; bottom, Re=600)

patients). These figures show flow patterns obtained in steady flow with the distal artery (DA) occluded (in the 30° anastomotic angle model with a vein-to-artery diameter ratio of 1.6) and fistula flow supplied wholly by the proximal artery (PA). The large swirl seen on the floor of the anastomosis is caused by the acute change in direction of the mainstream as it enters the vein and the increase in cross-sectional area at the anastomosis. As Figure 7.6 shows, although this vortex is axisymmetric,

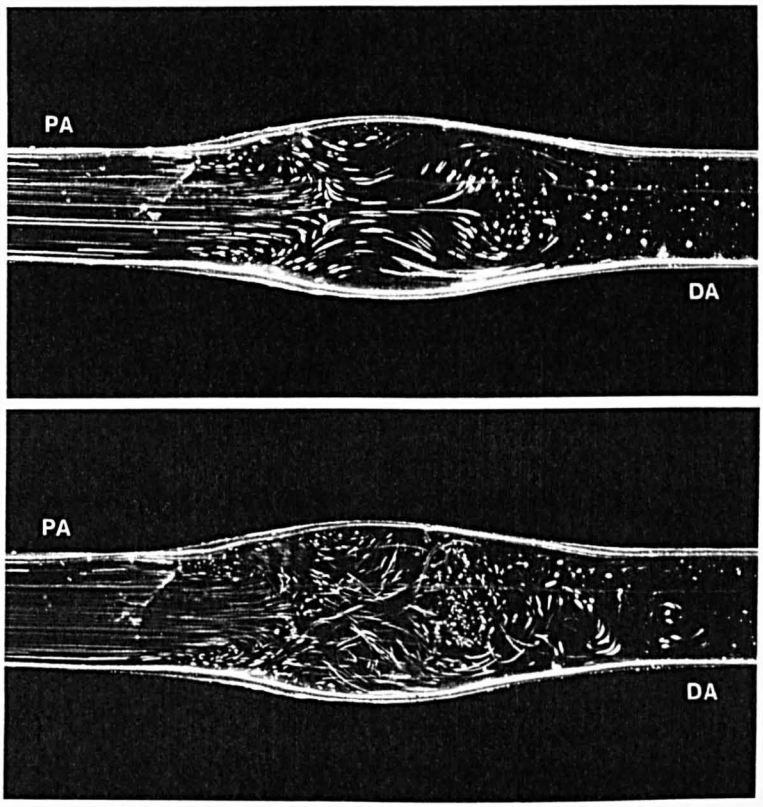

Figure 7.6 Flow patterns in steady flow (above, Re=100; below, Re=300) in y=0 plane

its axis curves towards the vein (probably due to the lower inertia of flow nearer the walls). Either side of this vortex are flow stagnation points (in Figure 7.6, where flow from the proximal artery begins to curl and the cluster of dots to the right of the anastomosis). As the artery expands at the anastomosis, recirculation regions form (Figure 7.6), bounded by the mainstream proximal flow and the wall at the heel of the anastomosis. A flow separation region is present at the artery-vein apical junction. Flow here trails in an anticlockwise helix into the bulk venous flow. As the flow rate increases, flow becomes more skewed towards the outer venous wall, secondary helical motion propagates along the vein and a train of counter-rotating vortices, driven by the one proximally adjacent, are seen in the distal artery. At the heel of the anastomosis, the separated region periodically sweeps backwards and forwards across the venous lumen. In the artery (Figure 7.6), the flow pattern goes

from being perfectly symmetrical about the plane of the anastomosis to being more chaotic at the anastomosis, under the influence of secondary currents.

7.3.2 Pulsatile flow

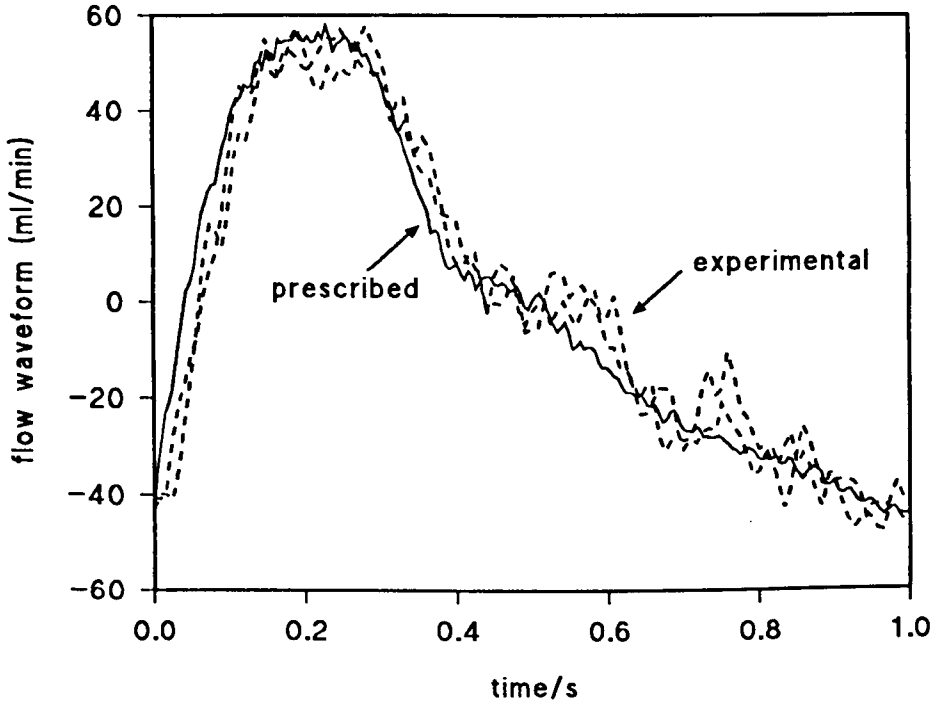

Figure 7.7 Two experimental flow waveforms (dashed lines) from the vein plotted against the clinical waveform (solid line)

Figure 7.7 shows the good agreement between the pulsatile waveform reproduced by the experimental system and the intraoperative waveform from which the pump displacement signal was derived. The experimental waveform shown has been obtained by averaging 32 cycles; a smoother waveform would have been exacted by averaging over a larger number of cycles to reduce the effects of random noise generated by the equipment and cables, and turbulent flow. Figure 7.8 shows the triggering of the camera shutter at 10 evenly spaced points in the cycle and the corresponding positions in the flow cycle.

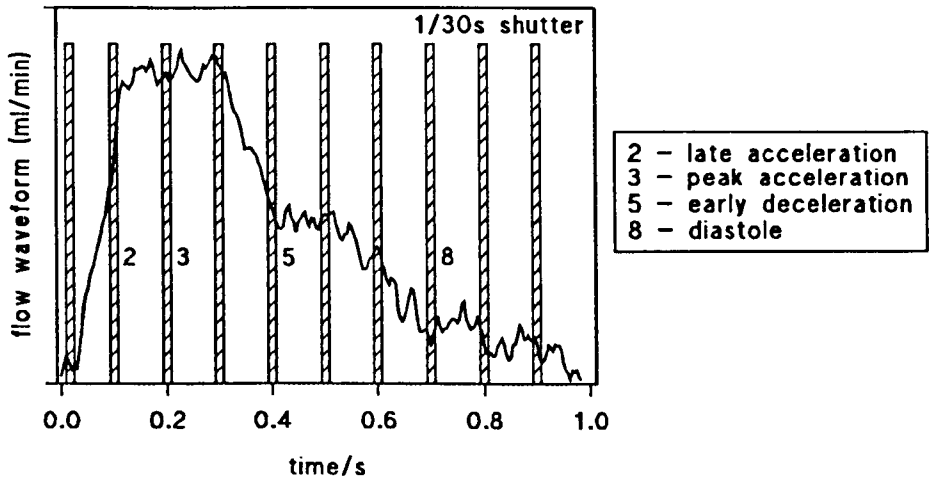

Figure 7.8 Triggering of the camera shutter in relation to the experimental flow cycle

Because of the low pulsatility of flow in the fistula (see Figure 7.9), there are few differences between the steady and pulsatile flow patterns (compare Figure 7.5 with Figure 7.10). The flow structures seen in pulsatile flow persist throughout the cardiac cycle (see Figures 7.11 and 7.12, showing flow patterns at 4 dynamically different points in the cycle, with the proximal artery supplying 75% of fistula flow and a mean Reynolds number of 600 - the typical flow condition in a patient). In pulsatile flow, the stagnation points and the size of the main vortex fluctuate and so the flow patterns in the artery are no longer perfectly symmetrical (Figure 7.12). There are also no appreciable differences in the observed flow patterns using the 1.0 or 1.6s period cycles (corresponding to α=4.7 and α=3). Therefore, the rest of this section is devoted to pulsatile flow (α=4.7).

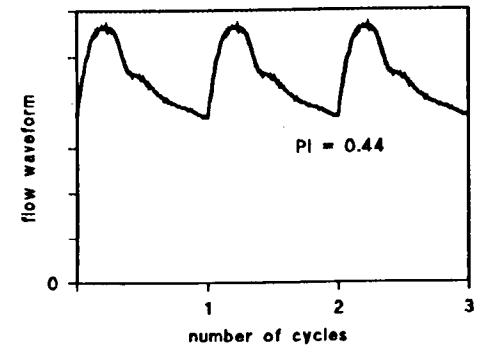

Figure 7.9 Venous flow waveform

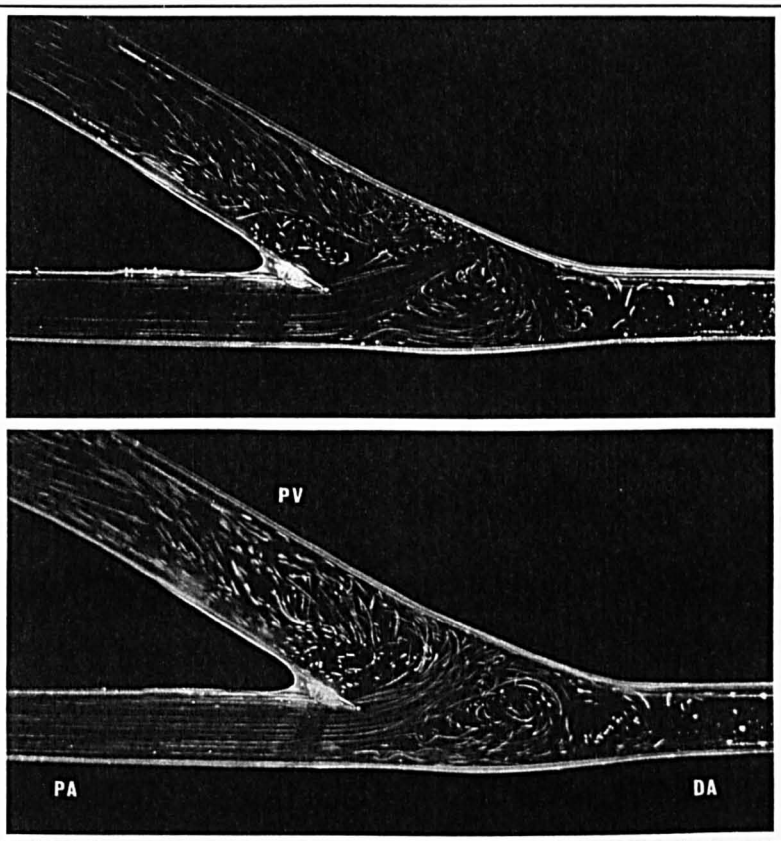

Figure 7.10 Flow patterns in pulsatile flow (above, Re=300; below, Re=600)

7.3.3 The effects of varying the flow distribution

The effects of varying the ratio of proximal to distal artery inflow into the vein are imperceptible upstream of the anastomosis (see Figure 7.13 showing pulsatile flow at a mean Reynolds number of 600). The main differences lie in the location of the vortices and the union of proximal and distal arterial flow at the anastomosis. The large vortex on the floor of the artery serves as a mixing phenomenon. However, when there is an equal contribution from the proximal and distal artery, this vortex disappears, small transient vortices (rotating both towards and away from the union) form and decay at the union, and flow at the toe of the anastomosis is thrust vertically before it joins the mainstream. This is another feature of the expansion of the artery cross-section at the anastomosis; a small recirculation region is also apparent at the anastomotic toe when distal arterial inflow is 25% of

venous flow. Also, as distal arterial inflow increases to 25% of fistula flow, the vortex appears more rounded and moves away from the arterial floor. Secondary flow components in the vein seem to diminish when there is no flow through the proximal artery (in this case, a more gentle flow progression into the vein). Even in the case of antegrade flow in the distal artery, the flow at the anastomosis follows the same general pattern, with part of the proximal arterial flow being drawn into the large vortex on the floor of the anastomosis and being shed into the distal artery in a helical swirl (see Figure 7.14). As a result, the vortex is more elongated and spans the whole length of the anastomosis (compare with Figure 7.5). A horseshoe vortex (at a Reynolds number of 100) caused by recirculation at the heel of the anastomosis emanates into the vein. In Figure 7.14, fistula flow is three times distal artery flow.

7.3.4 The effects of varying the anastomotic angle

Flow visualization in the models with different anastomotic angles revealed a similar picture: the flow features apparent in the 30° model mirrored those seen in the 50° and 70° models (see Figure 7.15). However, flow into the vein was much more disturbed (or the disturbance propagated further into the vein) in the case of the 30° model because of the greater deviation of flow into the vein from the proximal artery. Figure 7.15 represents the typical patient case: a mean Reynolds number of 600 and the proximal artery supplying 75% of fistula flow. As the distal artery flow contribution increases in the 50° (Figure 7.16) and 70° models (Figure 7.17), disturbances in the vein become greater with increasing anastomotic angle. In this case, the flow from the distal artery, the larger portion of venous inflow, undergoes less of a deviation into the 30° vein. When there is equal venous inflow from the proximal and distal arteries, fistula flow in the 50° anastomosis model seems least disturbed and secondary velocity components in the vein appear substantially reduced.

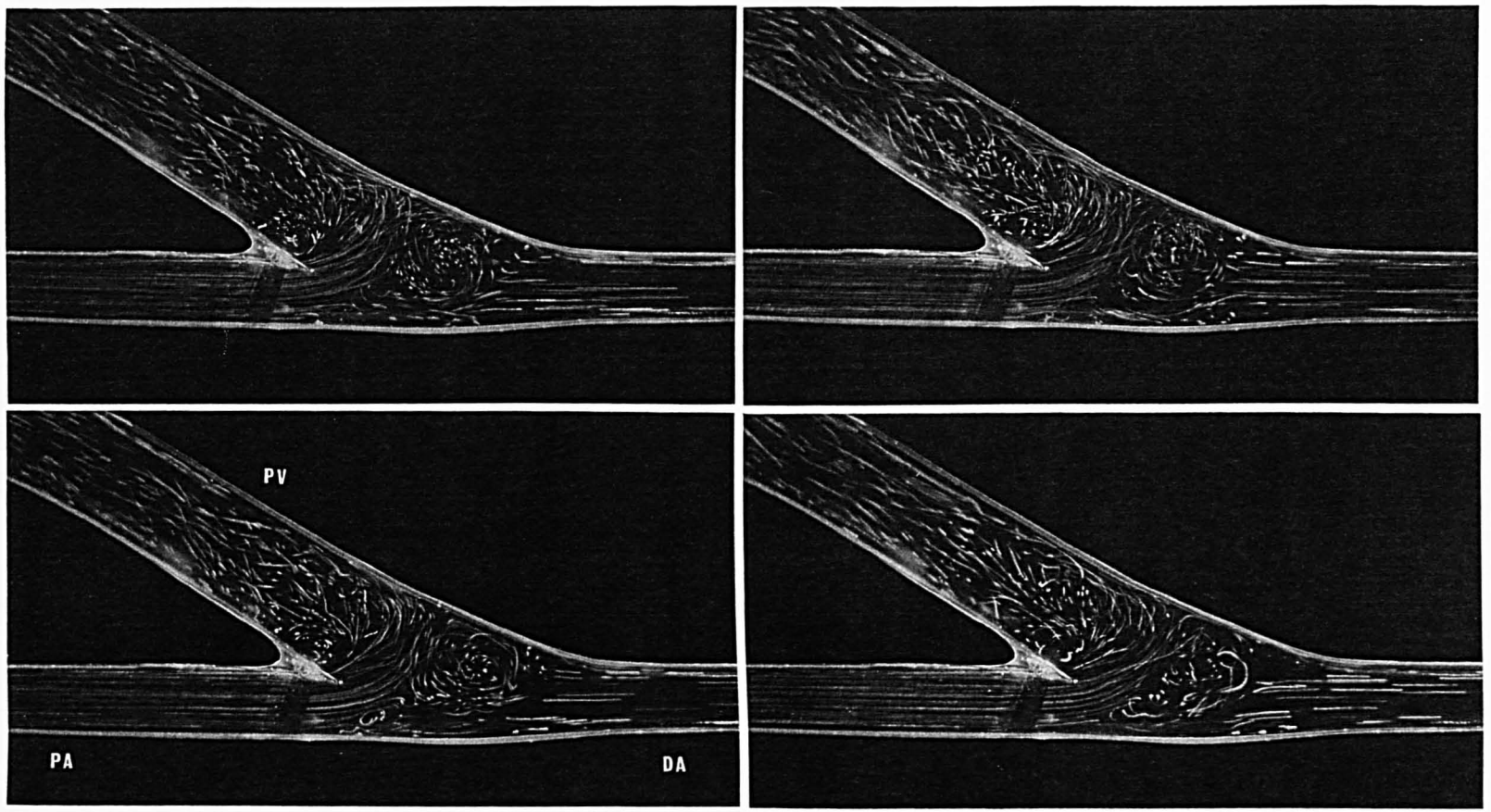

Figure 7.11 Flow patterns at points 2, 3, 5 and 8 in the pulsatile cycle (Re=600, and fistula flow = 75% PA and 25% DA flow)

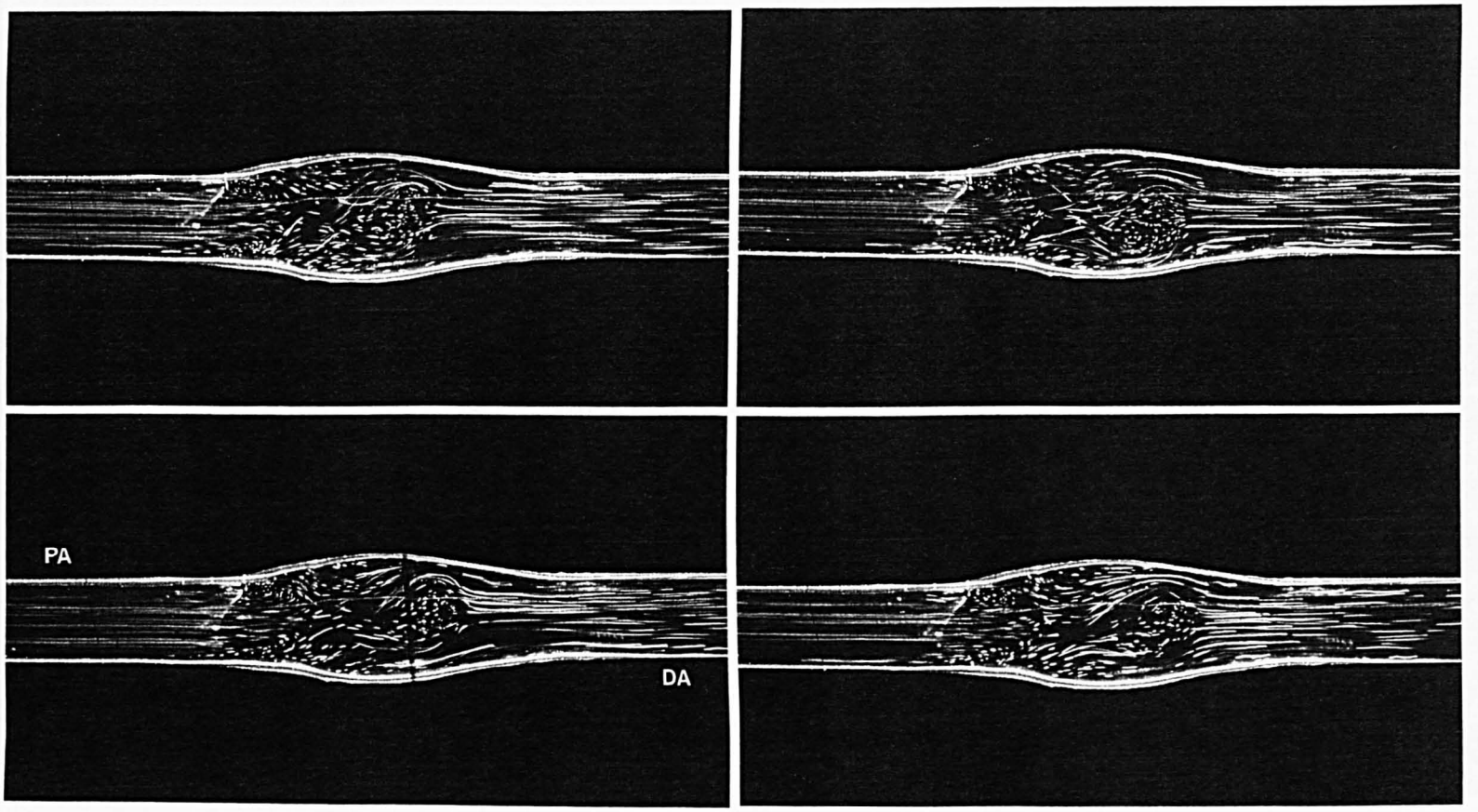

Figure 7.12 Flow patterns at points 2, 3, 5 and 8 in the pulsatile cycle (same flow conditions as in Figure 7.10) in the y=0 plane

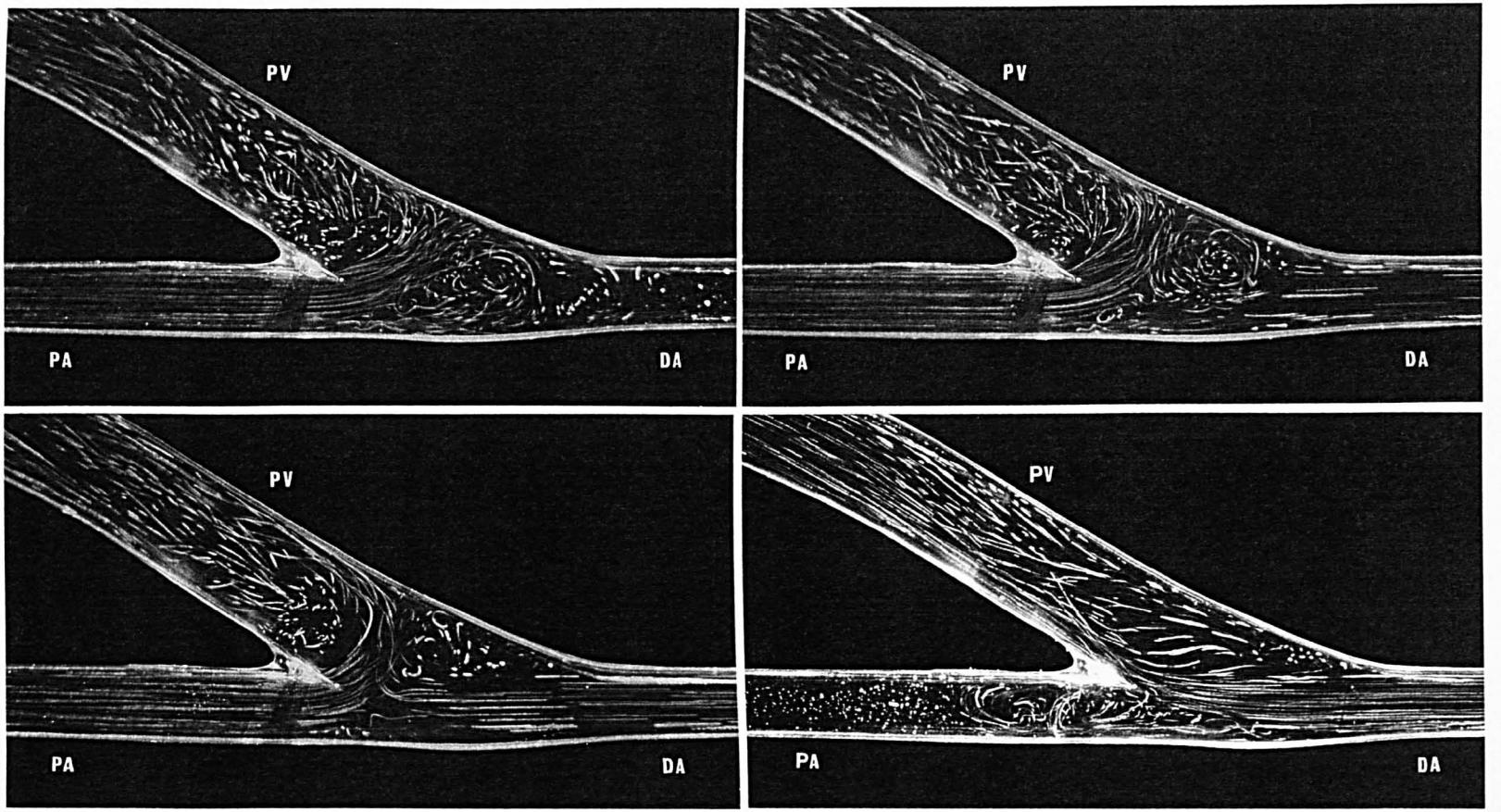

Figure 7.13 Pulsatile flow patterns with different flow distributions in the 30° model (Re=600; top left, DA occluded; right, 75% PA and 25% DA flow in vein; bottom left, equal PA and DA flows in vein; right, PA occluded)

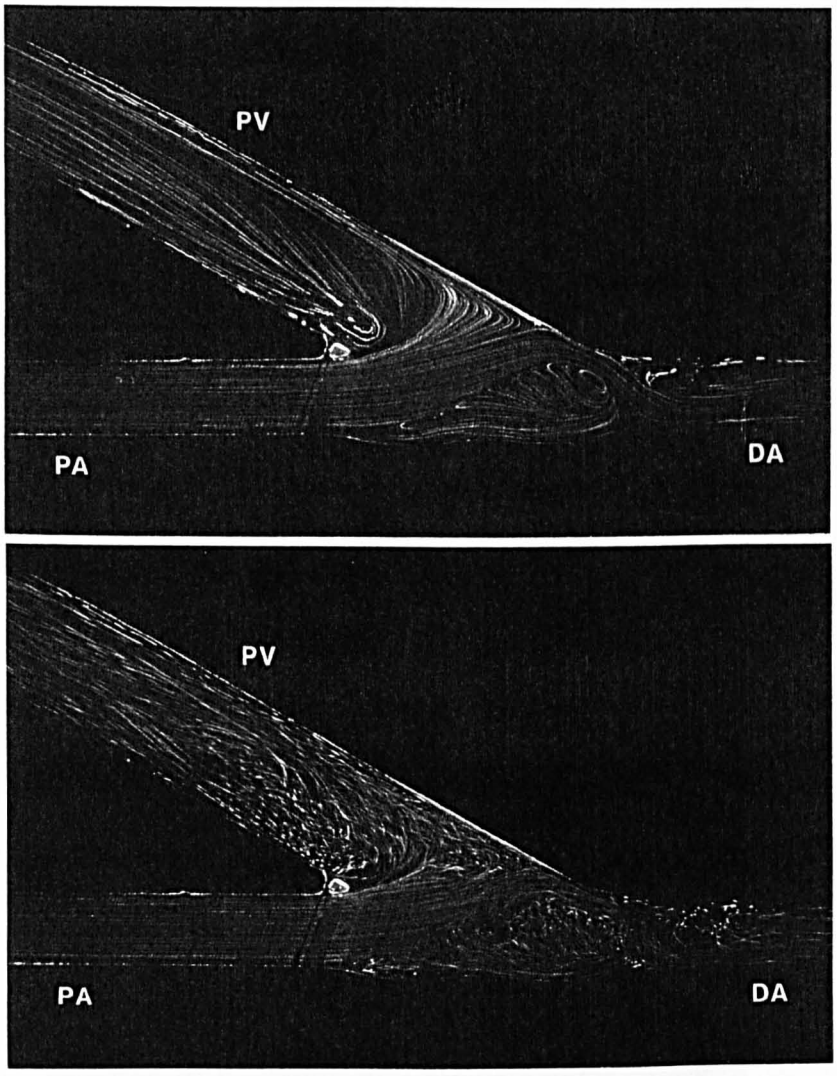

Figure 7.14 Flow patterns when distal artery flow is antegrade (above, Re=100; below, Re=600)

For this flow distribution very slow moving particles are seen recirculating in a small region on the floor of the artery. A similar region, smaller in area, is also seen in the corresponding flow patterns for the 70° anastomosis model. Additional helical components are superimposed on the more proximal axial flow in the vein by its curvature; although, it is difficult to perceive differences between these models or varying flow distributions (at the maximum Reynolds number of 900 investigated).

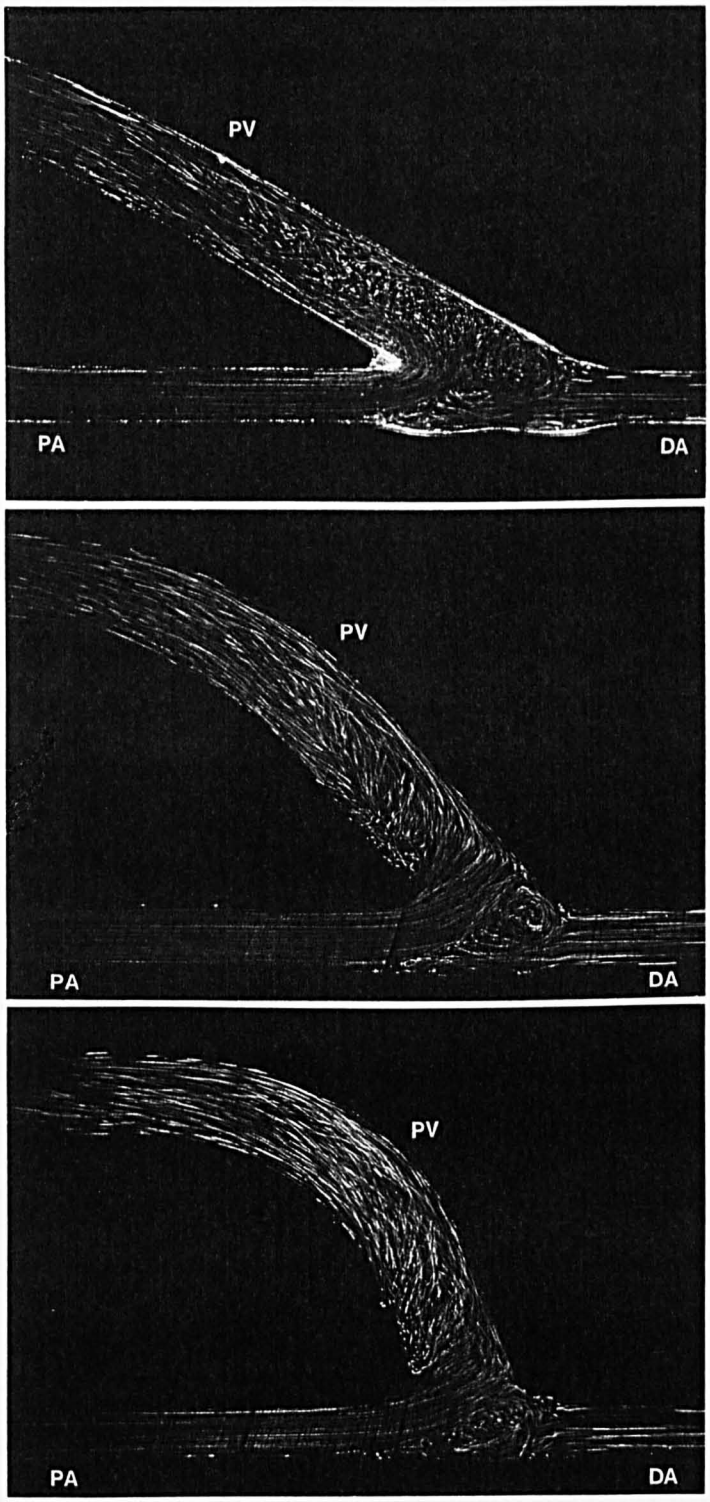

Figure 7.15 Comparative pulsatile flow patterns in the 30°, 50° and 70° anastomosis fistula models (Re=600)

7.3.5 The effects of varying the vein-to-artery diameter ratio

Due to the lower flow rates needed to achieve the same Reynolds number in a smaller vein, the flow patterns in the 0.8 vein-to-artery diameter ratio model (Figure 7.18) are much more ordered than those in the previous figures. The critical numbers for the transition to turbulence in this model would, therefore, be much higher than in the other models. However, flow at the entrance to the vein does appear more disturbed when there is no flow in the distal artery and least disturbed when the proximal artery is occluded. This point is more pronounced in this set of flow patterns than those in Figure 7.13, also with a 30° anastomotic angle. The rounding of the main vortex and its movement away from the arterial floor, as distal arterial flow increases to 25% of fistula flow, is also more apparent in the 0.8 diameter ratio model than the 1.6 model. As the diameter of the vein increases, in the 1.25 diameter ratio model (Figure 7.19), the flow patterns begin to mirror the more disturbed state of the 1.6 diameter ratio model. It is no longer easy to qualify differences in the level of turbulence between the four flow distributions. The flow rates increase again in the 2.0 diameter ratio model for the same Reynolds number. Figure 7.20 shows the increased level of turbulence in this larger vein for all four flow distributions. The most noticeable difference in this set of flow patterns is the shifting of the main vortex in the top left flow pattern (representing distal artery occlusion) towards the distal artery. The mainstream in this case undergoes a more dramatic change in direction as it skews towards the outer wall of the vein at the anastomosis, creating a number of vortices along the suture line (an extension of the elongated recirculation region at the heel of the anastomosis seen at lower Reynolds numbers) that shed and produce a mixture of interfering secondary and tertiary velocity components in the vein. Although the wider anastomosis would also affect the flow patterns at the anastomosis in the other three flow distributions, this effect does not appear to be obvious. The three flow patterns appear largely similar to the corresponding flow patterns in the models with smaller veins but the main flow

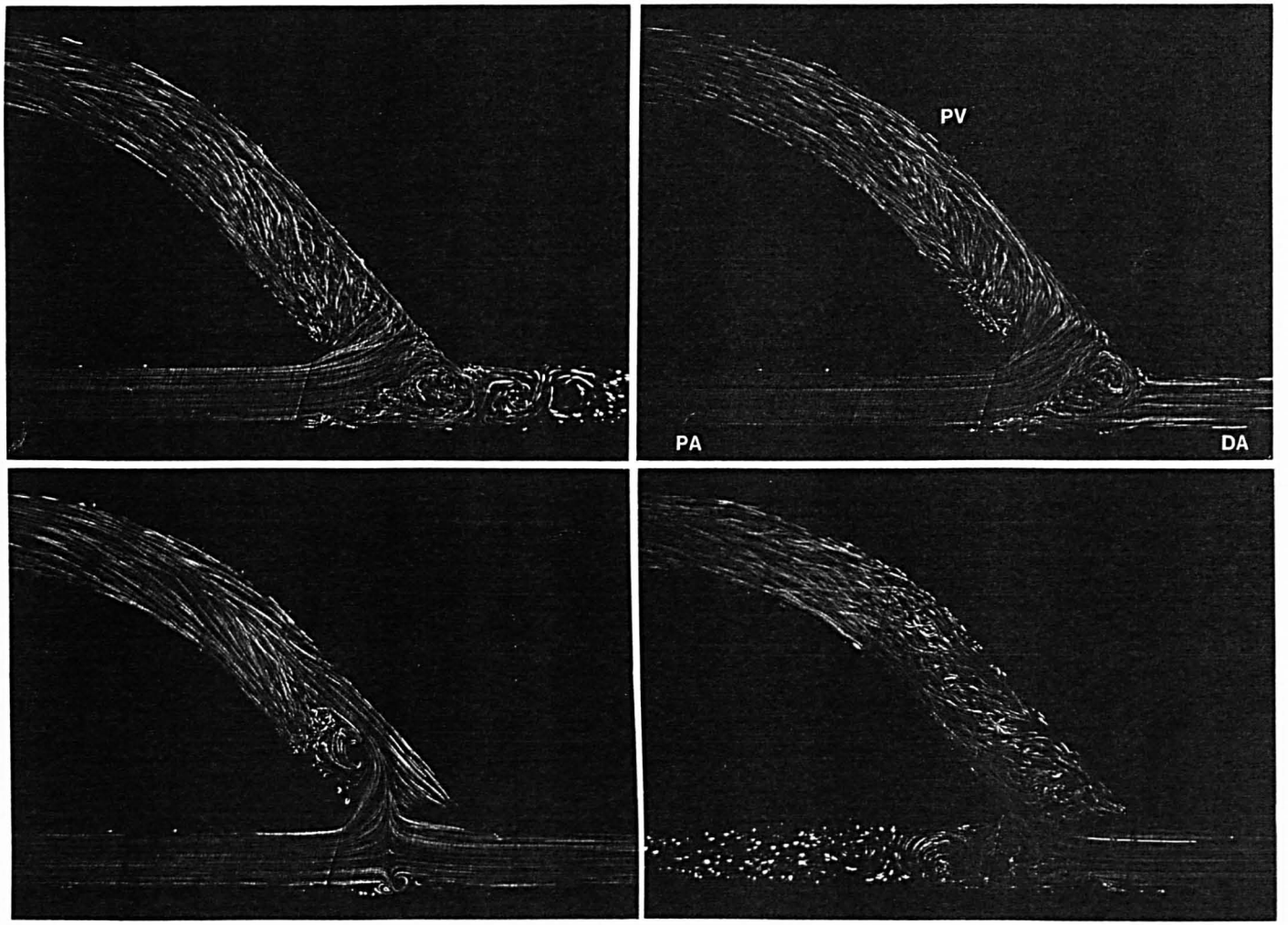

Figure 7.16 Pulsatile flow patterns with different flow distributions in the 50° model (Re=600; top left, DA occluded; right, 75% PA and 25% DA flow in vein; bottom left, equal PA and DA flows in vein; right, PA occluded)

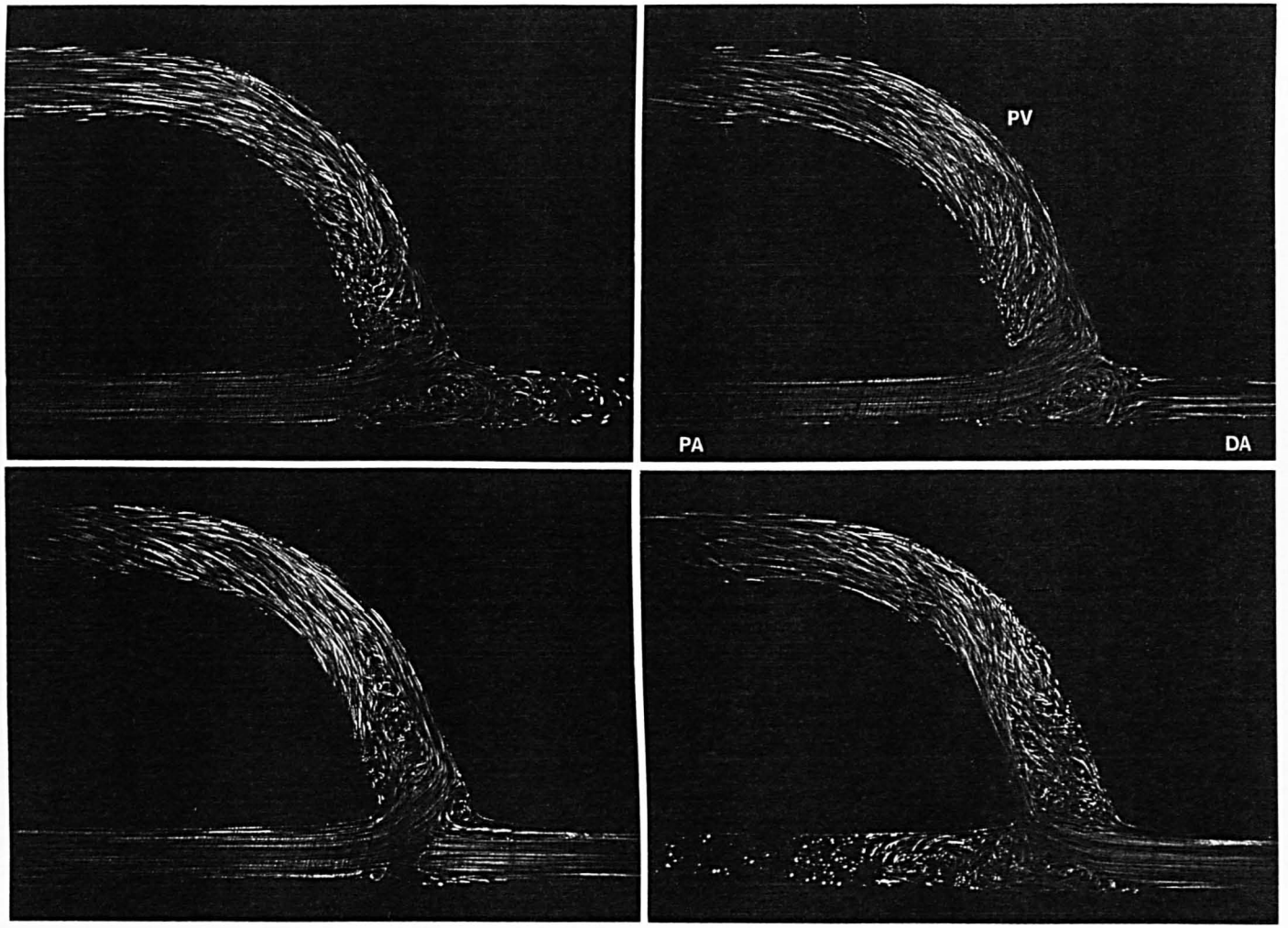

Figure 7.17 Pulsatile flow patterns with different flow distributions in the 70° model (Re=600; top left, DA occluded; right, 75% PA and 25% DA flow in vein; bottom left, equal PA and DA flows in vein; right, PA occluded)

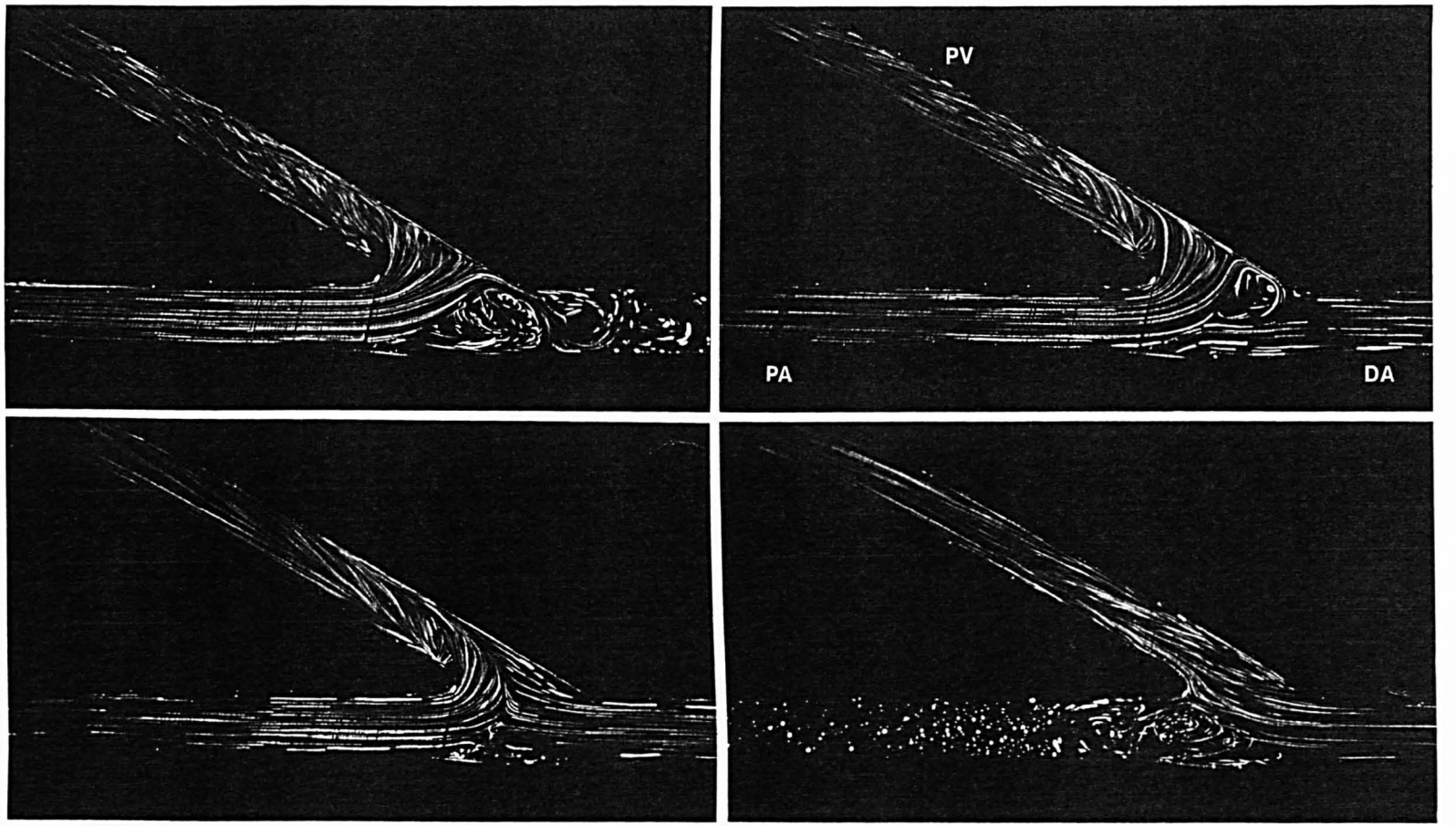

Figure 7.18 Pulsatile flow patterns with different flow distributions in the 0.8 diameter ratio model (Re=600; top left, DA occluded; right, 75% PA & 25% DA flow in vein; bottom left, equal PA & DA flows in vein; right, PA occluded

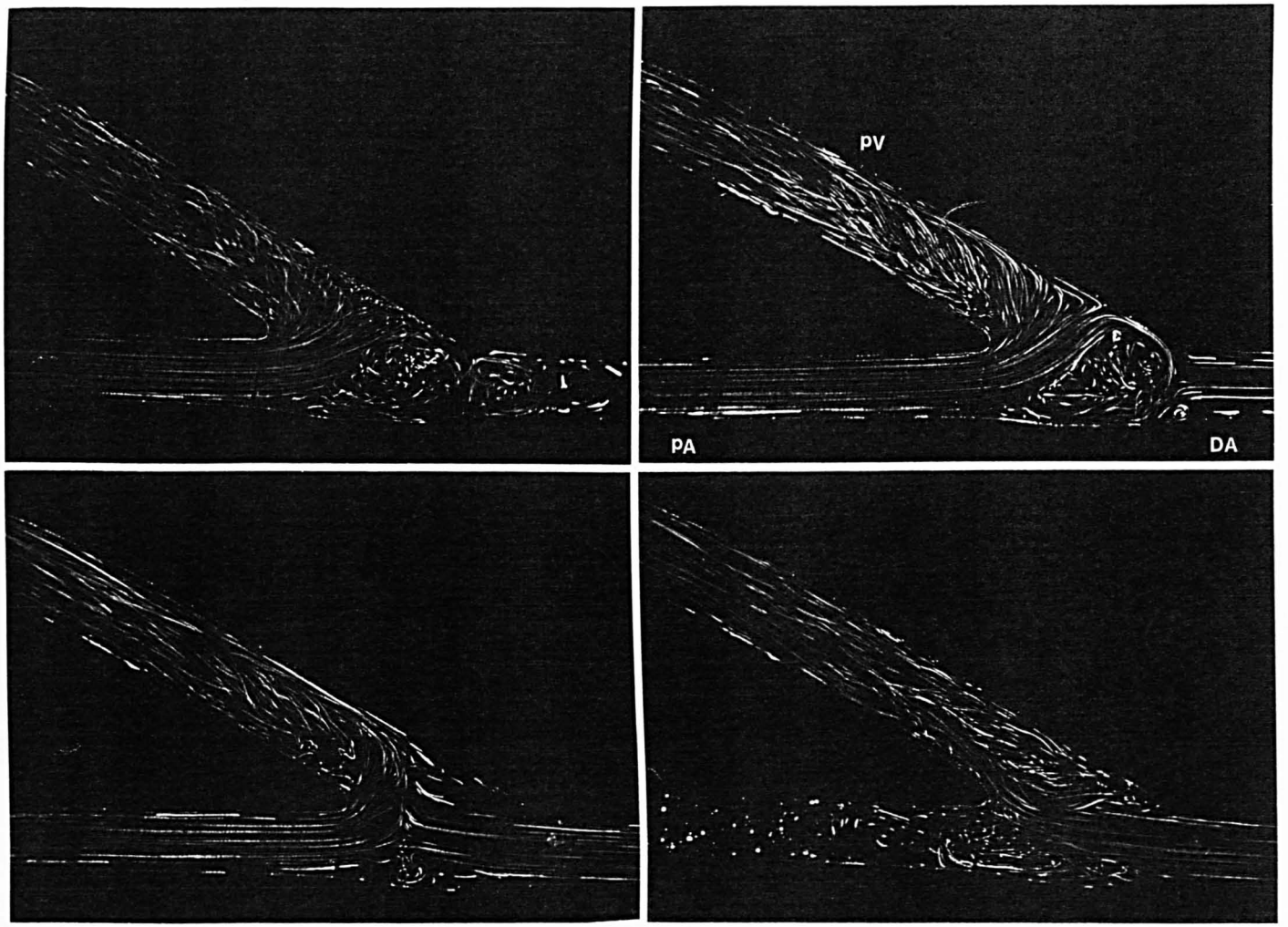

Figure 7.19 Pulsatile flow patterns with different flow distributions in the 1.25 diameter ratio model (Re=600; top left, DA occluded; right, 75% PA & 25% DA flow in vein; bottom left, equal PA & DA flows in vein; right, PA occluded

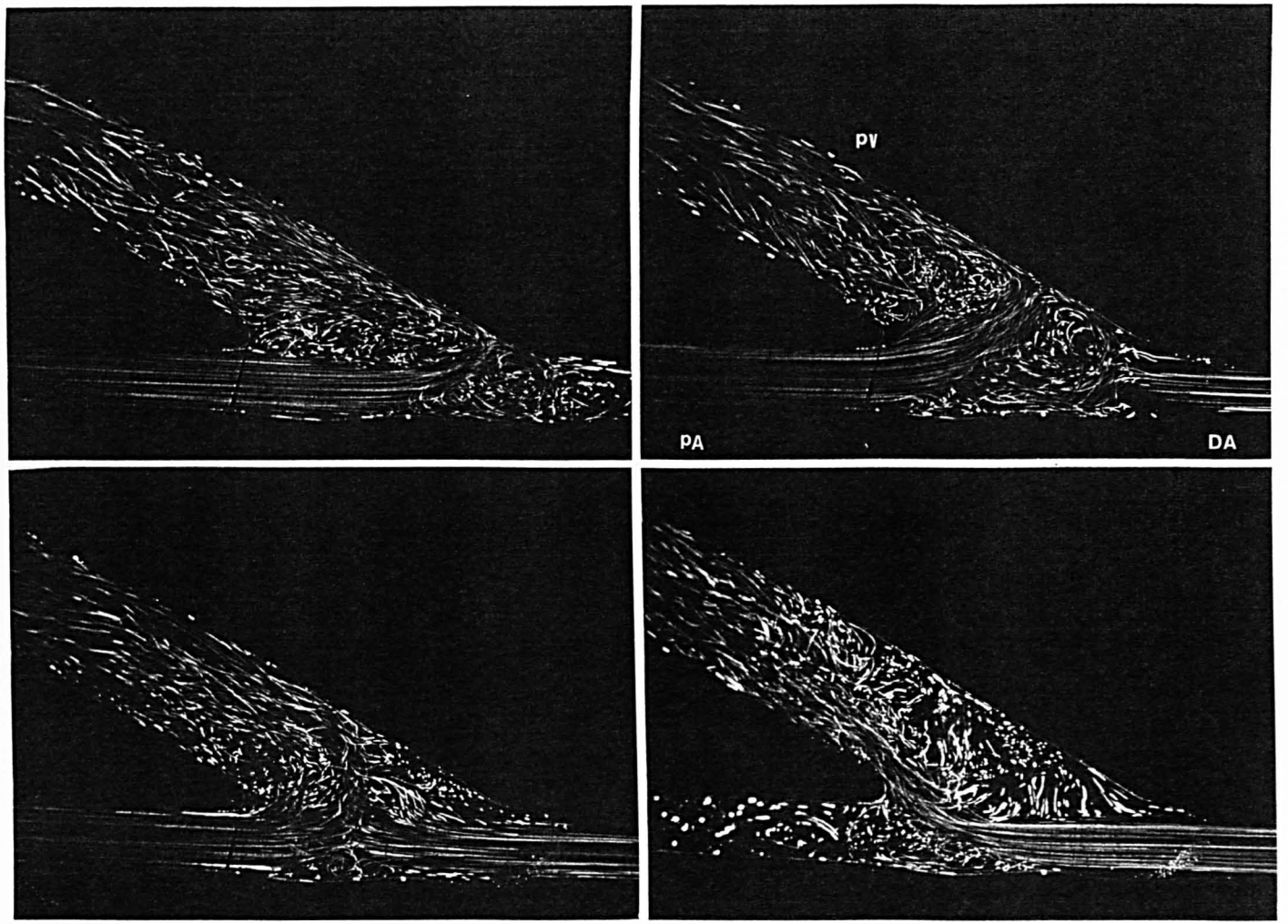

Figure 7.20 Pulsatile flow patterns with different flow distributions in the 2.0 diameter ratio model (Re=600; top left, DA occluded; right, 75% PA & 25% DA flow in vein; bottom left, equal PA & DA flows in vein; right, PA occluded)

features seem to occupy a larger area and, as a result, appear more irregular and unstable. As the Reynolds number is increased to 900, the flow patterns for the top right flow distribution undergoes a similar transformation to the 100% proximal flow pattern at a Reynolds number of 600 (see Figure 7.21). Here the main vortex seems to have been replaced by a number of transient vortices along the union. It is evident for the higher Reynolds number that flow further along the vein is more disturbed in the 100% proximal flow pattern than in any of the other flow distributions, mimicking the trend seen in the 0.8 diameter ratio model.

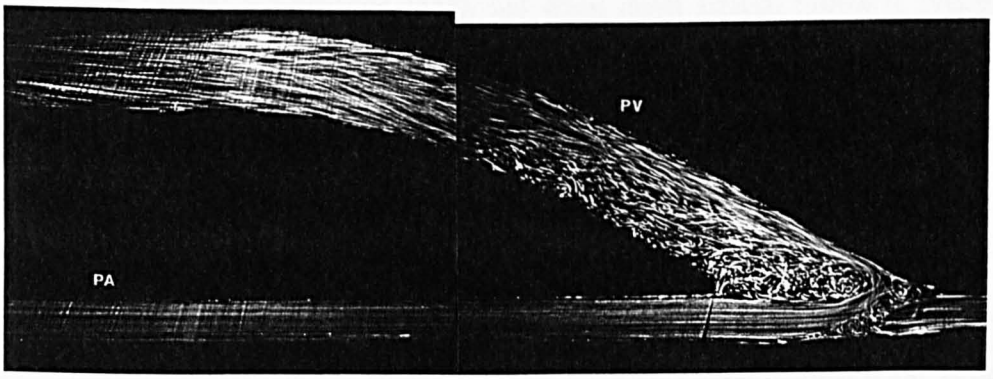

Figure 7.21 Pulsatile flow patterns in the 2.0 vein-to-artery diameter ratio model at Re=900 with PA flow equal to 75% of fistula flow

7.4 DISCUSSION

This *in vitro* study makes no effort to model the compliance of the vessels of an arteriovenous fistula. However, silicone rubber does have limited compliance and this factor obviously introduces an unknown element in the analysis and questions the validity of the results. Compliance has been regarded as a secondary consideration to the effects of haemodynamics throughout the planning strategy of these experiments. Care has been taken to ensure that the desired flow waveform in the vein has been accurately reproduced and that all the necessary clinical flow parameters have been satisfied.

There is little qualitative difference between the steady and pulsatile flow

patterns seen in the models. There also appears to be no appreciable difference between the two Womersley parameters used in the pulsatile flow experiments. Differences in varying the proximal and distal artery flow contributions are largely confined to the location of the stagnation points and vortices. The flow patterns are essentially the same in all the six models. Differences in the size of the vein govern the flow rate through the model and the level of flow disturbance at the anastomosis. Anastomotic flow disturbances also varied with anastomotic angle: when proximal arterial flow dominates distal arterial flow, there is a greater deviation of flow into the vein with smaller anastomotic angle, but when distal arterial inflow is greater than proximal, the deviation of the mainstream into the vein is greater with larger anastomotic angles; the deviation of the mainstream appear to correlate with the level of flow disturbance at the anastomosis and its propagation along the vein.

Turbulence appears to be the dominant feature in the model vein for Reynolds numbers within the normal range seen in patients. Turbulence is a feature in AV fistulae despite the fact that the Reynolds numbers encountered clinically are much lower than the critical Reynolds number for turbulence in a straight tube. This is largely due to the acute deviation of flow into the vein. The elevated shear stresses inherent in turbulent flow may damage endothelial cells and initiate cell proliferation. The large vortex seen on the floor of the anastomosis, at the union of proximal and distal arterial flow was a stable structure associated with high residence times of mitogens and chemoattractants; this may be a factor in stenosis. Also, at the union of proximal and distal arterial flow, there may be high spatial and temporal shear stress gradients caused by the continual shifting of this stagnation point over the cardiac cycle. The curvature of the vein introduces additional secondary flow components. The changes in the flow profile at the curvature of the vein and the interaction with the helical components propagating from the anastomosis have not been apparent from the results of flow visualization. The location of maximum axial

velocity would be expected to move towards the outer wall of the bend, lowering wall shear on the inner wall. Transport of accumulated lipids across the wall into the blood in this low shear region may be inhibited - a precursor to atherosclerosis.

Vessel dilatation as the fistula matures has not been ignored. The change in the haemodynamics of the fistula over time is intended to be represented by evaluation of the series of models with increasing vein diameters (as the mean vein-to-artery diameter ratio appears to increase with time, Section 5.2). From the analysis of these flow patterns, it appears that as the fistula matures, the level of turbulence in the vein may increase and propagate further from the anastomosis.

Flow visualization on its own cannot provide a full understanding of the haemodynamics in the fistula models. Although a number of inferences may be made regarding differences in the pertinent flow features in the different models and flow distributions, quantitative measurements are required to provide substantiative evidence to corroborate any possible theories. To this end, the results from flow visualization enable us to limit the number of quantitative measurements required (as these measurements are time-consuming) and define regions of interest and the necessary incremental positions (see Section 7.5).

7.5 SUMMARY

The main factors influencing the flow patterns observed in the fistula models were Reynolds number in the vein, diameter of the vein and flow distribution into the vein from the proximal and distal arteries. Anastomotic angle affected the flow patterns to a much lesser extent but did govern the level and propagation of flow disturbances at the anastomosis and further along the vein.

The flow patterns depart from laminar flow with its regular pathlines at Reynolds numbers around 300, and by a Reynolds number of 600, the patient mean, flow in the vein is very disturbed. The critical Reynolds number for turbulence in the vein is, however, governed by the diameter of the vein. It appears to be larger for the smaller model veins in which the flow rates are reduced for the same Reynolds number.

As the fistula matures and the vein-to-artery diameter ratio increases, it would appear that the flow disturbances at the anastomosis increase and propagate further into the vein. The increase in Reynolds number that may also occur over time would also enhance this trend.

The general pattern as the flow distribution into the fistula is altered remains essentially the same. Differences are largely confined to the anastomotic region. For almost all flow distributions (except the case when proximal and distal artery inflow is equal), there is a large vortex on the floor of the artery incorporating proximal and distal arterial flows. This vortex appears to be a stationary feature throughout the cardiac cycle (though, obviously, there are translational shifts in the locations of stagnation points depending on the proportions of proximal and distal arterial flow). When proximal and distal arterial flows into the vein are equal, transient vortices are seen to rapidly form and decay along the union. Also at the toe of the anastomosis, in this particular case, there is flow out of the plane of the anastomosis.

The effects of anastomotic angle depend on the flow distribution in the

fistulous vessels. When there is a larger proportion of venous inflow from the proximal artery, the flow disturbances seem more pronounced in the models with smaller anastomotic angle; when the distal artery supplies more of the fistula flow, the reverse is true. This phenomenon appears to be associated with the deviation of the majority flow as it enters the vein.

Stenoses in patients develop at the anastomotic junction and along the vein. Flow visualization showed that flow disturbances were confined to the region of the anastomosis and the segment of the vein just proximal to the anastomosis. The vortices seen at the anastomosis suggest that measurements of temporal wall shear stress all along the floor of the artery (1mm increments near the centre of the anastomosis, 2mm increments away from the centre and 5mm increments away from the anastomosis to a distance of 20mm proximal and distal to the centre of the anastomosis) are necessary. Two-dimensional turbulence measurements in the vein are also necessary but measurements along the centreline (2mm increments near the anastomosis and then 4mm increments to a distance of approximately 70mm) and across the vessel lumen at 5 representative points along the vein would be sufficient to sufficiently characterize the turbulence distribution. The measurements along the centreline and across the vessel lumen could also provide velocity profiles/distributions and Reynolds shear stress calculations.

CHAPTER 8

QUANTITATIVE FLOW MEASUREMENTS IN MODELS OF END VEIN-TO-SIDE ARTERY FISTULAE

QUANTITATIVE FLOW MEASUREMENTS IN MODELS OF END VEIN-TO-SIDE ARTERY FISTULAE

8.1 INTRODUCTION

The information that can be derived from flow visualization, as described in the previous chapter, is of a qualitative nature. Although this technique can chart particle pathlines, classify flow as laminar or turbulent and highlight regions of flow separation, quantitative measurements are still necessary to characterize the effects of the particular flow features visualized on the vessel walls themselves. Quantitative measurement can be time consuming, and so flow visualization enables us to first define regions of fluid mechanical interest. Laser Doppler anemometry has been used as an adjunct to flow visualization, to obtain quantitative measurements of velocity, shear stress and turbulence in *in vitro* models of the cardiovascular system (Bharadvaj, Mabon and Giddens, 1982; Shu, Noon and Hwang, 1987; Naiki, Hayashi and Takemura, 1995) for some time. It is an accurate method for making repeatable non-invasive velocity measurements in both steady and pulsatile flows.

8.2 PRINCIPLES OF LASER DOPPLER ANEMOMETRY

The basic principle governing the operation of the laser Doppler anemometer (LDA) is the Doppler effect: light scattered from a moving particle travelling across a laser beam undergoes a frequency shift dependent on the observer-to-particle trajectory angle and the velocity of the particle. As the frequency of light waves is approximately 6×10^{14} Hz, the Doppler shift is much too small to be measured by even the fastest detectors and electronics. This problem is eliminated by splitting the laser beam (of wavelength λ) and letting the two coherent beams cross each other at a specific angle (Θ). The volume of their intersection defines the sample volume for

velocity measurement. A photodetector collects light scattered from both beams by particles traversing this volume. At the photodetector the two slightly differing frequencies from the moving particle interfere (heterodyne) to produce a much lower frequency (f_{burst}) due to the particle motion across the sample volume (directly proportional to the particle velocity component perpendicular to the fringes, v_x).

$$f_{burst} = \frac{2v_x \sin\theta/2}{\lambda}$$

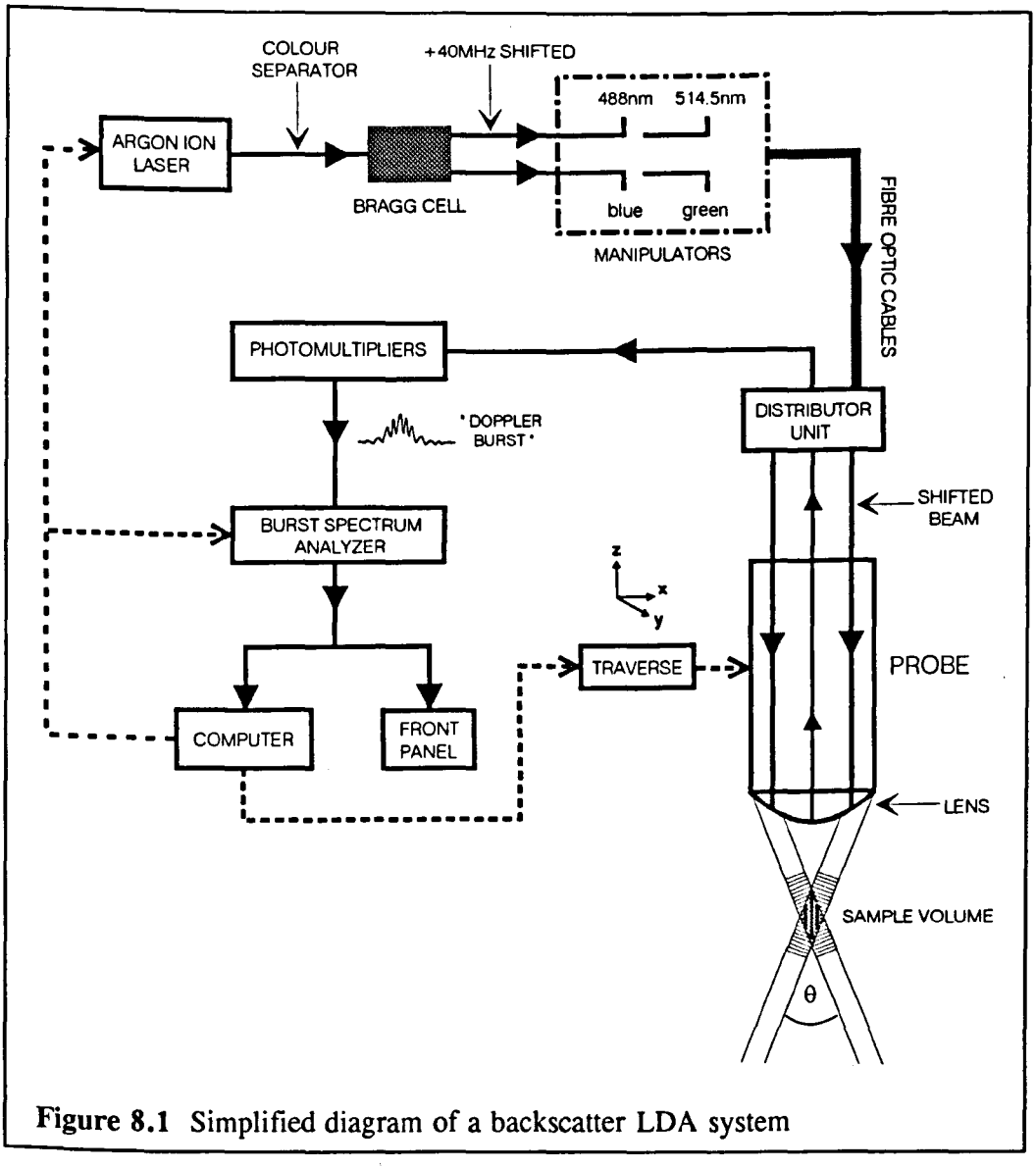

Figure 8.1 Simplified diagram of a backscatter LDA system

If the laser beams intersect at their beam waists, the wavefronts are virtually planar; this ensures a uniform velocity-frequency relationship over the entire intersection volume. However, the Doppler frequency shift in this arrangement does not distinguish between positive and negative velocities of the same magnitude. This problem has been overcome by frequency shifting one of the laser beams slightly. In this configuration, a stationary particle would produce interference at the shift frequency, and a moving particle would either increase or decrease this frequency, depending on its direction. Using frequency shifting, a greater spread of velocities within a particle population can be measured; this is important when measuring large relative fluctuations and turbulence. Optical frequency shifting (for example, with a Bragg cell) also enables complete separation of Doppler spectrum and the burst pedestal as this technique affects only the Doppler spectrum. The Doppler signal can then be easily filtered out.

The two beam LDA system measures only one component of velocity. To make 2- or 3-dimensional measurements of velocity, another pair or two pairs of laser beams must intersect at the same point in other planes. Signal processing is carried out on each velocity component. Logic gates can be applied to the burst detector signals from the separate processors to enable coincidence filtering.

Spectral analysis of the Doppler bursts is performed by the Burst Spectrum Analyzer (BSA). The frequency of the Doppler signal is obtained by converting the time signal into the frequency domain by applying a discrete Fast Fourier Transform (FFT). The whole signal is used in the analysis, as a result, the processor is able to extract Doppler frequencies from very noisy signals. The input signal is first bandpass filtered and then taken to a mixer unit which mixes the signal with the user preset centre frequency and shifts the signal downwards. The signal, represented in complex numbers (so that signal processing can be performed at half the sampling rate and still fulfil the Nyquist criterion), is low-pass filtered and then digitized. The

burst detector ensures that only signals satisfying certain criteria pass on to the FFT processor, to be sampled (at a sampling rate of 1.5 times the selected bandwidth). The post processor estimates the Doppler frequency from a parabolic fit of the measured spectrum. The measurement is rejected if there is no valid spectral peak i.e. if the ratio between the two largest local maxima in the frequency spectrum is less than 4. The Doppler frequencies/velocities of accepted measurements together with the respective arrival time of the particle into the measuring volume and its transit time through the volume are sent to the output buffer. The BSA has a maximum bandwidth of 32MHz and can cope with maximum data rates in excess of 1MHz.

Figure 8.1 shows a diagram of the LDA system utilized for quantitative measurement.

8.3 REFRACTIVE INDEX MISMATCH

The problem common to all optical measurement techniques is refraction of light passing through gas-solid or liquid-solid interfaces at the model and the vessel walls. With the LDA, this can lead to displacement and distortion of the measuring volume and misalignment of the laser beams. The fistula models described in Chapter 6 have flat surfaces. These have the advantages of not affecting the Doppler frequency and allowing for wall motion (although both the location and size of the measuring volume will be changed). Thus, when the optical axis is perpendicular to the faces of the models, the air-solid refraction errors can be ignored. To eliminate solid-liquid refraction problems at the curved vessel walls, the most effective method is to match the refractive indices of the model and the blood analogue fluid. It is possible to devise equations to correct for refraction errors, using Snell's law and the geometrical theorems, but this can be a laborious process with complex variable interactions away from the centreline. Another disadvantage with this method is that

the distortion is most apparent near to the vessel walls and may, therefore, affect the determination of wall shear stress.

The refractive index of a thin flat sample of the Sylgard 184 silicone rubber used to make the fistula models was measured using a refractometer (Delta Refractometer, range: 30-65% sugar (w/w), Bellingham & Stanley Ltd., Tunbridge Wells, Kent) to be equivalent to 1.414. An optically matched blood analogue of 46% aqueous glycerol solution and 14% salt (refractive index 1.414, also measured using the Delta Refractometer) was used in the LDA experiments.

8.4 MATERIALS AND METHODS

8.4.1 The blood analogue solution

A solution of 46% (w/w) aqueous glycerol and 14% (w/w) sodium chloride (refractive index 1.414) was substituted for the original blood analogue used in the flow visualization experiments to minimise refractive index mismatch at the model boundaries. The particles used in the LDA experiments were 5μm diameter polyamide 12 powder (Orgasol, Elf AtoChem. U.K. Ltd.) dissolved in isopropylalcohol (approximately, 20% concentration). The particle suspension was added gradually to the fluid circulating around the flow rig until the LDA data rate had reached a maximum. At this point an extra 20% of glycerol-salt solution was added to the fluid in the main reservoir.

The seeding particles for laser Doppler anemometry must be small enough to follow any flow fluctuations but large enough to scatter light effectively. Seeding particles suitable for laser Doppler anemometry range from 0.5 to 30 μm in diameter.

The density (ρ) and viscosity (μ) of the new analogue fluid were 1200kg/m^3 and 6.8 x 10^{-3} Pa s, respectively, giving a kinematic viscosity (ν) of 5.7 x 10^{-6} m^2/s.

For all the wall shear measurements, the venous profiles and the bulk of the

centreline turbulence measurements, 0.15% sodium azide was dissolved in the basic (46% aqueous glycerol and 14% salt) flow solution (refractive index 1.414). The sodium azide is a bactericide which extends the working life of solution. The sodium azide in suspension was found to produce sufficient micro-particles (along with the naturally occurring particulates in the aqueous glycerol solution) for LDA measurement, providing high data rates and high validation percentages. An additional advantage was that these particles did not appear to be attracted to the inner surface of the model unlike the polyamide particles.

8.4.2 The flow rig

A similar flow circuit to that used for flow visualization was employed in the LDA experiments (see Figures 7.2 and 7.3). A gear pump was used (instead of the peristaltic pump used in flow visualization) to achieve the mean Reynolds numbers needed with the more viscous LDA fluid. The model was mounted flat on an optical table. Movements of the laser head (mounted vertically) in the x-, y- and z-directions were motorized with a minimum translational increment of 12.5μm in any particular direction. A rotational stage was also fitted to orient the laser head with the vessel axes in the x-y plane (the plane of the anastomosis) with a maximum error of 0.5°.

8.4.3 Flow conditions

The pulsatile flow component, of frequency 1Hz (corresponding to α=3), was produced by the servo-motor in all the LDA experiments. A mean Reynolds number of 600 and a pulsatility index of 0.44 were used throughout. Axial and radial velocity components were measured in the symmetry plane of the anastomosis, along the floor of the artery, along the centreline of the vein and across the venous lumen at specific locations (4mm, 10mm, 24mm, 50mm and 70mm from the anastomosis). A range of flow distributions was studied, mirroring those investigated in the flow

visualization experiments.

8.4.4 Measurement

The LDA system used was a 2-dimensional laser Doppler anemometer (55X FiberFlow Series, Dantec, Denmark) operating in backscatter mode: a two-colour, four-beam system utilising the green and blue beams of an 100mW argon ion laser (514.5nm and 488nm, respectively) for measurement of velocity components in two orthogonal planes. A frequency shift of 40MHz was applied to one in each pair of beams using a Bragg cell (57N14 Frequency Shift Modules, Dantec). The Bragg cell was also utilised as a beam splitter in this system. The shape of the sampling volume was an ellipsoid of diameter 45μm and length 210μm in air. The laser beams were focused into the flow by an 85mm probe (focal length of lens, 160mm) which was also responsible for collecting scattered light. The data rate and validation were optimised by adjusting the signal gain and the High Voltage to the Photomultiplier (limitations: the noise level must not be amplified to the extent that it triggers the burst detector and the High Voltage must not be increased to the point where the anode current limiter becomes active) and by accurately specifying the centre frequency and bandwidth and adjusting the signal gain for each measurement position. The record length was set so that the record interval was close to the shortest of the Doppler bursts to prevent noise from being included in the record. Optimization was achieved by inspection of the readings on the front panel of BSA1 and the on-line histogram of the measured frequencies/velocities. Doppler frequencies were obtained with processors based on FFT analysis (57N10 and 57N25 Burst Spectrum Analyzers, Dantec). Conversion of the Doppler frequencies to velocity data was achieved using a calibration factor of 1.263m/s/MHz for the green channel and 1.198m/s/MHz for the blue channel. Data acquisition was carried out by a personal computer-based system running the BURSTware 3.1 software

(Dantec). Data acquisition was carried out with the BSAs operating independently (*coincidence private mode*) to maximize the data rates on both channels. BSA1 was the *clock master* and BSA2 the *clock slave*. A TTL level trigger pulse was sent to reset the BSA arrival time counter at the start of every cycle (*encoder enabled*). The arrival time and transit time of each of the samples of velocity information relative to the pulsatile cycle were stored alongside the velocity data for subsequent analysis.

The model was supported horizontally, with the head of the laser directly above it. For measurements at the wall, the wall was determined by watching the drop in the number of detected bursts to zero and the dramatic increase in amplitude of the carrier signal from the boundary, using an oscilloscope, and by examining the on-line histogram of the measured frequency/velocity distribution and the on-screen measured mean velocity and validated data rate. Separate parameter and traverse files were set up for each measurement point along the floor of the artery, containing 11 incremental positions of 0.025mm at the wall, and extending radially into the flow. For measurements along the vein, the head of the laser was rotated for each measurement point along the axis to match the direction of the spine specified in DUCT at that point. The traverse file for measurement points along the centreline of each model was also constructed from data provided by DUCT. Velocity measurements for calculating shear stress along the curved wall of the vein were made by traversing an integral number of x- and y- minimum translational increments in $\sim 25\mu$m steps perpendicular (approximately) to the wall. Axial (green channel - BSA1) and radial (blue channel - BSA2) velocity measurements were recorded. Subsequent analysis was carried out in MATLAB.

Velocity data processed by the BSAs have random arrival times and are, therefore, unevenly spaced in the time domain. For such data, it was not possible to carry out routine averaging procedures. Data must initially be sorted into individual cycles and then, sorted into time bins corresponding to their arrival times relative to

the external trigger.

8.4.5 Data analysis: wall shear stress

The velocity data were sorted into a hundred 10ms time bins and averaged in each bin to produced the mean cyclical variation in velocity. The mean velocity data were used to calculate the temporal variation in wall shear stress at each measurement point. This was done by curve-fitting to estimate the gradient of the near-wall velocity profile at the wall, and multiplying this figure by the viscosity of the blood analogue solution (see Section 3.2, Equation 3).

	Linear Fit	Parabolic Fit
Fitted equation	$y=3.9174x-0.025414$	$y=10.3409x^2+5.1729x-0.005086$
Sum of residual squares	0.002464	0.000588
Goodness-of-fit index	0.024821	0.008573
Mean axial velocity gradient near wall $(du/dx)_0$	3.9174 m/s/mm	5.1729 m/s/mm
Equivalent wall shear stress	26.6 N/m^2	35.2 N/m^2

One necessary consideration when calculating wall shear stress is curve-fitting and the order of the first order polynomial to fit to. Near the wall, the velocity profile largely tends to be linear in form. The disadvantage in assuming a parabolic fitting equation is that it is important to accurately define the position of the wall in relation to the dataset. When making velocity measurements, it is difficult to be precise about the location of the wall because of the clarity of the models, the pulsating wall and the finite sample volume; this uncertainty can of course be removed at the post-processing stage. Figure 8.2 and the table on the previous page give an indication of the errors associated with straight-line and parabolic fits to real data.

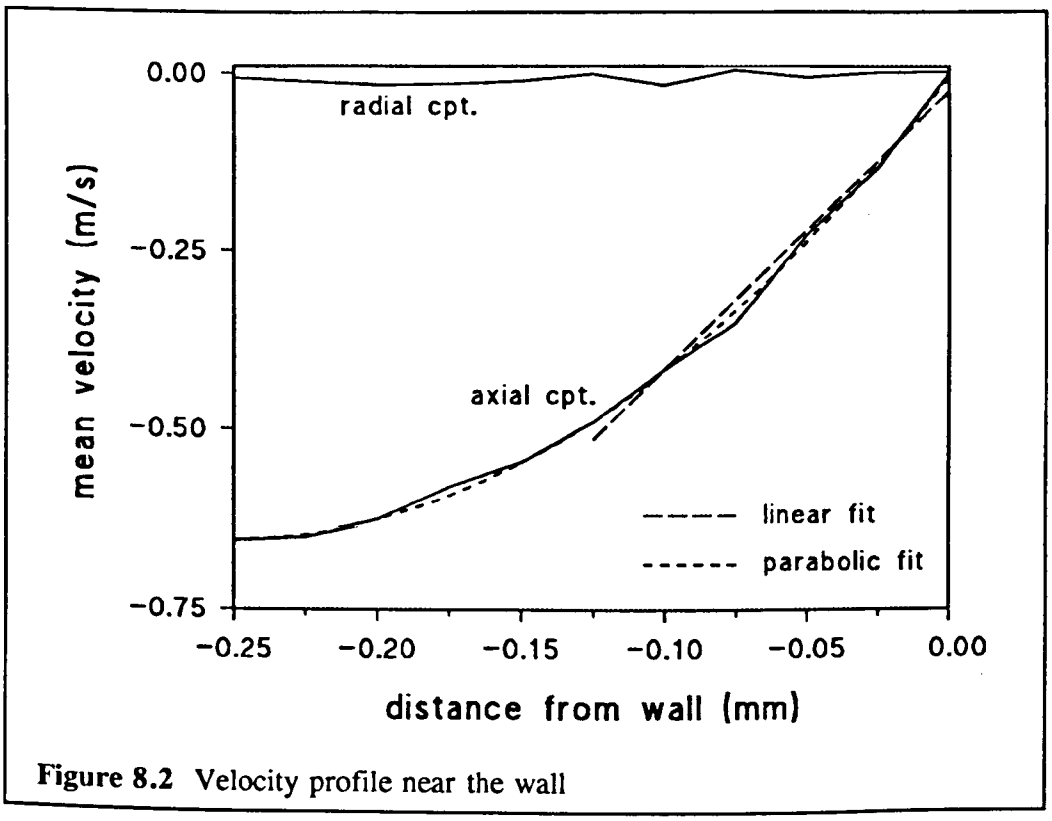

Figure 8.2 Velocity profile near the wall

By inspection, the near-wall velocity data appears to follow a parabolic shape. This fact is borne out by the differences in the sum of the residual squares and the goodness-of-fit index (the square root of the ratio of the sum of residual squares to the degrees of freedom) in the two cases. A conversion factor of 6.8 transforms the velocity gradients in m/s/mm into wall shear stresses in N/m^2. The shear stress value using the linear fit is 76% of the value produced by the parabolic fit. Further calculations at different points along the wall have shown that this approximation can over- or underestimate the shear stress value from the parabolic fit by a maximum of 175%. Even with an optimized curve-fit, there still remains some uncertainty due to unavoidable measurement errors, quantization errors, the limited number of data values used and the absence of data weighting.

In regions of flow disturbance or where the wall is curved, the velocity profile at the wall may not be follow the general parabolic pattern. Therefore, it is

necessary to limit the number of near-wall positions used in curve-fitting. The routine written to calculate wall shear stress was designed to fit a parabolic curve to the axial velocities at the 5 positions adjacent to the wall (with data rates above a minimum limit, to avoid positions where the wall intersects the sample volume). The position of the wall was more accurately specified by the nearest root of the quadratic fit equation, and the gradient was calculated at this point.

8.4.6 Data analysis: turbulence intensity

The velocity data were sorted into two hundred 5ms bins and averaged in each bin to produce the mean cyclical velocity variation. Spline-fitting of this waveform was carried out at the individual arrival times for the raw data in each bin. The variation (u) between the instantaneous (U) and mean velocities ($\bar{U}$) was calculated for each velocity measurement. $U - \bar{U} = u$ These values were then squared (u^2). To produce the temporal root-mean-square velocity variation ($\sqrt{\bar{u}^2}$), the squared velocity variations were averaged in their individual time bins and the square root value taken in each bin. To calculate the cyclic mean, the root-mean-square variations in each bin were averaged. The root-mean-square velocity fluctuation is also known as the absolute intensity of turbulence (u'). The root-mean-square velocity fluctuation was also used to calculate the turbulence intensity (the percentage ratio of the root-mean-square fluctuation to the local mean velocity at that point in the cycle). This process was repeated for both axial and radial components of flow.

$$\frac{u'}{\bar{U}} = \frac{\sqrt{\bar{u}^2}}{\bar{U}}$$

8.4.7 Data analysis: Reynolds shear stress

The Reynolds shear stress was calculated from the velocity data. Reynolds stress is the theoretical shear stress that acts tangentially on a surface of an element

of the fluid. It is calculated from the product of the mean fluctuating radial and axial velocity components and the density of the analogue fluid (Section 3.2, Equation 4).

To produce an accurate determination of the Reynolds shear stress it was essential that the axial and radial data were coincident in time (using an arrival time coincidence window of 43μs). The filtered velocity data were again sorted into 5ms time bins. Spline-fitting of both the mean velocity waveforms calculated above was carried out at the individual arrival times for the filtered data. The variation between the instantaneous and mean velocities was calculated for each velocity measurement. The "simultaneous" fluctuating part of the velocity components were then multiplied together and multiplied by the fluid density. The temporal Reynolds shear stress variation was obtained by averaging the products in the individual bins. The mean Reynolds shear stress was calculated by averaging the values in all the bins together.

8.5 RESULTS

The results presented in this section correspond to a mean Reynolds number of 600 in the vein, a pulsatility index of 0.44 and a Womersley parameter of 3. For wall shear measurements, velocity data were recorded for 100s. For measurements away from the wall, data were collected for variable lengths of time, depending on the data rate and validation percentage. A minimum of 15000-20000 validated bursts was achieved at most measurement positions by collecting for periods of 10s to 500s. The number of coincident data from both channels varied from position to position and model to model. At best, 50% of the velocity data were software coincidence filtered for the Reynolds shear stress calculation.

8.5.1 Near-wall measurements

Figures 8.3-8.5 show a plot of arterial wall shear stress and intermediate stages in this calculation. As the data rate drops dramatically near the wall, it is vital

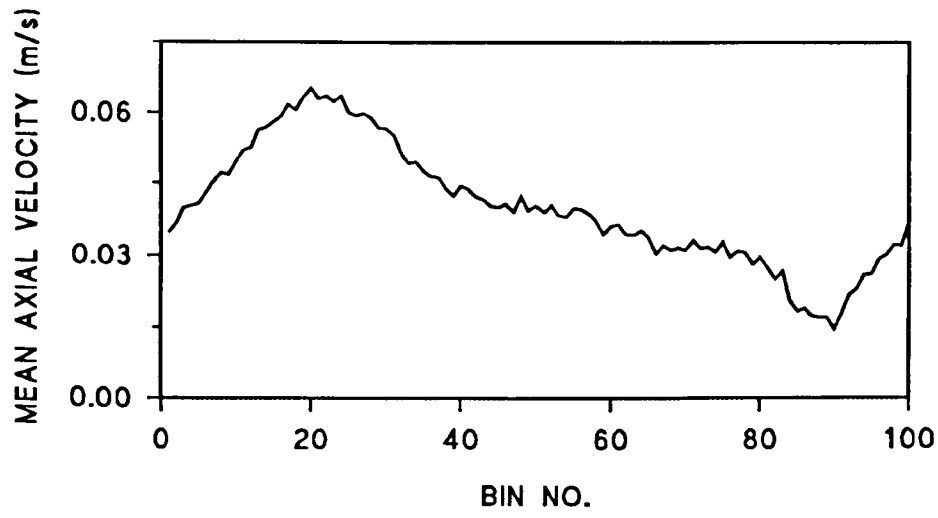

Figure 8.3 Mean near-wall velocity (0.15mm from wall) in the proximal artery

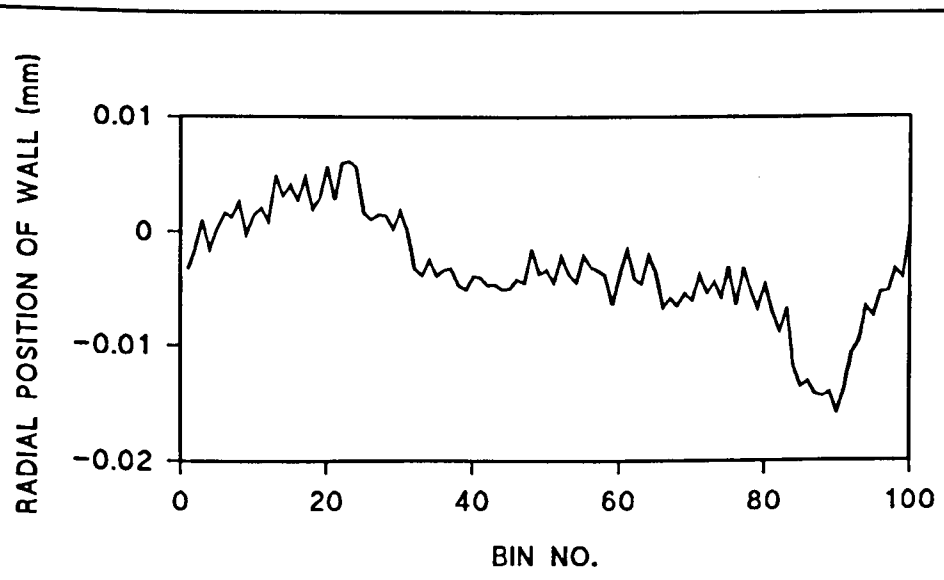

Figure 8.4 Position of the moving proximal arterial wall

to average several cycles to produce a meaningful representation of the mean velocity waveform. The mean temporal wall shear stress variation is calculated by fitting parabolic curves to the time-dependent near-wall velocity profile, and determining the gradient at the moving wall at 10ms intervals throughout the cycle. The wall shear stress calculation is highly sensitive to velocity fluctuations and to the accuracy

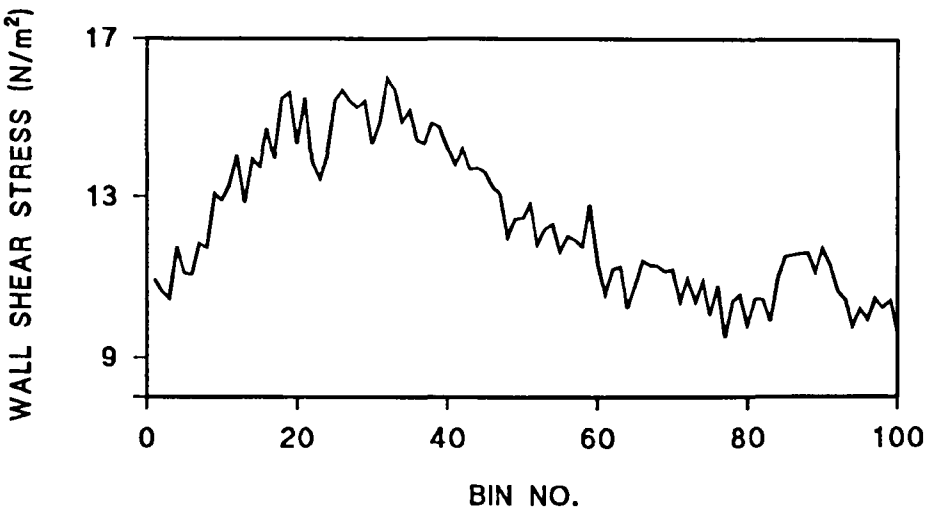

Figure 8.5 Cyclic wall shear stress along the proximal artery

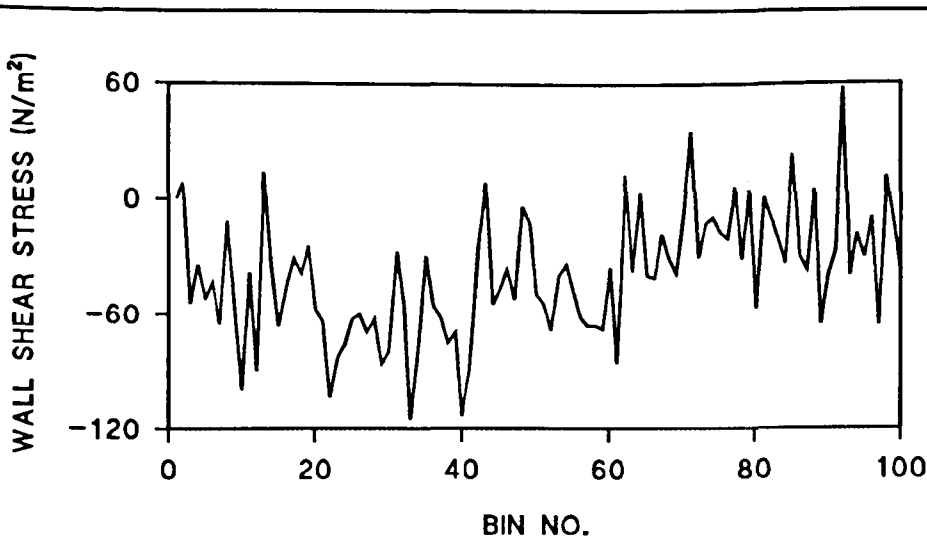

Figure 8.6 Cyclic wall shear stress on the arterial floor of the anastomosis

of the curve fitting parameters and, hence, the averaged waveform may appear noisy. This is more apparent in the region of the anastomosis where flow disturbances produce high temporal and spatial velocity gradients (Figure 8.6). Figure 8.4 demonstrates the limited compliance of the silicone rubber model. The movement of the wall spans 25μm (twice the minimum increment of the traverse). Hence, the difficulty in accurately defining the position of the wall during measurement.

8.5.2 Wall shear stresses along the arterial floor

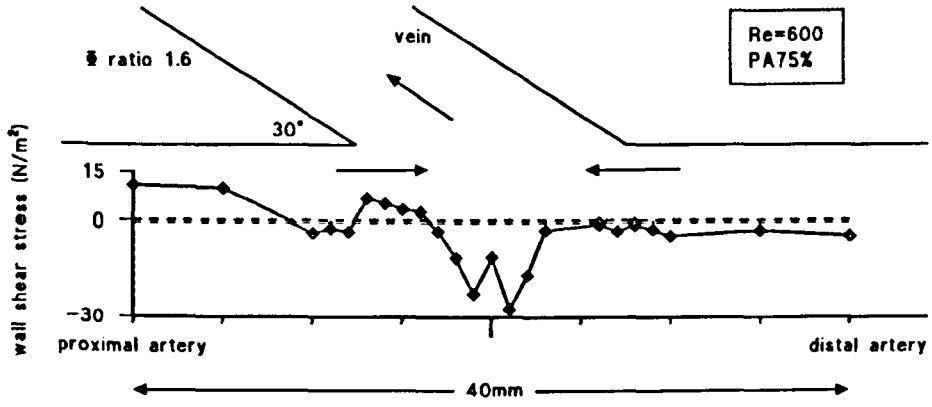

Figure 8.7 Mean wall shear stresses along floor of anastomosed artery (30°, 1.6 diameter ratio model, proximal artery supplying 75% of venous flow)

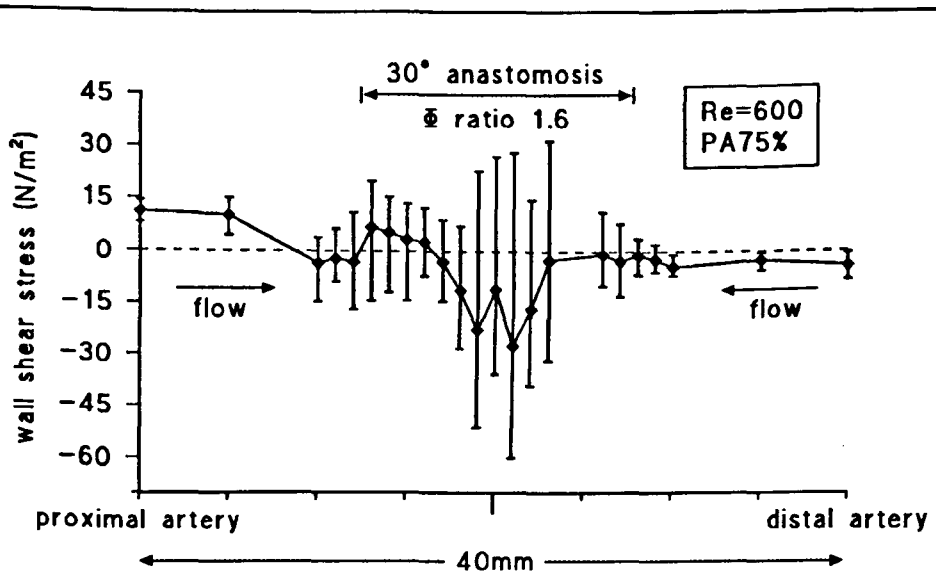

Figure 8.8 Oscillatory wall shear stresses along the arterial floor (30°, 1.6 diameter ratio model, proximal artery supplying 75% of venous flow)

Figure 8.7 shows a map of mean wall shear stress along the floor of the artery at the anastomosis. This figure corresponds to pulsatile flow with 75% of venous supplied by the proximal artery in the 30° anastomosis, 1.6 diameter ratio model. The changes in sign of the wall shear stress on the arterial floor clearly relate to areas of flow reversal captured by flow visualization (compare with Figure 7.13).

Flow reversal occurs twice near the proximal region of the anastomosis due to the formation of small counter-rotating vortices at the union of proximal and distal arterial flow. Positive shear stress corresponds to flow towards the distal artery. Hence, wall shear stresses in the distal artery are negative and approximately three times smaller than the magnitude of wall shear stresses in the proximal artery. The pertinent feature is the high shear stresses (approaching $30N/m^2$) in the region of the main vortex. Two peaks of roughly equal magnitude occupy ± 3mm about the centre of the anastomosis. Evidently, the wall shear stresses at the centre of the anastomosis are high, but the two peaks might be a feature of the shape of the floor of the anastomosis and the particular combination of anastomotic angle and vein-to-artery diameter ratio. The peak-to-peak variation in wall shear stress associated with each of the measurement points in Figure 8.7 is shown in Figure 8.8. The oscillatory shear is ten to fifteen times larger at the centre of the anastomosis than in the proximal artery. The oscillatory shear is generally much higher in the anastomotic region but the peak ($90N/m^2$) coincides with the maximum seen in the temporal mean shear stress distribution at a distance of 1mm from the centre of the anastomosis, towards the distal artery.

As the proportion of distal arterial flow entering the vein is reduced (Figure 8.9), the two wall shear stress peaks at the centre of the anastomosis coalesce into one with an absolute mean value of almost $130N/m^2$ and a peak-to-peak value of $100N/m^2$. A secondary maximum is seen at 5mm from the centre of the anastomosis towards the proximal artery. Although the mean wall shear stress value at this point is only $80N/m^2$, the oscillatory wall shear stress value reaches a peak of $150N/m^2$ at this point. The high temporal gradients observed would seem to relate to the fluctuating flow reattachment point (see Figure 7.13). The stagnation point is represented by the point at which wall shear changes from negative to positive. The positive peak in the occluded distal artery is associated with the secondary vortex

driven by the main vortex.

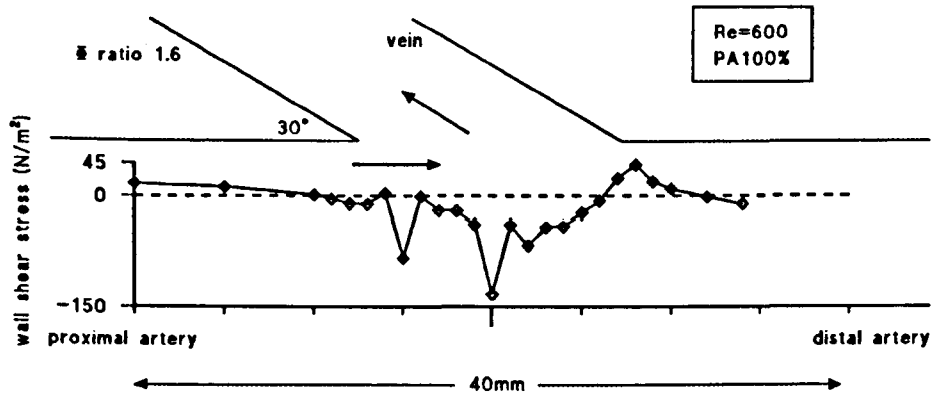

Figure 8.9 Mean wall shear stresses along floor of anastomosed artery (30°, 1.6 diameter ratio model, distal artery occluded)

As the proportion of distal arterial flow is increased, on the other hand, the mean wall shear stress maxima become positive. For the case of equal proximal and distal arterial contributions, the maximum mean wall shear stress is 35N/m^2 and is shifted proximally by 1mm. The peak in oscillatory shear (240N/m^2), however, is a further 6mm in the proximal direction, and again appears to correspond to the high temporal gradients at the union of proximal and distal arterial flows. The position of the maximum in the mean wall shear stress distribution (75N/m^2), for the case where the proximal artery is occluded, is again shifted proximally by another 5mm. This peak is much broader than seen in any of the other flow distributions studied and remains above or around 30N/m^2 for a distance of 12mm. Oscillatory wall shear stress levels remain fairly constant throughout the anastomotic region at 50N/m^2.

The mean wall shear distributions for the 50° and 70° anastomoses are largely similar to those for the 30° anastomotic model (compare Figures 8.10 and 8.11 with Figure 8.7). However, in the 50° model, the second central peak originally seen in Figure 8.7 is greatly reduced and, in the 70° model, it has disappeared. Also, as the anastomotic angle increases, the position of the maximum

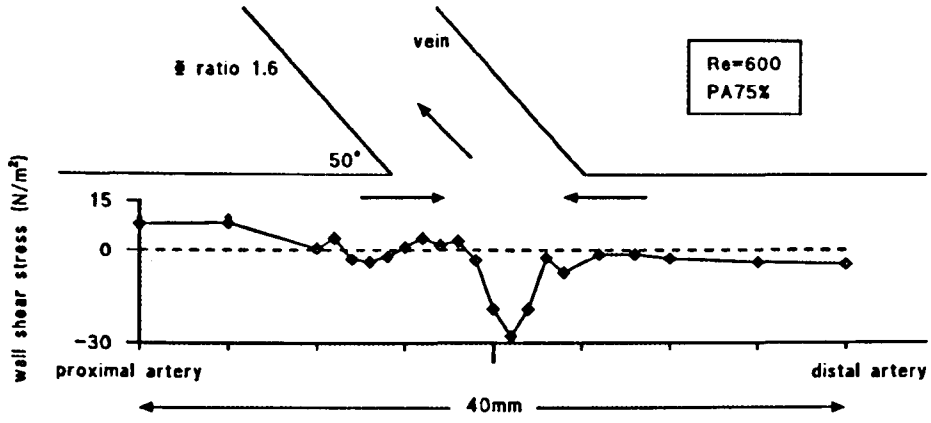

Figure 8.10 Mean wall shear stresses along the floor of the anastomosed artery (50°, 1.6 diameter ratio model, proximal artery supplying 75% of venous flow)

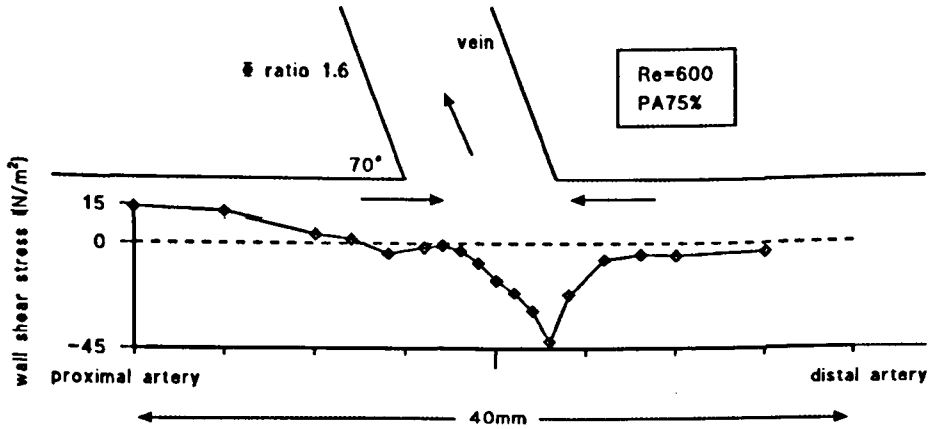

Figure 8.11 Mean wall shear stresses along floor of the anastomosed artery (70°, 1.6 diameter ratio model, proximal artery supplying 75% of venous flow)

moves further towards the distal artery. Another difference between the 70° model and the 30° and 50° models is that the magnitude of wall shear stress reaches 45N/m^2 in this model. Although peak oscillatory shear stress varies from 90N/m^2 in the 30° model, 60N/m^2 (at the secondary maximum) in the 50° model to 30N/m^2 in the 70° model, in general, the oscillatory wall shear stresses in the region of the anastomosis appear larger in the 30° model, followed by the 70° model and lastly, the 50° model.

The regular ordered pathlines of the 0.8 vein-to-artery diameter ratio model (Figure 7.18) and the lower flow rates are borne out by the corresponding arterial wall shear stress map. The polarity of the mean wall shear stress changes only once as it drops from 5N/m^2 in the proximal artery, to reach a negative peak of 3N/m^2 (at 4mm from the centre of the anastomosis, towards the proximal artery), reverses once again briefly, and then gradually assumes a constant distal artery value (2N/m^2). The low oscillatory shear stress values ($\leq$2N/m^2) in the anastomotic region also reflect the laminar flow regime at the anastomosis. The wall shear stress distribution for the 2.0 diameter ratio model follows a similar pattern to Figure 8.11. However, the peak in mean and oscillatory wall shear stress (45N/m^2 and 65N/m^2, respectively) occurs at the centre of the anastomosis.

8.5.3 Wall shear stresses along the vein

Mean wall shear stresses along the outer wall of the vein decrease from the anastomosis until the bend and then increase again (see Table 8.1). The opposite pattern occurs along the inner wall of the vein, although the oscillatory shear values do follow the same pattern (maximum values near the anastomosis and then a constant level after 24mm from the anastomosis) in both cases.

The outer wall mean shear along the 50° model decreases more rapidly towards the bend than the 30° model, and much more rapidly than in the 70° model. The oscillatory shear, however, does not appear to decrease as fast in the 50° and 70° models compared with the 30° model. The mean and oscillatory shear values near the anastomosis are greatest for the 70° model. At the curve of the vein, the outer wall shear stress levels reach a peak of 145N/m^2 in the 70° model. This pattern of increasing and then decreasing wall shear stress is also mirrored in the inner wall shear stress, although absolute values are lower. The most important features to note in the inner wall shear stress values are the low levels of oscillatory shear (2-4N/m^2)

at 70mm, and at 50mm from the anastomosis in the 30° and 50° models. Wall shear is bidirectional at 10mm from the anastomosis in the 30° model, at 24mm and 10mm in the 50° model, and 50mm (inner wall only) and 24mm in the 70° model.

Table 8.1 Mean and oscillatory wall shear stress along the vein in relation to anastomotic angle

Model	Distance from suture line	Wall shear stresses along vein (N/m^2)			
		Inner Wall		Outer Wall	
		Mean	Oscillatory Shear	Mean	Oscillatory Shear
30°	4mm	-	-	40	52
	10mm	1	36	14	57
	24mm	12	17	7	8
	50mm	5	3	9	8
	70mm	4	2	14	9
50°	4mm	-	-	46	36
	10mm	5	26	3	33
	24mm	5	26	0	23
	50mm	4	3	7	9
	70mm	4	4	5	18
70°	4mm	-	-	58	61
	10mm	8	17	34	35
	24mm	6	26	5	145
	50mm	0	15	9	15
	70mm	4	4	7	9

As the vein-to-artery diameter ratio increases, oscillatory wall shear along the inner wall gradually decreases then increases more gradually (see Table 8.2). The mean and oscillatory shear values are greatest for the 0.8 diameter ratio model, followed by the 2.0 ratio model. Apart from the 1.6 diameter ratio model, oscillatory shear does not drop to the low values seen in the previous set of models. As outer wall mean shear decreases in the 2.0 diameter ratio model, oscillatory shear follows the same pattern as in the 70° model, reaching a peak ($90N/m^2$) at 24mm. Outer wall

oscillatory shear reaches a minimum of $2N/m^2$ at 50mm in the 0.8 diameter ratio model. The trend in oscillatory shear with distance from the anastomosis is different to the other two models. Wall shear is bidirectional at 70mm and 50mm in the 0.8 diameter ratio model, at 10mm in the 1.6 ratio model and 70mm and 50mm (inner wall only) and 24mm in the 2.0 diameter ratio model. One strange feature is that outer wall mean shear 24mm and 70mm from the anastomosis in the 0.8 diameter ratio model is negative. No consistent trend is apparent with increasing diameter ratio.

Table 8.2 Mean and oscillatory wall shear stresses along the vein in relation to vein-to-artery diameter ratio

Model ϕ ratio	Distance from suture line	Wall shear stresses along vein (N/m^2)			
		Inner Wall		Outer Wall	
		Mean	Oscillatory Shear	Mean	Oscillatory Shear
0.8	4mm	-	-	NA	NA
	10mm	45	91	NA	NA
	24mm	42	99	-34	68
	50mm	19	78	0	2
	70mm	11	30	-33	16
1.6	4mm	-	-	40	52
	10mm	1	36	14	31
	24mm	12	17	7	8
	50mm	5	3	9	8
	70mm	4	2	14	9
2.0	4mm	-	-	30	38
	10mm	-	-	16	29
	24mm	3	79	6	90
	50mm	3	23	5	13
	70mm	3	12	4	9

Away from the anastomosis, the general trend in mean and oscillatory shear in the vein is similar for the different flow distributions (see Table 8.3). Outer wall

mean and oscillatory shear values near the anastomosis are greater for greater proximal contributions to venous flow. On the inner wall of the vein, however, the greatest oscillatory shear value (69N/m^2) is seen in the case of proximal artery occlusion, 10mm away from the suture line, while values decrease drastically at the other three positions. With the other flow distributions, declining oscillatory shear stress (initially, 31-16N/m^2) with distance from anastomosis is less marked.

Table 8.3 Mean and oscillatory wall shear stresses along the vein in relation to flow distribution in the 30°, 1.6 vein-to-artery diameter ratio model

Flow condition	Distance from suture line	Wall shear stresses along vein (N/m^2)			
		Inner Wall		Outer Wall	
		Mean	Oscillatory Shear	Mean	Oscillatory Shear
PA100%	4mm	-	-	109	83
	10mm	7	32	19	210
	24mm	9	13	8	6
	50mm	5	4	8	10
	70mm	3	3	10	8
PA75%	4mm	-	-	40	52
	10mm	1	36	14	57
	24mm	12	17	7	8
	50mm	5	3	9	8
	70mm	4	2	14	9
PA50%	4mm	-	-	9	26
	10mm	-2	16	18	22
	24mm	10	17	9	9
	50mm	4	4	9	8
	70mm	4	2	14	10
DA100%	4mm	-	-	6	14
	10mm	10	69	6	10
	24mm	9	9	6	8
	50mm	5	2	9	6
	70mm	4	2	11	9

Bidirectional wall shear stresses occur at 10mm in all flow distributions (both inner

and outer walls, only when there are equal contributions from the proximal and distal artery) and at 4mm (outer wall only) when there is equal or more distal than proximal artery flow in the vein.

8.5.4 Measurements in the vein

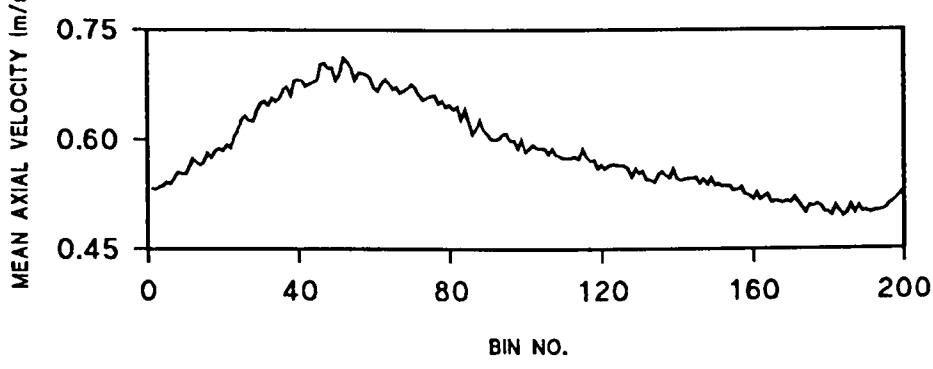

Figure 8.12 Mean axial velocity through the cycle

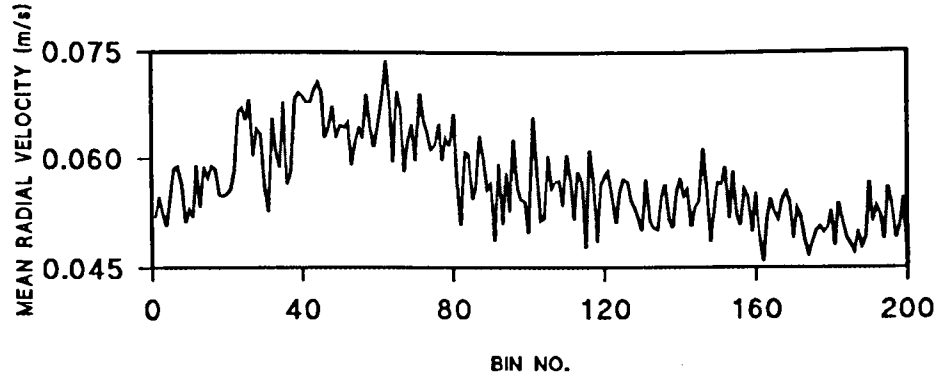

Figure 8.13 Mean radial velocity through the cycle

Figures 8.12-8.18 chart the intermediate stages in the determination of cyclic turbulence intensity variations and Reynolds shear stress. The data were obtained from the centreline of the vein, approximately 70mm from the anastomosis where flow is less disturbed. Although the mean axial velocity waveform (Figure 8.12) is

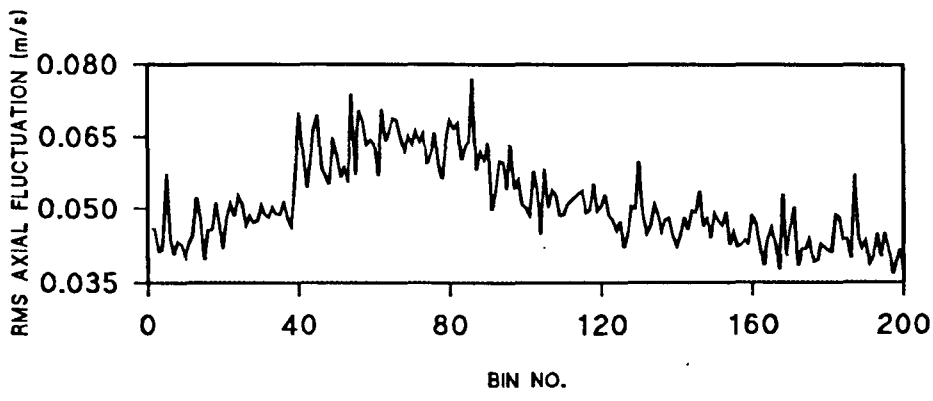

Figure 8.14 Root-mean-square axial velocity fluctuations

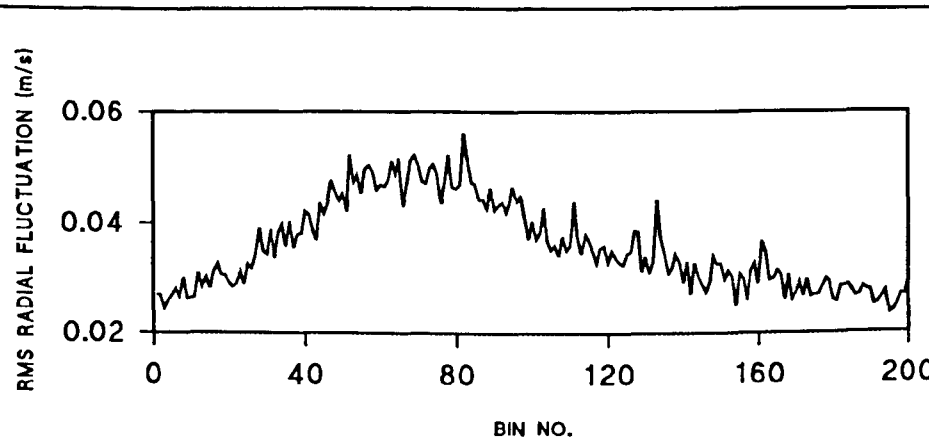

Figure 8.15 Root-mean-square radial velocity fluctuations

comparatively smooth, the radial component (Figure 8.13) is very noisy. This could be the result of poor averaging and insufficient data numbers but is more likely to be related to the differences in the velocity scales and greater errors in measuring smaller velocities. Paradoxically, the relative noise in the root-mean-square radial velocity fluctuations (Figure 8.15) is not as great. Noise is amplified in the Reynolds shear stress calculation (Figure 8.18) due to the highly random distribution of axial velocity data (demonstrated by the large fluctuations in the temporal root-mean-square axial velocity fluctuations in Figure 8.14, despite the smooth temporal mean velocity) and the product of the two components. The peak in turbulence intensity

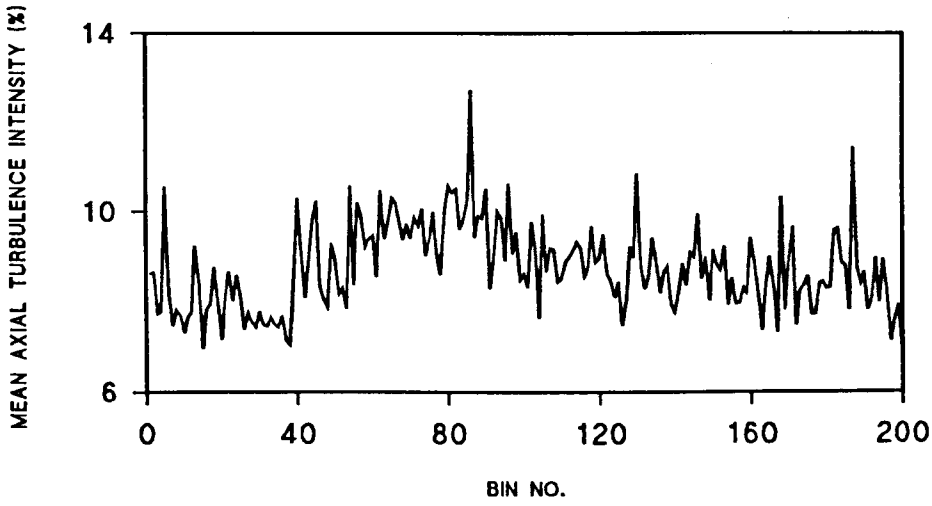

Figure 8.16 Axial turbulence intensity through the cycle

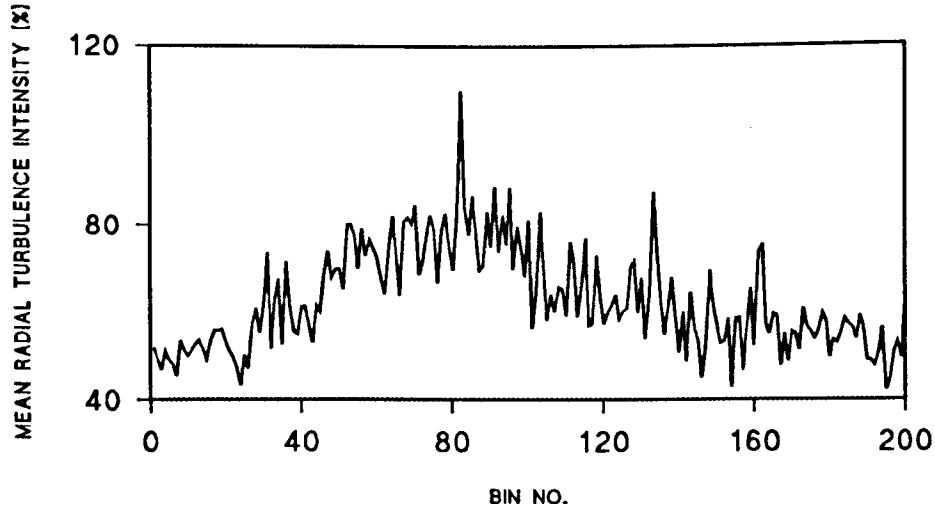

Figure 8.17 Radial turbulence intensity through the cycle

(Figures 8.16 and 8.17) occurs in the early decelerative phase of the cardiac cycle (following peak systole) in both components (when flow is most unstable) and at the same point in the Reynolds shear stress cyclic variation. Turbulence intensity and Reynolds shear stress appear in phase with velocity variations over the cycle. The apparently high radial turbulence intensity values can be misleading: they arise from much lower radial flow components even though the root-mean-square axial and

radial velocity fluctuations are of the same order of magnitude.

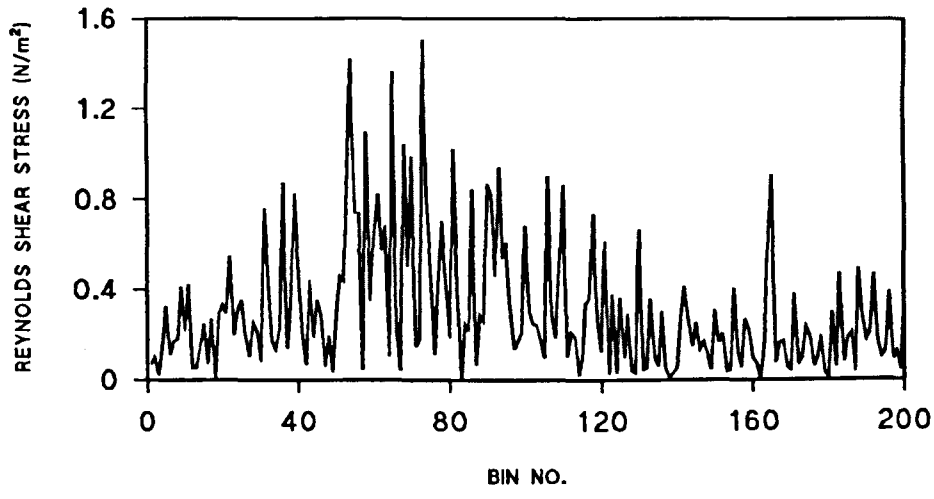

Figure 8.18 Cyclic Reynolds shear stresses

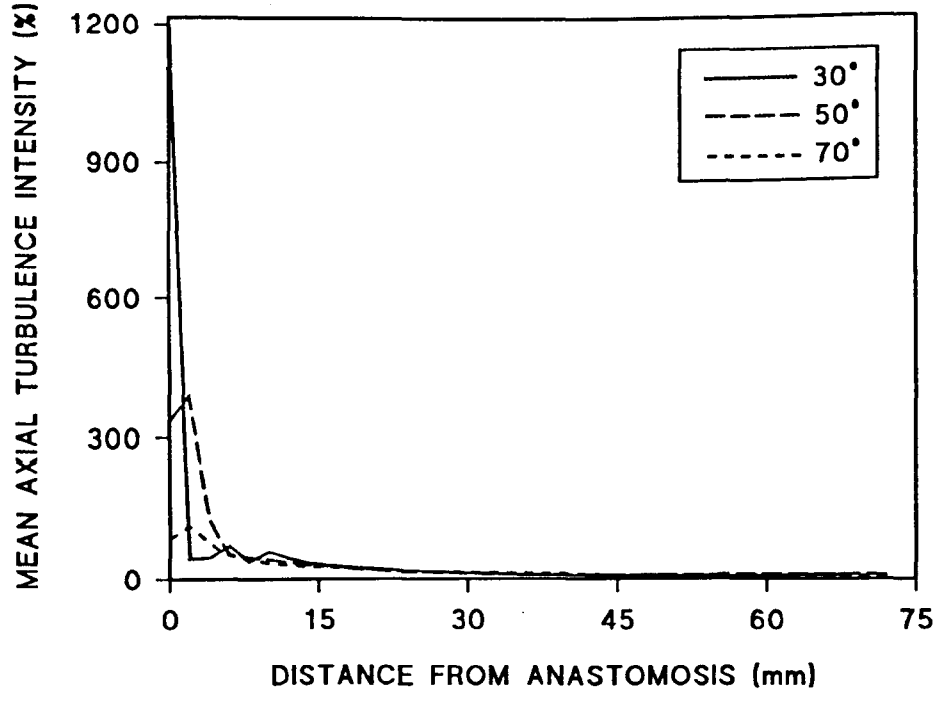

Figure 8.19 Mean axial turbulence intensity along the centreline of the 30°, 50° and 70° anastomotic angle model veins

Beyond 15mm from the anastomosis, there are few differences in the absolute

levels of axial turbulence intensity between the different anastomotic angles (Figure 8.19). Centreline turbulence intensity appears to decay rapidly from the anastomosis. Maximum values of mean axial turbulence intensity of 1200%, 390% and 120% are seen in the 30°, 50° and 70° models, respectively. Turbulence intensity appears to plateau beyond a distance of about 40mm from the anastomosis at a mean turbulence intensity level of approximately 10%. Axial and radial absolute turbulence distributions follow a similar pattern to that of the axial turbulence intensity, but decay less rapidly. Corresponding values of axial absolute turbulence range from 0.05-0.70m/s in the 30° model vein, 0.04-0.41m/s in the 50° vein and 0.05-0.38m/s in the 70° vein. Radial absolute turbulence values range from 0.02-0.30m/s, 0.06-0.36m/s and 0.03-0.37m/s in the 30°, 50° and 70° model veins, respectively. Whereas mean radial turbulence intensity levels remain below 400% in the 30° and 50° models, radial turbulence intensity shoots up to well above 2000% at a distance of 50mm from the suture line in the 70° model. The positions of subsidiary maxima near the anastomosis most probably relate to non-axisymmetric turbulence intensity profiles and to the varying effects of recirculation at the heel of the anastomosis (refer to Figure 7.15). Radial turbulence intensity increases from near zero at the anastomosis (where there is a large radial flow component) with one or more maxima before decreasing to zero again. Peaks in turbulence intensity correspond to very low radial flows components along the centreline in the curve of the vein.

Models with varying vein-to-artery diameter ratio exhibit similar trends in mean axial turbulence intensity, and axial and radial absolute turbulence (Figure 8.20) to those in Figure 8.19. However, the final (at 70mm from the anastomosis) level of mean axial turbulence intensity is significantly less in the 0.8 diameter ratio model. Although the level does eventually reach 10% in the 2.0 diameter ratio model, the slope is almost linear. The maximum level of axial turbulence intensity varied from a mean of 1200% in the 1.6 diameter ratio model, 350% in the 2.0

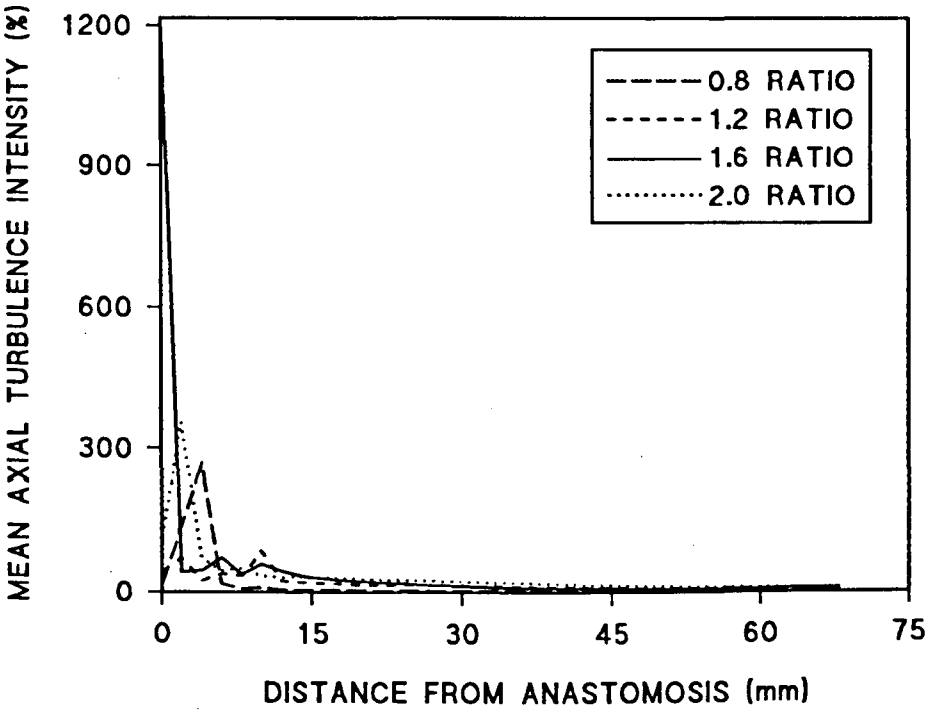

Figure 8.20 Mean axial turbulence intensity along the centreline of the 0.8, 1.2, 1.6 and 2.0 vein-to-artery diameter ratio model veins

diameter ratio model, 270% in the 0.8 diameter ratio model, to 90% in the 1.2 diameter ratio model. The maximum level of absolute axial turbulence, however, increases with increasing diameter ratio (range, 0.02-0.17m/s and 0.07-0.35m/s in the 0.8 and 1.25 diameter ratio veins) until the 1.6 diameter ratio vein (range, 0.05-0.70m/s) and then decreases in the 2.0 diameter ratio vein (range, 0.05-0.27m/s). Absolute radial turbulence shows a clearer distinction between larger and smaller diameter veins: the maximum levels are 0.29m/s in the two larger diameter veins and 0.14m/s in the two smaller model veins. The plateau level of absolute radial turbulence is again greatest in the 2.0 diameter ratio model (no difference in the axial direction, between the larger veins). Peaks in mean radial turbulence intensity (Figure 8.21) occur between 30-40mm from the anastomosis. The absolute levels (3200-4000%) are significantly higher in the 1.2 and 2.0 diameter ratio models. The

magnitude of radial turbulence intensity in the 0.8 diameter ratio vein is well below 100%.

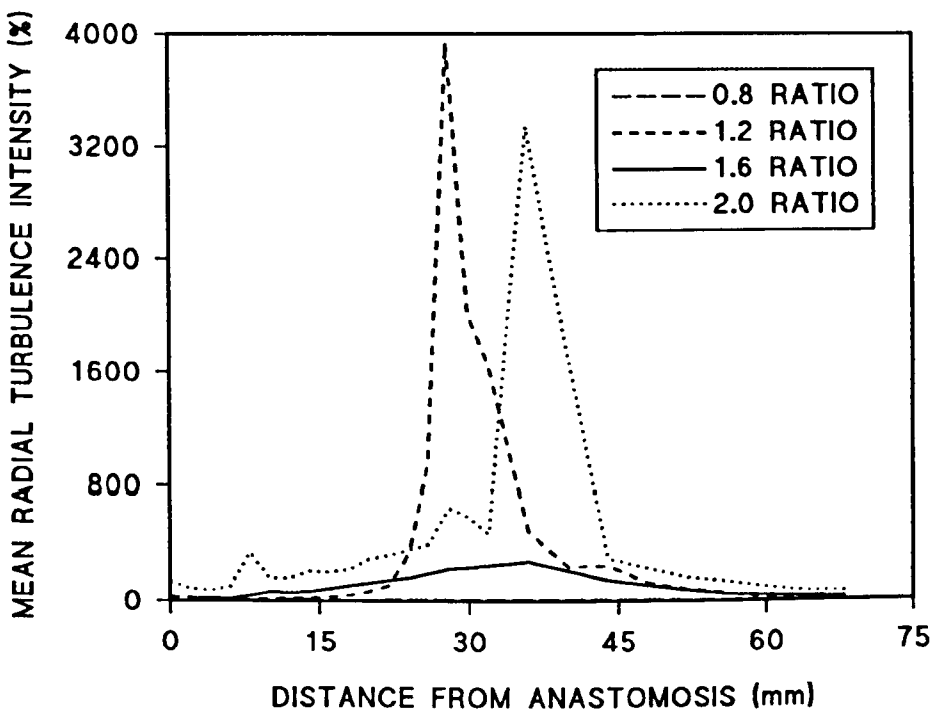

Figure 8.21 Mean radial turbulence intensity along the centreline of the 0.8, 1.2, 1.6 and 2.0 vein-to-artery diameter ratio model veins

The effects of varying the flow distribution on the mean axial turbulence intensity in the vein are not comparatively great. Although the maximum value is 1200% when the flow in the vein comprises 75% proximal and 25% distal artery flow, in all other cases, the peak does not exceed 150%. The plateau level for all four flow distributions is also similar. The initial rate of decay is slightly greater for the case where the proximal artery is occluded and slightly less when proximal and distal artery contributions to venous flow are equal. There is a more dramatic difference in the positions of maximum mean radial turbulence intensity (see Figure 8.22). The peak reaches almost 30000% when venous flow is wholly supplied by the distal artery, compared to only 300% when there is three times more proximal than

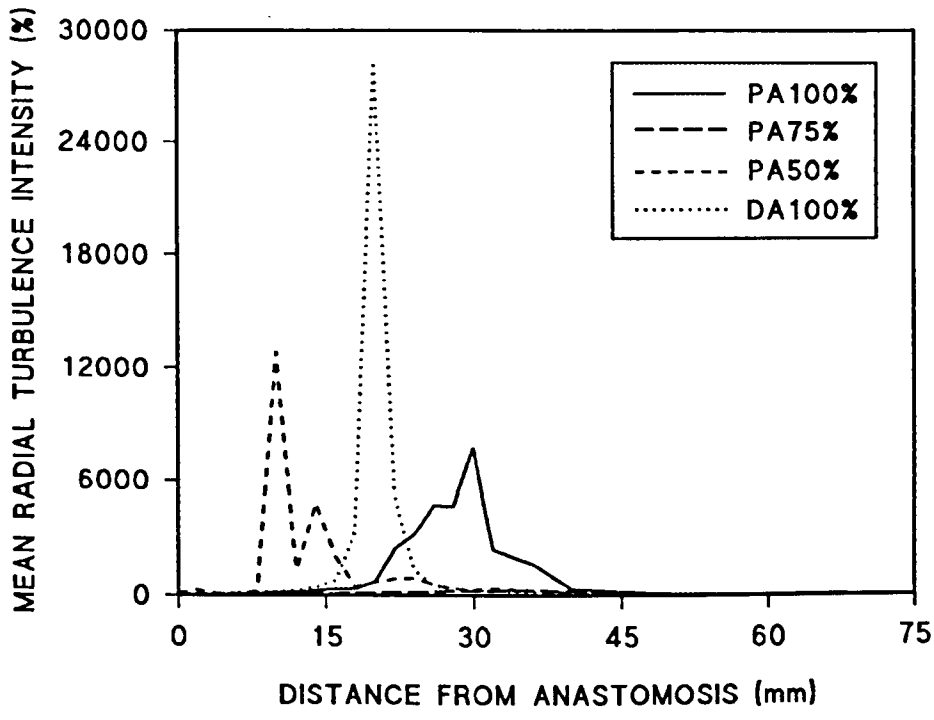

Figure 8.22 Mean radial turbulence intensity along the centreline of the 30°, 1.6 diameter ratio for varying flow distributions

distal artery flow into the vein. Whereas plateau levels for axial and radial absolute turbulence are similar for the different flow distributions (0.06m/s and 0.03m/s, respectively), maximum levels of absolute axial turbulence increase with increasing proximal artery flow. Maximum levels of absolute radial turbulence, on the other hand, do not show any obvious trend (values range from 0.27-0.51m/s for the different flow distributions).

Figures 8.23-8.27 show how mean absolute turbulence and the convective velocity vary across the lumen at different positions along the vein. At 4mm from the anastomosis, axial and radial turbulence peak towards the outer wall. However, at 10mm, the axial turbulence peak occurs more centrally while the radial turbulence profile flattens out. At 24mm, in the bend, the radial turbulence profile exhibits a broad peak, shifted slightly towards the outer wall. The maximum in axial

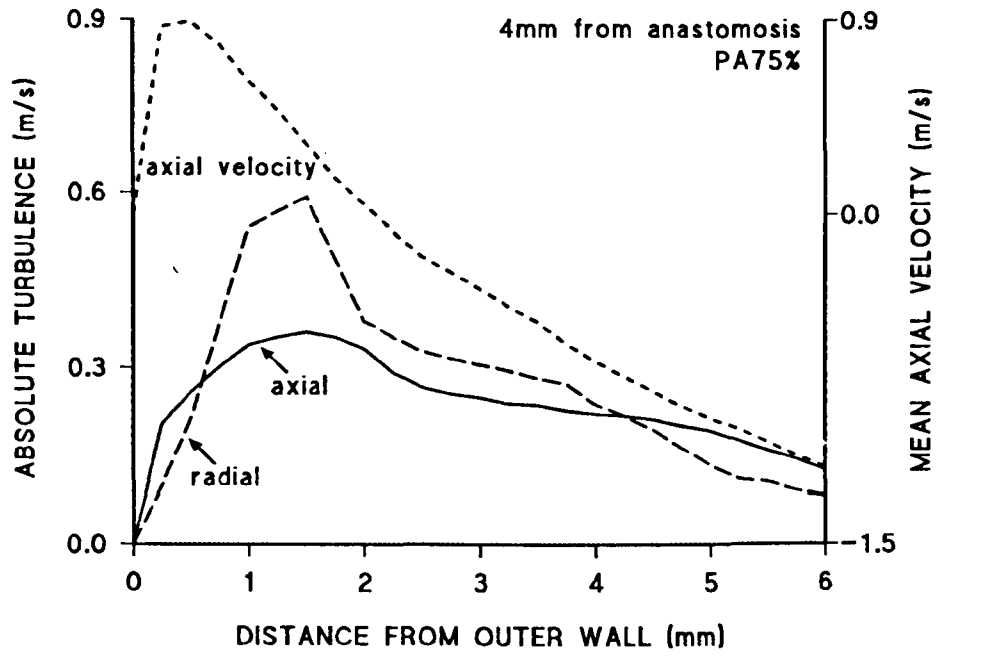

Figure 8.23 Turbulence intensity and velocity profiles in the 30°, 1.6 diameter ratio vein at 4mm from the anastomosis

turbulence, however, is near the inner wall, although the profile is largely flat, away from the walls. As the velocity profile becomes more symmetrical at 50mm, the radial turbulence profile becomes more symmetrical. The axial turbulence profile possesses a maximum near both of the walls and dips at the centre of the vessel. By 70mm from the anastomosis, the peak near the inner wall moves towards the centre of the vessel whilst in all other ways the profiles are similar to the previous set.

The peak in axial turbulence at 4mm shifts further away from the outer wall with increasing anastomotic angle. The profiles at 24mm are very similar for all three angles. At 70mm, however, the peaks in axial turbulence occur at 1.5mm from the inner wall and outer wall, respectively, in both the 50° and 70° models. The relative amplitude of the trough decreases as the anastomotic angle increases. The radial turbulence profile at this position is flatter in the 70° models. In general, the radial turbulence profiles for the 50° and 70° models exhibit much broader peaks.

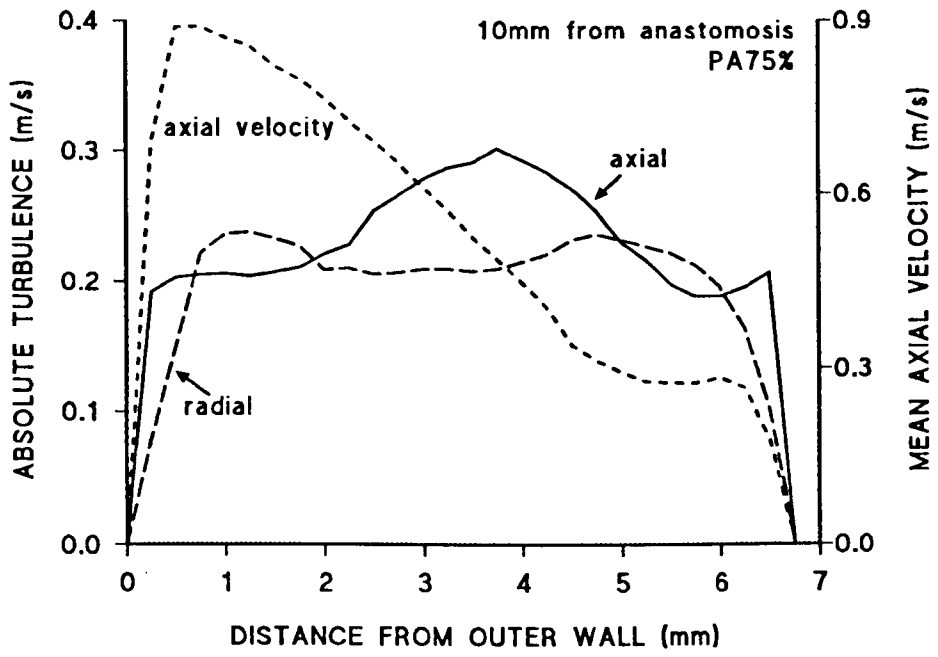

Figure 8.24 Turbulence intensity and velocity profiles in the 30°, 1.6 diameter ratio vein at 10mm from the anastomosis

At 24mm, in both these models, the peak is seen at 2mm from the outer wall.

Aside from magnitude, the turbulence profiles for the 0.8 and 2.0 diameter models are essentially the same as their 1.6 diameter ratio counterparts. However, the profiles at 4mm in the 2.0 diameter model, compare more directly with those obtained at 10mm in the 1.6 diameter ratio model.

The axial component of turbulence remains largely unchanged as the flow distribution is varied. Conversely, as the proportion of distal artery flow entering the vein is reduced, beyond 10mm from the anastomosis the radial peak becomes more prominent. Nearer the anastomosis the positions of the maxima in axial and radial turbulence intensity do vary depending on the flow distribution. As the proportion of distal artery flow entering the vein is increased, the maximum in radial turbulence intensity shifts towards the centre of the vessel.

Plot of peak cyclical turbulence intensity distributions and profiles produce

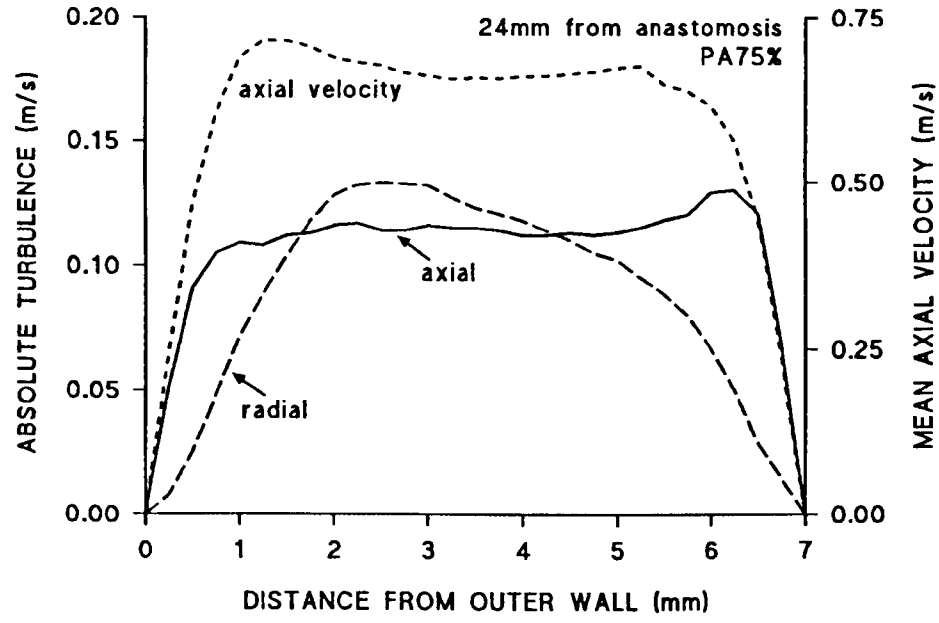

Figure 8.25 Turbulence intensity and velocity profiles in the 30°, 1.6 diameter ratio vein at 24mm from the anastomosis

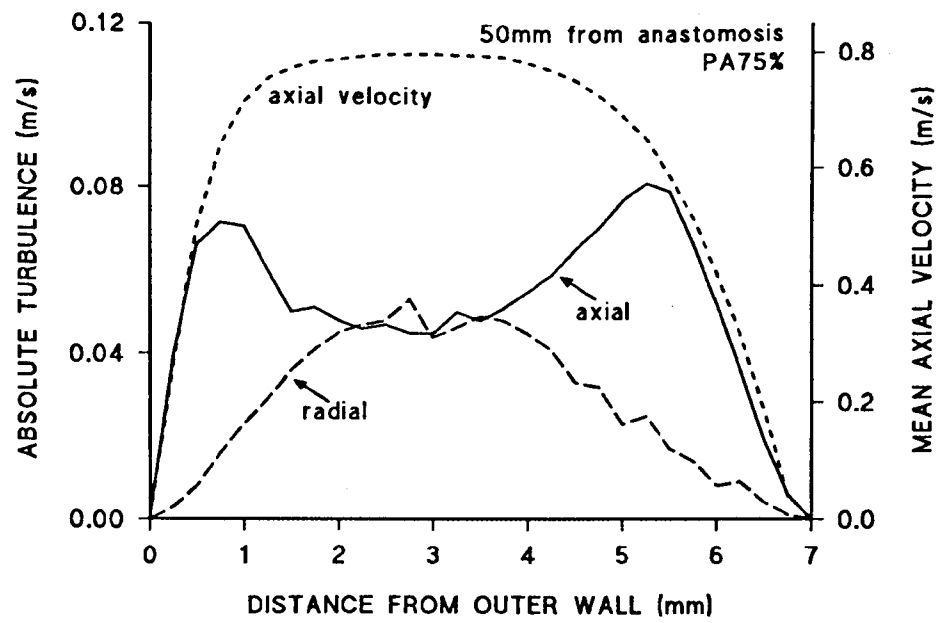

Figure 8.26 Turbulence intensity and velocity profiles in the 30°, 1.6 diameter ratio model vein at 50mm from the anastomosis

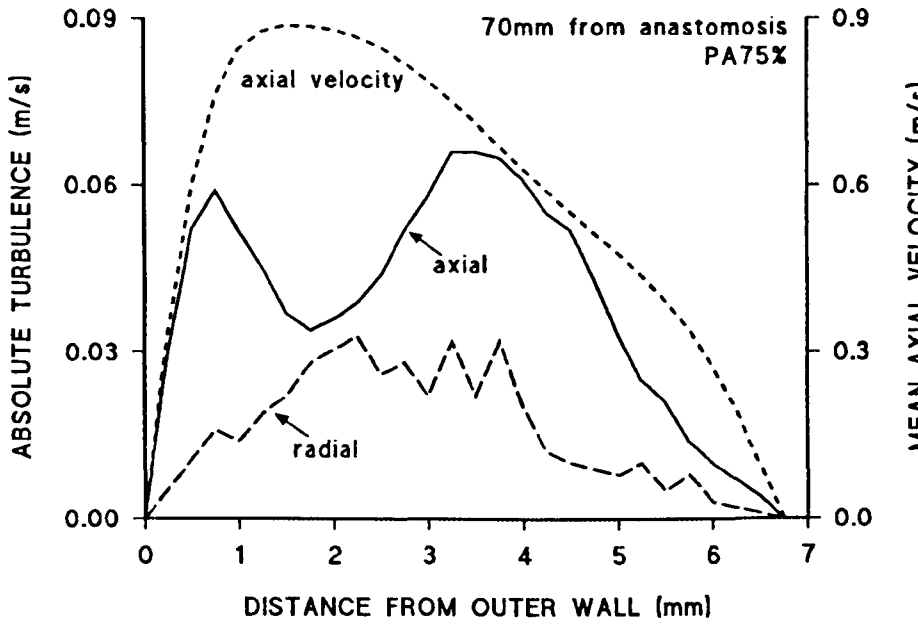

Figure 8.27 Turbulence intensity and velocity profiles in the 30°, 1.6 diameter ratio model vein at 70mm from the anastomosis

similar trends (scale factor 1.2-1.5) to those given above. Hence, only mean values have been quoted. Similarly, mean Reynolds shear stresses are scaled by a factor of approximately 2-3 to produce peak cyclical values.

Reynolds shear stresses profiles seem to follow a similar pattern to the axial turbulence intensity profiles. Likewise, Reynolds shear stress distributions for the series of models with varying anastomotic angle and diameter ratio (Figure 8.28) are very similar to Figures 8.19 and 8.20. Reynolds shear values decay from a maximum value at the suture line. At this point, peak Reynolds shear stresses vary from 150-500N/m^2 and mean values range from 50-250N/m^2.

8.6 DISCUSSION

Fry (1968) showed that shear stresses of 35-40N/m^2 can lead to deterioration of the endothelial surface within an hour of exposure. Lower stresses can increase

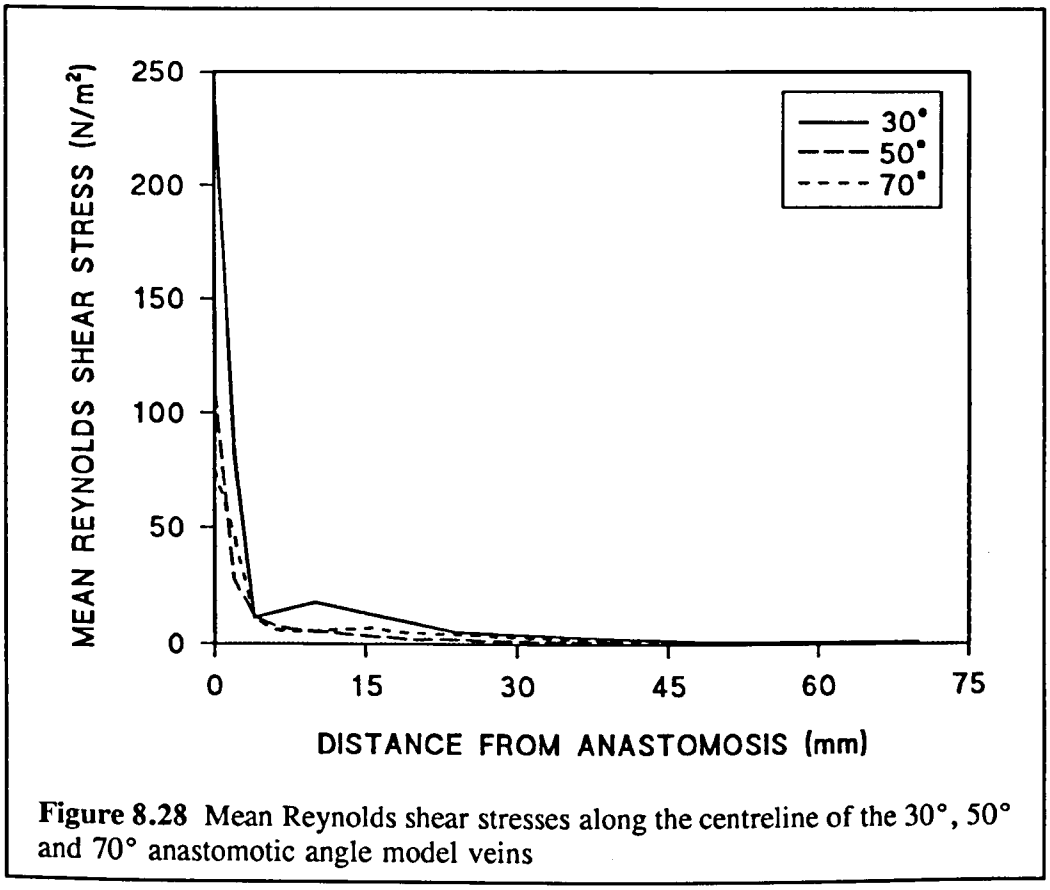

Figure 8.28 Mean Reynolds shear stresses along the centreline of the 30°, 50° and 70° anastomotic angle model veins

the permeability of the endothelial layer, damage erythrocytes (Blackshear, 1972) and cause enhanced platelet adhesiveness and increased platelet aggregation. Conversely, low wall shear stresses, below 2.5N/m^2, have been shown to be associated with a greater degree of intimal hyperplasia at vascular graft anastomoses (Salam *et al.*, 1996). Sites of oscillating bi-directional shear stresses have been found to show evidence of intimal cell proliferation and increased endothelial permeability (Ku and Giddens, 1983; Ku *et al.*, 1985). Studies have also revealed a correlation between the wall shear stress variation in the cardiac cycle and lower-limb graft occlusion (Inokuchi *et al.*, 1984; Okadome *et al.*, 1989) and the degree of intimal thickening (Morinaga *et al.*, 1985). These studies calculate wall shear stress from the intraluminal velocity profile (derived from volume flow measurements) and are, not, therefore, true measures of local oscillatory wall shear stress. However, their results

indicate that wall shear variations of below 6-7N/m^2 were associated with early-late graft failure. In curved geometries, such as the AV fistula, under pulsatile flow conditions, oscillatory wall shear stress levels may be a fairer indicator of future complications than mean shear stress levels.

The vortex on the arterial floor at the anastomosis must vary in size and intensity in phase with the upstream fluid velocity. This could produce high spatial and temporal shear stress gradients at the anastomosis. In addition, the vortex traps cells and aggregates of cells within the oscillating vortex, increasing particle-particle interactions and residence times (Karino *et al.*, 1987).

The results of the laser Doppler anemometer experiments did indeed indicate that there were high spatial and temporal wall shear stress gradients near the centre of the anastomosis. Spatial maps of wall shear stress along the floor of the artery correlated quite closely to the flow features captured by flow visualization. The oscillatory wall shear stresses in the region of the anastomosis were generally of an order of magnitude larger than the fluctuating stresses seen more proximally. The peak was found to correspond to either the primary maximum, coinciding with the centre of the main vortex, or the fluctuating flow reattachment point. The maxima in mean and oscillatory wall shear stress in the 1.6 vein-to-artery diameter ratio models ranged from 30-130N/m^2 and 30-240N/m^2, respectively. According to the studies discussed above, these levels of wall shear stress could be deleterious to the endothelial surface. Although there was no trend in the maximum value of mean wall shear stress with anastomotic angle, maximal oscillatory wall shear stress does, however, decrease proportionately to increasing anastomotic angle. On the other hand, there was no apparent trend in maximal oscillatory wall shear stress with vein-to-artery diameter ratio, while the maximum level of wall shear stress did appear to increase with increasing vein-to-artery diameter ratio. Whilst arterial wall shear stress levels for the 2.0 diameter ratio model remain within the ranges attributed to

the 1.6 diameter ratio models, levels in the 0.8 diameter ratio model were considerably smaller. Although, there may have been a substantial variation in wall shear stress magnitudes for different flow distributions, the absolute values were all above the threshold values for endothelial damage and damage to blood elements adhering to the surface.

The measurement positions in the vein corresponded to the angled portion of the vein leading away from the anastomosis (at 4mm and 10mm), the bend (at 24mm from the anastomosis) and the near-straight or straight portion of the vein after the curve (at 50mm and 70mm). Measurements of wall shear stress along the vein revealed a region of low oscillatory wall shear (2-4N/m^2) at 70mm from the anastomosis. This region of low shear appeared to extend to 50mm in the 30° and 50° anastomotic angle models. Oscillatory wall shear values were generally found to be less than 40N/m^2, except on the outer wall near the anastomosis in the 30° and 70° model veins (maximum, 145N/m^2 at 24mm in the 70° vein). Bidirectional wall shear fluctuations were also seen at 10mm from the anastomosis in the 30° model, at 10mm and 24mm in the 50° model vein and 24mm and 50mm (inner wall only) in the 70° model. As the vein-to-artery diameter ratio increased, the oscillatory shear values gradually decreased. However, at some point, this decline was counteracted by increased wall shear in larger diameter veins with greater flow through them to obtain the same Reynolds number. Thus, the magnitude of shear stress at 50mm and 70mm from the anastomosis in the 2.0 diameter ratio vein were larger than those in the 1.6 diameter ratio vein. Wall shear is bidirectional at 50mm and 70mm in the 0.8 diameter ratio vein and at 24mm, 50mm (inner wall only) and 70mm in the 2.0 diameter ratio vein. Mean and oscillatory wall shear stresses followed a similar trend for the different flow distributions. Bidirectional wall shear stresses occurred at 10mm in all flow distributions. Mean and oscillatory wall shear stresses along the vein were generally higher in the 0.8 diameter ratio model.

Sallam and Hwang (1984) found that the critical Reynolds shear stress level for incipient haemolysis was 400N/m^2, while Sutera (1977) found that prolonged exposure to Reynolds shear stresses of 150N/m^2 could induce haemolysis and Reynolds shear stresses of above 10N/m^2 could cause platelet lysis. However, the relationship between the magnitude of Reynolds shear stresses and the minimum corresponding duration for cellular damage is still unknown. Many reports cite turbulence as being potentially detrimental to blood components and the vascular wall, but very few of these studies have measured turbulence intensity *per se*. Studies have intimated a direct relationship between the amount of thrombus formation and axial turbulence intensity (Stein and Sabbah, 1974; Smith *et al.*, 1972) but even these have not been rigorous.

The compliant walls of blood vessels may reduce the absolute values of turbulent intensity found in less compliant models. Another factor that may lead to an over-estimation of turbulence intensity is that red blood cells, being deformable, are able to align their major axes with the direction of flow whereas non-deformable particles tumble and collide in an irregular fashion, augmenting turbulence effects.

The temporal peak in turbulence intensity and Reynolds shear stress occurred in the early decelerative phase of the cardiac cycle, when flow is most unstable. There was a great difference in the order of magnitude of turbulence intensity between the two velocity components measured. However, the two root-mean-square velocity fluctuation components were found to be similar in magnitude.

Centreline axial turbulence intensity, and absolute axial and radial turbulence decayed rapidly with distance from the anastomosis. Beyond 15mm from the suture line, there was little difference in the levels of turbulence between the models. Turbulence levels reached a plateau beyond a distance of 40mm. Near the anastomosis, mean axial turbulence intensity increased with decreasing anastomotic angle from 120% in the 70° model vein to 1200% in the 30° model vein. Similarly,

absolute axial turbulence near the anastomosis was much greater in the 30° model vein, whilst maximum values in the 50° and 70° model veins were similar. Mean radial turbulence intensity peaked along the curve of the vein. While the levels of mean radial turbulence intensity remained below 400% in the 30° and 50° model veins, it rose dramatically to in excess of 2000% in the 70° model. This finding explains the high outer wall oscillatory shear stresses discovered at the bend. The level at a distance of 70mm from the anastomosis of mean axial turbulence intensity was approximately 10% in the 1.25, 1.6 and 2.0 diameter ratio veins, but significantly lower in the 0.8 diameter ratio vein. There did not appear to be a clear trend in the maximum level of axial turbulence intensity with changing vein-to-artery diameter ratio. However, the maximum radial turbulence intensity was considerably larger in the 1.2 and 2.0 diameter ratio veins, whereas absolute radial turbulence values were highest for the 1.6 and 2.0 diameter ratio models. The effects of varying the flow distribution were only apparent for the axial absolute turbulence (increases as the proximal artery contribution increases) and radial turbulence intensity distributions.

Near the anastomosis, both axial and radial turbulence intensity profiles peaked near the inner vessel wall. As the convective flow profile became more symmetrical, axial turbulence intensity dipped in the centre of the vessel (at 50mm from the anastomosis). The inner wall peak shifted towards the centre of the vessel further away from the anastomosis. Peaks in radial turbulence intensity generally occurred near the centre of the vessel. In general, the radial turbulence intensity profiles for the larger anastomotic angle models exhibited much broader peaks. Small differences were seen in the amplitude and positions of the axial turbulence peaks and troughs with anastomotic angle and vein-to-artery diameter ratio.

Reynolds shear stress distributions and profiles showed a similar trend to axial turbulence intensity and absolute axial and radial turbulence. Reynolds shear stress

decayed, from a maximum at the suture line, with distance from the anastomosis. Reynolds shear stress values were found to increase with decreasing anastomotic angle. Peak Reynolds shear stresses varied from 150-500N/m^2 and mean values ranged from 50-250N/m^2. These peak values lie within the range found to produce adverse stresses on red blood cells and platelets. Erythrocytes and platelets exposed to such levels of Reynolds shear stress may be ruptured in the bulk flow at the anastomosis and their cellular contents and factors may be washed downstream. As the exposure to peak temporal Reynolds shear stress occurs for a fraction of each cycle, it is difficult to determine the effects of prolonged exposure to varying Reynolds shear stresses. The release of factors may well occur below lethal levels for haemolysis and platelet lysis.

The appearance of coherent transitional structures in the convective velocity waveforms has been shown to provide an indication of the level of flow disturbance in stenosis models (Talukder *et al.*, 1986; Lieber, 1990). Such large scale organised structures represent bulk fluid flow effects and preferred modes of oscillation, such as vortex shedding, induced by the accelerative/decelerative phases of the pulsatile cycle. Power spectral density distributions of the mean cyclic velocity at various points along the vein revealed the presence of frequencies above the fundamental component, but coherent frequency spikes, reported to be within the range 6-13Hz (Lieber, 1990; Hughes, Shortland and How, 1996) coincident to both channels were not seen. This may be due to the higher level of turbulence in this particular case masking the coherent contributions in the same frequency band, as coherent behaviour which contains slight phase and magnitude variations cycle by cycle can be attenuated by ensemble averaging. Critical Reynolds numbers are highly dependent on the geometry of the model and the flow distribution. Given the results of flow visualization from Chapter 7, it is possible that the range of Reynolds numbers over which vortex shedding occurs may be much lower in the AV fistula

than in other physiological models; at Re=600, the larger coherent structures may have already disintegrated into smaller eddies due to the relatively strong random fluctuations of flow, as is the case in moderate to severe stenosis models (Talukder *et al.*, 1986). Another argument could be that the low pulsatility of flow in the fistula may ensure the stability of the primary vortex throughout the cycle.

Talukder *et al.* (1986) also noted that the coherent structures seen in their model appeared earlier in systole with increasing degree of stenosis. Similarly, peak turbulence intensity and Reynolds shear stress appeared slightly earlier (20-30ms earlier) in the flow cycle as the angle of anastomosis was increased. Although, there was a noticeable difference (approximately 50ms) between the 0.8 diameter ratio and the 1.6 diameter ratio models, there was no appreciable shift in peak turbulence intensity between the 1.6 and 2.0 diameter ratio models. If there is a correlation between the relative position of peak turbulence and the level of flow disturbance, there may also be an analogous relationship between the angle of anastomosis, the vein-to-artery diameter ratio and the level of flow disturbance in AV fistulae.

8.6.1 Sources of error

One important source of error in the measurements made arises from the averaging of the LDA signal over a finite sampling volume. This is partly dictated by the alignment of the optics of the LDA, by refractive index matching at boundaries, by the positioning and symmetry of the wax cast and by the flatness silicone rubber surface.

Differences in resolution between the different frequency/velocity scales may produce discontinuities in velocity profiles due to the difference in quantization levels (as the resolution is dependent on the bandwidth chosen) and the certain combinations of centre frequency and bandwidth allowed. Another problem with the Dantec system used was that the only allowed negative centre frequency/velocity (in the

experimental range) was approximately 1m/s. As a result, in some cases, the choice was between increasing the bandwidth, reducing the resolution and the validated data rate, or clipping the higher/lower velocity data. This trade-off between increasing bandwidth and losing validation (and sometimes data rate) only becomes a problem in turbulent flow regimes; when flow is more laminar, increasing bandwidth results in better validation and a higher data rate. For measurements in the vein, the head of the laser was rotated through 180° so that the venous outflow followed the positive x-component direction to avoid difficulties with negative centre frequencies.

The BSA collects discrete Doppler bursts with random arrival times containing velocity information so, whereas regular sampling requires the Nyquist criterion to be satisfied (to be able to resolve the maximum frequency components of the signal), it is the number of bursts collected and the period of collection that limit the spatial and temporal resolution, and not the data rate in itself. By optimising the centre frequency, bandwidth and record length, lower intensity fluctuations outside the prescribed frequency range are effectively ignored. This is obviously a limitation on the accuracy of the turbulent intensity and Reynolds shear stress results, but assumed to be negligible. The data rate was found to be highly variable and dependent on the velocities of particles passing through the sample volume. Therefore, the data rate was highest along the centreline of the vessels, where the velocities were greatest, and lower near the walls and in areas of flow disturbance.

Unfortunately, LDA data collection was not an automated process. However, finding the wall at each measurement point and optimising the BSA settings for each of the 11 measurement positions before setting up a parameter file for automatic data collection would be a much lengthier process. The quickest method was found to be pausing between each position to allow changes of the BSA settings and repeat measurements, if necessary. The whole data collection process at each point was found to take approximately 30 minutes. Another problem associated with

measurements at the wall, was the traverse positioning errors caused when BURSTware creates the traverse files: the x- and y- position values inputted are rounded (down) to the nearest traverse increment and stored to 2 decimal places; when acquiring data, the traverse values are again rounded (down) to the nearest traverse increment, thus producing errors of up to 2 traverse minimum increments.

The increments between measurements along the wall are large considering that the spatial separation between locations of high and low shear stress can be very small. A full map of shear stress along the walls of the artery vein would have been desirable, but this would be a time-consuming process and only possible if there were a way to accurately produce transparent models to exact specifications (wax shrinkage, the use of filler and spray paint, imperfect alignment of the wax cast in the connectors and inadequate support distort the final model and make it impossible to define the surface to the required degree of accuracy for wall shear measurements). For the same reasons, axial and radial shear have been quoted even at points along the arterial floor where the tangent to the wall is not parallel to the axis of the artery. Also, the 12.5μm minimum incremental step of the traverse limits the accuracy of near-wall incremental measurements at an angle to the x- and y-axes. To counteract these errors, the laser was programmed to traverse in incremental steps, even though the trajectory may not have been exactly normal to the wall. At these points, however, the laser head was rotated so that true axial and radial velocity components were being measured. It is difficult to quantify errors that may arise from this procedure (despite experimental to theoretical angular errors of up to 12.5°) as they are highly dependent on the local flow field; and near-wall radial velocities were comparatively very small.

Inaccuracies in the comparative analysis between models may arise from the errors inherent in locating the origin of the model. The y=0 plane can be found by locating the walls of the proximal artery (however, this may not be an appropriate

reference if the vein is not properly aligned with the artery in the z-axis). The $z=0$ plane cannot be found in the same manner due to increasing refraction with depth in the model. A more realistic approximation can be obtained by positioning the sample volume near the wall of the proximal artery and watching for a maximum in the data rate as the traverse is moved up and down. Finding the $x=0$ plane can be a much trickier problem due to the clarity of the model and refractive index matching. It can be more accurately defined by matching the location of the floor of the artery in the anastomotic region (at several points) with the x- and y-values specifying the floor in DUCT.

The viscosity of the flow solution, and hence the flow rate, is highly temperature-dependent. To stabilize the fluid viscosity of the aqueous glycerol solution it was necessary to ensure that there was an adequate output for warm air generated by the laser through the LDA laboratory. Although an extraction system is incorporated into the laser itself, an external extractor fan was also required and the door to the laboratory was left open.

The variability in the proportion of validated data points that were coincidence filtered from position to position and between one model and another highlights errors in refractive index matching at the vessel walls due to poor surface finish of the original epoxy model or the wax cast, contact with wax while curing and the abrasive removal of paint.

It is important to remember that wall shear stresses are highly dependent on the exact local geometry of the fistula and so vary considerably from patient to patient. The results of this chapter merely characterize flow structures in the idealized situation to facilitate parametric comparison.

8.7 SUMMARY

Quantitative measurements of wall shear stress, absolute turbulence, turbulence intensity and Reynolds shear stress were made using laser Doppler anemometry from velocity data obtained from the *in vitro* models.

There were found to be high spatial and temporal wall shear stress gradients on the arterial floor near the centre of the anastomosis. Maxima occurred at a position coinciding with the centre of the main vortex and at the fluctuating flow reattachment point, the union of proximal and distal arterial flows. The maxima in mean and oscillatory wall shear stress ranged from 30-130N/m^2 and 30-240N/m^2, respectively, for the 1,6 and 2.0 diameter ratio models. These values lie within the range of wall shear stress levels that could potentially be detrimental to the endothelial surface and to blood elements in contact with the endothelium. Flow in the artery of the 0.8 diameter ratio model, however, appeared essentially laminar in character at the anastomosis.

Measurements of wall shear stress along the vein, revealed a region of low oscillatory wall shear stress (2-4N/m^2) at 70mm from the anastomosis. This region of low shear appeared to extend to 50mm in the 30° and 50° model veins. Oscillatory shear of this magnitude has been correlated with the degree of intimal thickening. Bidirectional wall shear fluctuations were seen near the anastomosis and into the curve. This region was seen to move proximally with increasing anastomotic angle and vein-to-artery diameter ratio. Sites of oscillating bi-directional shear stresses have been associated with intimal thickening and increased endothelial permeability. Oscillatory shear stress values decreased with increasing vein diameter from the 0.8 to 1.6 diameter ratio models. However, wall shear stresses then appeared to rise from the 1.6 to 2.0 diameter ratio veins. This finding must be a consequence of the difference in flow parameters when mainstream flow branches into a narrower vessel (i.e. the vein-to-artery diameter ratio is less than 1) to the case

where the branch and anastomosis are wider. Wall shear stresses were generally higher along the 0.8 diameter ratio vein. Mean and oscillatory wall shear stresses were similar for the different flow distributions.

Whereas the wall shear stress waveform was in phase with the convective velocity waveform, the temporal peak in turbulence intensity and Reynolds shear stress occurred in the early decelerative phase of the cardiac cycle, when flow is most unstable. Peak and mean axial turbulence intensity, axial and radial absolute turbulence values, and Reynolds shear stress distributions followed a similar pattern. There was a great difference between the magnitude of axial and radial turbulence intensity, due to the much larger convective flow component. However, axial and radial root-mean-square velocity fluctuations were found to be of the same order of magnitude. The differences in the shape of the axial and radial turbulence profiles may be an indication that the flow is far from axisymmetric even at a distance of 70mm from the anastomosis.

Turbulence was the dominant feature in the model vein. Axial turbulence intensity, absolute turbulence and Reynolds shear stresses decayed with distance from the anastomosis. Beyond a distance of 15mm there was little difference between the various models. A plateau was reached beyond a distance of 40mm from the anastomosis. The level of turbulence intensity at a distance of 70mm from the anastomosis was in the 1.25, 1.6 and 2.0 diameter ratio veins was around 10% (absolute value of 0.05m/s). Near the anastomosis, the axial turbulence intensity maximum increased with decreasing anastomotic angle from 120% in the 70° model vein to 1200% in the 30° model vein. No such trend was observed with changing vein-to-artery diameter ratio. Reynolds shear stress distributions followed a similar pattern to axial turbulence intensity. Peak Reynolds shear stresses varied from 150-500N/m^2 and mean values ranged from 50-250N/m^2. Exposure to such levels of Reynolds shear stresses at the anastomosis may result in haemolysis, platelet lysis

and the release of cellular contents and factors. Mean radial turbulence intensity peaked along the curve of the vein. While levels remained below 400% in the 30° and 50° model veins, it rose dramatically to in excess of 2000% in the 70° model. Maximal radial turbulence intensity was also larger in the 1.2 and 2.0 diameter ratio veins. The effects of varying the flow distribution were only apparent for absolute axial turbulence and radial turbulence intensity. Absolute axial turbulence in the vein increased with increasing proximal artery inflow.

CHAPTER 9

FINDINGS OF CLINICAL STUDY

9.1 INTRODUCTION

Radiocephalic fistulae were studied in 47 patients requiring primary access procedures for haemodialysis at the Royal Liverpool Hospital between May 1994 and April 1996 (including the 35 patients reviewed in Chapter 5). The 47 patients (37 men and 10 women) ranged in age from 15 to 83 years (mean, 60 years) at the time of fistula construction. Flow measurements (along with measurements of anastomotic angle and length) were taken intraoperatively immediately after construction of the fistula and 1 day postoperatively. There were 3 immediate (within 24 hours of surgery) failures and 1 death within a 2-week postoperative interval. In 33 cases, the development of the fistula was monitored at regular intervals for periods up to 27 months. Some patients who either live a substantial distance away from the hospital or who have moved out of the area, have been lost to follow-up. In a number of cases, the question of funding for patient transport was a limiting factor. All but 3 fistulae appeared to mature satisfactorily (in 2 cases after ligation of major cephalic branches stealing flow) according to duplex parameters. However, 5 of these 30 have not been subsequently used for dialysis: dehydration and diarrhoea caused one fistula to fail after 3 weeks, 3 patients died within 3 months of access surgery and in one patient, adipose tissue hindered palpation of the vein for needling. In the remaining 3 cases, the vessels did dilate but fistula flow was still insufficient to maintain dialysis after 3 months.

A total of 24 patients (one patient with 2 fistulae) have been follow-up regularly for at least 3 months, with a mean follow-up time of 1 year. The development, location and progression of stenoses was noted in each case. Sections 9.2 and 9.3 cover the findings in these 24 patients. Three of these patients have since died, 2 have had kidney transplants and in 6 cases, significant stenosis and fistula

failure have halted the postoperative follow-up.

9.2 PATIENT CASE STUDIES

The diagrams of the fistulae shown in this chapter have been produced by careful integration of hardcopies of successive ultrasound scans and notes, calculations and sketches made throughout the follow-up period. Each hardcopy (or split-screen image) only covers a probe length of 4cm. It may also be difficult to visualize all the fistulous vessels in one plane. Another problem is that the images take a long time to be printed out by the video printer. The most effective management of time can be achieved by storing 4 annotated images in split-screen mode but, inevitably, the individual images are considerably smaller and require detailed scrutiny and comparison with the images from previous scans. For the above reasons it is not possible to make a composite picture of the anastomosis and vein relying solely on the hardcopy output of the ultrasound scanner.

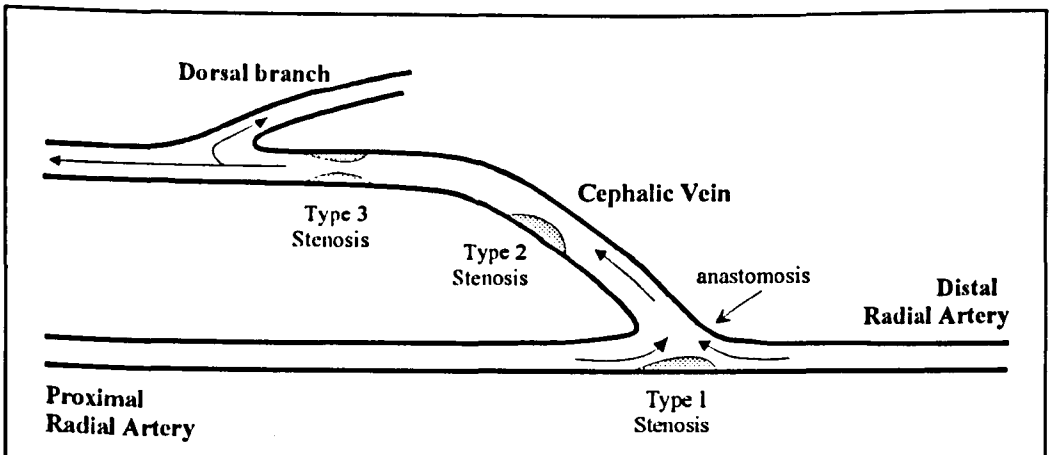

Figure 9.1 Sites of stenosis

Where pertinent to the clinical findings, patient medical history and details on the development of the fistula and stenoses have been included. All 24 patients were found to have stenoses. These stenoses have been categorised as progressive

or non-progressive, and according to their location: Type 1, on the floor of the artery at the anastomosis, Type 2, along the curved region of the cephalic vein, and Type 3, adjacent to the curvature of the vein (see Figure 9.1)

Patient 3: Type 1 stenosis apparent at 17 weeks (not progressive). Venous lumen has dilated to 65mm^2, carrying a flow of 750ml/min at 18 months. Vein was aneurysmal at the wrist. Anastomotic angle, 35° and length of arteriotomy, 10mm. Patient has ischaemic heart disease.

Patient 5: Type 1 apparent at 12 weeks (not progressive). Aneurysmal dilatation of vein. Branch about 3cm from anastomosis was ligated at 7 months. Luminal area has dilated to a maximum of 90mm^2, now appears to be gradually decreasing over time - no obvious cause. Anastomotic angle, 40° and length, 8.5mm. Patient suffers from angina.

Patient 6: Fistula flow largely supplied by retrograde flow through distal artery. The venous lumen has only doubled in size during the first year. However, it supplies a good flow of 700ml/min. Type 1 stenosis apparent (not progressive) at 10 months and Type 2 stenosis discovered at same time. Anastomotic angle, 65° and length, 6mm. Patient is a moderate smoker.

Patient 9: Type 1 stenosis present (not progressive). Evidence of a marked Type 3 stenosis, 1-2cm from the anastomosis at 15 months. Fistula flow and venous luminal area seen to decrease after 32 weeks: from a peak of 55mm^2 at 40 weeks to 35mm^2 at 15 months with fistula flow of only 230ml/min. Anastomotic angle, 70° and length 9mm. Previous

right wrist fistula failed after 16 months (thrombosis due to soft atheroma).

Patient 12: Type 3 stenosis (4-5cm from the anastomosis) was detected at 1 year, just after patient had a kidney transplant. The vein was aneurysmal at the wrist and displayed considerable tortuosity with reduced flow. Anastomotic angle, 60° and length, 9mm.

Patient 14: Type 2 (along inner wall) and 3 (3cm from the anastomosis) stenoses present at 9 weeks (not progressive). Arteries calcified; patient has peripheral arterial disease, angina and has had a myocardial infarction. Anastomotic angle, 29° and length, 8mm.

Patient 16: Type 3 stenosis was detected 3-4cm from the anastomosis at 27 weeks. Subsequently, vein gradually became less dilated as the flow through the fistula decreased until the fistula clotted at 10 months. Type 1 and 2 stenoses were also present (not progressive). Anastomotic angle, 45° and length 5.5mm.

Patient 18: Type 3 stenosis was detected at 18 months. Venous luminal increased from $17mm^2$ to $93mm^2$ over the first year but since then, no increase. Flow still a good 800ml/min but less than at 1 year. Anastomotic angle, 37° and length, 8mm. Patient is an mild smoker.

Patient 21: Fistula flow and luminal area reached a peak at 12 weeks. Marked decrease in fistula flow preempted the later discovery (at 37 weeks) of a Type 3 stenosis 2-3cm from the anastomosis. Anastomotic angle,

30° and length 11mm.

Patient 22: Type 3 stenosis apparent at 6 months (not progressive). The lumen of the vein has been steadily dilating to 87mm^2 at 18 months with a flow of 900ml/min. The artery is, however, calcified and does not appear to have dilated very much over the follow-up period. Anastomotic angle, 45°. Patient has angina.

Patient 24: Type 1 stenosis apparent at 3 months. The vein is aneurysmal at the anastomosis. Patient was not seen after the 3-month follow-up. Antegrade flow in the distal artery. Anastomotic angle, 60° and length, 11mm. Patient has angina and is a diabetic.

Patient 25: Type 3 stenosis present at 3 weeks (progressive and more pronounced at 5 months). Type 1 stenosis detected at 10 weeks (not progressive). Anastomotic angle, 50°.

Patient 27: Fistula failed at 6 months due to the poor calibre of the vein. A Type 3 stenosis was evident 2cm from the anastomosis at 6 weeks. Antegrade flow in the distal artery. Anastomotic angle, 60° and length, 6.2mm.

Patient 29: Mild Type 3 stenosis present 2cm from the anastomosis (not progressive). Anastomotic angle, 55° and length, 8mm.

Patient 32: Fistula failed at 11 months due to a Type 3 stenosis (detected at 4 months) 3cm from the anastomosis. Post-stenotic dilatation was

followed proximally by another stenotic region. Fistula flow had decreased from 500ml/min at 3 weeks to 240ml/min at 4 months. Anastomotic angle, 60° and length, 7mm. Patient has peripheral arterial disease and has had strokes.

Patient 33: Fistula failed at 18 weeks due to a Type 3 stenosis. Fistula flow decreased from 400ml/min at 3 weeks to 130ml/min at 3 months. Anastomotic angle, 50° and length of arteriotomy, 7.2mm. Patient has myeloma.

Patient 34: Possible Type 2 stenosis at 3 weeks. Fistula flow at 3 weeks was 400ml/min. Patient only scanned twice before his death. Anastomotic angle, 55°. Patient suffered from angina and peripheral arterial disease. The radial artery was calcified.

Patient 35: Type 1 and 3 stenoses present (not progressive). Antegrade flow in the distal artery. Anastomotic angle, 30°. Patient is anaemic.

Patient 38: Evidence of a Type 3 stenosis 5cm from the anastomosis. The vein becomes tortuous and flow is turbulent in this region. Fistula flow at 38 weeks was 200ml/min. Anastomotic angle, 30° and length, 9mm.

Patient 39: Type 1 and 3 stenoses detected (not progressive). Anastomotic angle, 50° and length 6.2mm. Patient is a diabetic and a moderate smoker.

Patient 41: The venous luminal area reached a maximum at 4 months and stabilised over the proceeding 4 months. Type 3 stenosis discovered

at 8 months. Fistula flow has decreased from 500ml/min to 330ml/min over this time interval. Antegrade flow in the distal artery. Anastomotic angle, 40°. Patient has had a minor stroke.

Patient 42: Type 1 stenosis detected (not progressive) at 12 weeks. Anastomotic angle, 25° and length, 9.5mm.

Patient 43: Long Type 3 stenosis detected 2cm from the anastomosis at 5 months - tight and progressive. Type 1 stenosis also observed (not progressive). Antegrade flow in the distal artery. Anastomotic angle, 45°. Patient has myeloma. This patient is also Patient 33.

Patient 44: Type 1 stenosis present (not progressive). Anastomotic angle, 40° and length of arteriotomy, 6mm.

Patient 46: Type 2 stenosis seen at 8 weeks. Patient died before next follow-up - unable to ascertain whether it was progressive. Anastomotic angle, 40° and length, 11mm. Patient suffers from hyperlipidaemia.

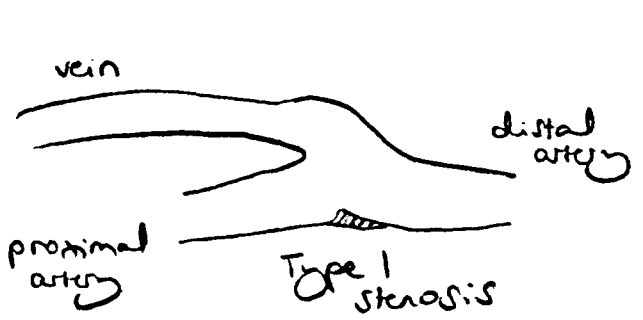

Patient 3 at 17 weeks

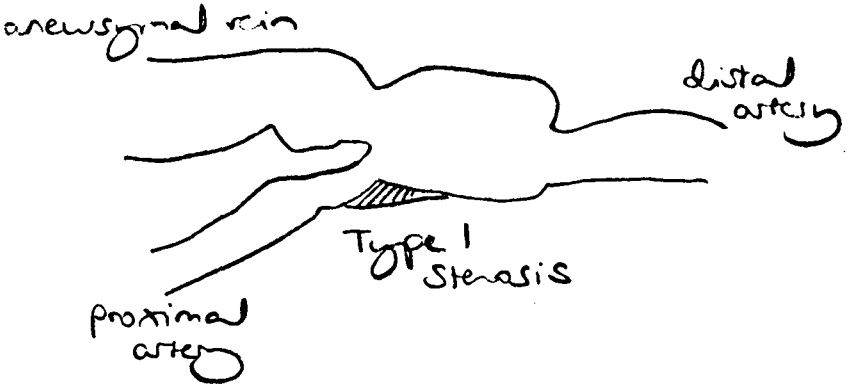

Patient 5 at 4 months

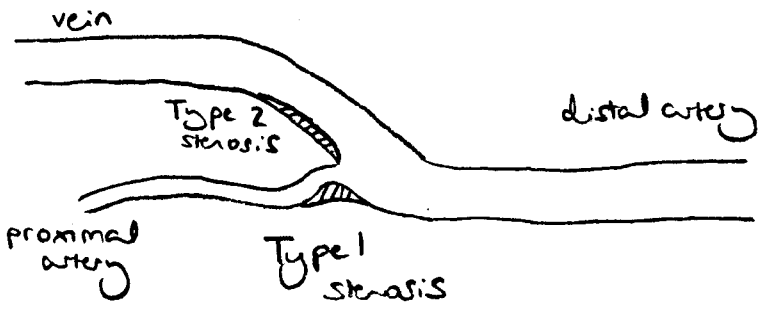

Patient 6 at 10 months

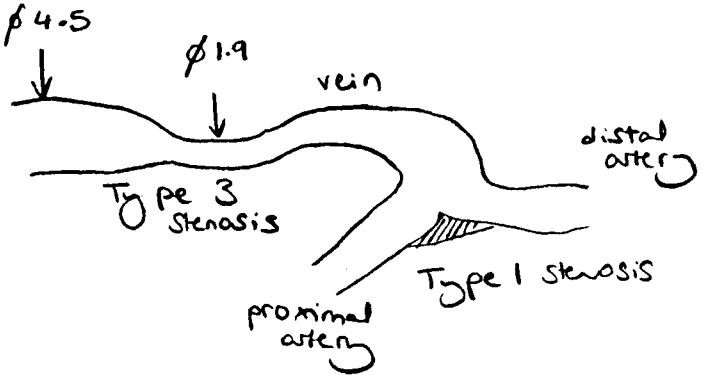

Patient 9 at 15 months

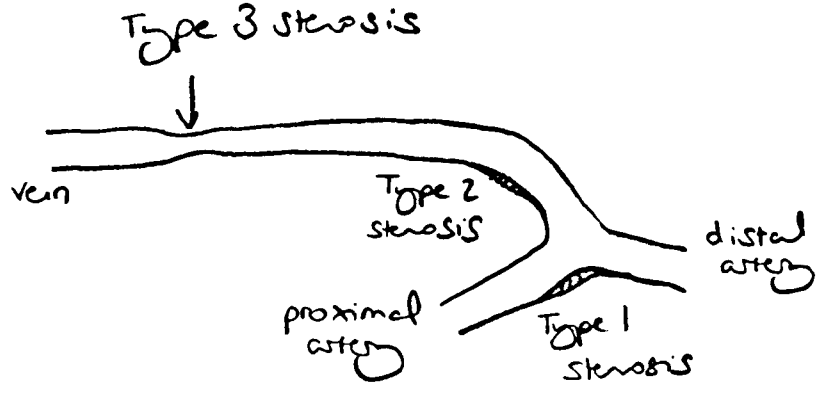

Patient 16 at 27 weeks

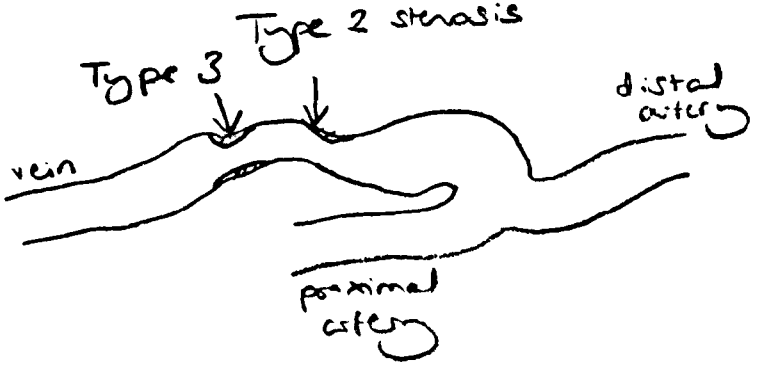

Patient 18 at 18 months

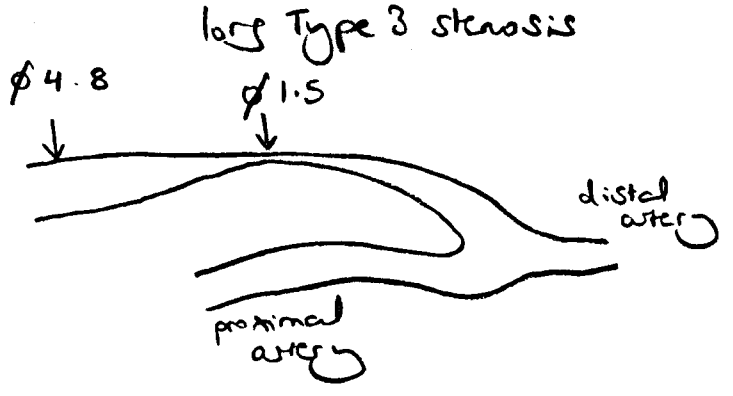

Patient 21 at 10 months

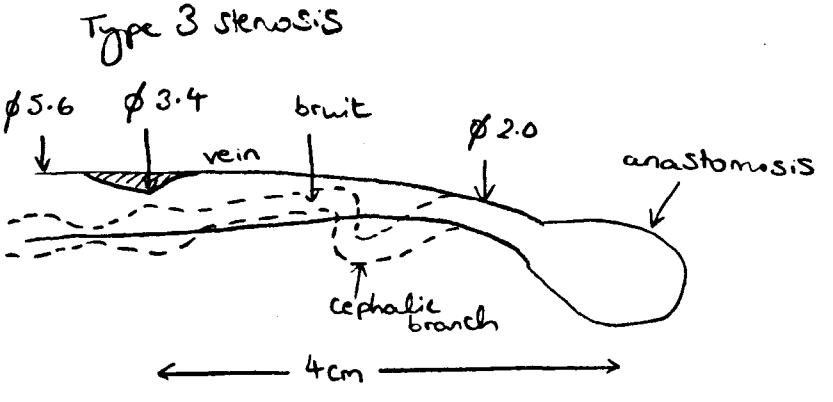

Patient 22 at 12 months

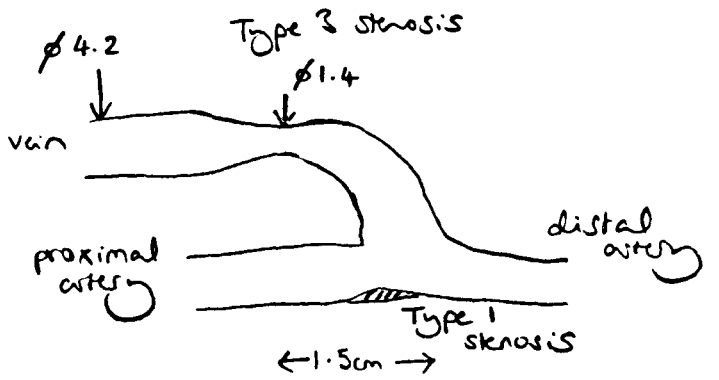

Patient 25 at 5 months

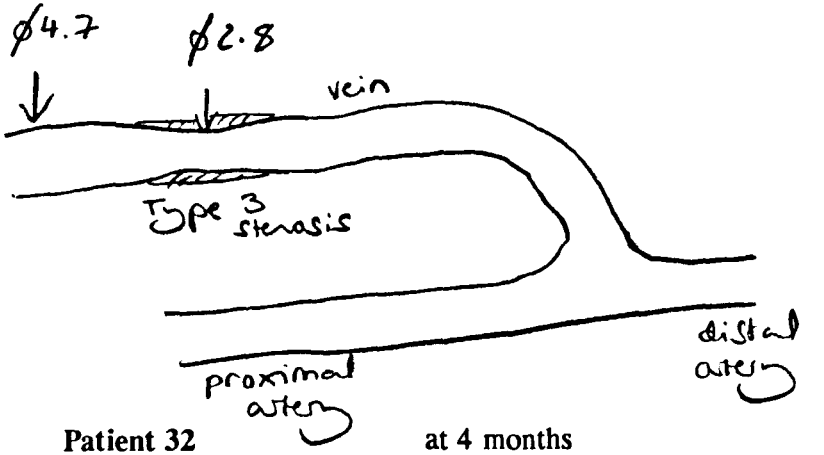

Patient 32 at 4 months

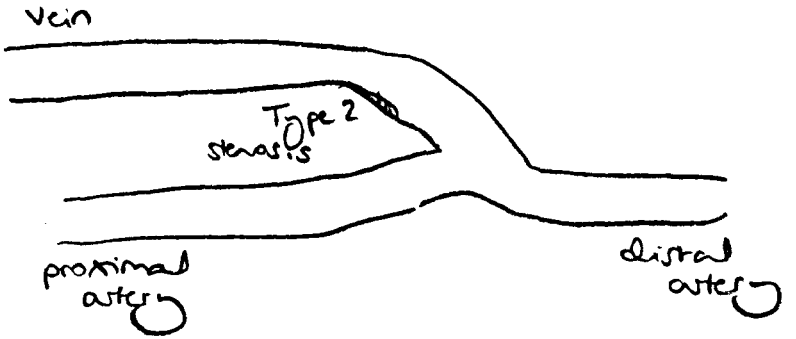

Patient 34 at 3 weeks

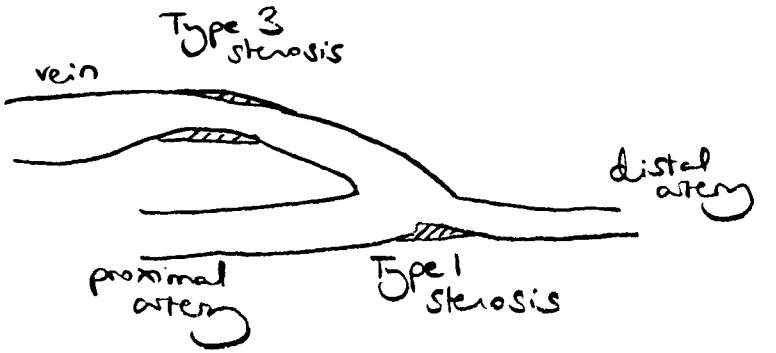

Patient 35 at 8 months

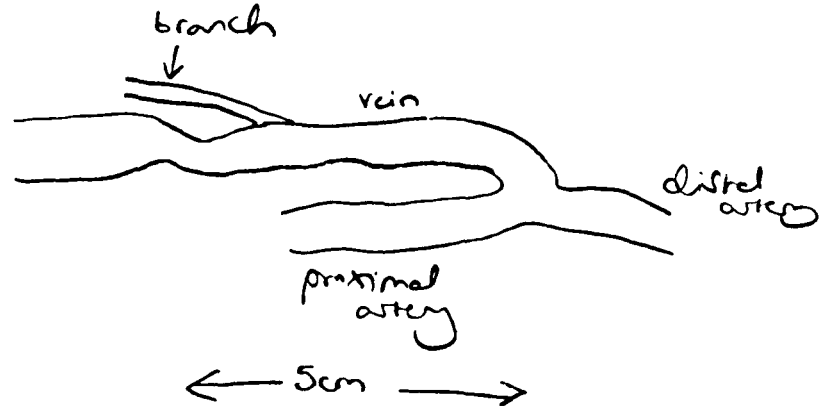

Patient 38 at 7 weeks

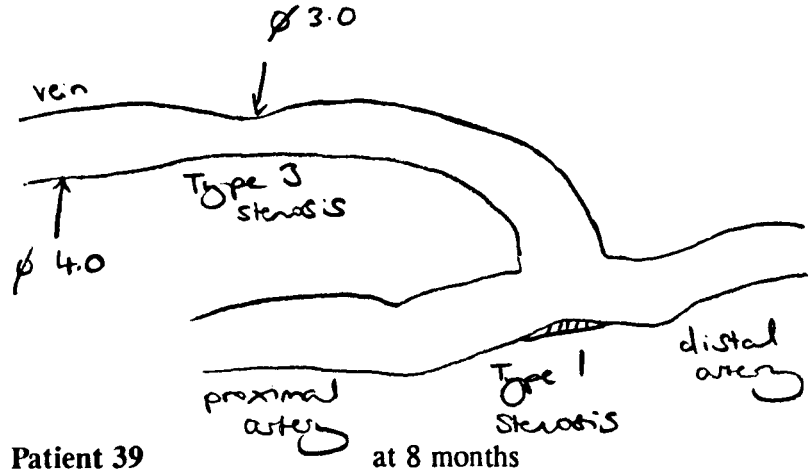

Patient 39 at 8 months

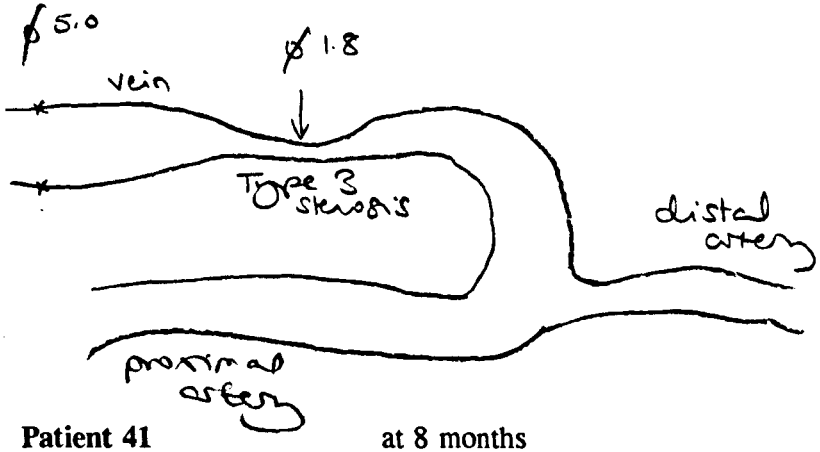

Patient 41 at 8 months

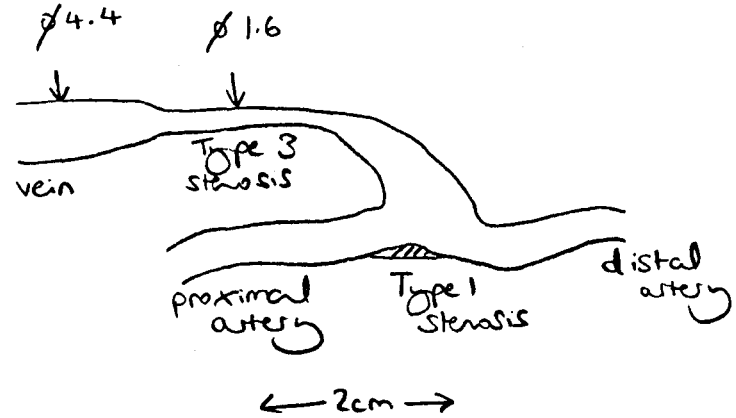

Patient 43 at 5 months

9.3 ANALYSIS OF RESULTS AND DISCUSSION

The results of the clinical study using duplex and colour-flow ultrasonography suggest that stenotic lesions can be isolated to three specific sites (Figure 9.1) in all the patients studied: at the anastomosis (Type 1 stenoses), on the curvature of the vein (Type 2 stenoses) and where the vein straightens out (Type 3 stenoses). It is important to note, however, that not all these stenoses are progressive or will become clinically significant. The localised development of intimal hyperplasia would seem to implicate the geometry of the fistula and haemodynamics in the aetiology of the process.

Table 9.1 Type and number of stenoses in 25 fistulae

Type 1 Stenoses	**12**
progressive	0
non-progressive	12
Type 2 Stenoses	**5**
progressive	1
non-progressive	4
Type 3 Stenoses	**17**
progressive	12
non-progressive	5
Total number of stenoses	**34**

Since fistula failure is multi-factorial and the processes leading to intimal hyperplasia are little understood at this time, it has been an impossible task to attribute any of the stenoses seen to a particular geometrical fistula configuration. Table 9.1 summarises the distribution of the stenoses discussed in the previous section. The majority of Type 1 and Type 2 stenoses do not appear to be progressive and are probably a direct result of adaptation to altered haemodynamics when the vein is anastomosed to the artery. In contrast, the majority of Type 3 stenoses appear to be progressive, eventually encroaching on the lumen and limiting blood flow.

The degree of stenosis appears to vary widely amongst the patients studied: the percentage luminal area reduction reaches approximately 90% at only 5 months in Patients 25 and 43, at 8 months in Patient 41, at 10 months in Patients 16 and 21 and greater than 10 months in Patient 9. The actual percentage stenosis at a particular time may not be an accurate assessment of the degree of stenosis due to the continuing dilatation of the vein. Dilatation progresses (albeit at a slower rate) long after the first two months, and so the stenosis may become flow reducing at a later stage than expected in other parts of the vascular system. Also, the aneurysmal dilatation and tortuosity of the vein with time make it difficult to gauge the relative luminal areas, especially along the curve of the vein which can be generally narrower than the proximal portion of the vein.

Table 9.2 presents the clinical data in patients with progressive and non-progressive stenoses. There does not appear to be any correlation for progressive versus non-progressive stenoses with sex and age. A large number of the patients do have some form of vascular disease (indicated by intermittent claudication on walking, a history of strokes, angina or heart attacks) or are diabetic. These factors do not seem to correspond to a greater incidence of progressive stenoses in these patients. In comparison, patients with previous access surgery show a increased risk of developing progressive stenoses. Myeloma and smoking could also be associated with a greater risk of developing progressive stenoses (although the statistical evidence for this theory is limited in the present study).

There also seem to be slight differences in mean anastomotic angle and length between the two groups which imply that larger anastomotic angles and smaller diameter anastomoses could be additional risk factors. The size of the anastomosis is one major factor governing the flow through the fistula, so a smaller anastomosis may cause complications. Similarly, smaller anastomotic angles would be expected to lead to greater flow distortion at the anastomosis when fistula flow is largely

supplied by the proximal artery (as is the typical case in both groups); however, the results of the clinical study appear to contradict this theory. There is also no relationship between the vein-to-artery diameter ratio in these patients and the incidence of progressive stenoses.

Table 9.2 Clinical data and risk factors by type of stenosis

	Patients with progressive stenoses N=13	Patients with non-progressive stenoses N=12
Sex (male/female)	11/2	10/2
Mean patient age (yr)	61	61
Diabetes mellitus	0	2
Peripheral arterial disease, ischaemic heart disease, strokes	2	6
Myeloma	2	0
Hyperlipidaemia	0	1
Smoker	2	1
Previous AV fistulae	4	0
Mean vein-to-artery diameter ratio at 1 day	1.3	1.3
Retrograde/Antegrade flow in the distal artery	10/3	10/2
Mean flow division into the vein	77% PA, 23% DA flow	75% PA, 25% DA flow
Mean anastomotic angle	49°	42°
Mean anastomotic length	8mm	9mm

It is important to bear in mind that it is difficult to determine the individual effects of any particular clinical variable when its role in stenosis cannot be independently distinguished. In a number of cases, patients have been followed up for relatively short periods of time, and so patient records are not complete; this

factor must influence the results of the study and their statistical validity.

One point of ambiguity in the clinical findings is the effect of the dorsal branch and its diversion of flow on the location of Type 3 stenoses. Branches inevitably produce flow disturbances and regions of flow separation. In the case of the patients studied, there does not appear to be a venous tributary immediately adjacent to any of the stenoses along the straight portion of the cephalic vein. The distance of the dorsal cephalic branch from the anastomosis varies considerably in patients, so it is impossible to rule out any connection. This contingency has not been accounted for in the design of the fistula models, but it is necessary to limit the number of haemodynamic factors under investigation initially so as not to confound the results.

CHAPTER 10

CONCLUSIONS

10.1 RELATIONSHIP BETWEEN CLINICAL FINDINGS AND HAEMODYNAMIC DATA

The clinical study identified three specific sites of stenosis in patients with AV fistulae: at the anastomosis on the floor of the artery (Type 1 stenoses), on the inner wall of the curved region of the cephalic vein (Type 2 stenoses) and just proximal to this curved segment where the vein straightens out (Type 3 stenoses). The localized development of intimal hyperplasia would seem to implicate the geometry of the fistula and haemodynamics in the aetiology of intimal hyperplasia.

Stenoses were present in all the patients that were followed up for at least three months. However, a significant number of these stenotic lesions were found to be non-progressive and did not become clinically significant. The specific combination of geometry and flow conditions could be the mediating factor in the transition from non-progressive to occlusive state.

Type 1 stenoses were generally found to be non-progressive, and are, hence, more likely to be a feature of vascular remodelling. This site corresponded to the region occupied by the large vortex at the union of proximal and distal arterial flows. Large oscillating wall shear stresses (30-240N/m^2) were measured in the region of this vortex and at the flow reattachment point at the union. Wall shear stresses of this magnitude can lead to deterioration of the endothelial surface, damage erythrocytes and cause enhanced platelet adhesiveness and increased platelet aggregation. Also, the vortex is a stable structure and is associated with high residence time of mitogens and chemoattractants. Although there are variations in mean and oscillatory wall shear stress with anastomotic angle, vein-to-artery diameter ratio and flow distribution, values remain (except in the case of the 0.8 diameter ratio model) within the range injurious to the endothelium and blood particles in contact with it.

Remodelling of this region on the floor of the artery may be an attempt to adapt to the new non-anatomic configuration and reduce wall shear levels to within normal physiological limits.

Turbulence was the dominant feature in the vein. The high shear stresses inherent in turbulent flow may damage blood elements and initiate cell proliferation. The Reynolds shear stresses at the anastomosis (peak values, 150-500N/m^2) were found to be in the range associated with haemolysis (sub-lethal and lethal) and platelet lysis. Although, Reynolds shear stress values decayed rapidly away from the anastomosis, a coagulation cascade may be initiated at the anastomosis. Factors, aggregates and fragmented particles may be swept downstream until they reach a point where the wall shear is low enough to allow them to adhere to the endothelium. As coagulation cascades occur within a fraction of a second, it is quite feasible that the effects may be appreciable within centimetres of the anastomosis. Wall shear stresses on the inner wall of the vein were generally much lower than on the outer wall. This fact, combined with the bi-directional nature of the wall shear stresses along the curve of the vein, could explain the Type 2 stenoses. These stenoses are more likely to be influenced by anastomotic angle and vein-to-artery diameter ratio as the Reynolds stresses at the anastomosis varied considerably from model to model. In the case of the 50° and 70° anastomotic angle and 0.8 and 1.25 diameter ratio model veins, the lower peak and mean Reynolds shear stresses measured may intercede in the transition to progressive stenotic lesions.

The site of Type 3 stenoses coincided with a region of low oscillatory shear (2-4N/m^2) where the transport of accumulated lipids across the wall into the blood may be inhibited. Lipid deposition within the intima is generally seen to be a precursor to atherosclerotic plaque formation. This region of low shear was presented in all but the 0.8 vein-to-artery diameter ratio model vein (in the corresponding region of this model, oscillatory inner wall shear was approximately 80N/m^2) and 2.0

diameter ratio vein (in this model, it is possible that the low shear region was beyond the measurement range). The extent of this region, though, increased with increasing anastomotic angle, and when neither proximal nor distal arteries were occluded.

These results show a correlation between stenotic sites found *in vivo*, flow features visualized in the models and haemodynamic data. Of the parameters investigated, anastomotic angle appears to have the largest influence on the size and extent of the three types of stenosis and whether they may be progressive or non-progressive.

10.2 IMPLICATIONS FOR ACCESS SURGERY

This study has largely focused on two parameters in AV fistula geometry: anastomotic length and the vein-to-artery diameter ratio. One observation that can be made is that it is better to construct AV fistulae with large anastomotic angles, ideally with angles greater than or approximately equal to 50° (as there were only slight differences between the data for the 50° and 70° models). The information on varying vein-to-artery diameter ratio is less conclusive. However, small diameter veins (as in the case of the 0.8 diameter ratio model) which are associated with increased incidence of fistula failure (Wong *et al.*, 1996) generally possess much higher wall shear stresses. These veins dilate, but at a much slower rate, and wall shear stresses may not be lowered significantly over time. Chronic levels of high wall shear may increase the likelihood of endothelial damage. Arteriovenous anastomoses with small diameter veins should be avoided.

Progressive stenoses were identified in a large proportion of the patients followed-up. This finding would advocate the need for an effective surveillance programme to monitor fistula development. Routine surveillance has significantly improved patency in peripheral arterial bypass grafts. Stenotic lesions can be monitored, permitting the option of interventional procedures before the stenoses

become occlusive and the fistulae thrombose.

10.3 DISCUSSION

Although the clinical study has aptly provided the parameters for model-making and flow modelling, the results from the study are far from conclusive and remain the weak link in the overall picture.

In the new era of NHS Trusts, Business Directorates and effective cost management, clinical studies can appear low on the priority list. The cost of transporting patients was a large factor governing the number of patients followed-up after access surgery and their follow-up intervals. An additional problem was that patients are referred to the Royal Liverpool University Hospital for access procedures from places as far away as North Wales. These patients were inevitably followed-up nearer home.

The extent of renal impairment and the deteriorated state of health of patients requiring dialysis, already do not make the prognosis for fistula survival good. The varying levels of plasma constituents in between dialysis sessions and throughout the day even may have a larger impact on the development of the fistula than under normal circumstances. These patients also tend to suffer from other diseases, such as diabetes mellitus and ischaemic arterial disease, that may confound the results of the clinical study.

Surgeon-to-surgeon variability is another factor that has not been previously addressed. In such a small sample population, this may be as important a consideration as fistula geometry. A total of 7 different surgeons performed the anastomoses on the 47 patients included in the study and each has his own special technique.

The general policy of the consultant renal transplant surgeons here is to attempt a wrist fistula even when there may be some doubt as to the calibre of the

lower arm vessels. This may lead to a greater incidence of complications, further confusing the results of the clinical study.

Laser Doppler anemometry can be a time-consuming way of making quantitative measurements in flow models. Subsequent processing of the numerous velocity files can also involve a lengthy process. These factors impose a great limitation on the number of feasible measurement positions and flow conditions. Experimental time and measurement errors may be reduced by improving the surface finish and alignment of the models. By being able to produce exact replicas of the original CAD/CAM designs, it may be possible to use the computer aided design to define the traverse grid for the velocity measurements. In the future, more intelligent laser Doppler anemometry systems may exist which can accurately sense the position of the walls, thereby, saving a considerable amount of time.

10.4 SUGGESTIONS FOR FUTURE WORK

Parametrized models may provide considerable information on the haemodynamic effects of particular variables when such variables are difficult to isolate individually in a clinical situation.

To fully characterize the haemodynamics in the vein, it is necessary to find a more direct method of assessing wall shear stresses along the vein. One possibility is to employ a large number of shear-dependent transducers flush with the vessel walls.

Another useful adjunct to this set of experiments would be to remodel the fistula using histopathological data to monitor the altered haemodynamics as the fistula develops and stenoses progress. This might provide an insight into which

factors control the transition from non-progressive to occlusive stenoses.

As the links between haemodynamics and vascular pathology are still speculative, endothelial cell seeding on the surface of the model would be the next stage in *in vitro* modelling. Such models may be able to provide direct evidence of endothelial damage in response to haemodynamic factors. However, only experiments using whole blood would be able to identify the effects of high Reynolds shear stresses and the resulting thrombotic processes.

The ideal scenario would be to make *in vivo* measurements of wall shear stresses, absolute turbulence and Reynolds shear stresses and relate these to the sites of stenosis and fistula failure. With continual improvements in medical ultrasound system engineering and probe technology, clinical ultrasound systems may be able to routinely perform these calculations one day.

APPENDIX A

UPPER EXTREMITY ANATOMY

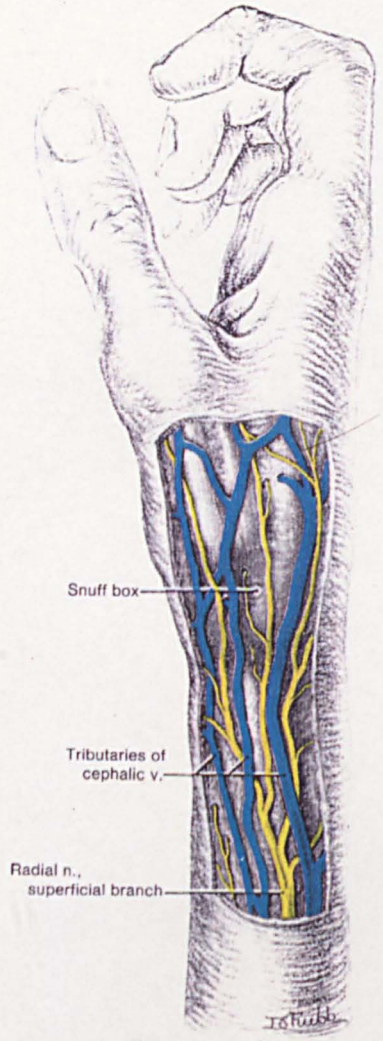

Figure A1.1 Dissection showing the superficial veins crossing the anatomical snuffbox (Hamilton, 1976).

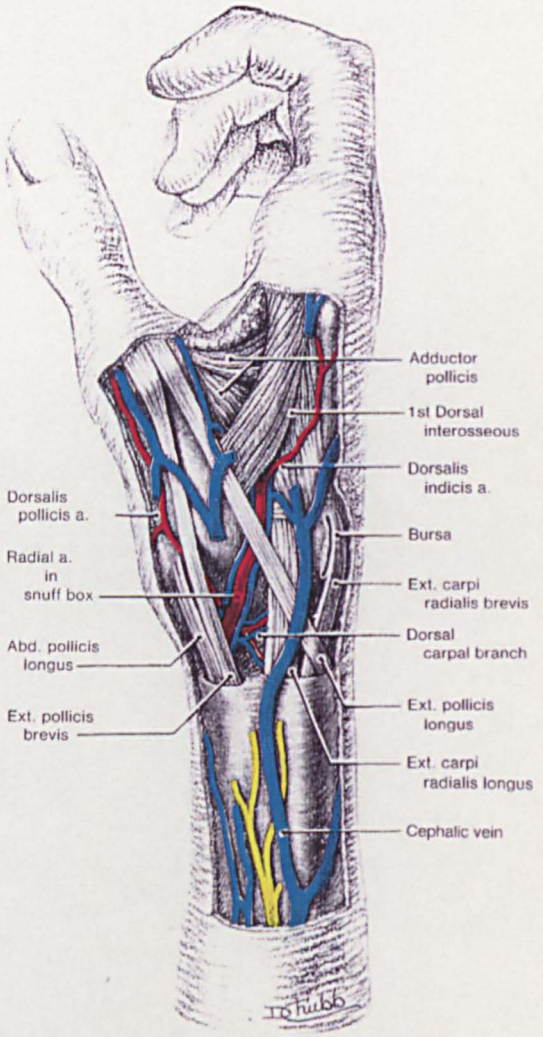

Figure A1.2 Dissection showing the three tendons of the thumb forming the sides of the triangular hollow known as the *anatomical snuffbox*, and the radial artery in its floor (Hamilton, 1976).

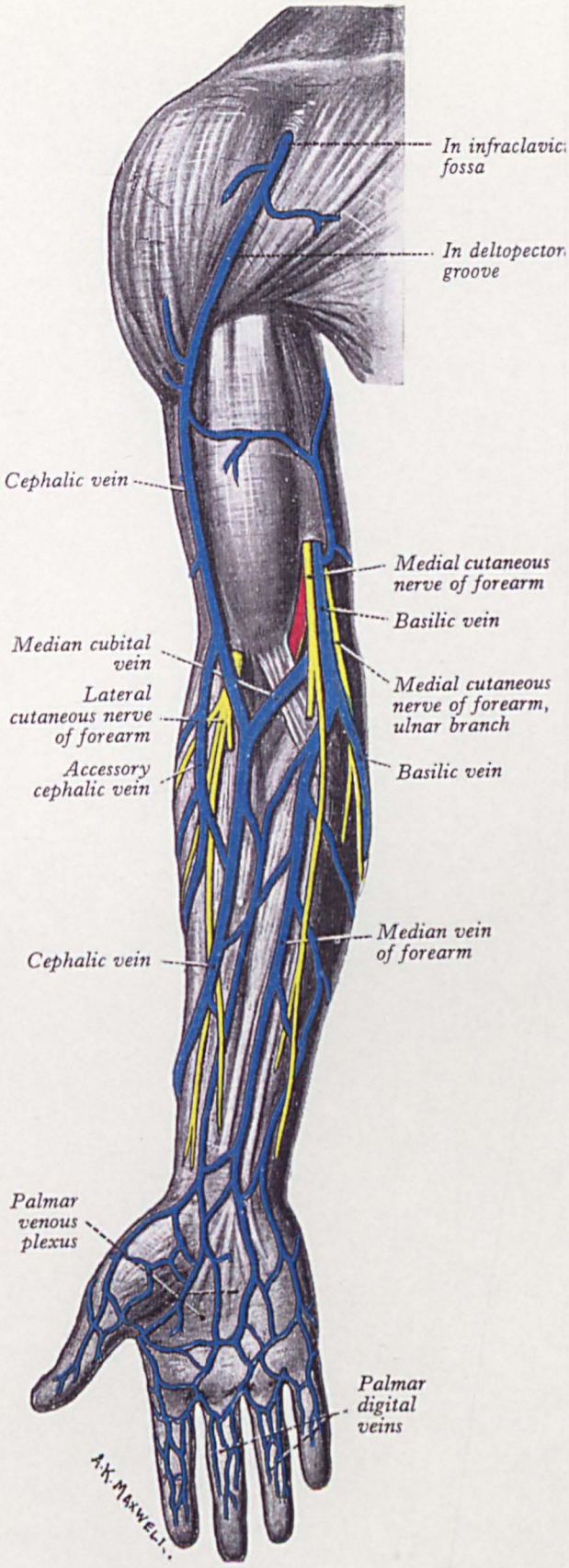

Figure A1.3 Veins of the upper extremity (Hamilton, 1976)

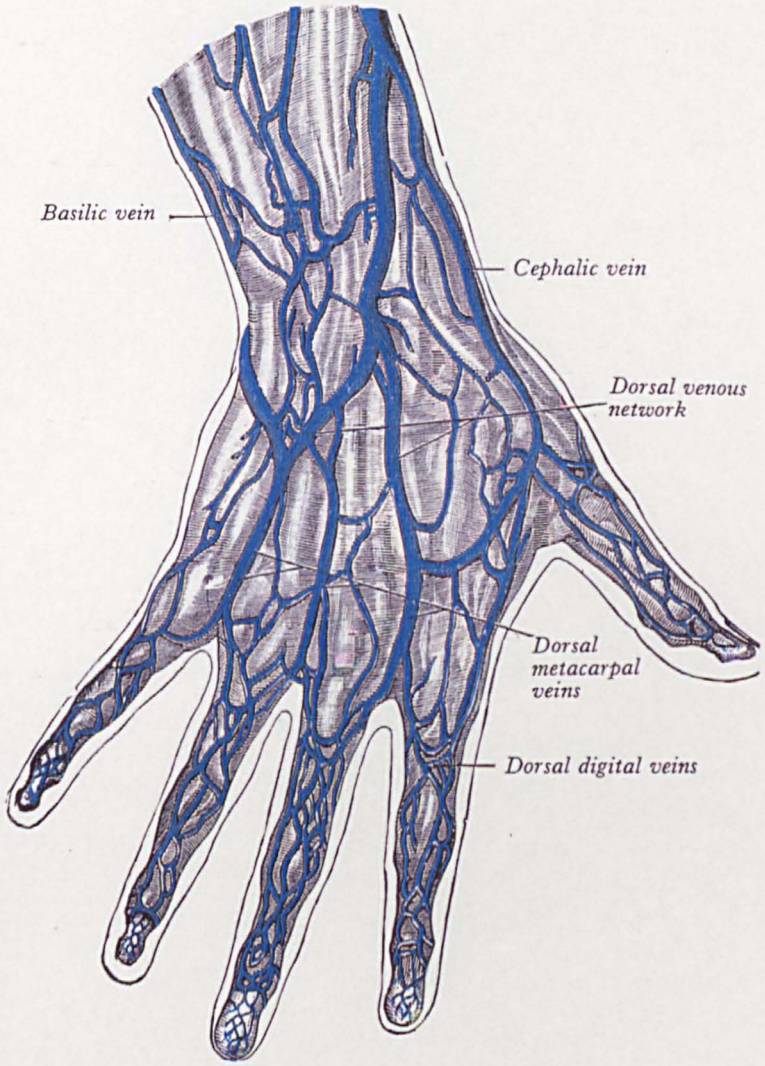

Figure A1.4 Veins of the dorsal aspect of the hand (Hamilton, 1976)

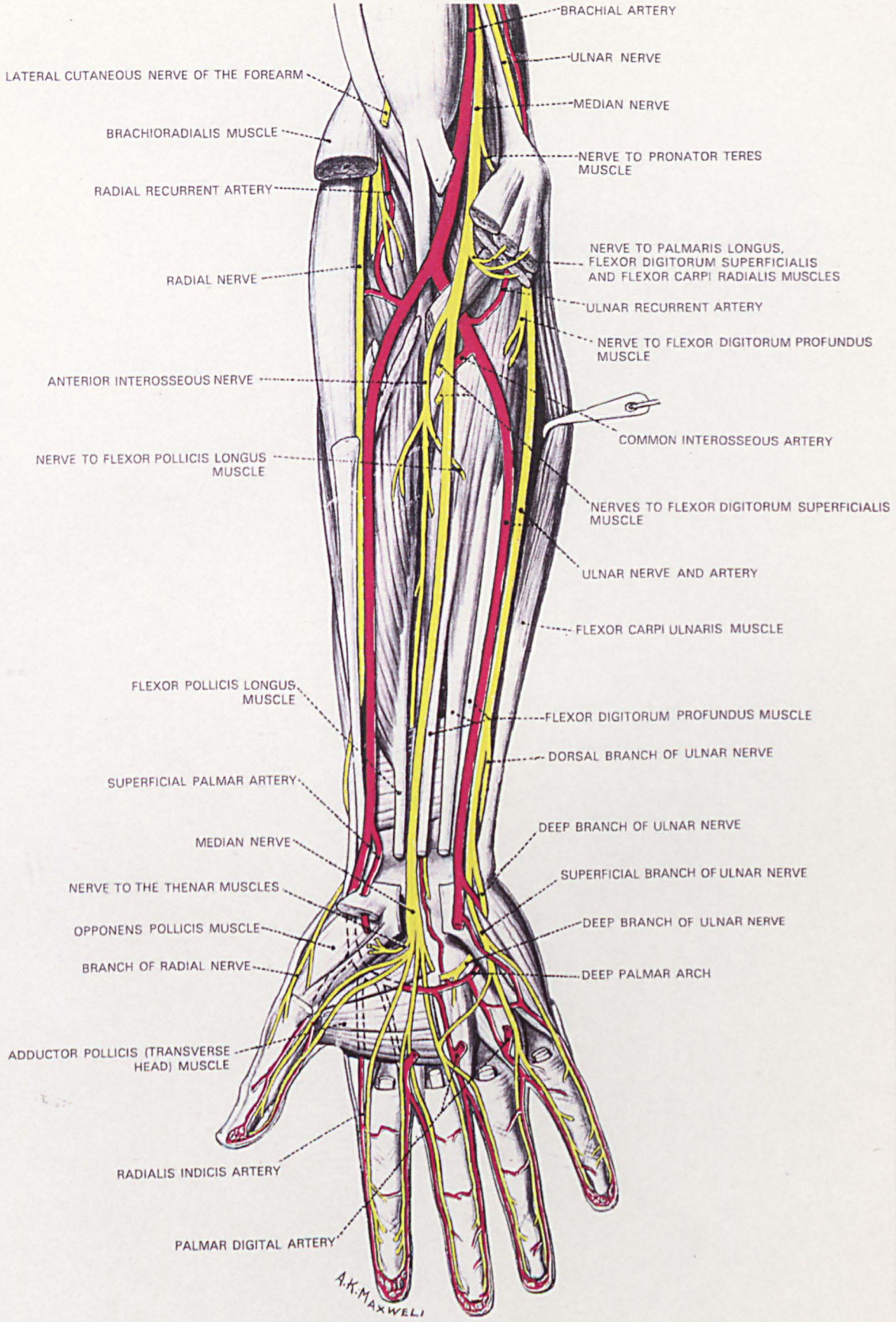

Figure A1.5 Arteries of the upper extremity (Hamilton, 1976)

APPENDIX B

MATHEMATICAL MODELLING OF FISTULAE

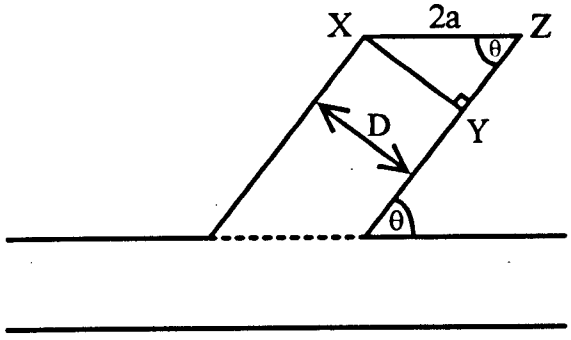

In triangle XYZ,

$$2a = \frac{D}{\sin\theta°}$$

$2b = D$

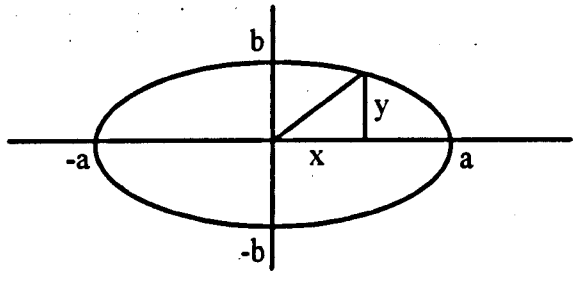

$$\frac{x^2}{a^2} + \frac{y^2}{b^2} = 1$$

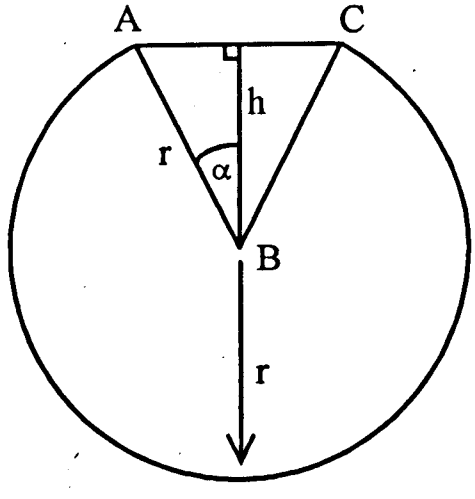

For arterial sections along the plane of the anastomosis:

In maintaining the original circumference of the artery,

$$r(2\Pi - 2\alpha^c) = 2\pi \times 2.25$$
$$= 14.14$$

$$r = \frac{7.07}{\pi - \alpha} \quad (1)$$

From triangle ABC,

$$y = r\sin\alpha \quad (2)$$

Substitute (1) into (2):

$$y = \frac{7.07 \sin \alpha}{\pi - \alpha} \qquad (3)$$

Fit parabolic curve to (3)
See graph below.

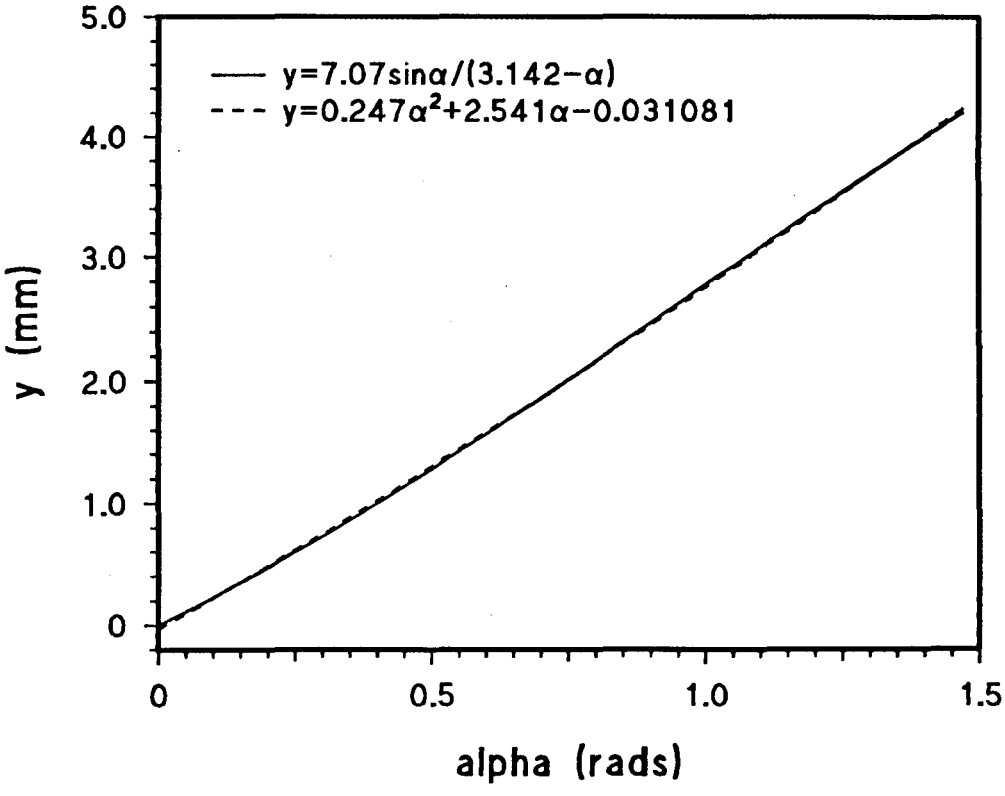

Solve the quadratic equation:

$0 = 0.247\alpha^2 + 2.541\alpha - (0.031081 + y)$ for each value of y

Find r from (2)

and, $h = r\cos\alpha$ (from triangle ABC)

Table B1 AV fistula model, diameter ratio 0.8 (vein and artery diameters 3.6mm and 4.5mm, respectively) and anastomotic angle 30°

x	y	α	r	h
±3.6	0	0	2.25	2.25
±3.5	±0.421	0.175	2.418	2.381
±3.4	±0.592	0.240	2.419	2.419
±3.3	±0.719	0.287	2.540	2.436
±3.2	**±0.825**	0.326	**2.576**	**2.440**
±3.1	±0.915	0.360	2.597	2.431
±3.0	±0.995	0.389	2.624	2.428
±2.5	±1.295	0.498	2.711	2.382
±2.0	±1.497	0.570	2.774	2.336
±1.5	±1.636	0.619	2.820	2.296
±1.0	±1.729	0.651	2.853	2.270
±0.5	±1.783	0.670	2.871	2.251
0	**±1.800**	0.676	**2.877**	**2.244**

Figures in bold have been used to specify sections in each of the DUCT models.

Table B2 AV fistula model, diameter ratio 1.25 (vein and artery diameters 5.6mm and 4.5mm, respectively) and anastomotic angle 30°

x	y	α	r	h
±5.6	0	0	2.25	2.25
±5.5	±0.527	0.215	2.470	2.413
±5.4	±0.742	0.296	2.544	2.433
±5.3	±0.904	0.356	2.594	2.431
±5.2	±1.039	0.405	2.637	2.424
±5.1	±1.157	0.448	2.671	2.407
±5.0	±1.261	0.485	2.705	2.393
±4.5	±1.667	0.630	2.830	2.286
±4.0	**±1.960**	0.731	**3.936**	**2.186**
±3.5	±2.186	0.809	3.021	2.085
±3.0	±2.364	0.869	3.096	1.998
±2.5	±2.505	0.916	3.158	1.923
±2.0	±2.615	0.953	3.208	1.858
±1.5	±2.698	0.980	3.249	1.810
±1.0	±2.755	0.999	3.276	1.773
0	**±2.800**	1.014	**3.298**	**1.743**

Figures in bold have been used to specify sections in each of the DUCT models.

Table B3 AV fistula model, diameter ratio 2.0 (vein and artery diameters 9.0mm and 4.5mm, respectively) and anastomotic angle 30°

x	y	α	r	h
±9.0	0	0	2.25	2.25
±8.9	±0.669	0.268	2.526	2.436
±8.8	±0.943	0.370	2.608	2.431
±8.7	±1.152	0.446	2.671	2.409
±8.6	±1.327	0.509	2.723	2.378
±8.5	±1.479	0.563	2.771	2.343
±8.0	**±2.062**	0.766	**2.974**	**2.143**
±7.5	±2.487	0.910	3.150	1.933
±7.0	±2.828	1.023	3.313	1.725
±6.5	±3.112	1.116	3.464	1.522
±6.0	±3.354	1.193	3.608	1.331
±5.5	±3.562	1.259	3.742	1.148
±5.0	±3.742	1.316	3.867	0.975
±4.5	±3.897	1.364	3.982	0.818
±4.0	±4.031	1.406	4.086	0.670
±3.5	±4.146	1.441	4.181	0.541
±3.0	±4.243	1.471	4.264	0.425
±2.5	±4.323	1.495	4.335	0.328
±2.0	±4.387	1.515	4.394	0.245
±1.5	±4.437	1.530	4.441	0.181
±1.0	±4.472	1.541	4.474	0.133
±0.5	±4.494	1.547	4.494	0.107
0	**±4.501**	1.549	**4.501**	**0.098**

Figures in bold have been used to specify sections in each of the DUCT models.

Table B4 AV fistula model, diameter ratio 1.6 (vein and artery diameters 7.0mm and 4.5mm, respectively) and anastomotic angle 30°

x	y	α	r	h
±7.0	0	0	2.25	2.25
±6.9	±0.589	0.238	2.494	2.433
±6.8	**±0.831**	0.329	**2.574**	**2.436**
±6.7	±1.014	0.396	2.629	2.426
±6.6	±1.166	0.451	2.674	2.407
±6.5	±1.299	0.499	2.714	2.383
±6.0	±1.803	0.677	2.878	2.243
±5.5	±2.165	0.802	3.013	2.095
±5.0	±2.449	0.897	3.133	1.955
±4.5	±2.681	0.975	3.240	1.818
±4.0	±2.872	1.037	3.335	1.697
±3.5	±3.031	1.089	3.420	1.585
±3.0	±3.162	1.132	3.493	1.484
±2.5	±3.269	1.166	3.556	1.401
±2.0	±3.354	1.193	3.608	1.331
±1.5	±3.419	1.214	3.649	1.274
±1.0	±3.464	1.228	3.678	1.236
±0.5	±3.491	1.237	3.695	1.211
0	**±3.5**	1.240	**3.701**	**1.202**

Figures in bold have been used to specify sections in each of the DUCT models.

Table B5 AV fistula model, diameter ratio 1.6 (vein and artery diameters 7.0mm and 4.5mm, respectively) and anastomotic angle 50°

x	y	α	r	h
±4.5	0	0	2.250	2.250
±4.4	±0.943	0.370	2.608	2.431
±4.3	±1.183	0.457	2.681	2.406
±4.2	±1.378	0.527	2.740	2.368
±4.1	±1.545	0.587	2.789	2.323
±4.0	**±1.691**	0.638	**2.839**	**2.281**
±3.5	±2.250	0.830	3.049	2.058
±3.0	±2.640	0.961	3.220	1.844
±2.5	±2.930	1.056	3.366	1.657
±2.0	±3.147	1.127	3.485	1.496
±1.5	±3.306	1.178	3.579	1.370
±1.0	±3.415	1.213	3.646	1.277
±0.5	±3.479	1.233	3.687	1.222
0	**±3.5**	1.240	**3.701**	**1.202**

Table B6 AV fistula model, diameter ratio 1.6 (vein and artery diameters 7.0mm and 4.5mm, respectively) and anastomotic angle 70°

x	y	α	r	h
±3.7	0	0	2.250	2.250
±3.6	±0.898	0.353	2.598	2.437
±3.5	±1.197	0.462	2.685	2.040
±3.0	**±2.074**	0.771	**2.976**	**2.135**
±2.5	±2.594	0.946	3.198	1.871
±2.0	±2.953	1.064	3.378	1.639
±1.5	±3.204	1.145	3.518	1.453
±1.0	±3.371	1.199	3.618	1.314
±0.5	±3.468	1.230	3.680	1.230
0	**±3.5**	1.240	**3.701**	**1.202**

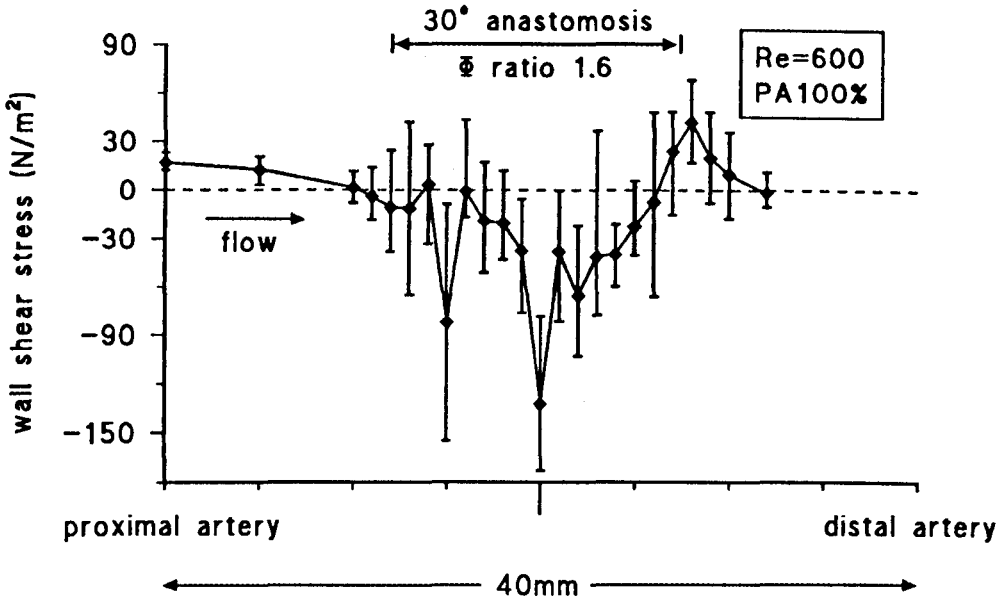

Figure C1.1 Oscillatory wall shear stresses along the arterial floor (30°, 1.6 diameter ratio model, distal artery occluded)

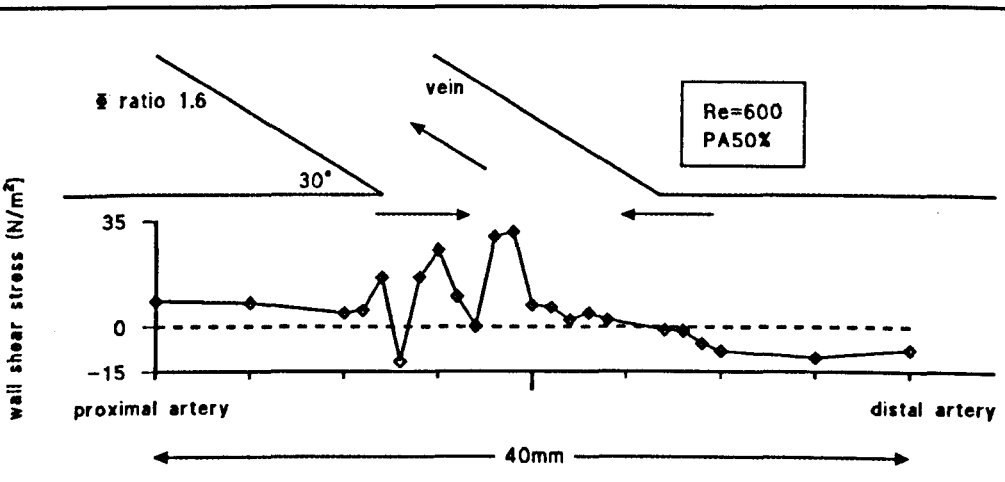

Figure C1.2 Mean wall shear stresses along floor of anastomosed artery (30°, 1.6 diameter ratio model, proximal artery supplying 50% of venous flow)

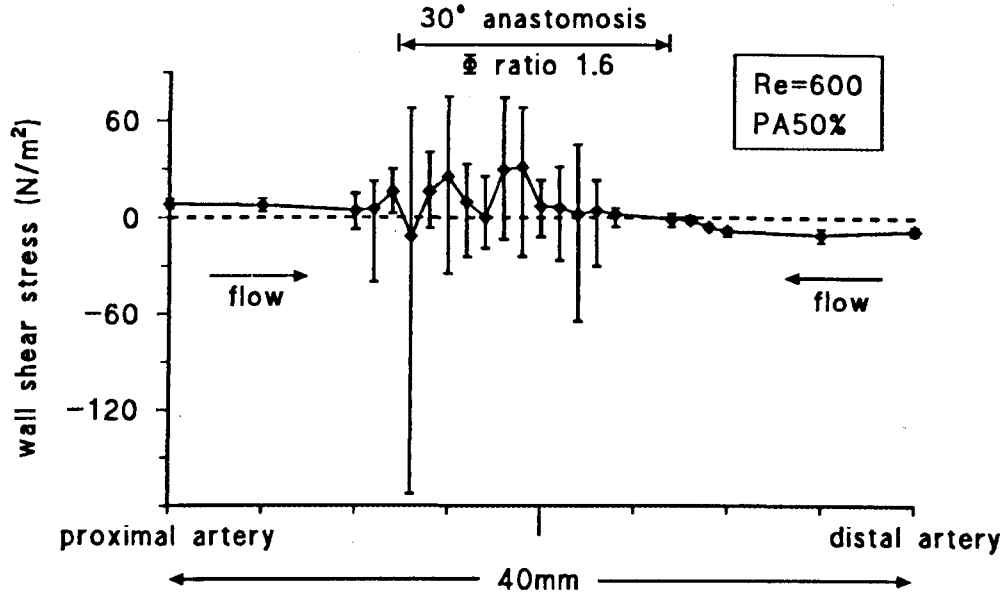

Figure C1.3 Oscillatory wall shear stresses along the arterial floor (30°, 1.6 diameter ratio model, proximal artery supplying 50% of venous flow)

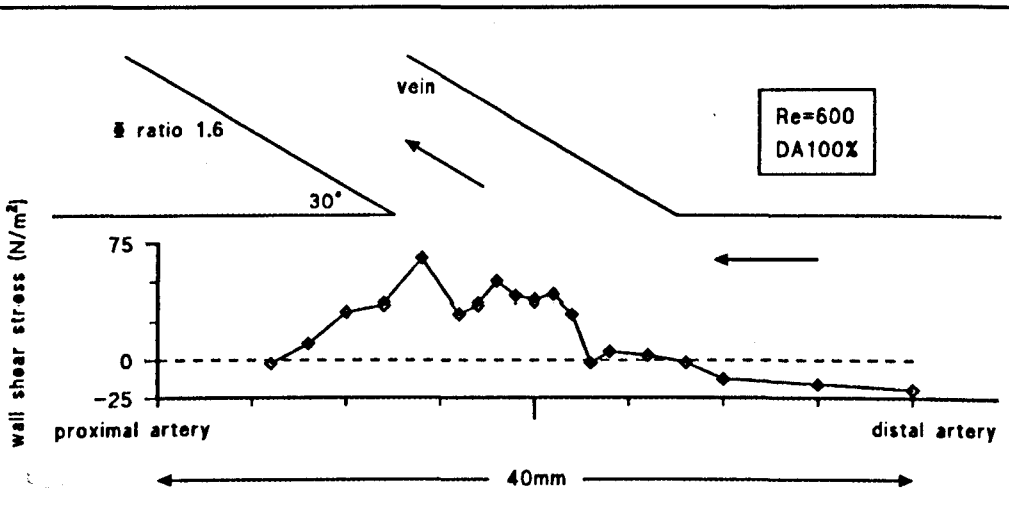

Figure C1.4 Mean wall shear stresses along floor of anastomosed artery (30°, 1.6 diameter ratio model, proximal artery occluded)

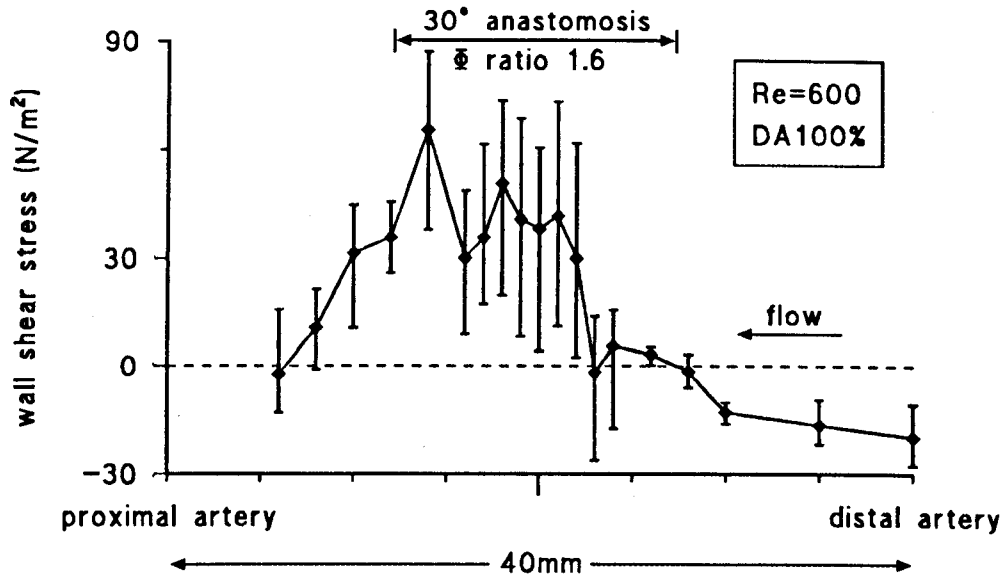

Figure C1.5 Oscillatory wall shear stresses along the arterial floor (30°, 1.6 diameter ratio model, proximal artery occluded)

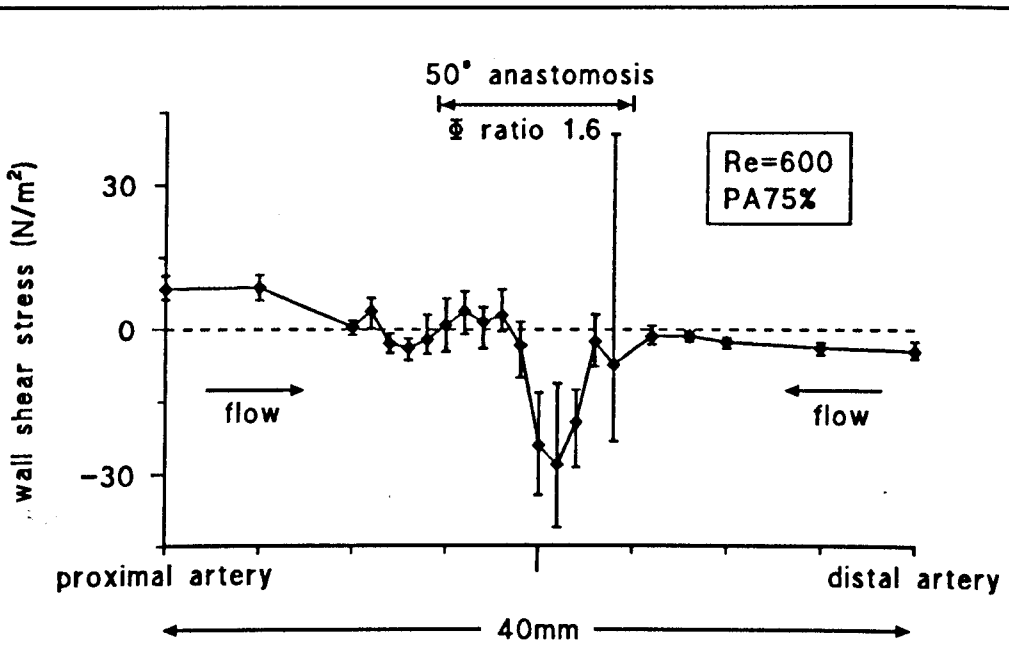

Figure C1.6 Oscillatory wall shear stresses along the arterial floor (50°, 1.6 diameter ratio model, proximal artery supplying 75% of venous flow)

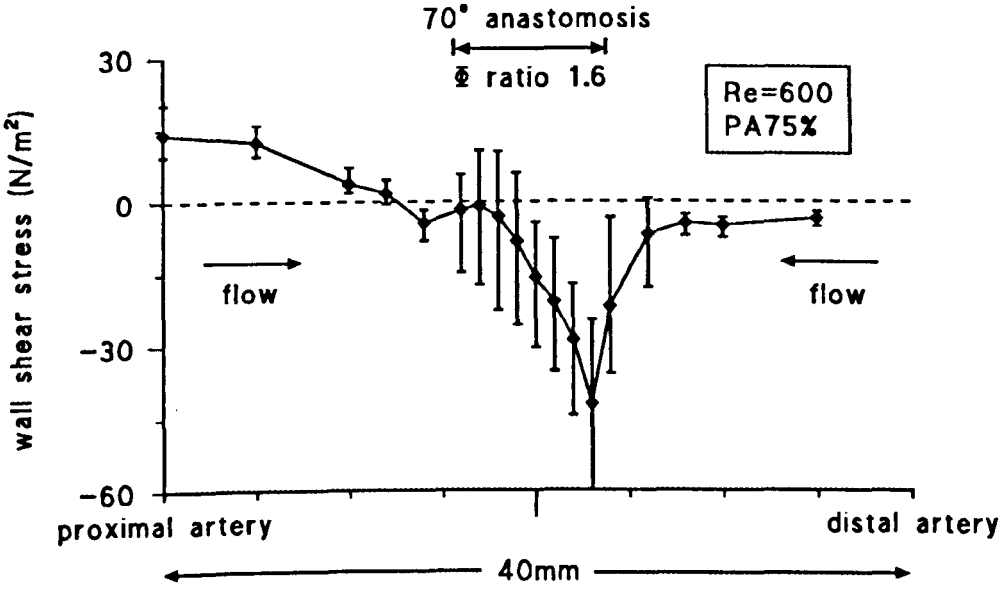

Figure C1.7 Oscillatory wall shear stresses along the arterial floor (70°, 1.6 diameter ratio model, proximal artery supplying 75% of venous flow)

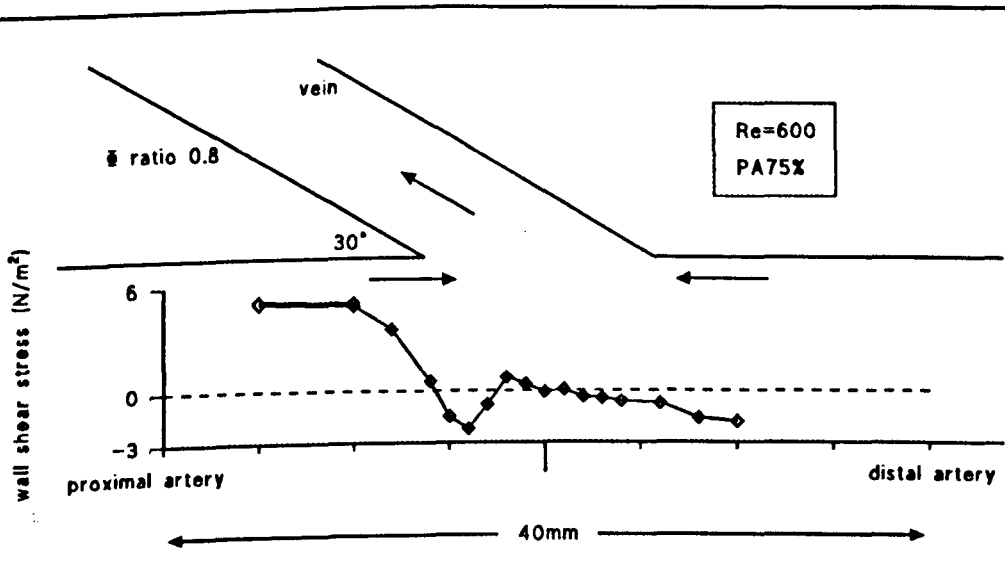

Figure C1.8 Mean wall shear stresses along floor of anastomosed artery (30°, 0.8 diameter ratio model, proximal artery supplying 75% of venous flow)

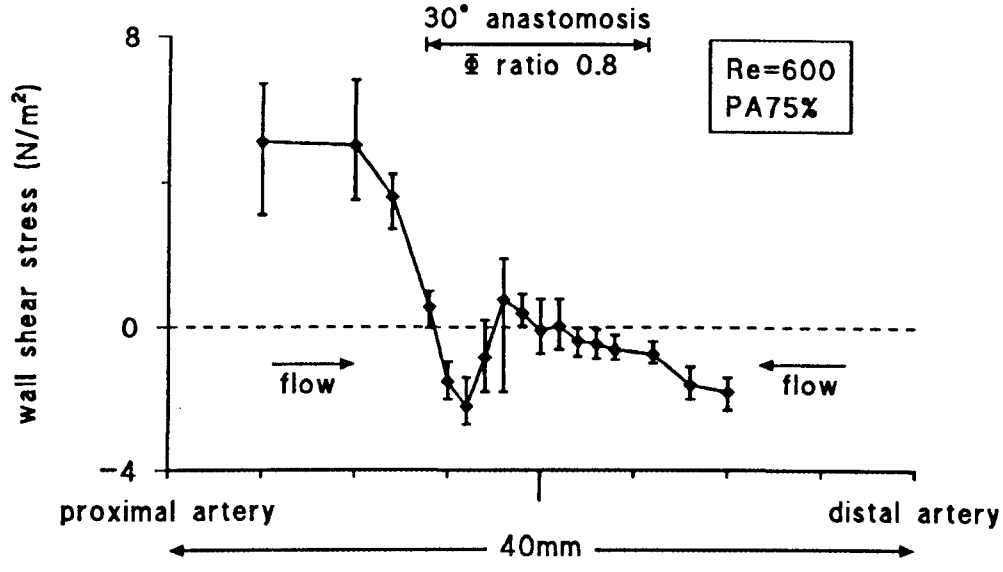

Figure C1.9 Oscillatory wall shear stresses along the arterial floor (30°, 0.8 diameter ratio model, proximal artery supplying 75% of venous flow)

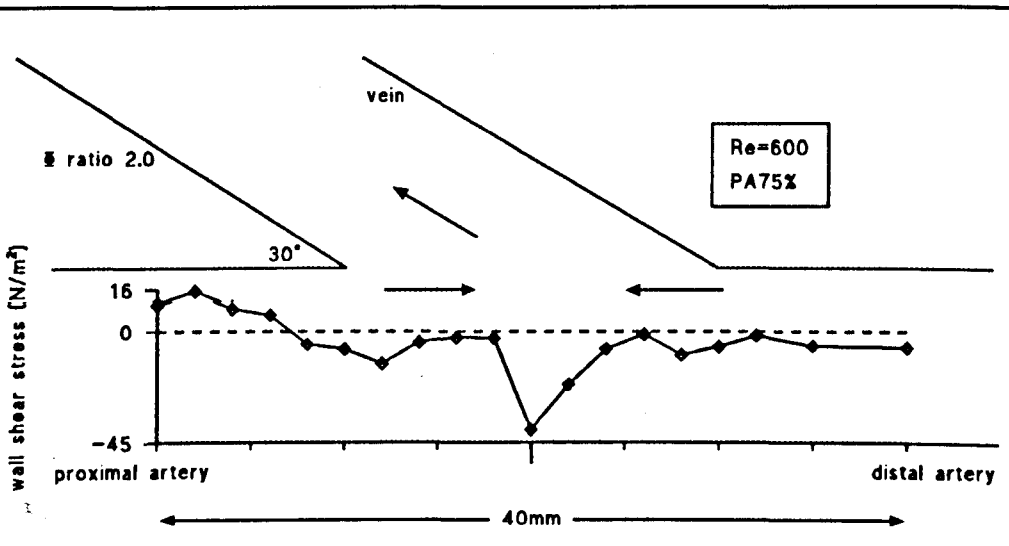

Figure C1.10 Mean wall shear stresses along floor of anastomosed artery (30°, 2.0 diameter ratio model, proximal artery supplying 75% of venous flow)

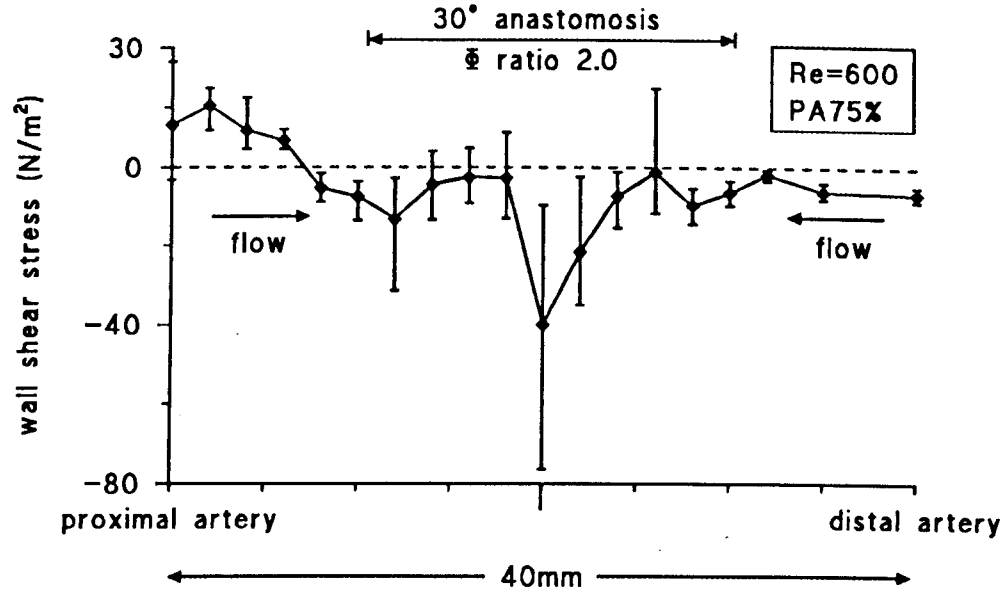

Figure C1.11 Oscillatory wall shear stresses along the arterial floor (30°, 2.0 diameter ratio model, proximal artery supplying 75% of venous flow)

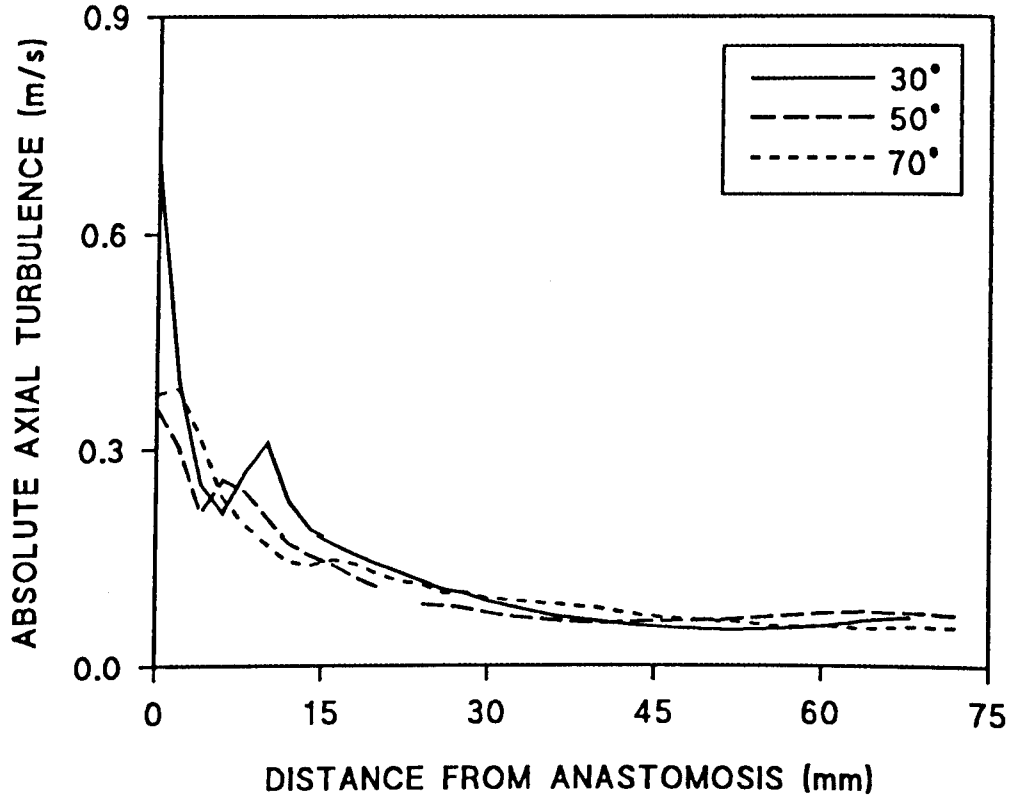

Figure C1.12 Mean axial absolute tubulence along the centreline of the 30°, 50° and 70° anastomotic angle model veins

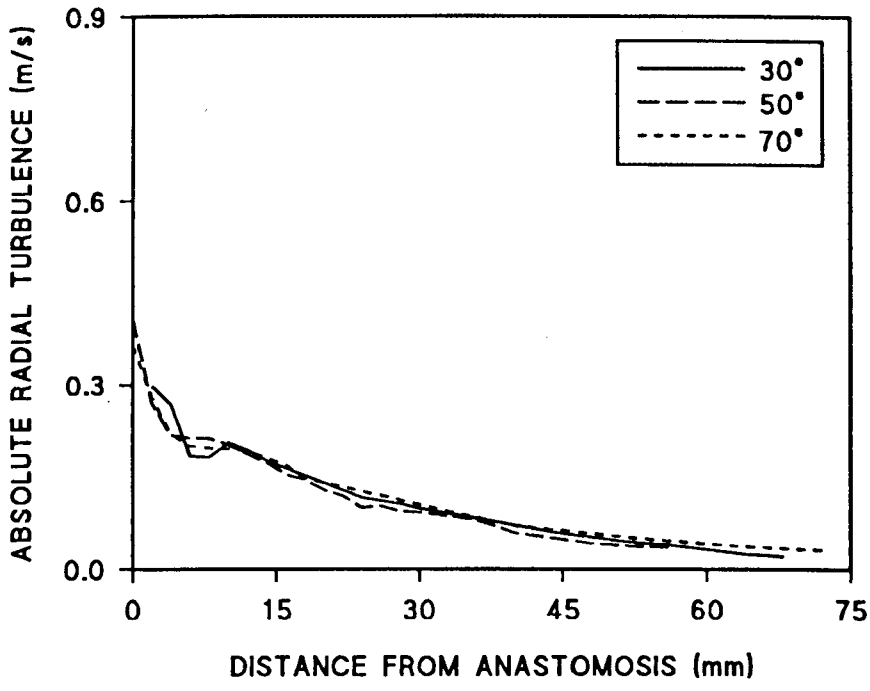

Figure C1.13 Mean radial absolute turbulence along the centreline of the 30°, 50° and 70° anastomotic angle model veins

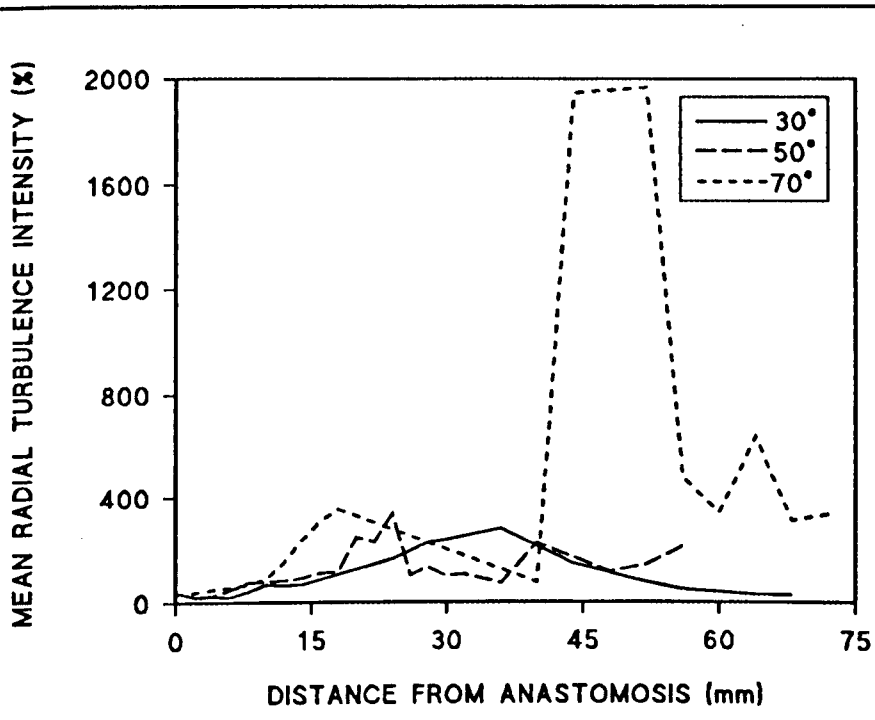

Figure C1.14 Mean radial turbulence intensity along the centreline of the 30°, 50° and 70° anastomotic angle veins

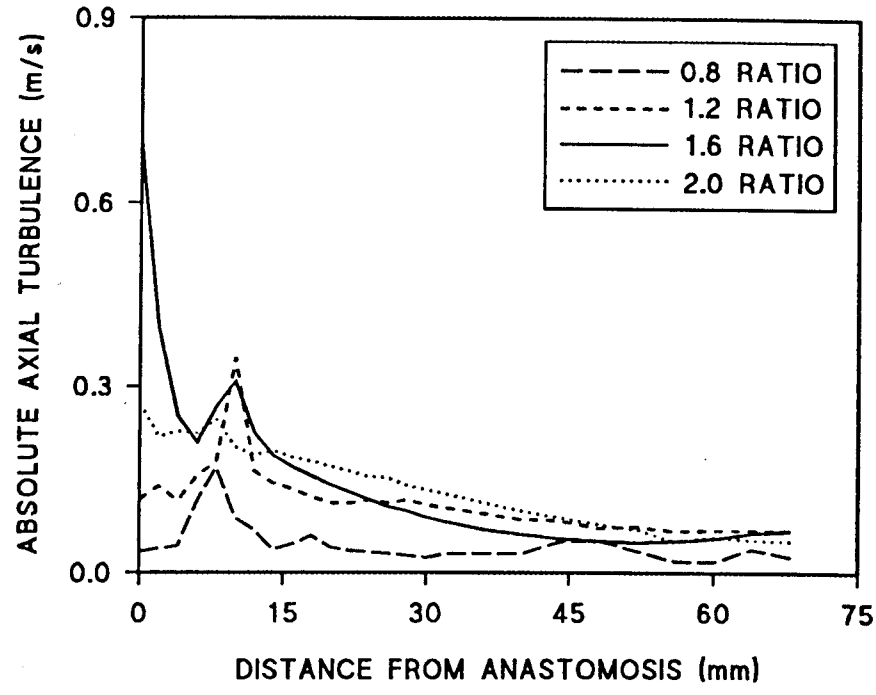

Figure C1.15 Mean axial absolute turbulence along the centreline of the 0.8, 1.2, 1.6 and 2.0 vein-to-artery diameter ratio model veins

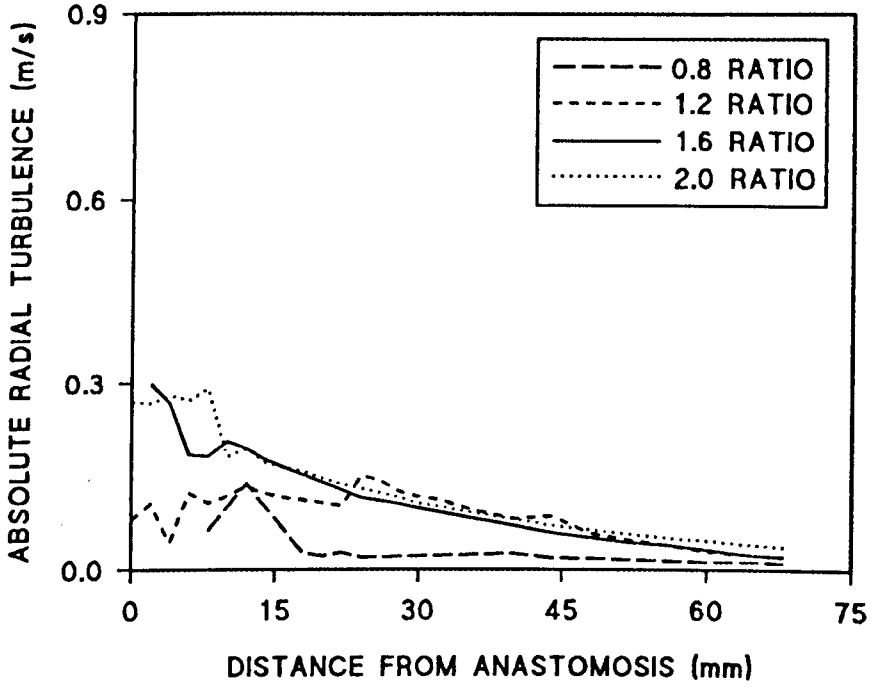

Figure C1.16 Mean radial absolute turbulence along the centreline of the 0.8, 1.2, 1.6 and 2.0 vein-to-artery diameter ratio model veins

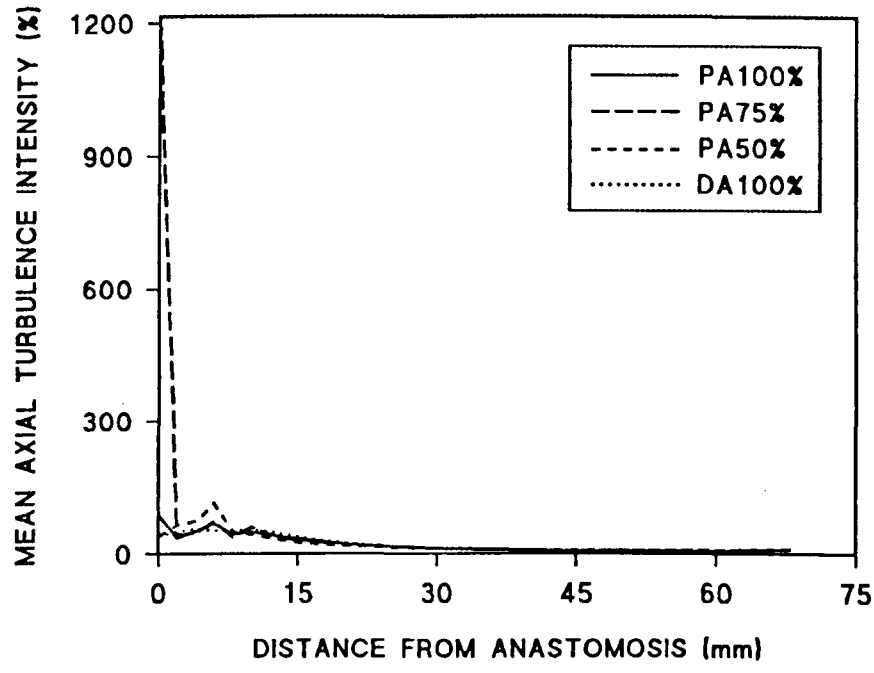

Figure C1.17 Mean axial turbulence intensity along the centreline of the 30°, 1.6 diameter ratio vein for varying flow distributions

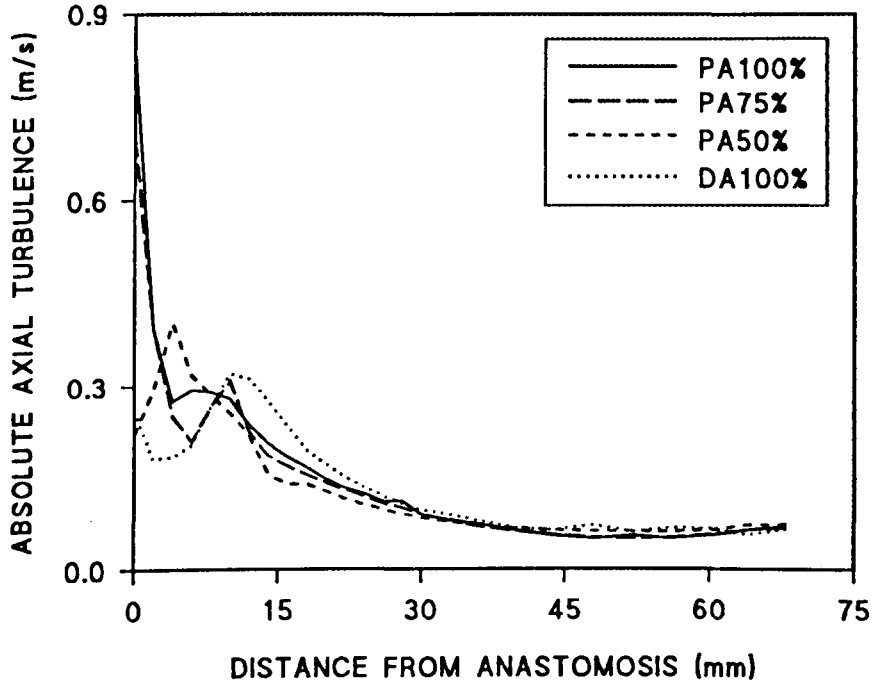

Figure C1.18 Mean axial absolute turbulence along the centreline of the 30°, 1.6 diameter ratio vein for varying flow distributions

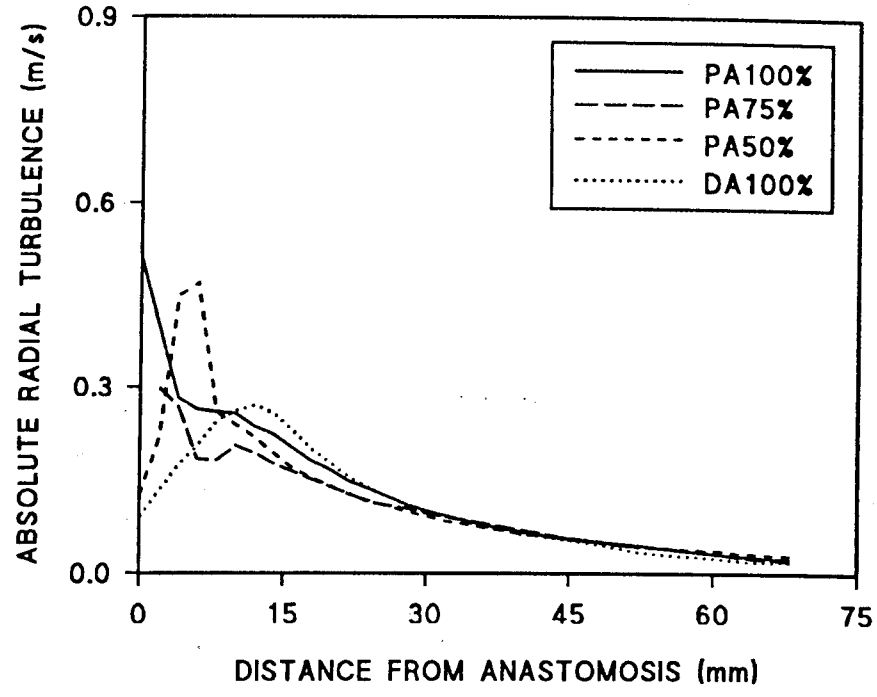

Figure C1.19 Mean radial absolute turbulence along the centreline of the 30°, 1.6 diameter rtio vein for varying flow distributions

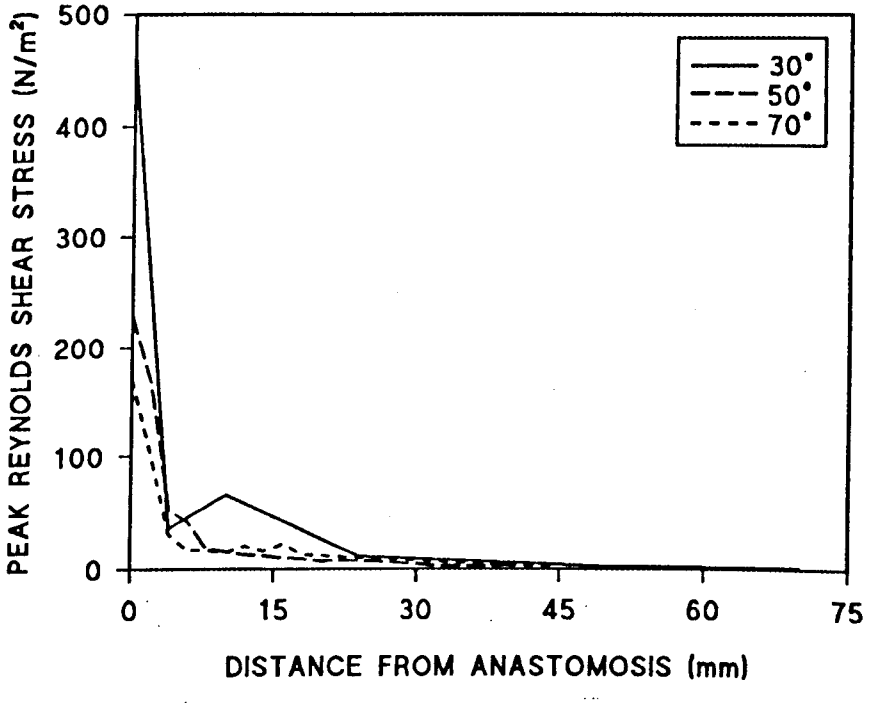

Figure C1.20 Peak Reynolds shear stresses along the centreline of the 30°, 50° and 70° anastomotic angle model veins

REFERENCES

ABBOTT JA, CAMPBELL M, BUSSELL JA and LIM RC (1973) Blood flow in end-to-side arteriovenous fistulas and saphenous vein grafts. *Kid. Int.* 3 342-344.

ABBOTT WM, MEGERMAN J, HASSON JE *et al.* (1987) Effect of compliance mismatch on vascular graft patency. *J. Vasc. Surg.* 5 376-382.

ALEXANDROV AV, BLADIN CF, MAGGISANO R and NORRIS JW (1993) Measuring carotid stenosis: time for reappraisal. *Stroke* 24 1292-1296.

ANDERSON CB, ETHEREDGE EE, HARTER HR, GRAFF RA, CODD JR and NEWTON WT (1977a) Local blood flow characteristics of arteriovenous fistulas in the forearm for dialysis. *Surg. Gynecol. Obstet.* 144 531-3.

ANDERSON CB, ETHEREDGE EE, HARTER HR, CODD JR, GRAFF RA and NEWTON WT (1977b) Blood flow measurements in arteriovenous dialysis fistulas. *Surgery* 81 459-461.

ANDERSON CB, CODD JR, GRAFF RA, GROCE MA, HARTER HR and NEWTON WT (1976) Cardiac failure and upper extremity arteriovenous dialysis fistulas. Case reports and a review of the literature. *Arch. Intern Med.* 136 292.

BAKER LD Jr, JOHNSON JM and GOLDFARB D (1976) Expanded polytetrafluoroethylene (PTFE) subcutaneous arteriovenous conduit: an improved vascular access for chronic hemodialysis. *Trans. Am. Soc. Artif. Intern. Organs* 22 382-387.

BEARD JD, SCOTT DJA, EVANS JM, SKIDMORE R and HORROCKS M (1988) Pulse-generated runoff: a new method of determining calf vessel patency. *Br. J. Surg.* 75 361-363.

BEEMER RK and HAYES JF (1973) Hemodialysis using a mandril grown graft. *Trans. Am. Soc. Artif. Intern. Organs* 19 43-48.

BITKER MO, ROTTEMBOURG J and MEHAMA R (1984) Les échecs précoces de la création des fistules artério-veineuses pour l'hémodialyse chez l'adulte. *Ann. Urol.* 18 98-102.

BLACKSHEAR PL. Mechanical hemolysis in flowing blood. In: *Biomechanics: Its foundation and objectives*. Eds. Fung YC, Perrone N and Anliker M, Prentice-Hall, Englewood Cliffs, 1972, pp 501-28.

BONALUMI U, CIVALLERI D, ROVIDA S, ADAMI GF, GIANETTA E and GRIFFANTI-BARTOLI F (1982) Nine years' experience with end-to-end arteriovenous fistula at the "anatomical snuffbox" for maintenance haemodialysis. *Br.*

J. Surg. 69 486-488.

BOUHOUTSOS J, MORRIS T, CHAVATZAS D and MARTIN P (1974) The influence of haemoglobin and platelet levels on the results of arterial surgery. *Br. J. Surg.* 61 984-986.

BRESCIA MJ, CIMINO JE, APPEL K and HURWICH BJ (1966) Chronic hemodialysis using venipuncture and a surgically created arteriovenous fistula. *N. Engl. J. Med.* 275 1089-1091.

BROWN CH III, LEVERETT LB, LEWIS CW, ALFREY CP Jr. and HELLUMS JD (1975) Morphological, biochemical, and functional changes in human platelets subjected to shear stress. *J. Lab. Clin. Med.* 86 462-471.

BROWN HW, MAHER JF, LAPIERRE L, BLEDSOE FH and SCHREINER GE (1962) Clinical problems related to the prolonged artificial maintenance of life by haemodialysis in chronic renal failure. *Trans. Am. Soc. Artif. Intern. Organs* 8 281-291.

BUSSELL JA, ABBOTT JA and LIM RC (1971) A radial steal syndrome with arteriovenous fistula for hemodialysis. *Ann. Intern. Med.* 75 387-394.

CARO CG, FITZGERALD JM and SCHROTER RC (1971) Atheroma and arterial wall shear: observation, correlation and proposal of a shear dependent mass transfer mechanism for atherogenesis. *P. Roy. Soc. Lond.* 177 109-159.

CHERVU A and MOORE WS (1990) An overview of intimal hyperplasia. *Surg. Gynecol. Obstet.* 171 433-447.

CHINITZ JL, YOKOYAMA T, BOWER R and SWARTZ C (1972) Self-sealing prosthesis for arteriovenous fistula in man. *Trans. Am. Soc. Artif. Intern. Organs* 18 452.

COLLER BS (1987) Blood elements at surfaces: platelets. *Ann. N. Y Acad. Sci.* 516 362-379.

DAVIES MJ and WOOLF N (1993) Atherosclerosis: what is it and why does it occur? *Br. Heart J.* 69 S3-S11.

DILLEY RJ, McGEACHIE JK and PRENDERGAST FJ (1988) A review of the histologic changes in vein-to-artery grafts, with particular reference to intimal hyperplasia. *Arch. Surg.* 123 691-696.

DRUKKER W. Haemodialysis: a historical review. In: *Replacement of renal function by dialysis: a textbook of dialysis.* Third edition. Ed. Maher JF, Kluwer Academic Publishers, 1989, pp 20-86.

EDITORIAL - anonymous (1966) Hemodialysis using an arteriovenous fistula. *N. Engl. J. Med.* 275 1134-1135.

EHRENFELD WK, GRAUSZ H and WYLIE EJ (1972) Subcutaneous arteriovenous fistulas for hemodialysis. *Am. J. Surg.* 124 200-206.

ESTERBAUER H, WÄG G and PUHL H (1993) Lipid peroxidation and its role in atherosclerosis. *Br. Med. Bull.* 49 566-576.

EVANS DH (1985) On the measurement of the mean velocity of blood flow over the cardiac cycle using Doppler ultrasound. *Ultrasound Med. Biol.* 11 735-741.

FLORES L, DUNN I, FRUMKIN E, FORTE R, REQUENA R, RYAN J, KNOPF M, KIRSCHNER J and LEVOWITZ BS (1973) Dacron arteriovenous shunts for vascular access hemodialysis. *Trans. Am. Soc. Artif. Intern. Organs* 19 33-37.

FORSBERG B, FORSBERG I, LINDSTEDT E, WESTLING H and WHITE T. Side-to-side, side-to-end or end-to-end anastomosis for Cimino-Brescia fistula? Preliminary report of a randomized study. In: *Access Surgery,* proceedings of the International Congress on Access Surgery, Maastricht, 22-24 April '82. Eds. Kootstra G and Jörning PJG, Pub. MTP Press Ltd., 1983.

FOX JA and HUGH AE (1966) Localization of atheroma: a theory based on boundary layer separation. *Br. Heart J.* 28 388-399.

FRANK CW, WANG H, LAMMERANT J, MILLER R and WÉGRIA R (1955) An experimental study of the immediate hemodynamic adjustments to acute arteriovenous fistulae of various sizes. *J. Clin. Invest.* 34 722-731.

FRY DL (1968) Acute vascular endothelial changes associated with increased blood velocity gradients. *Circ. Res.* 22 165-197.

FUCHS JCA, MITCHENER JS and HAGEN P-O (1978) Postoperative changes in autologous vein grafts. *Ann. Surg.* 188 1-15.

GLAGOV S and ZARINS CK (1989) Is intimal hyperplasia an adaptive response or a pathologic process? Observations on the nature of non-atherosclerotic intimal thickening. *J. Vasc. Surg.* 10 571-573.

GOLDWASSER P, AVRAM MM, COLLIER JT, MICHEL M-A, GUSIK S-A and MITTMAN N (1994) Correlates of vascular access occlusion in hemodialysis. *Am. J. Kidney Dis.* 24 785-794.

GORDON IL. Physiology of the arteriovenous fistula. In: *Vascular access surgery: principles and practice. 3rd Edition.* Ed. Wilson SE, Mosby-Year Book Inc., 1996, pp 29-39.

GROTENDORST GR, SEPPÄ HEJ, KLEINMAN HK and MARTIN GR (1981) Attachment of smooth muscle cells to collagen and their migration toward platelet-derived growth factor. *Proc. Natl. Acad. Sci. USA* 78 3669-3672.

HAIMOV M (1975) Vascular access for hemodialysis. *Surg. Gynecol. Obstet.* 141 619-625.

HAIMOV M, BAEZ A, NEFF M and SLIFKIN R (1975) Complications of arteriovenous fistulas for hemodialysis. *Arch. Surg.* 110 708-712.

HAIMOV M, SINGER A and SCHUPAK E (1971) Access to blood vessels for hemodialysis: experience with 87 patients on chronic hemodialysis. *Surgery* 69 884-889.

HALSTED WS (1918) Dilatation of great arteries distal to partially occluding band. *Proc. Nat. Acad. Sci. USA* 4 889.

HOLMAN E (1954) The obscure physiology of post-stenotic dilatation, its relation to the development of aneurysms. *J. Thorac. Surg.* 28 109.

HOLMAN E (1923) The physiology of an arteriovenous fistula. *Arch. Surg.* 7 64-82.

HUGHES PE, SHORTLAND AP and HOW TV (1996) Visualization of vortex shedding at the proximal side-to-end artery-graft anastomosis. *Biorheology* 33 305-317.

INGEBRIGTSEN R, FÖNSTELIEN E and SOLBERG LA (1970) Measurement of forces producing longitudinal stretching of the arterial wall, examined in the artery proximal to an arterio-venous fistula. *Acta Chir. Scand.* 136 569-573.

INGEBRIGTSEN R (1965) Experimental induction of hypertrophy of the median coat in fistulous arteries. *Acta Chir. Scand.* 129 156.

INOKUCHI K, OKADOME K, OHTSUKA K, MUTO Y, KUROKI M, MIYAZAKI T and TAKAHARA H (1984) A desktop computer to visualize the intraluminal velocity profile and its clinical application. *J. Vasc. Surg.* 1 787-794.

JOHNSON G Jr. and BLYTHE WB (1970) Hemodynamic effects of arteriovenous shunts used for hemodialysis. *Ann. Surg.* 171 715-723.

JOHNSON G Jr., DART CH Jr., PETERS RM and STEELE F (1966) The importance of venous circulation in arteriovenous fistula. *Surg. Gynecol. Obstet.* 123 995-1000.

KAEGI A, PINEO GF, SHIMIZU A, TRIVEDI H, HIRSH J and GENT M (1974) Arteriovenous-shunt thrombosis - prevention by sulfinpyrazone. *New Engl. J. Med.* 290 304-306.

KINNAERT P, GEENS M, VEREERSTAETEN P, HEUSE A, BUCHIN R, LECLERC JL, TOUSSAINT C and VAN GEERTRUYDEN J (1971) Experience with arteriovenous fistulas for chronic maintenance haemodialysis. *Br. J. Surg.* 58 104-108.

KARINO T, GOLDSMITH HL, MOTOMIYA M, MABUCHI S and SOHARA Y (1987) Flow patterns in vessels of simple and complex geometries. *Ann. N. Y Acad. Sci.* 516 422-441.

KLAUBER GT, BELITSKY P, MOREHOUSE DD and MacKINNON KJ (1971) Preventable problems with arteriovenous fistulas for hemodialysis. *Surg. Gynecol. Obstet.* 132 457-459.

KROVETZ LJ (1965) The effect of vessel branching on haemodynamic stability. *Phys. Med. Biol.* 10 417-428.

KU DN, GIDDENS DP, ZARINS CK and GLAGOV S (1985) Pulsatile flow and atherosclerosis in the human carotid bifurcation. *Arteriosclerosis* 5 293-302.

KU DN and GIDDENS DP (1983) Pulsatile flow in a model carotid bifurcation. *Arteriosclerosis* 3 31-39.

LEONARD EF (1972) The role of flow in thrombogenesis. *Bull. N. Y. Acad. Med.* 48 273-280.

LEUNG DYM, GLAGOV S and MATHEWS MB (1976) Cyclic stretching stimulates synthesis of matrix components by arterial smooth muscle cells *in vitro*. *Science* 191 475-477.

LIDMAN D and THOMSEN MB (1986) Patency, blood flow and histologic characteristics in end-to-end and end-to-side arteriovenous fistulas: comparisons in an experimental model. *Acta Chir. Scand.* 152 103-109.

LIEBER BB (1990) The decomposition of apparent stresses in disturbed pulsatile flow in the presence of large scale organized structures. *J. Biomech.* 23 1047-1060.

LYONS TJ (1993) Glycation and oxidation: a role in the pathogenesis of atherosclerosis. *Am. J. Cardiol.* 71 26B-31B.

MATTHEWS IP, GIBSON C and SAMUEL AH (1994) Sterilisation of implantable devices: review paper. *Clin. Materials* 15 191-215.

MAY J, TILLER D, JOHNSON J, STEWART J and SHEIL AGR (1969) Saphenous vein arteriovenous fistula in regular dialysis treatment. *N. Engl. J. Med.* 280 770.

McDONALD DA. *Blood flow in arteries.* Second edition. Pub. Edward Arnold, London, 1974.

MIDDLETON WD, PICUS DD, MARX MV and MELSON GL (1989) Color Doppler sonography of hemodialysis vascular access: comparison with angiography. *AJR* 152 633-639.

MORINGA K, OKADOME K, KUROKI M, MIYAZAKI T, MUTO Y and INOKUCHI K (1985) Effect of wall shear stress on intimal thickening of arterially transplanted autogenous veins in dogs. *J. Vasc. Surg.* 2 430-3.

MUSTARD JF, GROVES HM, KINLOUGH-RATHBONE RL and PACKHAM MA (1987) Thrombogenic and nonthrombogenic biological surfaces. *Ann. N. Y. Acad. Sci.* 516 12-21.

NEREM RM and CORNHILL JF (1980) The role of fluid mechanics in atherogenesis. *ASME J. Biomech. Eng.* 102 181-189.

NICHOLS WW and O'ROURKE MF. *McDonald's blood flow in arteries: theoretic, experimental and clinical principles.* Third edition. Pub. Edward Arnold, 1990.

NONNAST-DANIEL B, MARTIN RP, LINDERT O, MÜGGE A, SCHAEFFER J, LIETH HVD, SÖCHTIG E, GALANSKI M, KOCH K-M and DANIEL WG (1992) Colour doppler ultrasound assessment of arteriovenous haemodialysis fistulas. *Lancet* 339 143-145.

OKADOME K, YUKIZANE T, MII S, FUKUDA A and SUGIMACHI K (1989) *J. Cardiovasc. Surg.* 30 932-935.

OWENS ML and BOWER RW. Physiology of arteriovenous fistulas. In: *Vascular access surgery.* Eds. Wilson SE and Owens ML, Year Book Medical Publishers, 1980, pp 101-114.

PARTHASARATHY S, STEINBERG D and WITZTUM JL (1992) The role of oxidized low-density lipoproteins in the pathogenesis of atherosclerosis. *Ann. Rev. Med.* 43 219-225.

QUINTON WE, DILLARD DH and SCRIBNER BH (1960) Cannulation of blood vessels for prolonged hemodialysis. *Trans. Am. Soc. Artif. Intern. Organs* 6 104-113.

RAINES EW and ROSS R (1993) Smooth muscle cells and the pathogenesis of the lesions of atherosclerosis. *Br. Heart J.* 69 S30-S37.

REILLY DT, WOOD RFM and BELL PRF. A prospective study of the correlation between rheological factors and fistula failure. In: *Access Surgery*, Proceedings of the International Congress on Access Surgery, Maastricht, 22-24 April 1982. Eds. Kootsra G and Jörning PJG, Pub. MTP Press Ltd., 1983, pp 129-133.

REILLY DT, WOOD RFM and BELL PRF (1982) Prospective study of dialysis

fistulas: problem patients and their treatment. *Br. J. Surg.* 69 549.553.

ROSS R (1993) The pathogenesis of atherosclerosis: a perspective for the 1990s. *Nature* 363 801-809.

ROSS R (1986) The pathogenesis of atherosclerosis - an update. *N. Engl. J. Med.* 314 488-500.

ROSS R, GLOMSET J and HARKER L (1977) Response to injury and atherogenesis. *Am. J. Path.* 86 675-684.

SABIN FR (1917) Origin and development of the primitive vessels of the chick and of the pigs. *Contributions to Embryology, Carnegie Institute* 6-7 61.

SALLAM AM and HWANG HC (1984) Human RBC hemolysis in a turbulent shear flow: contribution of Reynolds shear stresses. *Biorheology* 21 783-797.

SALLAM TA, LUMSDEN AB, SUGGS WD and KU DN (1996) Low shear stress promotes intimal hyperplasia thickening. *J. Vasc. Invest.* 2 12-22.

SCHWARTZ CJ, VALENTE AJ and SPRAGUE EA (1993) A modern view of atherogenesis. *Am. J. Cardiol.* 71 9B-14B.

SCHWARTZ CJ, VALENTE AJ, SPRAGUE EA, KELLY JL and NEREM RM (1991) The pathogenesis of atherosclerosis: an overview. *Clin. Cardiol.* 14 1-16.

SCRIBNER BH, BURI R, CANER JEZ, HEGSTROM R and BURNELL JM (1960) The treatment of chronic uremia by means of intermittent dialysis: a preliminary report. *Trans. Am. Soc. Artif. Intern. Organs* 6 114-122.

SHALDON S (1969) The use of the arteriovenous fistula in home dialysis. *Proc. Eur. Dial. Transplant. Assoc.* 6 94-96.

SHORTLAND AP, BLACK RA, JARVIS JC and SALMONS S (1996) Technical note: a novel video technique for visualizing flow structures in cardiovascular models. *J. Biomech.* 29 239-244.

SHU MCS, NOON GP and HWANG NHC (1987a) Phasic flow patterns at a hemodialysis venous anastomosis. *Biorheology* 24 711-722.

SHU MCS, NOON GP and HWANG NHC (1987b) Flow profiles and wall shear stress distribution at a hemodialysis venous anastomosis: preliminary study. *Biorheology* 24 723-735.

SMITH RL, BLICK EF, COALSON J and STEIN PD (1972) Thrombus production by turbulence. *J. Appled Physiol.* 32 261-264.

SOTTIURAI VS, YAO JST, BATSON RC, LIM SUE S, JONES R and NAKAMURA YA (1989) Distal anastomotic intimal hyperplasia: histopathologic character and biogenesis. *Ann. Vasc. Surg.* 3 26-33.

SOTTIURAI VS, LIM SUE S, FEINBERG EL II, BRINGAZE WL, TRAN AT and BATSON RC (1988) Distal anastomotic intimal hyperplasia: biogenesis and etiology. *Eur. J. Vasc. Surg.* 2 245-256.

STARY HC, BLANKENHORN DH, CHANDLER AB, GLAGOV S, INSULL W Jr., RICHARDSON M, ROSENFELD ME, SCHAFFER SA, SCHWARTZ CJ, WAGNER WD and WISSLER RW (1992) A definition of the intima of human arteries and of its atherosclerosis-prone regions. *Arterioscler. Thromb.* 12 120-134.

STEHBENS WE (1992) The role of thrombosis and variants of the thrombogenic theory in the etiology and pathogenesis of atherosclerosis. *Prog. Cardiovasc. Dis.* 34 325-346.

STEHBENS WE and Karmody AM (1975) Venous atherosclerosis associated with arteriovenous fistulas for hemodialysis. *Arch. Surg.* 110 176-180.

STEHBENS WE (1974) Blood vessel changes in chronic experimental arteriovenous fistulas. *Surg. Gynecol. Obstet.* 127 327-338.

STEIN PD, WALBURN FJ and BLICK EF (1980) Damping effect of distensible tubes on turbulent flow: implications in the cardiovascular system. *Biorheology* 17 275-281.

STEIN PD and SABBAH HN (1974) Measured turbulence and its effect on thrombus formation. *Circ. Res.* 35 608-614.

STEINBRECHER UP, PARTHASARATHY S, LEAKE DS, WITZTUM JL and STEINBERG D (1984) Modification of low density lipoprotein by endothelial cells involves lipid peroxidation and degradation of low density lipoprotein phospholipids. *Proc. Natl. Acad. Sci. USA* 81 3883-3887.

SUTERA SP (1977) Flow-induced trauma to blood cells. *Circ. Res.* 41 2-8.

TAWA NE Jr. and TILNEY NL. Angioaccess in the renal failure patient. In: *Replacement of renal function by dialysis: a textbook of dialysis.* Third edition. Ed. Maher JF, Kluwer Academic Publishers, 1989, pp 218-228.

TORDOIR JHM, HOENEVELD H, EIKELBOOM BC and KITSLAAR JEHM (1990) The correlation between clinical and Duplex ultrasound parameters and the development of complications in arterio-venous fistulae for haemodialysis. *Eur. J. Vasc. Surg.* 4 179-184.

TORDOIR JHM, de BRUIN HG, HOENEVELD H, EIKELBOOM BC and

KITSLAAR PJEHM (1989) Duplex ultrasound scanning in the assessment of arteriovenous fistulas created for hemodialysis access: comparison with digital subtraction angiography. *J. Vasc. Surg.* 10 122-128.

TALUKDER N, FULENWIDER JT, MABON RF and GIDDENS DP (1986) Poststenotic flow disturbance in the dog aorta as measured with pulsed Doppler ultrasound. *J. Biomech. Eng.* 108 259-265.

VANDERWERF BA, WILLIAMS T and KOEP LJ. Haemodynamics of arteriovenous fistulas. In: *Access Surgery,* Proceedings of the International Congress on Access Surgery, Maastricht, 22-24 April 1982. Eds. Kootstra G and Jörning PJG, Pub. MTP Press Ltd., 1983, pp 129-133.

WALBURN FJ and STEIN PD (1981) Effect of vessel tapering on the transition to turbulent flow: implications in the cardiovascular system. *J. Biomech.* Eng. 103 116-120.

WALBURN FJ, BLICK EF and STEIN PD (1979) Effect of the branch-to-trunk area ratio on the transition to turbulent flow: implications in the cardiovascular system. *Biorheology* 16 411-417.

WEDGWOOD KR, WIGGINS PA and GUILLOU PJ (1984) A prospective study of end-to-side vs. side-to-side arteriovenous fistulas for haemodialysis. *Br. J. Surg.* 71 640-642.

WHEELER DC, SWENY P, VARGHESE Z and MOORHEAD JF. Hyperlipidaemia and atherosclerosis in chronic dialysis patients. In: *Replacement of renal function by dialysis: a textbook of dialysis.* Third edition. Ed. Maher JF, Kluwer Academic Publishers, 1989, pp 798-807.

WHITE GH. Planning and patient assessment for vascular access surgery. In: *Vascular access surgery: principles and practice.* 3rd Edition. Ed. Wilson SE, Mosby-Year Book Inc., 1996, pp 6-11.

WONG V, WARD R, TAYLOR J, SELVAKUMAR S, HOW TV and BAKRAN A (1996) Factors associated with early failure of arteriovenous fistulae for haemodialysis access. *Eur. J. Vasc. Surg.* 12 207-213.

ZWOLAK RM, ADAMS MC and CLOWES AW (1987) Kinetics of vein graft hyperplasia: association with tangential stress. *J. Vasc. Surg.* 5 126-136.